



TECHNISCHE
UNIVERSITÄT
WIEN

DIPLOMARBEIT

CFD Analysis of the solidification in the inlet area of a direct contact latent heat storage

zur Erlangung des akademischen Grades

Diplom-Ingenieur

im Rahmen des Studiums

Physikalische Energie- und Messtechnik

eingereicht von

Romeo

Ralón Rosales

Matrikelnummer 0925652

ausgeführt am Institut für Energietechnik und Thermodynamik
der Fakultät für Maschinenbau der Technischen Universität Wien

Betreuung

Betreuer: Ao. Univ. Prof. Dipl.-Ing. Dr. techn. Heimo Walter

Mitwirkung: Dipl.-Ing. Stefan Krimmel

Wien, 22.10.2019

(Unterschrift Verfasser/in)

(Unterschrift Betreuer/in)

MASTER THESIS

CFD Analysis of the solidification in the inlet area of a direct contact latent heat storage

executed for the purpose of obtaining the academic degree
of a Master of Science

under supervision of
Ao. Univ. Prof. Dipl.-Ing. Dr. techn. Heimo Walter

filed on the Technical University Vienna
Faculty of Technical Physics

from
Romeo Ralón BSc
Traunuferstraße 25c
4052 Ansfelden

Ansfelden, 10/22/2019

Foreword

This thesis is the finish of my studies in Physical Energy and Measurement Engineering and was written at the Institute of Energy Systems and Thermodynamics of the University of Technology Vienna. This document forms a part of the investigations on direct contact latent heat storages [9], [10], [19], which were developed in cooperation with the Lucerne University of Applied Sciences and Arts and would not have been possible without the resources of VSC-3 and the support of the team of the Vienna Scientific Cluster.

Special thanks to my supervisors Ao. Univ. Prof. Dipl.-Ing. Dr. techn. Heimo Walter and Dipl.-Ing. Stefan Krimmel for their continuing support from the beginning of the project until its very end.

Further I would like to thank the complete research team of the Institute of Energy Systems and Thermodynamics for their input and helpful ideas. I would especially like to emphasize Michael Kainz BSc, who worked on his master thesis during the same period and always took the time to exchange information on ANSYS Fluent.

My biggest thanks go to my parents Christine and Dipl. Ing. Romeo Ralón Rosales, who have always been there for me during my studies, especially during these last months of writing the thesis.

I would also like to give my thanks to my brother Felipe, who had plenty of ideas on how to improve the LaTeX template and has been a lot of help during the writing of this thesis.

Abstract

The aim of this master thesis was to create a computer model in ANSYS Fluent with the intention of evaluating the droplet formation of the properties of the thermal oil D12 in a direct contact latent heat storage with the properties of water and water-TBAB during the solidification process of the storage material. The thesis will introduce the reader into the basics of the jet and droplet formation and briefly explain the used model before presenting and discussing the results of the parameter study.

As computational fluid dynamic calculations need a significant amount of PC resources, the model was created to fit just the incoming stream and the first droplet. Setting the complete top wall of the model geometry as outlet resulted in back-flow conditions effecting the heat flux on a great scale. For the parameter study, the so-called mushy parameter for solidification, the inlet temperature and the inlet velocity were varied. 5 of 11 calculations experienced similar behaviour and no sufficient solidification, 2 calculations showed a behaviour contradicting global laws of physics. Of the 4 calculations with exploitable data only 2 experienced a solidification process slow enough to be evaluated fully. The other 2 could not be completely resolved due to a saving interval of 0.5s caused by the intention of minimizing necessary disk space.

The results show that CFD calculations can be used for modelling the solidification in a direct contact latent heat storage, although the boundary conditions have to be set carefully.

Kurzfassung

Ziel dieser Diplomarbeit war es, ein Computermodell in ANSYS Fluent zu erstellen, um die Tröpfchenbildung der Eigenschaften des Thermoöls D12 in einem Latentwärmespeicher mit den Eigenschaften von Wasser und Wasser-TBAB während des Erstarrungsprozesses des Speichermaterials zu analysieren. Die Arbeit führt den Leser in die Grundlagen der Strahl- und Tröpfchenbildung ein und erklärt kurz das verwendete Modell, bevor die Ergebnisse der Parameterstudie vorgestellt und diskutiert werden.

Da strömungsdynamische Simulationen eine beträchtliche Menge an PC-Ressourcen benötigen, wurde das Modell auf die notwendige Größe für den eingehenden Strahl und den ersten Tropfen zugeschnitten. Das Einstellen der kompletten oberen Wand des Modells als Auslass führte zu Rückströmungsbedingungen, die den Wärmestrom in großem Maßstab beeinflussten. Für die Parameterstudie wurden der sogenannte Mushy-Parameter für die Erstarrung, die Eintrittstemperatur und die Eintrittsgeschwindigkeit variiert. 5 von 11 Berechnungen zeigten ein ähnliches Verhalten und keine ausreichende Erstarrung, 2 Berechnungen zeigten ein Verhalten, das den Grundgesetzen der Physik widerspricht. Von

den 4 Berechnungen mit auswertbaren Daten erfuhren nur 2 einen Erstarrungsprozess, der langsam genug war, um vollständig ausgewertet zu werden. Die anderen 2 konnten aufgrund eines Speicherintervalls von 0,5 s, mit der Absicht, den erforderlichen Festplattenspeicher zu minimieren, nicht vollständig aufgelöst werden.

Die Ergebnisse zeigen, dass CFD-Berechnungen zur Modellierung der Erstarrung in einem direkt Latentwärmespeicher verwendet werden können. Allerdings müssen dafür die Randbedingungen sorgfältig eingestellt werden.

Contents

1	Introduction	1
2	Thermal Energy Storage - Overview	2
2.1	Common thermodynamic difficulties in a latent heat storage	6
2.2	Pros and cons of a direct contact heat storage compared to a pipe heat exchanger	6
3	Describing the flow and the solidification	8
3.1	Droplet behaviour	8
3.2	Temperature change	10
3.3	Phase change	11
3.4	A global energy equation	13
4	Modelling fluid flow	16
4.1	Governing equations	16
4.2	Formation and Breakup of Fluid Particles	20
5	The computer model	23
5.1	Coordinate System	23
5.2	Solidification - The Mushy Parameter	24
5.3	Set-up	26
5.3.1	Material Properties	26
5.3.2	Geometry and Mesh	28
5.3.3	Calculation Settings	29
5.4	Energy balance	30
6	Final preparations for the parameter study	34
6.1	Computational Resources needed	34
6.2	Results of the comparison of the main mesh sizes	35
6.3	Discussion of the comparison of the main mesh sizes	45
6.4	Reproducibility	48
6.5	Final Model Changes	51

7	Parameter Study	55
7.1	The base model	56
7.2	Mushy-Parameter variations	65
7.3	Inlet Temperature variations	77
7.4	Inlet Velocity variations	91
7.5	Results Summary	97
8	Conclusion and Outlook	98
	Appendices	100
A	Data Sheet for Therminol D12	100
B	Model choosing process	102
B.1	Geometry and mesh	102
B.2	time-step-size	105
C	Full Scale Diagrams of the parameter study	106

List of Figures

1	Scheme of the real life model used by Andreas Anmann for his experiments [9]	5
2	Stream and delayed droplet formation at around $5 \cdot 10^{-6} \frac{\text{m}}{\text{s}}$ for oil in water [22]	9
3	Droplet behaviour for an inlet velocity of around $2 \cdot \frac{\text{m}}{\text{s}}$ [22]	10
4	Image showing the frozen heat exchanger [9]	12
5	Coalescent behaviour, milk coloured transition phase during water solidification [9]	12
6	Strong foaming, crystallization around temperature sensors, cables [9]	14
7	Conduits left behind by HTF, porous structure [9]	14
8	Solidification of PCM, pushed to top from HTF [9]	14
9	Sketch showing a non-isotropic surface for the geometric derivation of the Young-Laplace-Equation	19
10	Dimensionless jet length plotted by orifice flow rate or velocity showing a typical jet development categorized into different stages. 7.4	21
11	Total heat transfer for $\Delta T = 1 \text{ K}$, $\Delta T = -11.6 \text{ K}$	31
12	Heat flux at outlet, corresponding volume fraction at 5.720 s	32
13	Surface area for $\Delta x = 0.1, 0.3 \text{ mm}$ in H_2O	35
14	Liquid fraction for $\Delta x = 0.1, 0.3 \text{ mm}$ in H_2O	36
15	Volume fraction for $\Delta x = 0.1, 0.3 \text{ mm}$ in H_2O	36
16	Image series showing a visualisation of the model with D12 and H_2O for 0.1 mm	37
17	Visualisation of the local-liquid-fraction at the centred xy-plane	38
18	Image series showing a 3D visualisation of the model with D12 and H_2O for 0.3 mm	39
19	Surface area for $\Delta x = 0.1, 0.3 \text{ mm}$ in PCM2	40
20	Liquid fraction for $\Delta x = 0.1, 0.3 \text{ mm}$ in PCM2	41
21	Volume fraction for $\Delta x = 0.1, 0.3 \text{ mm}$ in PCM2	41
22	Image series showing a 3D visualisation of the model with D12 and PCM2 for 0.1 mm	42
23	Local liquid-fraction on the centred plane for PCM2 at 25s	43
24	Image series showing a 3D visualisation of the model with D12 and PCM2 for 0.3 mm	44

25	Surface area from the calculation started at $t = 0$ s in comparison to a calculation started at the first time step	49
26	Visualisation of the jet breakup and droplet formation from CFD-simulations for droplet on demand ink-jet printers by Wang [27]	52
27	Image series showing a 2D visualisation of different contact angles	53
28	First 2 s of the surface area for the base model	57
29	Liquid-fraction for the base model	57
30	First 2 s of the volume-fraction for the base model	57
31	Heat transfer at the inlet for the base model	57
32	First 2 s of the heat transfer at the outlet, as well as the sum of inlet and outlet, for the base model	58
33	First 2 s of the heat flux	58
34	Screen-shot of the heat-flux contour on the outlet of the base model at 25 s	59
35	Screen-shot of the heat-flux contour on the outlet of the base model at 25.5 s	59
36	Outlet temperature side by side with the corresponding volume fraction of the base model	60
37	Heat flux side by side with the corresponding volume fraction of the base model	60
38	FFTs of the base model	61
39	Average temperature of PCM2 of the base model	62
40	Average temperature of D12 of the base model	62
41	Liquid-fraction for different mushy parameters	66
42	Screen-shot sequence of the total-liquid-fraction for the solidification steps with $A_{mush} = 10^6$	67
43	Screen-shot sequence of the total-liquid-fraction for the solidification steps with $A_{mush} = 10^9$	68
44	Volume-fraction for different mushy parameters	69
45	First 20 s of the heat flux for different mushy parameters	69
46	Screen-shot of a visualisation of the heat transfer at the outlet at 19 s for $A_{mush} = 10^6$	71
47	Screen-shot of a visualisation of the heat transfer at the outlet at 20 s for $A_{mush} = 10^9$	71
48	Amplitude and frequency of the Fourier transformations of $A_{mush} = 10^6$	72
49	Average temperature of PCM2 for different mushy parameters	72

50	Average temperature of D12 for different mushy parameters	72
51	Liquid-fraction for different inlet temperatures	78
52	Screen-shot sequence of the total-liquid-fraction for the solidification steps with $\Delta T = -15$ K	79
53	Screen-shot sequence of the total-liquid-fraction for the solidification steps with $\Delta T = -20$ K	80
54	Volume-fraction for different inlet temperatures	81
55	Heat flux for different inlet temperatures	82
56	Screen-shot of a visualisation of the heat flux at the outlet at 43.5 s for $\Delta T = -20$ K	83
57	Amplitude and frequency of the FFTs of $\Delta T = -15$ K	84
58	Average temperature of PCM2 for different inlet temperatures	85
59	Average temperature of D12 for different inlet temperatures	85
60	Liquid-fraction for different inlet velocities	91
61	Screen-shot sequence of the total-liquid-fraction for the solidification steps with $v_{in} = 0.2 \frac{m}{s}$ K	92
62	Screen-shot sequence of the total-liquid-fraction for the solidification steps with $v_{in} = 0.3 \frac{m}{s}$ K	93
63	Volume-fraction for different inlet velocities	94
64	First 6 s of the heat flux for different inlet velocities	94
65	Average temperature of PCM2 for different inlet velocities	95
66	Average temperature of D12 for different inlet velocities	95
67	Droplet formation of D12 in water in a 2D axisymmetric model	102
68	Droplet formation for different geometry and Δx	104
69	Front view ($z = 5$ mm) of the same calculation at the same time for different Δt	105
70	First 2 s of the surface area for the base model	106
71	Liquid-fraction for the base model	107
72	First 2 s of the volume-fraction for the base model	108
73	First 0.1 s of heat transfer at the inlet for the base model	109
74	First 2 s of the heat transfer at the outlet, as well as the sum of inlet and outlet, for the base model	110
75	First 2 s of the heat flux for the base model	111
76	Outlet temperature side by side with the corresponding volume fraction . .	112

77	Heat flux side by side with the corresponding volume fraction	113
78	Amplitude and frequency of the Fourier transformations from the base model calculation	114
79	Average temperature of PCM2	115
80	Average temperature of D12	116
81	First 2 s of the heat transfer coefficient	117
82	A comparison of the liquid-fraction for different mushy parameters	118
83	A comparison of volume-fraction for different mushy parameters	119
84	First 20 s of the heat flux for different mushy parameters	120
85	Amplitude and frequency of the Fourier transformations of 10^6	121
86	Average temperature of PCM2 for different mushy parameters	122
87	Average temperature of D12 for different mushy parameters	123
88	A comparison of the liquid-fraction for different inlet temperatures	124
89	A comparison of the volume-fraction for different inlet temperatures	125
90	Heat flux for different inlet temperatures	126
91	Amplitude and frequency of the Fourier transformations of $\Delta T = -15 \text{ K}$	127
92	Average temperature of PCM2 for different inlet temperatures	128
93	Average temperature of D12 for different inlet temperatures	129

List of Tables

1	Important parameters in a real life model of a direct contact latent heat storage	7
2	Material properties of H ₂ O, D12 and water-TBAB	26
3	Material properties used for PCMs and HTF	27
4	Important values from fig. 11	31
5	A comparison of calculation times on VSC3 of different mesh sizes	34
6	Important values of the surface area for $\Delta x = 0.1, 0.3$ mm from fig. 13 . .	36
7	Important values of the liquid fraction of $\Delta x = 0.3$ mm from fig. 14	36
8	Important values of the volume fraction of $\Delta x = 0.1, 0.3$ mm from fig. 15	36
9	Important values of the surface area for $\Delta x = 0.1, 0.3$ mm from fig. 19 . .	41
10	Final values of the liquid fraction of $\Delta x = 0.1, 0.3$ mm from fig. 14	41
11	Important values of the volume fraction of $\Delta x = 0.1, 0.3$ mm from fig. 15	41
12	Relative changes of additional calculations compared to the first for H ₂ O and PCM2 with 0.1 mm and 0.3 mm mesh	50
13	Geometric results for different contact angles, as seen in fig. 27	51
14	Parameters varied for the parameter study	56
15	Important values of the liquid fraction for the calculations with different A_{mush} in fig. 41	65
16	Important values of the average volume fraction for the calculations with A_{mush}	69
17	Average heat fluxes for all calculations in fig. 45, as well as the corresponding values for hand calculations	70
18	Changes in the behaviour of the PCM temperature in fig. 49	73
19	Important values of the liquid fraction for different ΔT	78
20	Important values of the volume fraction for different ΔT	82
21	Important values of the heat flux for different ΔT	83
22	Changes in the behaviour of the PCM temperature in fig. 58	85
23	Important values of the liquid fraction for the calculations with $\Delta T = -15$ K and $A_{mush} = 10^6$	86
24	Time-steps of the changes in the behaviour of the PCM temperature for the calculations with $\Delta T = -15$ K and $A_{mush} = 10^6$	87
25	Important values of the liquid fraction for the calculations with $v_{in} = 0.2, 0.3 \frac{m}{s}$	91

26	Important values of the volume fraction for the calculations with $v_{in} = 0.2, 0.3 \frac{\text{m}}{\text{s}}$	94
27	Important values of the heat flux fraction for the calculations with $v_{in} = 0.2, 0.3 \frac{\text{m}}{\text{s}}$	94
28	Changes in the behaviour of the PCM temperature in fig. 65	95
29	Results for the variations of the mushy parameter	97
30	Results for the variations of the inlet temperature	97
31	Results for the variations of the inlet velocities	97
32	Geometric measurements of fig. 68	104
33	Geometric measurements of fig. 69	105

Formula symbols of latin letters

Symbol	SI-Unit	Meaning
a	m	amplitude
A	m^2	surface area
A_1	—	temperature independent constant
A_{mush}	—	Mushy Parameter, defining the solidification
B_1	—	temperature independent constant
c	$\frac{\text{J}}{\text{kgK}}$	specific heat capacity
c	$\frac{\text{mol}}{\text{V}^3}$	concentration
D	$\frac{\text{m}^2}{\text{s}}$	diffusivity constant
E	J	total energy
g	$\frac{\text{m}}{\text{s}^2}$	gravitational constant
h	$\frac{\text{J}}{\text{kg}}$	specific enthalpy
H	J	enthalpy
J	$\frac{\text{mol}}{\text{m}^2\text{t}}$	diffusion flux
k	$\frac{\text{W}}{\text{m}^2\text{K}}$	thermal transmittance
k_E	$\frac{\text{J}}{\text{Kmol}^{\frac{2}{3}}}$	Eötvös Constant
K	N	momentum from external sources
l	—	liquid fraction
L	m	length
m	kg	mass
\dot{m}	$\frac{\text{kg}}{\text{s}}$	mass flow
n	—	number of cells
p	Pa	pressure
P	W	power from surrounding sources
q	$\frac{\text{W}}{\text{m}^2}$	heat flow per surface area unit
Q	J	heat
\dot{Q}	W	heat flow
r	m	radius
S	$\frac{\text{kg}}{\text{s}}$	Carman-Koseny parameter
t	s	flow time
Δt	s	time between each data point
T	K	temperature
T_Θ	K	material specific temperature by Eötvös
ΔT	K	inlet temperature minus solidification temperature

(wird fortgesetzt)

Symbol	SI-Unit	Meaning
u	$\frac{\text{J}}{\text{kg}}$	specific internal energy
U	J	internal energy
v	$\frac{\text{m}}{\text{s}}$	velocity
\mathbf{v}	$\frac{\text{m}^3}{\text{kg}}$	specific volume
V	m^3	Volume
x	m	axial coordinate defining the width
Δx	m	mesh cell width in all directions
y	m	axial coordinate defining the height
z	m	axial coordinate defining the depth

Formula symbols of Greek letters

Symbol	SI-Unit	Meaning
α	$\frac{\text{W}}{\text{m}^2\text{K}}$	average heat transfer coefficient
δ	—	identity matrix
ϵ	—	dampening factor
ϕ	°	contact angle to bottom wall
μ	Pas	dynamic viscosity
ν	$\frac{\text{m}^2}{\text{s}}$	kinematic viscosity
λ	$\frac{\text{W}}{\text{mK}}$	heat conductivity
ρ	$\frac{\text{kg}}{\text{m}^3}$	density
σ	Pa	surface tension
τ	Pa	internal friction stresses
υ	—	volume fraction
ω	Hz	angular frequency

Textsubscript Indexes

Index textsub- script	Meaning
0	value at initialisation of the simulation
<i>a</i>	value at ascension
<i>at</i>	value for atomisation at the orifice
<i>A</i>	amplitude of Fast Fourier Transformation of transient value
<i>C</i>	critical value
<i>d</i>	value for the droplet of the heat transfer fluid
<i>D12</i>	heat transfer fluid D12
<i>e</i>	equivalent value
<i>fr</i>	value for friction
<i>G</i>	value for gravity
<i>HTF</i>	heat transfer fluid
<i>in</i>	value at the inlet
<i>jet</i>	value at the jet
<i>l</i>	liquid phase
<i>loss</i>	losses
<i>m</i>	value at the melting point
<i>max</i>	maximum value
<i>melt</i>	value at the melting point
<i>mol</i>	value for 1 mol
<i>noz</i>	value at the nozzle
<i>or</i>	value at the orifice
<i>out</i>	value at the outlet
<i>p</i>	value at constant pressure
<i>ref</i>	reference value
<i>rev</i>	value for a reversible process
<i>PCM</i>	phase change material
<i>PCM2</i>	phase change material number 2
<i>s</i>	solid phase
<i>save</i>	difference between two saved data files
<i>t</i>	technical
<i>V</i>	value at constant Volume
<i>wall</i>	average value on the walls of the model
+	average over all positive values

Textsuperscript Indexes

Index	Meaning
Textsu- per- script	
<i>back</i>	value for resulting back-flow
–	average value
→	vector
<i>T</i>	transposed

Shortcuts

Shortcut	Meaning
2D	2 Dimensional
3D	3 Dimensional
CFD	Computational Fluid Dynamics
HTF	Heat Transfer Fluid
Nu	Nusselt-Number
Re	Reynolds-Number
PCM	Phase Change Material
TBAB	Tetra-Butyl-Ammonium-Bromide
TES	Thermal Energy Storage
UV	Ultra-Violet
VOF	Volume Of Fluid method

1 Introduction

Working with a real life model of a direct contact latent thermal storage can be an expensive and difficult task. With modern computer power and tools like ANSYS Fluent it is possible to create simulations of specific situations in order to understand the fluid-dynamics and thermal behaviour of the materials on a simpler and more efficient basis. A model of a complete storage would, however, still be too extense and exceed available resources due to necessary high local and time resolution. Computer simulations can be viewed as a good addition to experimental research but still not as a replacement. This is why CFD simulations focus in general on one or two specific and interesting features only.

This thesis builds upon experimental research from Krimmel [19] and Anmann [9] examining solutions with two different fluid materials. A direct contact thermal storage has in general more efficient heat transfer and control of heat than a thermal storage with indirect contact solutions. On the downside the fluid-dynamic and thermodynamic behaviour of the fluids can result in difficulties. When examining two fluid solutions, one is used as a storage material and the other for heat transfer. This means that the storage material always has to stay in the tank and the heat transfer fluid, in short HTF, has to enter and leave again, while interacting with the storage material for storing or withdrawing thermal energy. This however, leads to fluid-dynamical difficulties, as these two fluids should be able to interact with each other without actually mixing. Due to heat exchange, solidification or melting of the storage material is part of the process. The differences in the material properties can lead to interesting behaviour, like small droplets of the storage material emulsifying into the heat transfer fluids. It is also possible that the heat transfer fluid gets surrounded by solidified storage material and the formed structure gets moved through the other still fluid parts of the storage due to the currents. The task of this thesis was not only to get an impression of the simulation of different parameters but also to evaluate if these real life model difficulties can also appear in the simulation.

In previous research by Anmann [10] a computer simulation of an oil droplet moving through the storage was created in a 2D axissymmetric model but no computer simulation on the incoming stream was done. As a contrast, this thesis focuses on the solidification on the area near the inlet during the droplet formation. The model was created in 3 dimensions to experience a broader range of thermodynamic and fluid-dynamic influences on the stream and droplet behaviour of Therminol D12 in water and a storage material using similar properties of water and a combination of water with tetra-butyl-ammonium-bromide. The original intention was not only to include the nozzle but to simultaneously be able to evaluate the heat transfer fluid shortly before leaving the tank. This did, however, not work with every storage material and will be explained further in this theses.

2 Thermal Energy Storage - Overview

The following discussion of the required basic terminology, when working with thermal storages has been adapted to the structure of the book "Kältespeicher" by Thorsten Urbaneck [26] with minor changes and additions from other sources, specified when applied.

- **Thermal Energy Storage - TES**

"An apparatus, a construction or a geological structure for storing thermal energy. Depending on the type of application it is distinguished between hot and cold storages." As the name says, a hot storage is for storing "positive" heat, a cold storage for storing "negative" heat. This means the temperature difference between the storage material and the heat transport fluid is exactly the opposite. In this thesis the topic is the solidification process. This means that the heat transfer fluid enters the storage with a lower temperature and takes heat from the storage material. The sign of the heat transfer has therefore to be negative. A thermal energy storage is composed out of four different units, divided by function.

Storage material: This can be of liquid or of solid type. A prominent fluid example would be water, due to its high heat capacity. Water is used for both, a hot and a cold storage, the later is possible due to its tendency to super-cool, meaning it cools below the solidification temperature before solidifying, until $T = -38^\circ\text{C}$. [26] Another option can be a mixture of 60 % water and 40 % tetra-butyl-ammonium-bromide (TBAB). The resulting compound has still similar properties like density but loses the anomaly of plain simple water. Water-TBAB compresses during solidification, starting at 11.8°C , therefore increasing in density and sinking to the ground. This properties should prevent the outlet from freezing and minimize thermal losses through the walls. Sadly the properties of water-TBAB are not well known and TBAB is a material also used for phase transfer catalysis, leading to the possibility of parts of the heat transfer fluid (HTF, used for the heat exchange with the storage material) moving into the fluid phase. [9]

Charging and discharging system: The necessary components for energy supply and extraction, such as heat exchanger and pumps.

Storage tank wall construction: The wall is an important component, as its function is the inclusion of the storage material, including suppression of convection and diffusion, mechanical stability, minimization of thermal losses due to thermal damping and shielding the system from environmental influences, such as air humidity, rain water, ground water and UV-Rays.

Long life materials, such as stainless steel, are used as walls. [25]

Additional equipment for safety and against corrosion, as well as additional mechanical components are needed, just to name a few.

- **Internal energy**

The internal energy of the storage material changes by energy transfers at the boundaries via the following methods: Temperature change, phase change, ad- or ab-/desorption, as well as reversible chemical reactions.

- **Loading and unloading**

A fluid material is used to transfer the thermal energy to and from the storage. It is therefore called a Heat Transfer Fluid (HTF). In direct loading solutions the HTF is inserted directly into the same storage on one side, depending on the density. In the model of this project the HTF has a lower density as the used storage material and has therefore to be inserted at the bottom to ascend to the top. The resulting heat flow \dot{Q} is described through the mass stream \dot{m} , the specific heat of the HTF c_{HTF} and the temperature difference between inlet T_{in} and outlet T_{out} :

$$\dot{Q} = \dot{m}c_{HTF}(T_{out} - T_{in}), \quad (1)$$

where $\dot{Q} > 0$ for loading a heat storage or unloading a cold storage and $\dot{Q} < 0$ for unloading a heat storage or loading a cold storage. There exist also indirect loading solutions, which will not be explained here but can be reviewed in [25].

- **Energy losses**

External: Streams of heat, enthalpy and / or mass over the system boundary. This includes thermal conduction through the storage walls and leaking of the storage material. The change of the internal energy U of the storage is therefore the sum of all changes, heat transfers at the inlet and outlet $\dot{Q}_{in,out}$ and changes in the heat losses \dot{Q}_{loss} :

$$\Delta U = \int (\dot{Q}_{in} + \dot{Q}_{out} + \dot{Q}_{loss})dt \quad (2)$$

Internal: Balancing effects in the storage, mixing and heat transfers of other parts in the storage produce a rise in its entropy. Then the limitation of the unloading process can be reached faster due to a lower storage temperature at the same capacity.

Depending on the thermal behaviour there are two types of classifications for heat storages[4]:

- **Sensible heat storage**

A sensible heat storage is a storage using a material that changes it's temperature but does not undergo a phase transition.

- **Latent heat storage**

In this storage type the material used undergoes a phase change and is therefore called phase change material (PCM). During the phase transition the energy density is high and the temperature stays constant, as no further heat can be absorbed or ejected, until the phase transition is complete. Of course, to reach the point of the phase change heat transfer is necessary, originating in a temperature gradient through interaction with the HTF. The PCM and the HTF can be separated by some solid material in the form of plates, spheres, cylinders or micro capsules, although there also exist direct contact solutions. There the used HTF has to be matched in it's properties to the PCM. Additional to the density already mentioned it is important that the two fluids don't mix with each other, as the PCM should stay in the tank for storing thermal energy, while the HTF has to leave the tank again for transport. This means that both materials have to be of opposite lipophilic / -phobic grade and therefore hydrophobic / -philic grade. During the phase transition the energy density is high and the temperature stays constant, as no further heat can be absorbed or ejected until the phase transition is complete. Of course, to reach the point of the phase change heat transfer is necessary, originating in a temperature gradient through interaction with the HTF. The PCM and the HTF can be separated by some solid material in the form of plates, spheres, cylinders or micro capsules, although there also exist direct contact solutions. There the used HTF has to be matched in it's properties to the PCM. Additional to the density already mentioned it is important that the two fluids don't mix with each other, as the PCM should stay in the tank for storing thermal energy, while the HTF has to leave the tank again for transport. This means that both materials have to be of opposite lipophilic / -phobic grade and therefore hydrophobic / -philic grade.

The PCM undergoes, in general, the phase transition solid-fluid, to be able to control the volume increase in closed storage tanks. However, there do exist thermochemical storages that are based on the fluid-gas transition, e.g. with using silica gel. [9]

Fig. 1 shows a schematic of the function of a direct contact latent heat storage including all necessary components. This was one of the preliminary studies working as fundamentals for computer simulations of this research group in [10]. There, the task was to model and analyse the fluid flow of a direct contact latent heat storage by use of the properties for a thermal oil as HTF and water-TBAB as PCM. Furthermore a comparison of different types of computer models was done. More importantly the volume of fluid method is

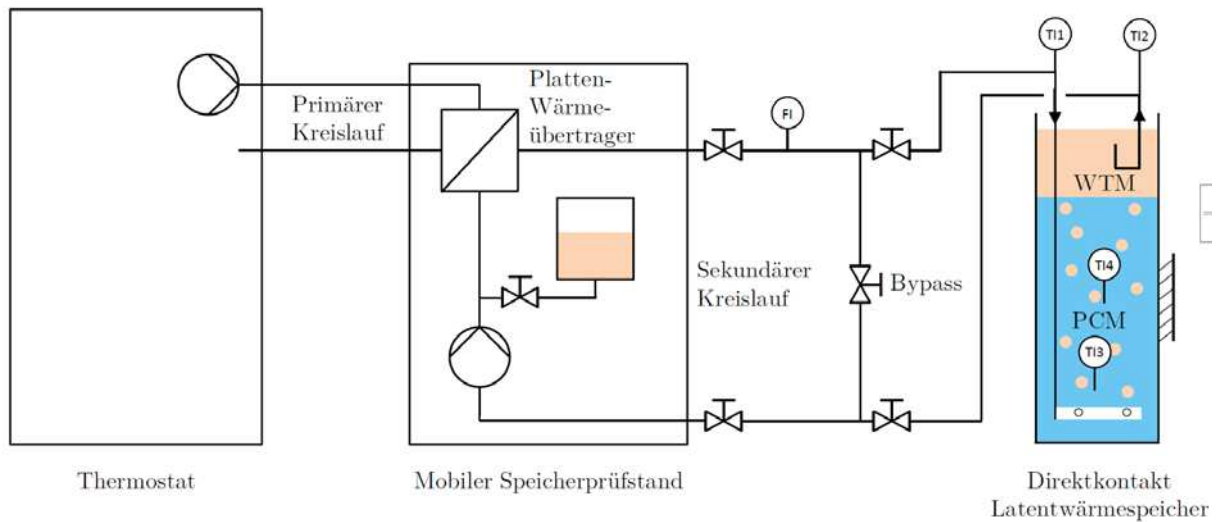


Figure 1: Scheme of the real life model used by Andreas Anmann for his experiments. The system is composed out of three parts, from left to right: A thermostat (primary circuit - "Primärer Kreislauf") as heat source, the storage test rig (secondary circuit - "Sekundärer Kreislauf"), for isolating the storage from the thermostat, and the thermal storage, including the inlet ($T/3$) and the outlet ($T/2$). The system includes multiple pumps for moving the HTF ("WTM"). The HTF is inserted at the top through a pipe ($T/1$), where it exits at the bottom, to ascend through the PCM in droplet form, where it is extracted. [9]

explained, that calculates every value of each cell according to a factor specifying the relative amount of each phase.

The present project will focus on simulating and evaluating the thermodynamic processes of cooling and solidification in the area of the incoming jet and the forming droplet by using the properties of a thermal oil with a lower viscosity compared to [10] and a PCM with the density and melting enthalpy of water-TBAB. Additionally one simulation using the properties of clean simple water will be discussed for comparison purpose.

For the solidification process it is important to state that ANSYS Fluent is not able to really calculate a phase change, it simply set the viscosity of the fluid to infinity and adjusts the liquid fraction, a factor specifying the relative amount of "liquid" volume for each phase in each cell. For optimal reading the quotation marks will be left out in the rest of this thesis. Nevertheless it is emphasized that even a completely solidified cell is actually still fluid according to ANSYS Fluent. The expansion of the solidification front is calculated by a hardly understood parameter, called Mushy Parameter A_{mush} , that is not explained in the manual of the program. This parameter will be introduced with the results and discussion of a research by Kheirabadi et al. according to [13] and be monitored and discussed closely with other important thermal results from this parameter study.

2.1 Common thermodynamic difficulties in a latent heat storage

A main problem of a latent heat storage according to [25] is the heat transfer during unloading. When using conventional heat exchanger in the tank its surfaces become the coolest parts during the energy out-take and therefore the parts where the PCM crystallizes firstly. This leads, however, to a decrease in the heat transfer, with further reduction in faster time. One idea for a solution was to split the PCM into multiple parts by using plates placed 1 cm away from each other, with high heat transfer coefficients connected to the heat exchanger. Then the heat can be transported through the crystal layers with the help of these plates. Due to additional parts in the tank the volume of the used PCM is lower and therefore the storage capacity decreases. A main problem encountered was the sedimentation of the solid phase due to the different densities.

When using water as PCM one has to take the so called "anomaly of water" into account. Due to the lower density of solid ice in comparison to fluid water the ice does not drop to the bottom but instead creates a boundary layer in between the HTF and the still fluid water. Due to the density gradient the frozen water ascends to the top, possibly blocking the outlet completely. It can also happen that the solidification does not start at the top but at the bottom, to be precise at the inlet. Then it is possible for the HTF to get in direct contact with the fluid. This drastically decreases the heat exchanging capabilities of the system.

2.2 Pros and cons of a direct contact heat storage compared to a pipe heat exchanger

The list containing pros and cons was found in [9] and translated into English by the author of this thesis. All original sources were confirmed and stated.

- + Better control of the heat power [25]
- + HTF temperature stays constant [26]
- + Factor heat transfer power to storage volume is bigger [9]
- + More efficient heat transfer due to smaller temperature gradient [26]
- + Convection of the HTF stirs the PCM, preventing segregation [25], [26]
- + Hardly any subcooling or none at all when using salt hydrates [25]
- Needs additional control mechanisms [9]
- HTF needs additional pumps [9]
- Contamination of the PCM through the HTF [9]

Last but not least for this section a short table of all parameters to be taken into account, when working with a real life model of a direct contact heat exchanger presented in tab. 1

parameter	location	variable
mass stream	rotary pump	yes
	throttle valve	yes
number of droplets	mass stream	yes
	inlet diameter	no
	number of inlets	no
size of droplets	mass stream	yes
	inlet diameter	no
ascension time	storage height	no
	viscosity difference	no
inlet temperature	mixing valve	yes
temperature difference between inlet and outlet	ascension time	no
heat transfer power	mass stream	yes
	ascension time	no
	viscosity PCM	no
	viscosity HTF	no

Table 1: Important parameters in a real life model of a direct contact latent heat storage. To clarify, when a value is defined constant this means that it stays constant when using the same (geometrical) set-up. The table belongs to fig. 1 and was translated by the author of this thesis.

3 Describing the flow and the solidification

3.1 Droplet behaviour

This chapter will describe the droplet flow from it's creation around it's ascension through the PCM until it leaves the storage at the outlet. This includes fluid mechanical equations, as well as qualitative observations of size, velocity and flow of droplets of different types of HTF from other researchers. All mentioned experiments describe at least one of the materials used in this project: the PCM water and water-TBAB and the HTF Therminol D12 and Therminol ADX10 products from the company Fragol.

When the HTF enters the storage it's parameters are defined from the mass flow and the diameter of the inlet. After some time a droplet builds that will eventually drop off the stream. From this moment on, the droplet is in equilibrium with it's surroundings. To be specific, the ascension force in direction of the outlet counterweights gravity, which is in direction of the inlet at the bottom. The effect of the ascension force, however, gets reduced due to the action of friction. As described in [15] the friction force is defined by Stokes' Law, the gravitational force depends on the density of the material itself and the ascension force is calculated by the pressure gradient and the density of the surrounding fluid:

$$F_{fr} = 6\pi\mu r v \quad (3)$$

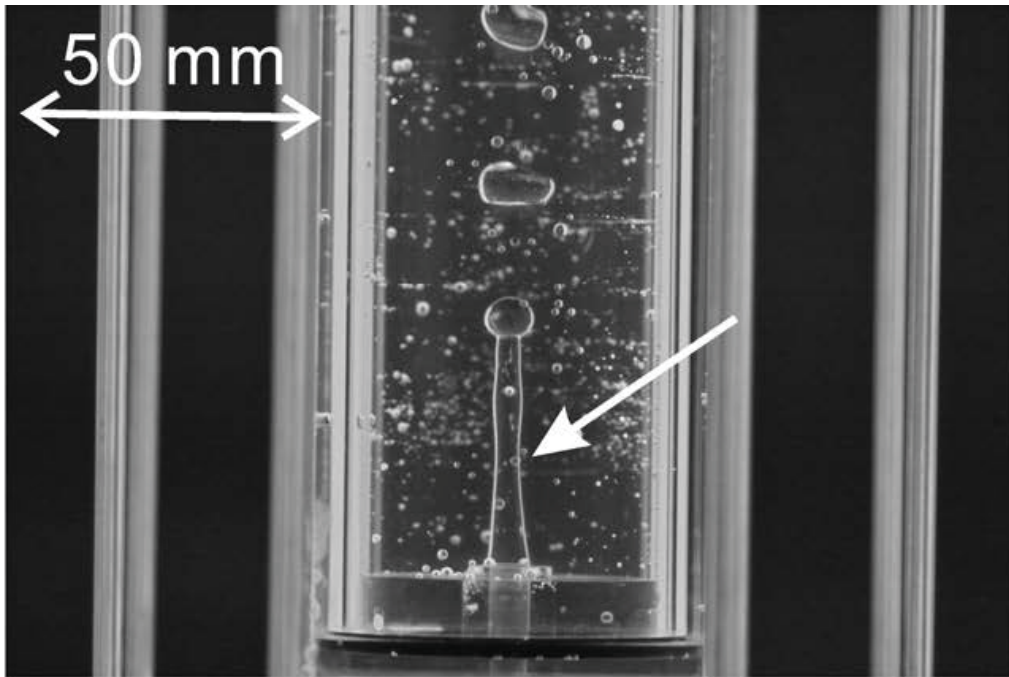
$$F_G = \rho_d V g \quad (4)$$

$$F_a = (\rho_{PCM} - \rho_{HTF}) g A y = \Delta\rho g V \quad (5)$$

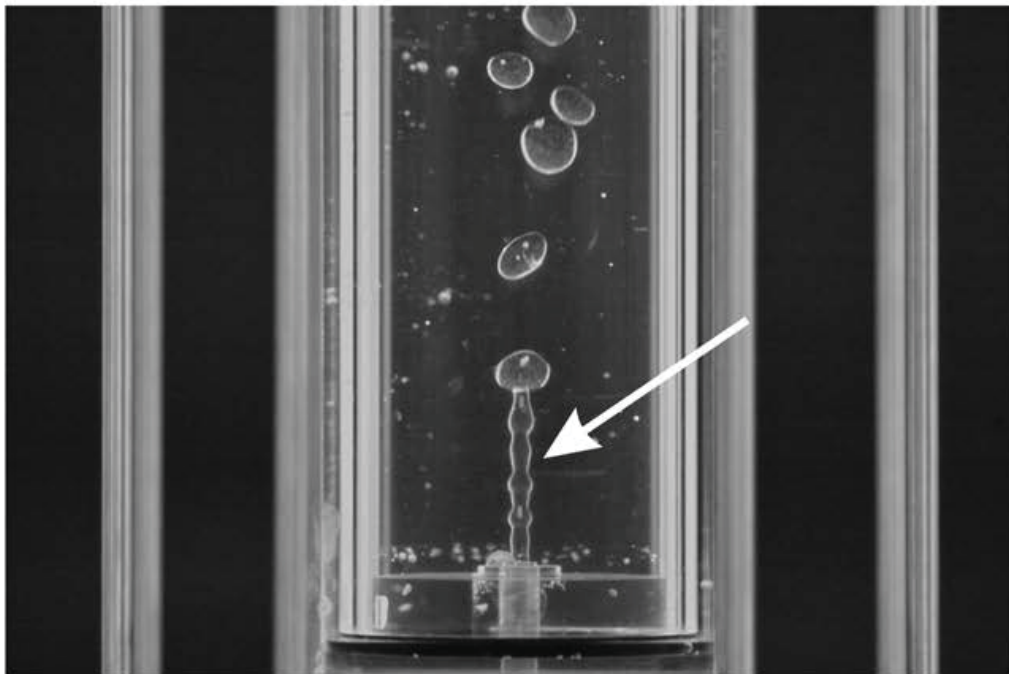
Nogami et al. [22] researched the droplet formation of an oil in water and sodium acetate trihydrate in dependence of the nozzle geometry. They state that the droplet diameter is directly proportional to the diameter of the nozzle, as seen in fig. 2. The droplet number is indirectly proportional to the inlet velocity and therefore to the mass stream. For high flow rate there is an incoming stream from which droplets detach after some time. When lowering the flow rate the HTF splits into droplets immediately after entering the storage, resulting in a flow of atomized droplets. When these droplets are big enough, however, they accumulate and build a thick cluster around the inlet that increases for lower flow rate. (fig. 3) When inserting (3) and (4) into (5) one realizes that gravity and ascension exist basically in the same form, only dependent on different densities. After further forming of this equation this leads to the following result for the ascension velocity of the HTF droplets:

$$v_a = \frac{2}{9} \frac{r_d^2 g}{\mu_{PCM}} (\rho_d - \rho_{PCM}) \quad (6)$$

Lindner and Scheuman investigated the droplets during their ascension in their report. [25] They used a glass storage tank with the dimension (300, 220, 240) mm that was filled to around 60% with sodium sulphate. The used HTF were the thermal oils



(a) d_{noz} : 6 mm, flow rate: high



(b) d_{noz} : 3 mm, flow rate: high

Figure 2: Stream and delayed droplet formation at around $5 \cdot 10^{-6} \frac{\text{m}}{\text{s}}$ for oil in water

a) 6 mm nozzle resulting in three big droplets

b) 3 mm nozzle resulting in 6 slightly smaller droplets than in a)

[22]

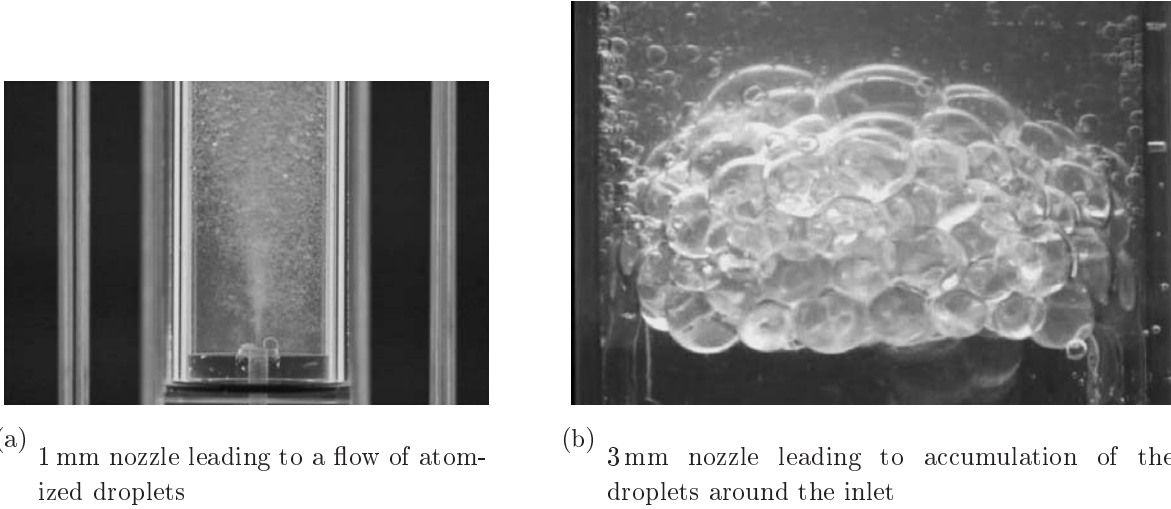


Figure 3: Droplet behaviour for an inlet velocity of around $2 \cdot \frac{\text{m}}{\text{s}}$ [22]

ADX10, as well as Therminol D12 and HVS 13. The time frame during the ascension is the only possible stage, in which the heat exchange can occur. This time is not only dependent on the density difference between PCM and HTF and of the geometric setting, but also of the size of the droplets. For optimal heat exchange droplets should have a big surface compared to the volume. As the resulting droplets are sphere shaped, with good approximation, the resulting fraction of surface area by volume is therefore $\frac{3}{r}$, with the radius r . This concludes that the droplets should be as small as possible. Additionally, smaller droplets tend to follow the flow easier than big droplets. When taking turbulence into account, this means, that small droplets will have more time to interact with the PCM than big droplets. As explained before droplets cannot be made infinite small as at some point they cannot separate anymore from each other and build an emulsion. The optimal droplet size was achieved with an inlet diameter of $2-3 \text{ mm}$ and an inlet velocity of $0.2 - 0.3 \frac{\text{m}}{\text{s}}$. The HTF enters the inlet as stream that splits into standalone droplets with about the same velocity and a size of $3 - 4 \text{ mm}$. The heat transfer coefficient is at $393 \frac{\text{W}}{\text{m}^2\text{K}}$. A lower inlet velocity leads to a high possibility of a resulting back-flow, due to the higher pressure of water. The PCM is then able to enter the inlet and therefore constrict the passage for the HTF. [25]

3.2 Temperature change

When the mass flow is set to the desired value the experiment can begin. A thermal storage can however only be put to good use when there is a thermal flow. This means that the HTF has to have a distinct temperature from the PCM in order to load the storage with or unload it. Therefore this and all following subsections of this chapter will deal with the thermodynamic part of the behaviour in the tank, starting by the cooling process and leading through the mathematical description by including the solidification to a global energy balance equation. The exact processes happening during the cool-down or heating

are well described in [26]. During the temperature change of the PCM the internal energy u and the enthalpy h change accordingly. Both values are necessary, when calculating the isochore and isobar heat capacities, that describe the possible amount of energy to be stored. The following equations describe the mentioned changes and are written in their specific form, meaning the values are divided by their mass.

$$du = \left(\frac{\partial u}{\partial T}\right)_v dT + \left(\frac{\partial u}{\partial v}\right)_T dv = c_v(T, v) + \left(\frac{\partial u}{\partial v}\right)_T dv \quad (7)$$

$$dh = \left(\frac{\partial h}{\partial T}\right)_p dT + \left(\frac{\partial h}{\partial p}\right)_T dp = c_p(T, v) + \left(\frac{\partial h}{\partial p}\right)_T dp \quad (8)$$

The Enthalpy is defined the following way:

$$H = U + pV, \quad U = mc_v(T - T_{Ref}) \quad (9)$$

with the reference Temperature T_{ref} , which is set to 273.15K in most cases.

3.3 Phase change

The exact process happening during heating and melting is well described in [25]. During the heating, temperature rises until the phase change to liquid begins. Even with increased heat flow the temperature stays constant until the whole body is melted, as the energy has to be used against the binding energy of the molecule inside the solid body. After completion of the melting the temperature is able to rise again. The same goes for the phase change liquid to gaseous.

For cooling the processes are similar but not exactly the same. The cooling temperature is in general below the melting temperature. This effect is called supercooling and means that the amount of energy needed for the phase change is greater when solidifying than when melting. During the supercooling the fluid is in a metastable state until the nucleation occurs and this crystals grow into the supercooled region. [17] Then latent heat is released from the solidified liquid into the supercooled liquid. The temperature returns to the melting temperature after the process has been completed. If the metastable state exists during the storage process, only sensible energy can be stored. This strongly reduces storage capacity. It is therefore important to prevent supercooling.

This can be achieved by inducing other elements in order to lower the potential energy and start the crystallization process at the optimal temperature. An important example, as it is also topic of this thesis and of the preliminary studies by Anmann [9] and [10], is the combination of water with tetra-butyl-ammonium-bromid (TBAB).

The energy change during the phase transition is defined as the melting enthalpy ΔH_m .

Anmann [9] did preliminary work for the development of this project on a real life thermal storage by using water and water-TBAB with ADX10 in investigating the solidification process in a direct contact latent heat storage. This stage appears to be generally more

complicated than the melting process. The system used for the experiments is shown and explained in fig. 1.

Water as PCM

Fig. 4 shows the frozen heat exchanger at the beginning of the solidification.

During the crystallization a milk coloured transition phase was created at the process of the solidification. (fig. 5) This phase was composed out of oil and small water droplets through emulsion. After some time the water flowed with the HTF to the heat exchanger, connecting the primary and secondary circuit (fig. 1), where it solidified and interrupted the flow. Therefore no more HTF could enter the storage preventing the PCM from fully solidifying.



Figure 4: Image showing the frozen heat exchanger due to water drifting alongside ADX10 [9]



Figure 5: Coalescent behaviour, milk coloured transition phase during water solidification [9]

Water-TBAB as PCM

Fig. 6 shows strong foaming dependant of the mass stream. Furthermore, crystallisation is visible, especially around the temperature sensors and the cables. This beginning of the solidification has appeared in most of the runs. In some experiments, however, a variety of crystals got created throughout the whole PCM floating in the fluid flow creating a porous structure in water-TBAB. (Fig. 8) Furthermore the phase boundary between the PCM and the HTF moved to the top of the storage, while the global fluid level stayed constant. Anmann proposed that part of the HTF got surrounded from the ice blocking, or at least hindering, the passage. Due to the continuing flow of the incoming HTF this structure got pushed to the top where the still fluid PCM could finally crystallize. Additionally the narrowing could have introduced a forced flow, instead of the natural ascension, reducing the interaction time between HTF and PCM and therefore the temperature effectiveness. The effect of the freezing on the heat exchanger and the emulsion of small PCM droplets into the HTF could be visible by using water-TBAB as PCM in similar manner as when using water as PCM, as described earlier.

3.4 A global energy equation

A complete process including the cooling of the PCM and the solidification is written by integrating (8) under consideration of ΔH_m :

$$\Delta U = m \int_{T_0}^{T_m} dT c_p + \Delta H_m, \quad (10)$$

This equation can, of course, be used for the process of vaporization, when the parameters are adjusted accordingly. For calculating a temperature change including both phase changes one has simply to sum up the different integrals and enthalpy changes for each process in order to retain the complete change of the internal energy.

For small temperature changes the specific heat is independent of temperature. Therefore its value can be approximated with the average value and the equation changes to:

$$\Delta U = m \bar{c}_p \Delta T + \Delta H_m \quad (11)$$

In this project the PCM temperature was set 1 K above solidification temperature for faster solidification. This means that in such cases the melting enthalpy is the important factor, which differs from material to material.

Until now the energy equation was only written for the PCM. For a global equation, of course, the HTF also has to be taken into account. This part of the process is explained well in [9]. The total energy change originates not only in a thermal component and a volumetric component, the last one can be neglected, but in contrast to the PCM also in the incoming and outgoing fluid. The additional two locations are described each in three different terms (enthalpy, potential and kinetic energy) resulting in the following



Figure 6: Strong foaming, crystallization around temperature sensors, cables[9]



Figure 7: Conduits left behind by HTF, porous structure[9]



Figure 8: Solidification of PCM, pushed to top from HTF[9]

equation, with the time dependence not directly stated for every term in order to achieve better reading:

$$\frac{dE}{dt} = \sum_i \dot{Q}_i + \sum_j \dot{W}_{tj} + \sum_{in} (\dot{m}_{in}(h_{in} + gy_{in} + \frac{1}{2}v_d^2) + \sum_{out} (\dot{m}_{out}(h_{out} + gy_{out} + \frac{1}{2}v_d^2) \quad (12)$$

Previously this chapter dealt only with the balancing equation of force and now additionally with the energy balance. In fluid-dynamics there is, however, an important third balancing equation that will come to effect. There always has to be balance in mass. This means that the exact same amount of mass entering the control volume has to leave the control volume again.

$$\dot{m}_{in} = \dot{m}_{out} = \dot{m}_{HTF} \quad (13)$$

When applying additional approximations, that ascension has to outweigh gravity in order for the storage to function and the in-compressibility of the HTF (defined by $\text{div } \vec{v} = 0$), the terms for the potential energy and for the kinetic energy both cancel themselves out, leaving only the heat transfer and the enthalpy terms. As the storage effect is quasi-stationary, the complete energy change for the HTF sums up to 0:

$$\frac{dE}{dt} = \dot{Q}_d + \dot{Q}_{loss,HTF} + \dot{m}_{HTF}c_{HTF}(T_{in} - T_{out}) = 0 \quad (14)$$

The heat transfer power of a droplet is calculated by the following equation:

$$\dot{Q}_d = kA_d\Delta T_m = kA_d \frac{\Delta T_{in} - \Delta T_{out}}{\ln \frac{\Delta T_{in}}{\Delta T_{out}}}, \quad (15)$$

$\Delta T_{in} = T_{PCM} - T_{in}$, $\Delta T_{out} = T_{PCM} - T_{out}$, the thermal transmittance k and the average logarithmic temperature difference ΔT_m . The thermal transmittance has the same unit as the heat transfer coefficient α ($\frac{W}{m^2K}$) but describes the rate of transfer of heat through a fluid or a solid, similar to the thermal conduction, while the heat transfer coefficient, on the other hand, describes the efficiency a material can absorb or reject thermal energy. All three values are in a relationship with each other, including the droplet radius, described by the following equation:

$$\frac{1}{k} = \frac{1}{\alpha_{d,in}} + \frac{r}{\lambda_{HTF}} + \frac{1}{\alpha_{d,out}}, \quad (16)$$

The thermal coefficient can be calculated with the dimensionless Nusselt number, that describes the ratio of convective and conductive heat transfer:

$$Nu = \frac{\alpha}{\frac{\lambda_{fl}}{L}}, \quad (17)$$

with the characteristic length L .

4 Modelling fluid flow

This section will prepare the reader for the method of Computational Fluid Dynamics, in short CFD, especially the used Volume Of Fluid method (VOF). When executing a simulation with the computer it is important to know what the program is actually doing in the background. ANSYS Fluent and other available tools are unable to actually calculate one perfect solution. In reality they use a numerical approach to achieve the best possible solution after a specified number of iterations. The equations running in the background were already shown in a short, simple and understandable way in chapter 3. Section 4.1 lists these equations now in dependence of time and density. The chapter intensifies the discussion of the fluid-dynamic part from chapter 3, especially the surface tension, a very important value when dealing with droplet formation, which is described in section 4.2. This discussion is based upon a book describing bubbles, drops and particles by Clift, Weber and Grace. [14] The relevant parts for this thesis were included, for more information it is referred to the book, as it summarizes different results and approaches for a wide scale of different cases. The way of incorporating the governing equations and boundary condition of this chapter will be explained in the following section 5, including a review of the “Volume Of Fluid” method and the solidification model used, as well as presentation of the specifications used in the parameter study.

4.1 Governing equations

For the introduction of the fluid-dynamic equations the script of Braun [12] was used. When taking the balance of the mass stream of (13) and reforming the equation by including the density and the so-called transport theorem, the following result will be achieved for the continuity equation:

$$\frac{Dm}{Dt} = \frac{D}{Dt} \int_V \rho dV = \int_V \left(\frac{D\rho}{Dt} + \rho \nabla \cdot \vec{v} \right) dV = \int_V dV \left(\frac{\partial \rho}{\partial t} + \nabla \cdot (\rho \vec{v}) \right) dV = 0 \quad (18)$$

The equation of motion is written in a similar way as (18) and takes (3), (4) and (5) into account. Gravity stays as a separate term, while the friction and ascension forces are included through the viscosity in the stress tensor $\sigma_{ij} = \tau_{ij} - p\delta_{ij}$. The main difference between the equation of motion and the mass balance is that the velocity has to be multiplied by the density.

$$\frac{D\vec{p}}{Dt} = \frac{D}{Dt} \int_V \rho \vec{v} dV = \oint_{\partial V} \vec{n} \sigma dA + \vec{F}_G = \int_V (\nabla \cdot \sigma + \rho \vec{g}) dV \quad (19)$$

The resulting momentum balance including here not present external sources $K = 0$ is therefore:

$$\int_V \left(\frac{\partial(\rho \vec{v})}{\partial t} + \nabla \cdot (\rho \vec{v} \otimes \vec{v}) \right) dV = \int_V \left(-\nabla p + \nabla \cdot \tau + \rho \vec{g} \right) dV + K \quad (20)$$

For the energy balance another multiplication in the left side increment of (20) by the velocity is necessary, as well as taking the internal energy and the heat transfer into account. All powers from surrounding sources are included in the letter P . The sum of all energies is furthermore equivalent to the sum of all heat changes, according to the first law of thermodynamics, as written in [15].

$$\begin{aligned}\frac{DE}{Dt} &= \frac{DQ}{Dt} = \frac{D}{Dt} \int_V \rho \left(\frac{\vec{v}^2}{2} + u \right) dV = \oint_{\partial V} \vec{n} \sigma \vec{v} dA + \int_V \rho g dV + P - \oint_{\partial V} \vec{n} \vec{q} dA \\ &= \int_V \vec{\nabla} (\sigma \vec{v}) dV + \int_V \rho g dV + P - \int_V \vec{\nabla} \vec{q} dV\end{aligned}\quad (21)$$

With the definitions for the specific enthalpy ($h = u - \frac{p}{\rho}$) and the heat transfer for heat conductance ($\vec{q} = -\lambda \vec{\nabla} T$) after a few modifications the energy balance can be written in the following way:

$$\int_V \left(\frac{\partial(\rho h)}{\partial t} - \frac{\partial p}{\partial t} + \vec{\nabla}(\rho \vec{v} h) \right) dV = \int_V \left(\vec{\nabla}(\lambda \vec{\nabla} T) + \vec{\nabla}(\vec{v} \tau) + \rho \vec{v} g \right) dV + P \quad (22)$$

The stress tensor is defined by the dynamic viscosity μ and can be calculated by combining (20) and (22):

$$\sigma = \mu \left(\vec{\nabla} \vec{v} + (\vec{\nabla} \vec{v})^T - \frac{2}{3} \delta \vec{\nabla} \vec{v} \right) \quad (23)$$

For the incompressible case and constant material parameters (18), (20) and (22) become shorter and, more important, easier:

$$\frac{Dm}{Dt} = \int_V \frac{D\rho}{Dt} dV = \int_V \left(\frac{\partial \rho}{\partial t} + \rho \nabla \cdot \vec{v} \right) dV = \int_V \rho \nabla \cdot \vec{v} dV = 0 = \nabla \cdot \vec{v} \quad (24)$$

$$\frac{D\vec{p}}{Dt} = \int_V \rho \frac{D\vec{v}}{Dt} dV = \int_V \rho \left(\frac{\partial \vec{v}}{\partial t} + \vec{\nabla}(\vec{v} \otimes \vec{v}) \right) dV = \int_V \left(\rho \vec{g} - \vec{\nabla} p + \mu \vec{\nabla}^2 \vec{v} \right) dV \quad (25)$$

$$\frac{DE}{Dt} = \int_V \rho \frac{D}{Dt} \left(\frac{\vec{v}^2}{2} + u \right) dV = \int_V \left(\rho c \frac{DT}{Dt} \right) dV = \int_V \lambda \vec{\nabla}^2 T dV + P \quad (26)$$

As the discussion of the models for the droplet formation and breakup was done in reference to [14] the equations have to be adapted for a better understanding. Clift et al [14] had a different approach for the continuity equation. In this case there are two fluids in direct contact with each other, the mass transfer can be described with the process of diffusion. This means one can use Fick's first law by stating that the particle current density equals the product of a factor called the diffusivity coefficient D and the concentration c gradient.

$$\vec{J} = -D \vec{\nabla} c \quad (27)$$

The derivation can be looked up in [15]. Although here process of diffusion is explained by observation of two gases instead of two fluids the equation can be used on a global basis,

simply by changing the diffusivity coefficient accordingly. Differentiating this equation leads to the second law of Fick, which originates on the conservation of mass between a non-reactive solute in a dilute solution in an incompressible fluid, leading to an equivalent to (24).

$$\frac{Dc}{Dt} = D \vec{\nabla}^2 c \quad (28)$$

All governing equations apply simultaneously for each phase. For solving, additional boundary conditions are necessary. Of course, Newton's third law applies, meaning that normal and shear stress are equal at the boundary. The interface is often defined with the help of the surface tension or the viscosity. When surface viscosity can be neglected the normal stress condition reduces from a complex system of tensors, which will not be stated here, to a simple equation. Before starting the derivation it is necessary to discuss surface tension and its origin.

Particles on the surface of a fluid or solid phase have a higher energy than the ones on the inside. As molecules in general always tend to reach the minimum in order to gain stability this means that they tend to align on the inside of the resulting form. As there always has to be an outside, this means, that the boundary is composed out of as few particles as possible, therefore ideally reaching a state of a perfect sphere. However, the edge is not only assembled by just one layer of molecules, there is always a transition zone between the inner molecules and the surroundings of the material. The fact that the boundary is not sharp leads to the following definition of a phase: The area is called a phase, when there exist additional particles to the ones on the surface boundary with an energy at the level of molecules in a vast volume.

The surface boundary has two important properties for fluids:

- It's size depends on the geometric dimension
- It is an equipotential

One realizes that this means that each characteristic is isotropic for each of the two fluid phases in the intended direct contact thermal storage. In the surface boundary, however, the attributes change continuously between these two phases. A simple way of looking at this behaviour is by defining a tension area on the boundary. Now a control volume will be defined that consists of both phases. In the first step the volume will be compressed in a way that the area of the phase boundary will be reduced. In the second process the volume will be rolled back to the original size, although by keeping the phase boundary at the smaller size. The reversible work is therefore only dependent on the specific free energy of the surface boundary and its area, for constant volume and constant temperature.

$$-dW_{rev} = \sigma dA \quad (29)$$

It is important to highlight, however, that this model is based on assumptions with the intention of simplifying the setting. This explanation relied on the instant transfer of

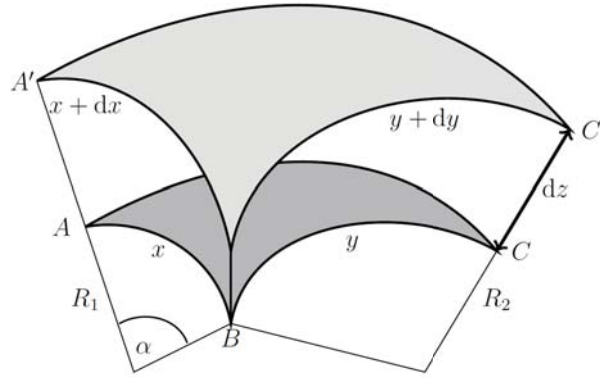


Figure 9: Sketch showing a non-isotropic surface ABC with its radii $R_{1,2}$ and the edges $x = \overline{AB}$ and $y = \overline{BC}$ before and after its extension to $A'BC'$ with the borders $x + dx = \overline{A'B}$ and $y + dy = \overline{BC'}$ for the geometric derivation of the Young-Laplace-Equation. The angles are largely over-subscribed, probably for visualization. In the calculations α is small and therefore $\sin\alpha \approx \alpha$. [20]

molecules from the continuous phase into the gaps, after the expansion of the surface boundary, and the keeping of its composition during the process. Both simplifications do not always have to be the case.

The surface tension for cooling processes changes mostly in the range of $10^{-5} \frac{\text{J}}{\text{m}}$ and $10^{-4} \frac{\text{J}}{\text{m}}$ until the critical point is reached and can be approached by:

$$\sigma = A_1(T_C - T)^{B_1} \quad (30)$$

with the temperature independent constants A_1 and B_1 , as well as the critical temperature T_C .

When cooling down further the changes become linear. The product of surface tension and the area of 1 mol of the densest close-packing of equal spheres is defined as the free surface enthalpy and can be calculated by the following equation:

$$\bar{\sigma} = \sigma \bar{A}_{mol} = k_E(T_C - T_\Theta - T) \quad (31)$$

The right part describes the free surface enthalpy below the critical point and includes the Eötvös Constant k_E and a material specific temperature T_Θ , found by empirical methods by Loránd Eötvös. [20]

All earlier explained equations dealing with the surface tension were described on flat surfaces. As the incoming oil stream in a direct contact latent heat storage splits up into droplets the surface tension behaviour has to be reviewed. This can be done on a non-isotropic surface ABC , as shown in figure 9 of [20] or on a nearly circular surface, as in [23]. There the intentions and assumptions made by the writers are explained in detail. It is assumed, although not directly specified in the literature, that the same concept is applied to the calculation in [20] due to the similarities of the equations. Sigveland et al. assumed an interface without thickness and constant tension. The points forming the

surface shall not be far away from the centre, as the equilibrium conditions are full-filled perfectly on the centre point. Therefore the radius of the nearly circled shape and the edges of this model tend to 0, leading to a very small angle α . This means that the surface changes of this model can be calculated by multiplication of both sides resulting in the following applied work, over the moved length of dz , with $dx dy \approx 0$:

$$dW = \int ds F = \Delta p xy dz = \sigma(x dy + y dx) = \sigma dA \quad (32)$$

With the small angle approximation $\sin \alpha \approx \alpha$ the angle can be calculated in the following way:

$$\frac{x}{R_1} = \alpha = \frac{x + dx}{R_1 + dz} \quad (33)$$

A trivial reforming of this equation for x and y leads to the following dependences of dz :

$$dx = \frac{x}{R_1} dz, \quad dy = \frac{y}{R_2} dz \quad (34)$$

Inserting (34) into (32) leads to the finished Young-Laplace-Equation for calculating the Laplace pressure. It is important to notice that the shape of the area does not matter as it gets divided by itself when calculating the pressure, which is defined as force by area. Therefore both surfaces, result in the same final equation. For oil droplets of D12 and ADX10 that are nearly sphere shaped, it is possible to set $R_1 = R_2 = R$ with good approximation. For completeness the corresponding tangential and normal stresses were re-added to the equation.

$$p_d + (\tau_{nn})_d - p - \tau_{nn} = \sigma \left(\frac{1}{R_1} + \frac{1}{R_2} \right) = \sigma \frac{2}{R} \quad (35)$$

The corresponding tangential stress condition is then written as followed:

$$\tau_{nt} - (\tau_{nt})_p = \nabla \sigma \quad (36)$$

4.2 Formation and Breakup of Fluid Particles

According to [14] there are different regimes of jet formation depending on the flow rate at the orifice. The diagram in fig. 10 shows that for extremely low flow rates the drop formation occurs directly at the nozzle. When increasing the flow rate up to Q_{jet} a jet originates due to Rayleigh instability resulting in an axisymmetric breakup, as example, growing until the flow rate Q_{max} . In this flow regime the denser fluid penetrates downwards and breaks the bond between the droplet and the jet. For low viscosity fluids the equivalent diameter can be approximated by $\sqrt{\frac{\sigma}{g \Delta \rho}}$. Further increase in the flow rate leads to a sinus shaped jet that gets shorter due to an increase in asymmetric disturbances until it disappears at Q_{at} and the droplets form again at the nozzle, resulting in an atomized flow. While the original data for this diagram published in [21] could not be accessed a blurred preview could be and the shape of the curve could be confirmed. As

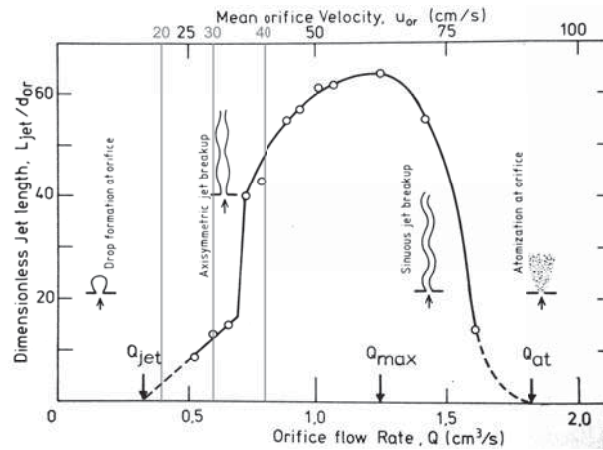


Figure 10: Dimensionless jet length plotted by orifice flow rate or velocity showing a typical jet development categorized into different stages. Until a specific flow rate Q_{jet} is reached the droplets form directly at the nozzle. Then the jet length rises linear with the flow rate and the curve turns parabolic shaped after further increase of the flow rate. For lower flow rates the jet breakup is axisymmetric and the length continuous to increase after Q_{max} is reached. This is where the jet becomes sinus shaped. The drop length starts to decrease until Q_{at} is reached and the droplets form again directly at the orifice, although now they become atomised. The plotted results for heptane in water were supposed to be taken out of [21] and incorporated into the diagram in [14]

The grey marked lines specify the velocities evaluated in the parameter study in 7.4

$$d_{or} = 0.16 \text{ cm}, \quad \mu_p = 0.00393 \text{ poise} = 0.393 \text{ mPas}, \quad \rho_p = 0.683 \frac{\text{g}}{\text{cm}^3}, \quad \sigma = 36.2 \frac{\text{dynes}}{\text{cm}} = 36.2 \frac{\text{mN}}{\text{m}}$$

the exact values could not be seen the diagram can only be used as a qualitative reference for the different stages of the jet. It is however, noticeable, that the organization into the different regimes could not be spotted on the blurred preview from the diagram in the original paper. While it is not stated explicitly this raised the impression that the original data was reviewed and incorporated into the different regions from the authors of the book.

As the parameter study done in this project observed inlet velocities $v_{in} > 0.15 \frac{\text{m}}{\text{s}}$ the expectations for all calculations were a stream of different length at the nozzle. Therefore the droplet formation at the orifice will not be discussed and it is referred to [14].

The calculation of the formation by jet integration in the range $Q_{jet} < Q < Q_{at}$ is based upon the idea of linearised stability by Strutt and Rayleigh. [24] The instabilities in fluid jets are described as capillary forces rendering an infinite cylinder unstable and turning it into small pieces of mass. It is proposed that the surface of the cylinder changes according to the wavelength λ of the disturbances, here specified as ω (q in the article) and a small time dependant factor $a(t)$.

$$r = a + a(t)\cos(kz), \quad k = \frac{2\pi}{\lambda}, \quad a(t) \propto e^{\omega t} \quad (37)$$

The time dependant factor can be solved by the energy equation with the help of the Bessel functions. The results correspond to a maximal wavelength of $\lambda_{max} = 4.508 \cdot 2a$ and is proportional to the diameter of the cylinder. According to [14] the equivalent drop size can be calculated by the maximal wavelength and the diameter of the orifice, by neglecting viscosity.

$$d_e = (1.5\lambda_{max}d_{or})^{\frac{1}{3}}d_{or}, \quad d_{e,max} \approx 1.9d_{or} \quad (38)$$

Describing the mass transfer at the droplet formation and the detachment is pretty difficult. In [14] only calculations for the droplet formation below Q_{jet} are considered, while there exist solely empirical correlations for the droplet detachment.

The breakup in stagnant media due to Rayleigh-Taylor instability, appearing for fluids in direct contact, when the one with the lower density experiences acceleration, was discussed in [11]. They describe two fluids of infinite depth. A vertical interface is on the plane $y = 0$ and the initial perturbation is described by $\cos(kx)$, with a small amplitude A_0 compared to the wavelength. The interface is described through a time and location dependent function $y = \eta(x, t)$ that is to be determined from fluid-dynamic equations. Furthermore the fluid is considered as incompressible and only linear terms are used. The governing equations are written in a similar manner as shown in 4.1 by using the velocity components.

$$v_x + v_y = 0, \quad v_t + \frac{p_x}{\rho} = 0, \quad v_t + \frac{p_y}{\rho} - g = 0 \quad (39)$$

As the pressure at the interface has to be equal ($p_1 = p_2$) the interface can be calculated with a combination of an exponential and trigonometric term ($v \propto \pm A_0 e^{-ky} f(t) \cos(kx)$) to

$$\eta = \frac{kA_0}{n} \cosh(nt) \cos(kx) \quad (40)$$

This equation shows that the amplitude of the disturbance increases with greater n for $\vec{g} < \vec{0}$ and therefore the interface motion is unstable for all $k > 0$, meaning for all wave lengths of the initial disturbance.

After taking the effects from surface tension into account it was found that the disturbance can only grow if

$$\lambda_{min} > 2\pi \sqrt{\frac{\sigma}{g\Delta\rho}} \quad (41)$$

As a contrast to (41) the authors of [16] set an upper limit, as bigger wavelengths result in gross deformations contradicting the assumption of perturbations of the interface:

$$\lambda_{max} = \frac{\pi d_e}{2} \quad (42)$$

For other breakup mechanisms, like resonance, velocity gradients ($Q > Q_{max}$) and turbulences it is referred to [14], as these do not correlate with the model from this project.

5 The computer model

As explained in the last chapter, when working with ANSYS Fluent the governing equations run in the background. This means, calculation itself is the simple part. The main task in ANSYS is, except for the data evaluation process, the building of the model. This starts by specifying the geometry, followed by the mesh. The meshing can be done by various tools, ANSYS Mesher or ICEM, to name two examples, but the process is always based on the same principle. The user defines the size and shape of each cell and therefore the number of cells where ANSYS Fluent shall calculate the governing equations. Fluent solves the equations for each cell numerically and returns the value at each centre. This shows the mesh can be viewed as the resolution of the results. In general the finer the mesh the more details can be visualised. The final part is to specify the model and by that telling Ansys Fluent which equations to use, followed by the material properties and the boundary conditions and therefore to define enough parameters for solving these equations. Further adjustment by changing convergence criteria and saving intervals is also possible. Then the solution can be initialised by specifying the fluid and thermal properties at the beginning and the settings for the calculation. Now the only thing to do is to wait until Fluent has finished and finally analyse and interpret the results.

As stated earlier, each cell consists only of one value for the whole cell. To be more precise, this value depends on a function v_i specifying the amount of liquid of a specific phase, the so-called volume fraction, in each cell. It's value reaches from 0 - non-existent - to 1 - fully occupying the cell. With the help of the following algorithm it is possible to locate free boundaries in a sufficient manner while additionally keeping the stored information on a minimum level. This is basically how the Volume Of Fluid Method works.

$$\frac{\partial v_i}{\partial t} = v_x \frac{\partial F}{\partial x} + v_y \frac{\partial F}{\partial y} + v_z \frac{\partial F}{\partial z} \quad (43)$$

This equations has been adapted from [18] for the 3D case, as this was used for the parameter study in this thesis.

5.1 Coordinate System

When setting up the model it is important to decide which coordinate system should be used. This is done in two ways: Firstly, by setting the coordinate room to 2D, 2D - axisymmetric or 3D and secondly, by setting starting and boundary conditions in a way that they suffice the wanted observer of the model.

In any mechanical calculation or simulation there are two distinct possibilities for setting the centre of the coordinate system: In the Lagrangian setting the model is viewed by the point of view of the physical body under evaluation, in this case the HTF itself. A grid is laid over the fluid for calculating the different values / properties. When the fluid moves, this grid moves accordingly. Therefore this method is relatively straightforward to simulate and works well with e.g. a droplet moving through a fluid storage material.

In the Eulerian setting the grid of the model is viewed from an observer on the outside. This means the same grid laid over the fluid stays at its original location, during the motion of the fluid. The calculation of this flow therefore requires an averaging of the properties of all elements in each mesh cell over the whole run time of the simulation. This averaging, however, can be a problem, as it results in a smoothing of all values and a smearing of surfaces. It is recommended to avoid this uncertainties by three steps: numerically describing the location and shape of the boundary, finding an algorithm computing the time dependent changes of the boundary and imposing the wanted boundary settings on the mesh. [18]

For the parameter study in this thesis the Eulerian setting was used. As the model consists not only of the droplet but also of the stream at the inlet, the Lagrangian model would have been more complicated. Setting the coordinate system into the droplet would have made an additional term in the calculations necessary in order to compensate the relative movement between the droplet and the inlet, as from the droplet's point of view the inlet and the incoming stream move downwards. Furthermore after a sophisticated solidification the droplet is hindered in its closing to the outlet, merging again with the stream.

5.2 Solidification - The Mushy Parameter

When dealing with solidification in ANSYS Fluent the parameter to be discussed in this section is the so-called mushy parameter, which will be referred to A_{mush} and reaches from 10^3 to 10^{10} depending on the research, its standard value set to 10^5 . As this parameter is not very well described in the official manuals, additional research material had to be reviewed. An analysis of different mushy parameters was discussed by Kheirabadi and Grouls in [13] and will be summarised here, including the necessary equations for understanding how Fluent models phase transfer.

The technique used assumes a phase change to occur over a finite temperature range, creating the mushy region, where the liquid fraction varies from 0 - solid phase - to 1 - liquid phase, similar to the volume fraction explained before. In between it is dependent of the temperature. This also means that the velocity of the fluid inside the mushy region varies from 0 - solid phase velocity - to the natural convection velocity of the liquid phase.

$$\begin{aligned}
 l(T) &= 0, \quad T < T_m - \frac{\Delta T}{2} \\
 &= \frac{T - (T_m - \frac{\Delta T}{2})}{\Delta T}, \quad T_m - \frac{\Delta T}{2} < T < T_m + \frac{\Delta T}{2} \\
 &= 1, \quad T > T_m + \frac{\Delta T}{2}
 \end{aligned} \tag{44}$$

When working with ANSYS Fluent it is necessary to adapt the values for the liquid fraction for an easier understanding of the process. Fluent is unable to correctly distinguish

the materials. When calculating the results for the liquid-fraction PCM Fluent not only uses the values from the cells with $\geq 50\%$ volume-fraction PCM but interprets the HTF values as "0". This is, of course, wrong as the values should actually be ignored and becomes a problem, when calculating average values, as it falsifies the actual results. The liquid-fraction has therefore be re-calculated to it's original value. The average of a value is by definition the sum of all values divided by the number of values. This is possible for the average liquid-fraction. The sum can be split up into two sums, each per material, which is useful, as the liquid-fraction of the HTF has to be always equal to 1. Furthermore a sum of values can be interpreted as the number of values multiplied by the average value, highlighted by a bar over the parameter. Additionally the number of cells n of one material divided by the sum of all cells is the same as the belonging volumes, due to the homogeneous mesh, and therefore the volume fraction v_i . This leads to the following equation for the liquid-fraction l :

$$l = \frac{\sum_{PCM} l_{PCM} + \sum_{HTF} l_{HTF}}{n} = v_{PCM} \bar{l}_{PCM} + v_{HTF} \bar{l}_{HTF} \Rightarrow \bar{l}_{PCM} = \frac{l - (1 - v_{PCM})}{v_{PCM}} \quad (45)$$

Kheirabadi and Groulx [13] modelled a (0.05, 0.12) m 2D cavity filled with lauric acid and enclosed with 0.025 m plexiglass on every side except the top. Furthermore the right side was sealed with a 35 mm thick aluminium plate at a constant temperature of 343.15 K. The system was initialised at 299.15 K solid phase and heated until fluidised. The impulse balance in ANSYS Fluent is calculated by including a temperature dependant term in the impulse balance in (20). This is done by introduction of the parameter $S(T) [\frac{\text{kg}}{\text{s}}]$. The parameter is defined through the Carman-Koseny equation from the liquid fraction and a constant factor ϵ and works as a dampening term.

$$S(T) = A_{mush} \frac{(1 - l(T))^2}{l(t)^3 + \epsilon} \quad (46)$$

For the discussion of the mushy parameter 9 simulations were done by [13], with temperature differences of 1, 2, 5 K, $A_{mush} = 10^5, 10^6, 10^7$ with time steps of 1 s for total 180 min and 50 – 300 iterations, depending on the stage of the simulation. They found out that at the beginning conduction was the dominant heat transfer, while at the end natural convection took over. Results of the mushy parameter show that lower values tend to over predict the melting rate, while higher values lead to under predictions. $A_{mush} = 10^5$ resulted in an acceleration of 60 min for 5 K and 40 min for 1, 2 K, while $A_{mush} = 10^7$ resulted in a delay of 20 – 40 min compared to experimental results. Furthermore the temperature changes had a stronger influence on lower Mushy Parameters. It was therefore more practical to vary the temperature instead of the Mushy Parameter due to the wide range of melt interface locations. For $A_{mush} = 10^3, 10^5$ non-physical results were achieved, as the PCM at the top melted faster due to natural convection than the PCM at the bottom, that got heated only by conduction. Lower values of the Mushy Parameter increased the convection. The best correlation achieved was in the first 20 min at a value

of 10^7 under the influence of conduction. Nevertheless this calculation started to lag behind shortly after. The best overall correlation was achieved with $A_{mush} = 10^6$ and $\Delta T = 1,2\text{K}$. In all simulations the melt interface shape differed strongly from experiments at the end. In general, the melt interface shape showed sharper curvature than experimental results at the later stages of all simulations. The authors could not find any explanation for this and left that to future studies. They did note, however, that this discrepancy to the experimental results was stronger for higher Mushy Parameters. For 10^5 the shape correlated pretty good for the whole calculation, for 10^6 after 60 min the solid PCM began to square off. When taking everything into account $A_{mush} = 10^6$ gave the overall best results. The overall effect of the mushy parameter and the melting rate showed the expected results: The Carman-Koseny equations dampened the moment equation as soon as the liquid fraction approached 0 and high mushy parameter increased the area of static PCM in the mushy region and thus reduced convection and heat transfer.

5.3 Set-up

The intention of this subsection is to present the material properties and global calculation settings used in all models throughout this thesis. All real materials, that were intended to be used are listed in tab. 2, while the actual calculation properties are listed in tab. 3.

5.3.1 Material Properties

Real material properties			
values at 273.15 K temperature dependence included	H ₂ O ₁ ¹ PCM1	water-TBAB ₁ [10] PCM2	D12, Appendix A HTF
density $\frac{kg}{m^3}$	998.2	1030	776
heat capacity $\frac{J}{kgK}$	4182	2500	2025
thermal conductivity $\frac{W}{mK}$	0.6	0.33	0.113
dynamic viscosity $Pa\cdot s$	0.001003	0.012	unknown
molecular weight $\frac{kg}{kmol}$	18.0152	unknown	unknown
standard state enthalpy $\frac{J}{kgmol}$	$-2.854812 \cdot 10^8$	unknown	unknown
pure solvent melting heat $\frac{J}{kg}$	334000 [2]	193	unknown
solidification temperature K	273.15	284.95	unknown

Table 2: Material properties of H₂O, D12 and water-TBAB

¹Values taken from the ANSYS Fluent database, except were specified

Defined properties for the calculations

values at 273.15 K	H2O		D12 K
temperature dependence included	PCM1	PCM2	HTF
density $\frac{kg}{m^3}$	998.2	1030	pw, 776
heat capacity $\frac{J}{kgK}$	4182	4182	pw, 2025
thermal conductivity $\frac{W}{mK}$	0.6	0.6	$\propto T^2$, 0.1128
dynamic viscosity $Pa \cdot s$	0.001003	0.012	pw, 0.00193
molecular weight $\frac{kg}{kmol}$	18.0152	18.0152	28.966
standard state enthalpy $\frac{J}{kgmol}$	$-2.854812 \cdot 10^8$	$-2.854812 \cdot 10^8$	0
reference temperature K	298	298	298.15
pure solvent melting heat $\frac{J}{kg}$	334000	185000	0
solidification temperature K	273.15	285.15	0
melting temperature K			

Table 3: Material properties used for PCMs and HTF. The values for D12 were either entered in temperature dependence as piecewise-linear (marked by an additional "pw"), as a polynomial second order or as a constant value. If a value is written explicitly, the value for 273.15 K was chosen, as a reference to the solidification point of H_2O . All other values can be looked up in appendix A

The thermal conductivity of D12 was entered as a polynomial second order, created from appendix A, with the following equation: $0.1128 - 0.0001T - 2 \cdot 10^{-7}T^2$.

It can be clearly seen that some of the H_2O data is identical with the TBAB data. As the initial testing was done without solidification, it was not possible to enter any thermodynamic values into Fluent. The values of density and viscosity were set accordingly to one calculation by Andreas Anmann. When activating additional solving settings in ANSYS Fluent, that changed material properties. The program then uses the values of H_2O automatically for fluids and asks for reviewing these settings. For the testing runs with solidification the author simply forgot to review the material parameters from [9]. The values of solidification temperature and melting heat were set after consulting the co-supervisor. These settings were kept for the final calculations. The error has been detected only after the calculations of the parameter study already had been completed. Since the intention of this thesis was only to give an impression of the effects of the parameter changes to the results, the correctness of the material properties would have been a fine addition but nevertheless not completely necessary. The PCM2 is therefore referred to as PCM2, instead of water-TBAB. Furthermore mistakenly no temperature dependence for the density of the PCM set. The value is constant at all times. This means that the freezing process is only defined in an infinite viscosity as in the standard setting by fluent. The HTF was saved with temperature dependence as in the data sheet in the appendix A with the intention of sharing a complete fluent database file with the rest of the team for future simulations that may have a wider temperature range. Nevertheless, the values could have been set to constant for the most part, as the temperature

differences are relatively small. The properties necessary for the phase change were not specified and left at 0 intentionally, as a phase transition of the HTF is unwanted and impossible under the parameter range used for all simulations of this project.

5.3.2 Geometry and Mesh

An evaluation of the results for different geometries, mesh and time-step sizes resulted in the following model:

- $(x, y, z) = (5, 10, 5)$ mm, originally intended with H_2O
- $(x, y, z) = (5, 12.5, 5)$ mm, final geometry with PCM2
- $\Delta \leq \frac{40s}{3m} \Delta x$

For further references the detailed process is explained in Appendix B. However, one specific change due to the mesh settings has to be discussed shortly. All models during the testing stage consist of an outlet $r_{out} = 0.4 \text{ mm} = r_{in}$ at one corner at the top with a circular shape, defined in the geometry as circular. The inlet was always placed at the bottom centre, resulting in the same mesh specific change. Using different types of mesh for the inlet and the surrounding area resulted in uneven cells for the bottom. As this would be more complicated to calculate and to evaluate, it was decided to lay a multi-zone hexagonal mesh over complete geometry. This, however, resulted in incorrect inlet shapes, as Fluent had to find the closest possible adaptation, which, of course, is easier the smaller the grid was chosen. As the simulations are designed to evaluate the interaction between PCM and HTF, as well as the fluid-dynamic and thermal behaviour over the whole model, the uncertainties are negligible. The intended area would be $5.0 \cdot 10^{-7} \text{ m}^2$ when using the formula for a circle. With an area of $4.6 \cdot 10^{-7} \text{ m}^2$ for a mesh width of 0.1 mm this comes close enough (8 % smaller). For a 0.3 mm mesh width the value is only $3.5 \cdot 10^{-7} \text{ m}^2$ and is smaller by one third. This mesh differences mean, of course, that geometric values can only be taken in regard to the resolution. A value of, e.g., 1.8 mm for $\Delta x = 0.3 \text{ mm}$ means therefore actually a value in the range of [1.65;1.95] mm and is essentially the same value as, e.g., 1.9 mm.

For the inlet with a density of $783 \frac{\text{kg}}{\text{m}^3}$ for D12 at 263.15 K and $776 \frac{\text{kg}}{\text{m}^3}$ at 273.15 K (inlet temperature is 10 K below solidification temperature of the PCM and 11 K below initialisation temperature) this results in a mass stream of $\dot{m} = \rho \dot{V} = \rho A v = 1.4 \cdot 10^{-4} \frac{\text{kg}}{\text{s}}$ for a mesh of 0.1 mm and $1.1 \cdot 10^{-4} \frac{\text{kg}}{\text{s}}$ for 0.3 mm. In Reynolds numbers this means with a kinematic viscosity of $1.93 \cdot 10^{-3} \text{ Pas}$ an intended value of 128.7 and by calculating the equivalent diameter for a circle 123.1 for 0.1 mm and 106.8 for 0.3 mm.

5.3.3 Calculation Settings

The following settings were used during initial testing:

- Global settings: pressure-based solver , absolute velocity, transient
- $\vec{g} = \begin{pmatrix} g_x \\ g_y \\ g_z \end{pmatrix} = \begin{pmatrix} 0 \\ -9.81 \\ 0 \end{pmatrix} \frac{\text{m}}{\text{s}^2}$
- Model settings:
 - Multiphase (VOF):
 - 2 eulerian phases, explicit, sharp interface, volume fraction cut-off 10^{-6}
 - courant number 0.25, implicit body force
 - $\sigma = 0.0173 \frac{\text{N}}{\text{m}}$, continuum surface force, wall adhesion on
 - Energy
 - viscous (laminar)
 - solidification & melting
- Material properties of PCM2 and D12, see tab. 3
- Wall boundary: no slip condition², $\phi = 90^\circ$ on all walls
- Solver settings³:
 - Pressure-velocity-coupling – SIMPLE
 - Pressure gradient – Least Squares Cell Based
 - Volume fraction – Geo-Reconstruct
 - Energy – Second order Upwind
 - Transient formulation – First Order Implicit
- Residuals: continuity, $v_{x,y,z}$, energy – absolute convergence of 10^{-6}
- Initialisation: $T_0 = T_m + 1 \text{ K}$, $v_{HTF} = 0$

²The tangential velocity on the phase boundary is equal for both phases.[14]

³As used in the preliminary studies in [10], which was done for understanding the transient behaviour and limiting the heat transfer coefficient in computer simulations describing the HTF droplet and the incoming stream in a direct contact latent heat storage with water-TBAB and Therminol ADX10.

5.4 Energy balance

According to the ANSYS Manual the computation of the heat transfer rate through the face depends on the boundary type. As the main equations in ANSYS Fluent didn't change over time the first source found was taken. This includes the manuals for the ANSYS Versions 12.0, 18.0 and 19.1. [3, 6, 7] For flow boundaries, as the inlet or the outlet, it is the flow rate of the conserved quantity. For combined modes the total heat transfer rate is calculated with the heat transfer coefficient α , the surface area of the heat transfer A and the temperature difference between the solid surface and the surrounding fluid $T_{1,2}$ [8]:

$$\dot{Q} = \alpha A (T_2 - T_1), \quad \alpha = \frac{q}{T_2 - T_1} \quad (47)$$

The heat transfer rate was calculated by ANSYS Fluent for the inlet and for the outlet at each time-step for a longer flow time. An linear extrapolation of short test calculations not shown here predicted a complete solidification after 36 s. This was therefore the setting used in the next step. As will be shown later, the freezing process starts approximately linear but becomes more and more asymptotic after longer time. The actual liquid fraction achieved was at 26 % for $\Delta x = 0.3$ mm and at 28 % for $\Delta x = 0.1$ mm. Due to the longer simulation time more resources were needed.

From this point on all calculations were done with the Vienna Scientific Cluster 3 (VSC3). The VSC 3 is a general-purpose Linux cluster with 2800 compute nodes and NVIDIA GeForce GTX 1080 GPUs. The accessed nodes for this project were each equipped with two Intel Xeon E5-2650v2, processors and 128 GB or 256 GB of RAM. [5] The only disadvantage of using the VSC3 was that calculations could not be run for longer than 72 h without special authorisation. It was therefore tried to achieve a model that is able to produce sufficient results around this time frame.

A comparison of the heat transfer for one calculation with solidification and temperature changes ($T_{in} = T_{out} - 12.6$ K) and one calculation without solidification and temperature changes ($T_{in} = T_{out}$) is presented in fig. 11. The intention was to check the energy balance on a calculation with the boundary settings that were later used for the base model, although the material properties had to be changed. It was expected that the total heat transfer rate equals 0, as no heat can be lost or gained in the tank. This is fulfilled with sufficient precision for the most part of the calculation, except at the beginning during the first droplet formation process. The second calculation with solidification was intended as a future reference for the calculation of the parameter study. As the material properties had to be changed this is not the case any-more. Nevertheless this diagram shows in an efficient way the behaviour of the heat transfer when using H₂O and can be used as future reference. Furthermore it binds the changes in the heat flux to changes in the HTF volume fraction, as will be explained in the following text.

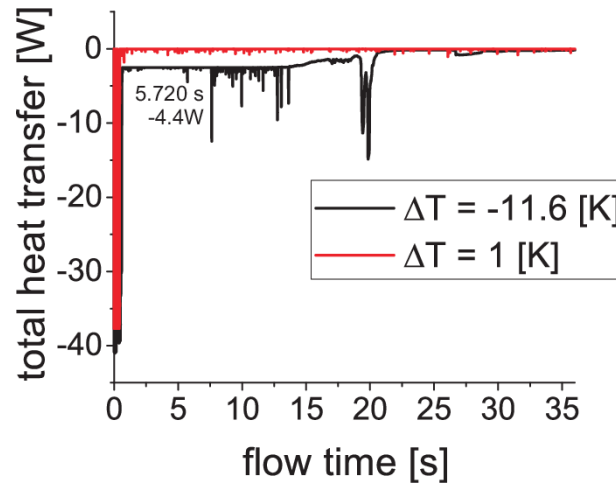


Figure 11: Total heat transfer for $\Delta T = 1\text{ K}$, $\Delta T = -11.6\text{ K}$. The intention of this comparison is, firstly, checking the correctness of the energy balance without solidification and secondly showing that the heat transfer during solidification should always be negative and in dependence of the amount of HTF leaving the model. The marked peak at 5.720 s shows an increase in value due to a drop in the HTF volume fraction, as shown in 12. The actual heat transfer values that can be evaluated exclude the values from the peaks, as they correspond to fully leaving HTF)
 $D12$, H_2O , $(x, y, z) = (5, 10, 5)\text{ mm}$, $r_{in} = 0.4\text{ mm} = r_{out}$, Mesh: multi-zone, hexagonal, 0.3 mm time-step size 4 ms , $v_{in} = 0.4\frac{\text{m}}{\text{s}}$, $T_{out} = 274.15\text{ K}$

ΔT [K]	\dot{Q} [W]			
	$t = 0.008\text{ s}$	$t = 0.448\text{ s}$	$t = [0.644; 13.672]\text{ s}$	$t = 21.740\text{ s}$
-11.6	-40.8	-17.3	-2.5	-0.2
1	-37.7		0	

Table 4: Important values from fig. 11. The calculation with solidification reaches a more or less constant value (except for the downward facing peaks) at 0.664 s , where it stays after 13.672 s , followed by a decrease to it's final value at 21.740 s . The calculation without solidification stays at 0 with sufficient precision from 0.448 s

Both models start with relatively high values compared to the rest of the calculation from 0.008 s and reach a stagnation at $0.5 \pm 0.15\text{ s}$, as listed in tab. 4. While the line without solidification reaches 0, where it stays close for the rest of the calculation, the line with solidification experiences multiple downward facing peaks, followed by a second stagnation, where it reaches it's final value, with the exception of one increase to -0.84 W between 26.7 s and 28.7 s .

When analysing more closely the behaviour of the total heat transfer rate without solidification, one realises that the heat transfer rate at the inlet always stays constant from the first data point during the whole 36 s at -5.4 W . This means that the heat transfer rate at the outlet has to compensate this value. A visualisation of the fluid flow in CFD Post showed that this is only the case when the HTF exits the outlet. The heat transfer rate

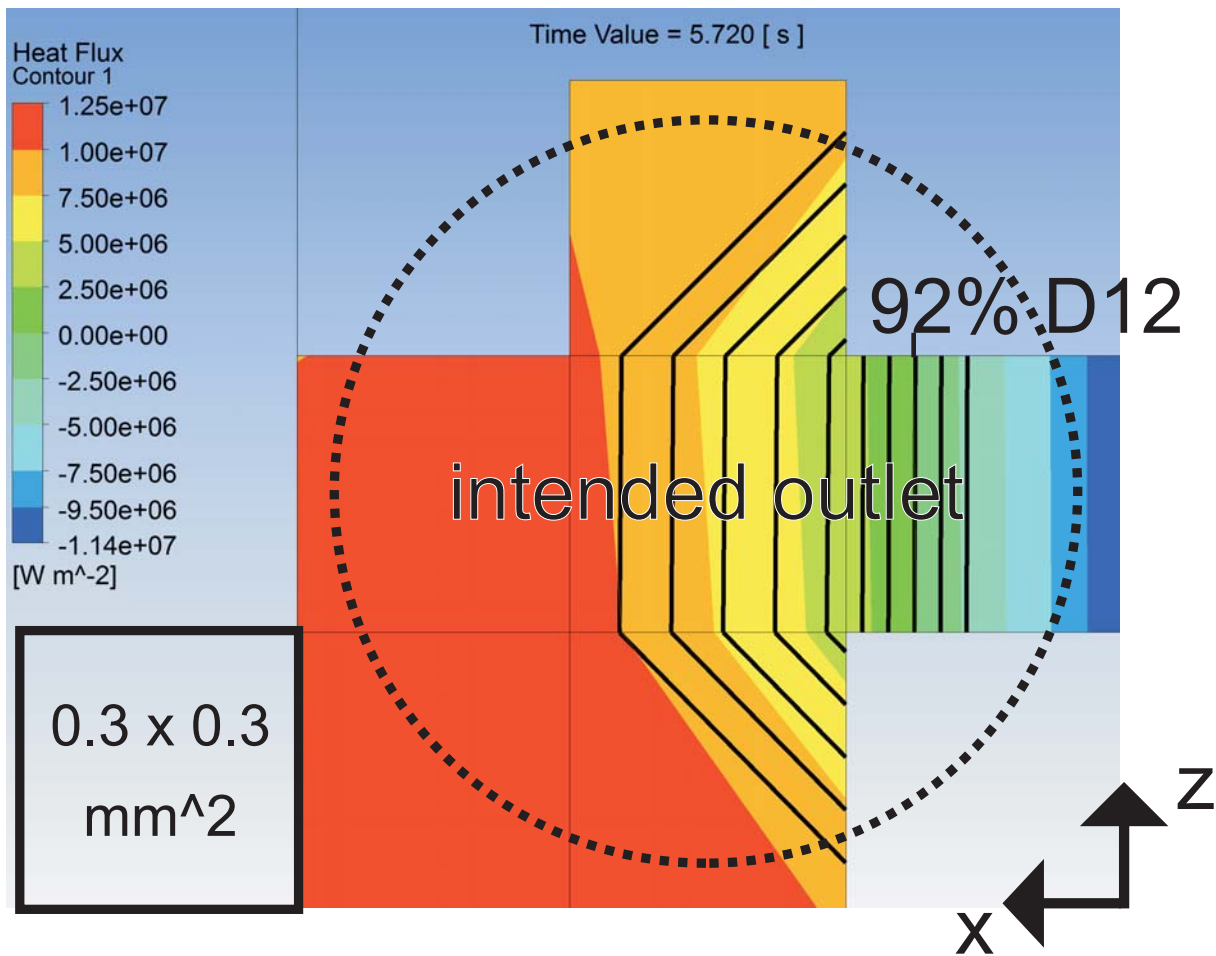


Figure 12: Heat flux at the outlet and corresponding volume fraction in the range of $[1;0.9]$, presented through the black lines in steps of 0.01, at 5.720 s. The circle marks the area that was defined in the geometry as outlet, before the meshing step.

D12, H_2O , $(x,y,z) = (5,10,5)$ mm, $r_{in} = 0.4$ mm = r_{out} , Mesh: multi-zone, hexagonal, 0.3 mm time-step size 4 ms, showed time-step 5.720 s, $v_{in} = 0.4 \frac{m}{s}$, $T_{out} = 274.15$ K

can therefore be a parameter for monitoring the fluid flow. During the droplet formation the heat transfer rate on the outlet is negative, as no HTF is leaving the tank. When the first droplet hits the top wall and part of it exits the outlet for a short time the heat transfer rate turns positive and is able to compensate the heat transfer rate at the inlet. There remains some HTF on the top. A few droplets later more and more HTF sticks to the top wall creating a thin layer of 1.8 mm HTF.

When calculating temperature changes and solidification it is clear that some heat gets “lost” within the system as the combined system of PCM and HTF always tries to acquire an energy balance according to the first law of thermodynamics. Therefore not all (in this case negative) heat entering the system is able to leave the system and the sum of both cannot cancel each other out any more. The overall behaviour of the heat transfer rate is the same as in the discussion before. Leaving HTF leads to a value next to zero, in case

no HTF comes close to the outlet the heat transfer rate at the outlet remains negative and adds to the inlet leading to peaks that can be clearly seen in the diagram, although they always stay below 50 % of the starting value. The heat transfer rate at the inlet stays once again constant, in this case at -8.2 W , with one exception. The first calculated value after initialisation at 0.004 s is at -8.1 W , which is by 0.1 W lower than the final value. A reason could be that the number of iterations was set too small and Fluent was not able to find the correct value before the next time-step.

After 0.644 s the total heat transfer rate tries to hold -2.5 W , although there appear major discrepancies, only present in calculations including temperature changes and solidification.

At 5.720 s a drop to -4.44 W is visible, correlating with a drop of $\approx 10\%$ of the volume fraction in about half a cell, as seen in fig. 12. This image was chosen to show that even a small decrease in the HTF transfer at the outlet can lead to clearly visible changes in the heat flux. As the outlet was intended to be circular but the mesh was done hexagonal for the whole system in order to evade uncertainties at the mesh transition zone between the outlet and the surrounding area, the outlet had to be calculated by fluent as a composition of multiple blocks of the same size. As the resolution was only about a third of the outlet diameter this led to a non symmetric and irregular structure. The image shows about three quarters of a cell with a negative local heat flux leading to a total heat transfer rate of -4.4 W of inlet and outlet. The sign change occurs at 92 % volume fraction. It is interesting to note that the changes in heat flux can have similarities with changes in volume fraction. For example the $5\frac{\text{MW}}{\text{m}^2}$ line has a similar shape than the 95 % volume fraction line. However for higher heat flux these similarities disappear. The part with $> 90\%$ volume fraction is furthermore at the edge of the model, while the parts with lower volume fraction are nearer to the centre. It could be confirmed for other downward facing peaks that they match a decrease in the HTF flow at the outlet.

6 Final preparations for the parameter study

6.1 Computational Resources needed

As explained in the last chapter mesh sizes of 0.3 mm and 0.1 mm gave both qualitative sufficient results. It was therefore decided to run one short simulation each, as well as additional simulations at higher resolutions, in order to estimate time and required effort. An additional calculation with a mesh size of 0.5 mm was done to see if the calculation time would be significantly slower. All calculations were done with the earlier mentioned settings and stopped after 2 s flow time or 72 h, depending on what was reached first. To be clear, only the calculations were run on the VSC3. The preparation of the mesh and calculation settings in Fluent still had to be done on the Notebook or a PC-Tower with similar resources. This also limited the resolution as the PC had to create the mesh and load it into Fluent, which can be a pretty long process when working with relatively (if compared to the VSC3) slow CPU. The mesh specifications and calculation time needed are stated in tab. 5

mesh size [mm]	time step [ms]	nodes	cells	calculation time [h]	flow time [s]
0.03	0.4	11,769,408	11,601,824	68	0.3
0.07	0.5	953,891	922,752	16	2
0.1	1	327,726	312,500	4	2
0.3	4	13,932	12,138	1	2
0.5	5	3,146	2,500	1	2

Table 5: A comparison of calculation times on VSC3, written with a precision of hours, of different mesh sizes for the $(x, y, z) = (5, 12.5, 5)$ m model with H_2O and D12. The intended simulation time was 2 s. The calculation time written for the 0.03 mm mesh was taken by the last data file saved with a saving interval of 0.1 s

After this short tests it was clear that the best two resolutions were problematic due to their high calculation time. The last simulation is practically useless as 0.3 mm does not take significantly more time, even when extrapolated to half a minute model time. A quantitative comparison of the area of the ISO-surface for 50 % volume fraction was therefore done for the same mesh settings used in the last chapter to finally determine the best resolution for the parameter study and will be presented shortly. The surface area was chosen, as it describes thermal and fluid-dynamical changes in the model in a good way. However, the flow time was increased from the earlier 36 s to 45 s to be able to achieve at least 25 % solidified PCM.

Another important topic is the necessary storage space. The higher the mesh, the greater the resulting data files. In order to minimize storage space every calculation saved the data files every 0.5 s. Additionally parameters like heat flux, surface area, liquid fraction

and volume fraction were calculated and saved at each time step in an additional text file, that needs far less space than the complete data file that contains every value per cell and time step. This means, however, that values extracted from the data files, like local temperatures and screen-shots for visualisation, could only be extracted every 0.5s with the intention of minimizing storage size. This means, that changes in the flow can only be given with a time resolution of 0.5s. When a time index of such a value is specified as, e.g., 1.5s this means therefore after 1.0s but before 1.5s.

6.2 Results of the comparison of the main mesh sizes

H₂O as PCM

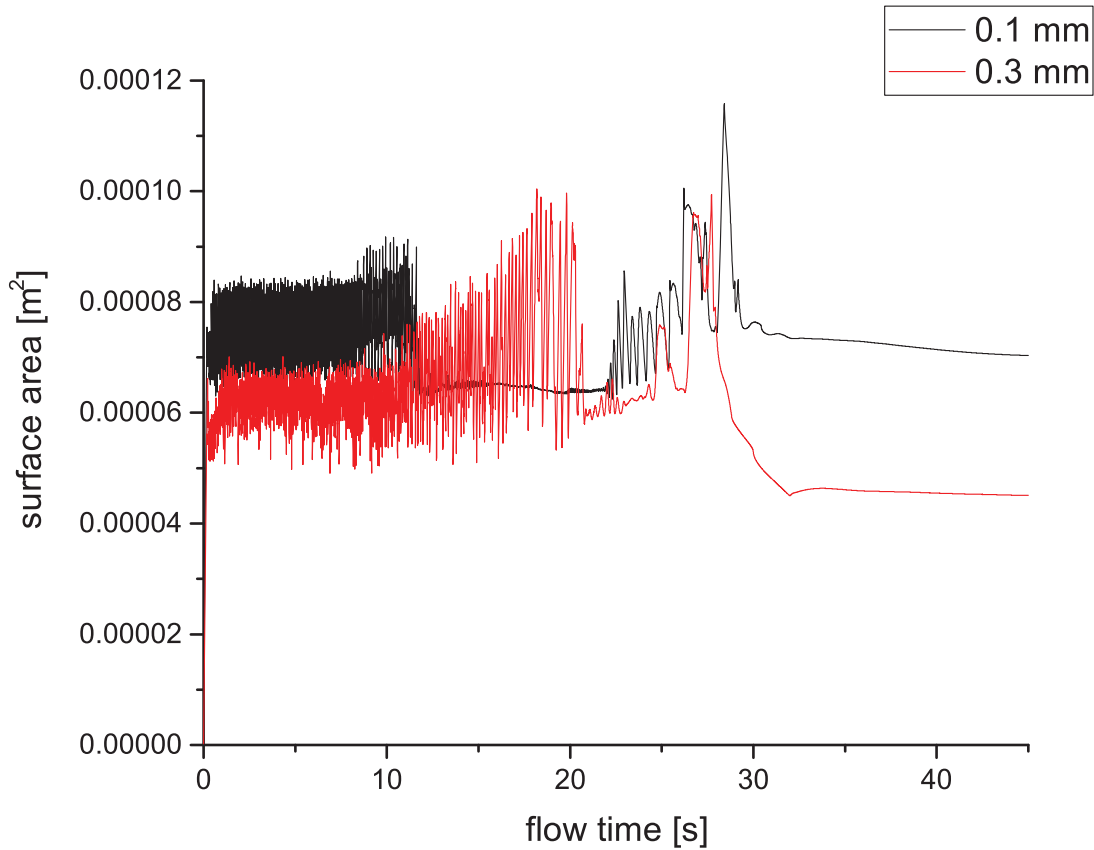


Figure 13: Surface area for $\Delta x = 0.1, 0.3 \text{ mm}$ in H_2O
 $D12$, H_2O , $(x, y, z) = (5, 12.5, 5) \text{ mm}$, $r_{in} = 0.4 \text{ mm} = r_{out}$

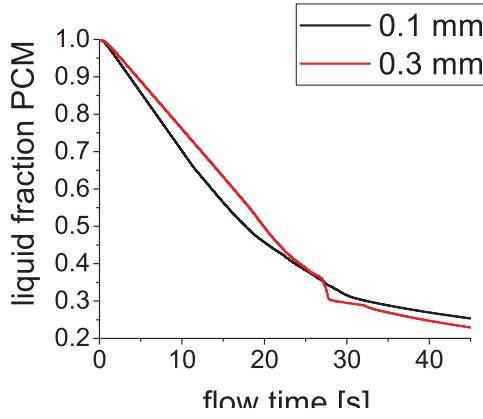


Figure 14: Liquid fraction for $\Delta x = 0.1, 0.3 \text{ mm}$ in H_2O
 $D12, H_2O, (x, y, z) = (5, 12.5, 5) \text{ mm}$
 $r_{in} = 0.4 \text{ mm} = r_{out}$

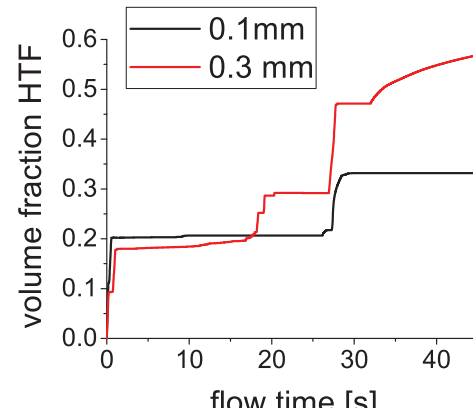


Figure 15: Volume fraction for $\Delta x = 0.1, 0.3 \text{ mm}$ in H_2O
 $D12, H_2O, (x, y, z) = (5, 12.5, 5) \text{ mm}$
 $r_{in} = 0.4 \text{ mm} = r_{out}$

Δx [mm]	period	increase	$(t_0 [\text{s}], A[10^{-5} \text{m}^2])$				$A[10^{-5} \text{m}^2]$ $t=45.0 \text{ s}$
0.1	(0.2, 7.5)	(10.8, 7.7)	(12.3, 6.4)	(28.412, 11.6)	(29.5, 7.5)		7.0
0.3	(1.2, 6.3)	(18.2, 8.8)	(21.0, 6.0)	(27.712, 9.9)	(32.0, 4.5)		4.6

Table 6: Important values of the surface area for $\Delta x = 0.1, 0.3 \text{ mm}$ from fig. 13, sorted by the type of change. For “increase” the final time step and the highest value are stated, for all other parts the starting time step and surface area are stated

Δx [mm]	$l_{PCM} [\%]$		
	$t = 27.0 \text{ s}$	$t = 28.0 \text{ s}$	$t = 45 \text{ s}$
0.1	36	34	25
0.3	36	30	23

Table 7: Important values of the liquid fraction of $\Delta x = 0.3 \text{ mm}$ from fig. 14, the relatively strong drop from 27s to 28s and the final value. The values of $\Delta x = 0.1 \text{ mm}$ were added for comparison

Δx [mm]	$(t [\text{s}], v_{HTF} [\%])$				$v_{HTF} [\%]$ $t = 45 [\text{s}]$
	Plateau 1	Plateau 2	Plateau 3	Plateau 4	
0.1	([0.5;26.0],20)	([29;45],33)	none	none	33
0.3	([0.2;0.7],9)	([1.2;16.6],[18;20])	([20.4;26.9],29)	([28.0;32.0],47)	56

Table 8: Important values of the volume fraction of $\Delta x = 0.1, 0.3 \text{ mm}$ from fig. 15, sorted by their plateau

The surface area in fig. 13 for $\Delta x = 0.1$ shows a periodic part after a linear increase at the beginning, followed by a stagnation part. After 22s flow time a period returns, followed

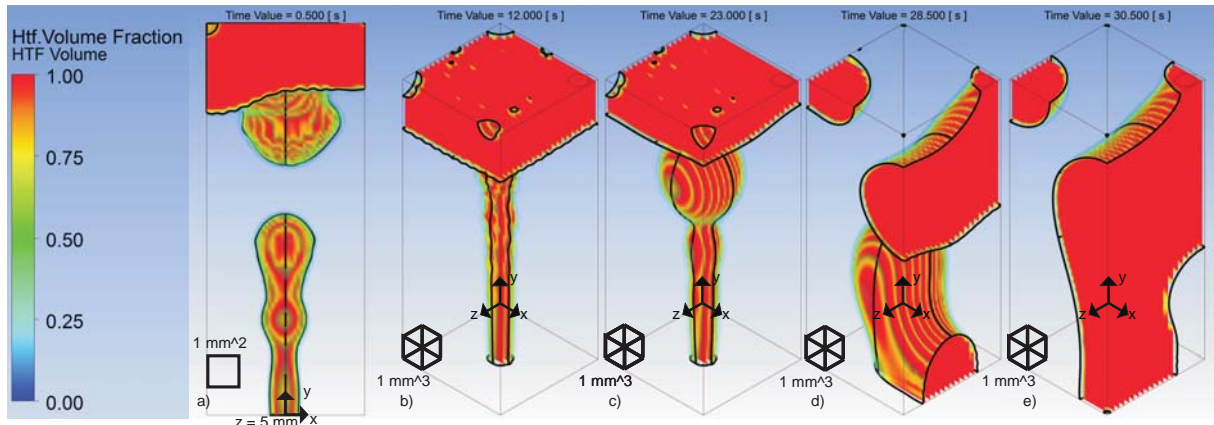


Figure 16: Image series showing a 3D visualisation of the important steps of the model with D12 and H_2O for 0.1 mm

- a) 3D image from the front view at $z = 5$ mm showing the droplet formation at 0.5 s
- b) 3D image showing a continuous stream to the top without any sign of droplets at 12.0 s
- c) 3D image showing the final droplet formation at 23.0 s
- d) 3D image showing the HTF flow in contact with the side wall at $x = 5$ mm in 2 areas (top and bottom), as well as a left-over part of HTF in the left corner
- e) 3D image showing that the HTF coats almost the complete right wall and a left-over part on the left corner

D12, H_2O , $(x, y, z) = (5, 12.5, 5)$ mm, $r_{in} = 0.4$ mm = r_{out} , Mesh: multi-zone, hexagonal, 0.1 mm

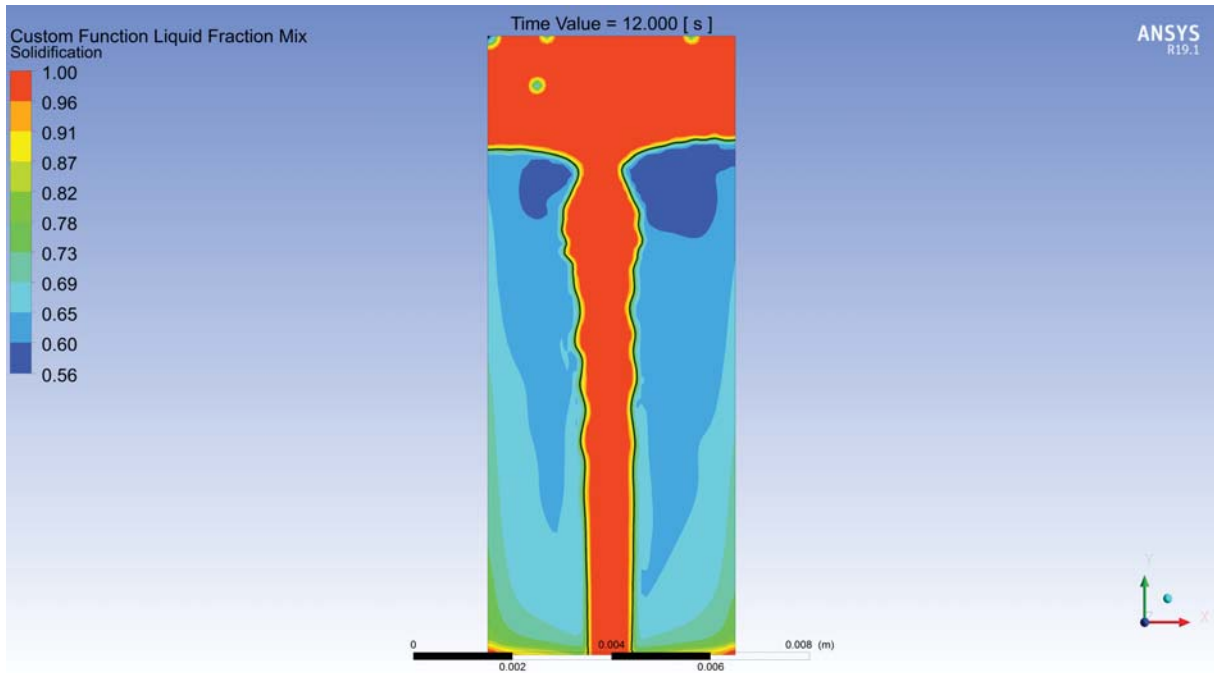
by the main peak. At 29.5 s the line reaches it's final value that equals the average value of the first period.

The $\Delta x = 0.3$ plot in fig. 13 shows also a periodic behaviour after a linear increase. This is followed by a visible increase leading almost directly to the main peak. A small periodic behaviour for about 5 s can be seen in between. After the peak the value becomes constant. The starting times of each stage and the according surface areas can be seen in tab. 6.

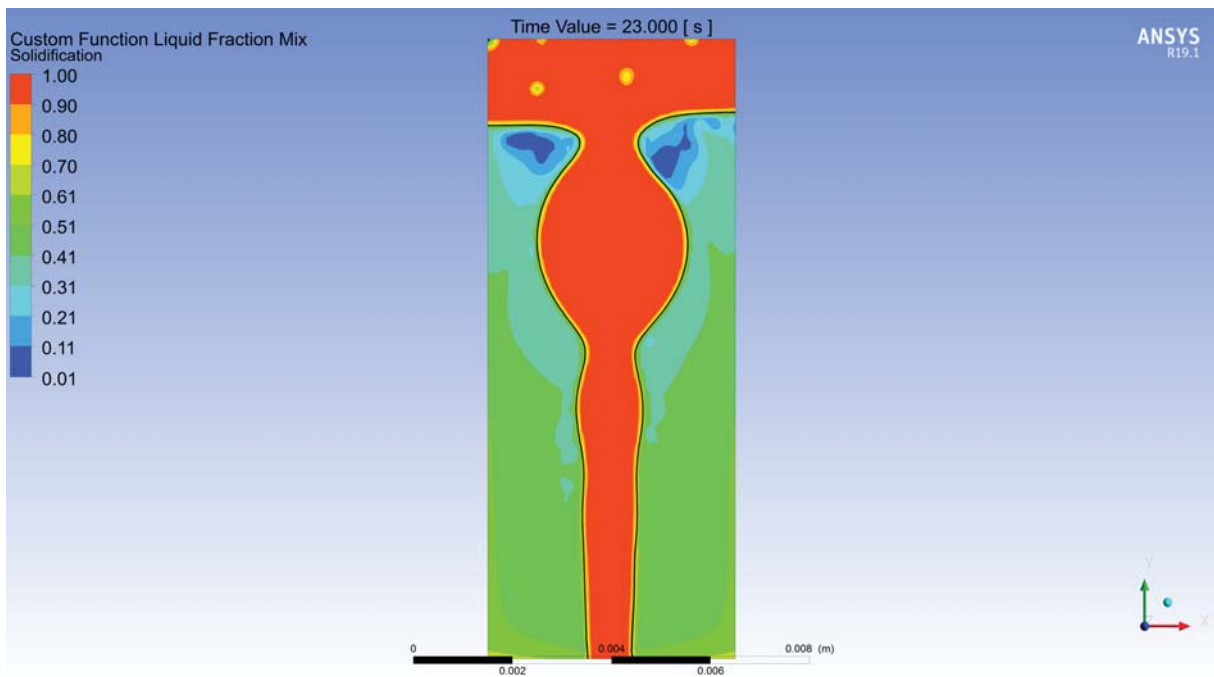
The behaviour of the liquid fraction for $\Delta x = 0.1, 0.3$ mm is shown in fig. 14. While the 0.1 mm line shows no interesting features, the 0.3 mm line experiences an almost vertical drop, as listed in tab. 7.

The behaviour of the volume fraction for $\Delta x = 0.1, 0.3$ mm is shown in fig. 15. The 0.1 mm line shows 2 more or less even plateaus, while the 0.3 mm line consists of 4 plateaus, one of them climbing slightly. The values are listed in tab. 7.

The visualisation shows in fig. 16 a) the droplet formation which stays basically the same until 12 s. The incoming jet has a length of 6.4 mm and it's widest part at the top is of 1.9 mm. In the upper part of the tank a drop with a width of 3.1 mm is visible, that is merging with a top layer of [2.2; 2.9] mm.



(a) Image showing that at 12 s the PCM at freezes from the top to the bottom at both sides of the jet



(b) Image showing that at 23 s the PCM directly on the top sides of the forming drop is almost completely frozen

Figure 17: Visualisation of the local-liquid-fraction at the centred xy -plane at two different time steps.

$D12$, H_2O , $(x, y, z) = (5, 12.5, 5) \text{ mm}$, $r_{in} = 0.4 \text{ mm} = r_{out}$, Mesh: multi-zone, hexagonal, 0.1 mm

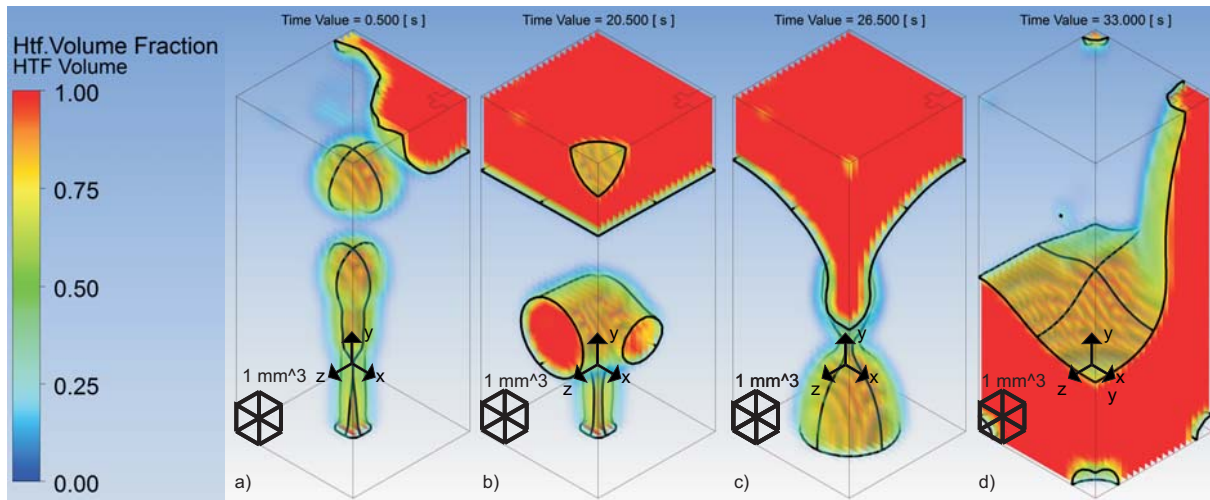


Figure 18: Image series showing a 3D visualisation of the model with D12 and H_2O for 0.3 mm
a) showing the droplet formation at 0.5 s
b) the incoming stream creates a channel leading from the front wall to the right wall and the top layer is completely coated at 20.5 s
c) the stream forms a droplet directly at the inlet connected via the front corner to the top layer at 26.5 s
d) almost half of the tank is filled with a more or less flat layer of HTF, which is leaving through a channel on the right edge to the outlet at 33.0 s
D12, H_2O , $(x, y, z) = (5, 12.5, 5)$ mm, $r_{in} = 0.4$ mm = r_{out} , Mesh: multi-zone, hexagonal, 0.3 mm

At 12 s (fig. 16 b)) there is no more drop formation but a stream of up to 1.5 mm width that flows up directly into the top layer of 2.2 mm height.

At around 23 s (fig. 16 c)) droplet formation tries to start again. The incoming jet has a forming droplet on the top with the dimensions of $(x, z) = (3.0, 4.0)$ mm. The rest of the stream has a width of 1.3 mm. The top layer has a height of [1.4; 1.7] mm.

At 28.5 s (fig. 16 d)) the top layer has almost completely disappeared, except for a curved shaped left over in the left corner. The stream connects to the right wall at the bottom and near the top.

At 30.5 s (fig. 16 e)) the left over keeps it's basic shape. The right wall is almost completely covered, except for one part at the top and one in the bottom right corner.

Fig. 17(a) shows the corresponding liquid fractions of the centre plane for fig. 16 b) increasing from top to bottom.

Fig. 17(b) shows the corresponding liquid fractions of the centre plane for fig. 16 c). The values on the top near the forming droplet are close to 0, while the part surrounding the stream below is between 51 % and 61 %.

The visualisation shows in fig. 18 a) the droplet formation which stays basically the same until 20.5 s. The incoming jet has a length of 6.9 mm and it's widest part at the top is of

1.8 mm. In the upper part of the tank a drop with the dimensions $(x, y) = (2.4, 2.1)$ mm is visible, just under the top layer of up to 2.1 mm D12.

At 20.5 s (fig. 18 b)) the incoming stream bends into x and z-direction leading to imprints on the wall. The one on the xy-plane is circular shaped with a diameter of 2.7 mm, while the other one is slightly elliptic shaped with $(y, z) = (1.5, 1.8)$ mm. Furthermore the top layer increased to completely filled 2.7 mm height, except for an area in the front right corner.

At 26.5 s (fig. 18 c)) a v-shaped layer is visible that is already disappearing. Furthermore an incoming droplet at the bottom is visible. The complete figure is symmetric in the xy-plane and yz-plane. The incoming droplet has the dimensions of $x = y = z = 3$ mm and the flow in between has a diameter of 2.4 mm in the middle.

At 33 s (fig. 18 d)) the top layer has completely disappeared, as well as the forming droplet. The image, again symmetric in the xy-plane and the yz-plane, shows a completely covered bottom with a height of $[4.2; 5.1]$ mm, except for three holes in the corners. The D12 leaves the tank through a column on the side with a width of $[1.2; 2.4]$ mm.

PCM2

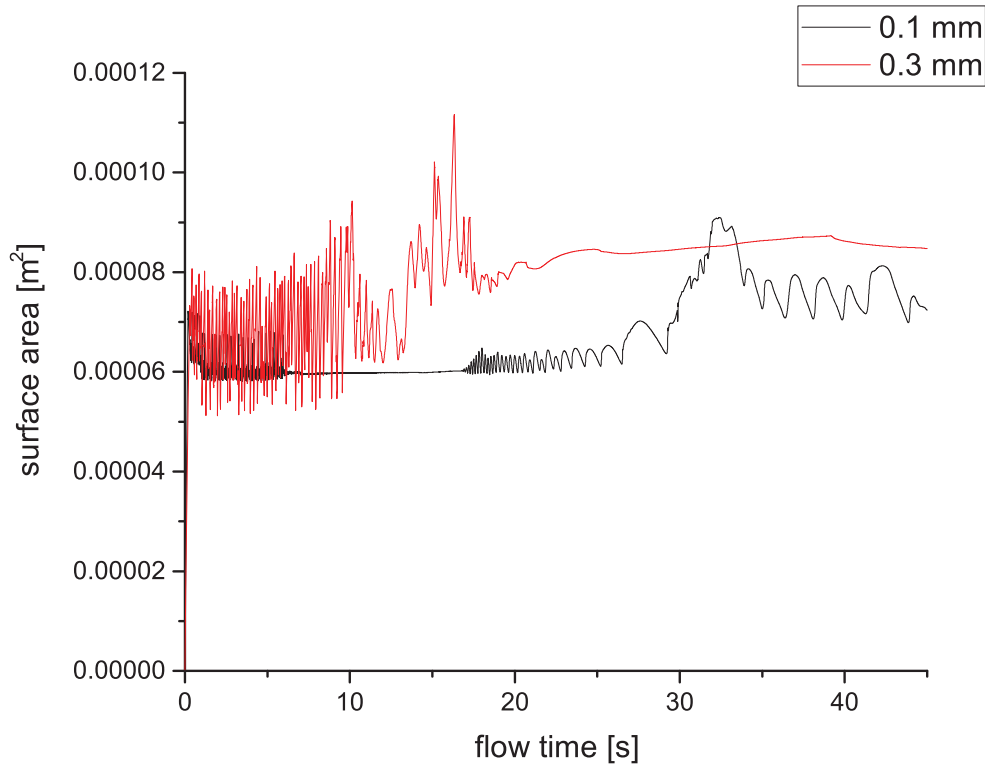


Figure 19: Surface area for $\Delta x = 0.1, 0.3$ mm in H_2O
D12, PCM2, $(x, y, z) = (5, 12.5, 5)$ mm, $r_{in} = 0.4$ mm = r_{out}

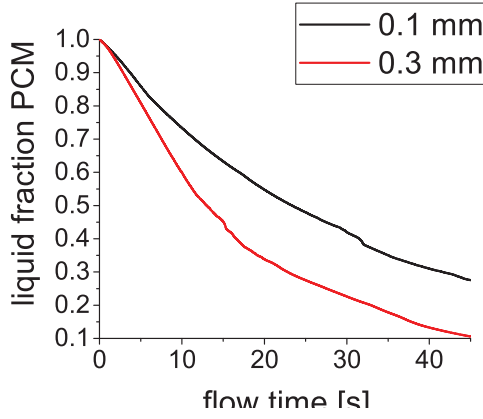


Figure 20: Liquid fraction for $\Delta x = 0.1, 0.3 \text{ mm}$ in PCM2
D12, PCM2, $(x, y, z) = (5, 12.5, 5) \text{ mm}$
 $r_{in} = 0.4 \text{ mm} = r_{out}$

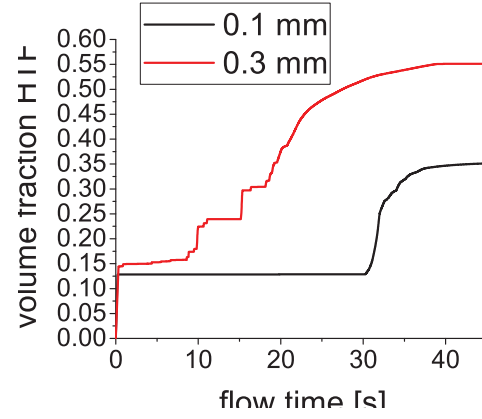


Figure 21: Volume fraction for $\Delta x = 0.1, 0.3 \text{ mm}$ in PCM2
D12, H_2O , $(x, y, z) = (5, 12.5, 5) \text{ mm}$
 $r_{in} = 0.4 \text{ mm} = r_{out}$

Δx [mm]	$(t_0 [\text{s}], A[10^{-5} \text{m}^2])$				
	part 1	part 2	part 3	part 4	main peak
0.1	$(0.2, 6.5) \searrow$	$(1.0, 6.0 \pm 0.2)$	$(6.0, 6.0)$	$(16.8, 6.2 \pm 0.2)$	$(32.472, 9.1)$
0.3	$0.3, 6.7 \pm 1.3$	$\nearrow (10.1, 7.6 \pm 1.8)$	$(12.1, 6.8 \pm 0.6)$	$(16.332, 11.1)$	

Table 9: Important values of the surface area for $\Delta x = 0.1, 0.3 \text{ mm}$ from fig. 19, sorted by the type of change. As the the parts 1-4 do not have much in common the type is specified in a symbolic way near the value. An arrow stays for a periodic increase or decrease, depending on the direction, to a time step and surface area, if left from the value, and from, if placed right. The $\Delta x = 0.1 \text{ mm}$ line shows a final value of $(7.5 \cdot 10^{-5} \pm 0.5) \text{ m}^2$. The $\Delta x = 0.3 \text{ mm}$ line consists only of 3 different parts, except for the main peak. Therefore the main peak counts also as part 4. Its final value is $8.5 \cdot 10^{-5} \text{ m}^2$

Δx [mm]	$l_{PCM} [\%]$ $t = 45 \text{ s}$
0.1	28
0.3	10

Table 10: Final values of the liquid fraction of $\Delta x = 0.1, 0.3 \text{ mm}$ from fig. 14. The graph shows no interesting points

Δx [mm]	$(t [\text{s}], v_{HTF} [\%])$			$v_{HTF} [\%]$ $t = 45 [\text{s}]$
	Plateau 1	Plateau 2	Plateau 3	
0.1	$([0.3; 30.2], 13)$	none	none	35
0.3	$([0.3; 8.6], [14; 16])$	$([11.1; 15.1], 24)$	$([15.4; 18.0], 30)$	55

Table 11: Important values of the volume fraction of $\Delta x = 0.1, 0.3 \text{ mm}$ from fig. 15, sorted by their plateau

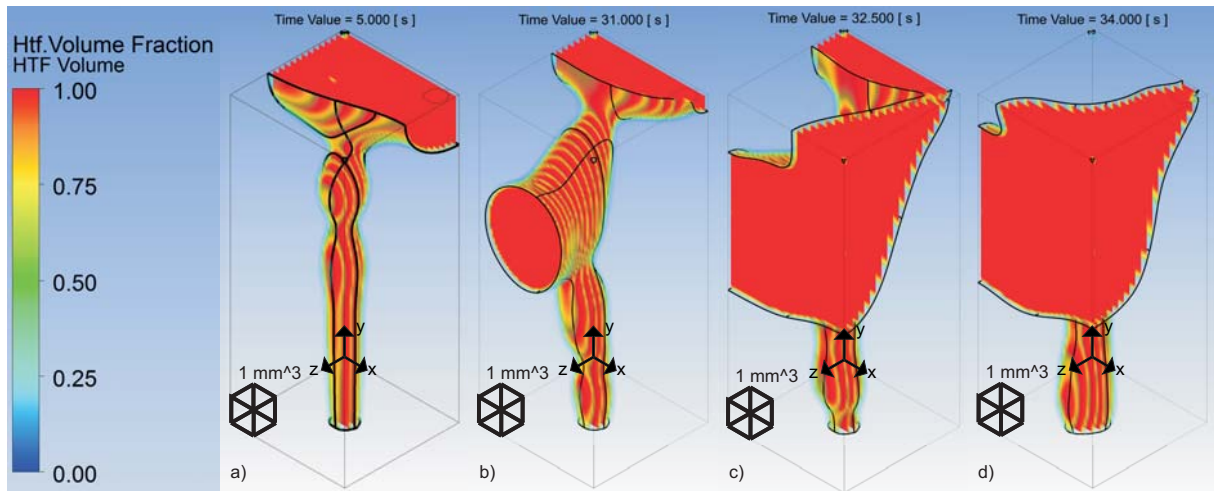


Figure 22: Image series showing a 3D visualisation of the model with D12 and PCM2 for 0.1 mm

a) image showing a try in the droplet formation at the top of the incoming stream connected to a HTF layer on the top wall at 0.5 s

b) image showing an additional path to the front wall at 31.0 s

c) image showing distributed HTF to almost all walls at 32.5 s

d) image showing that the HTF left the back wall at 34.0 s

D12, PCM2, $(x, y, z) = (5, 12.5, 5)$ mm, $r_{in} = 0.4$ mm = r_{out} , Mesh: multi-zone, hexagonal, 0.1 mm

The surface area in fig. 19 for $\Delta x = 0.1$ shows a periodic behaviour after a linear increase for 0.2 s. The next 0.8 s the average value decreases. For the next 10.8 s the value stays constant. The periodic part appears again leading to the main peak and finishing in a periodic part.

The $\Delta x = 0.3$ plot shows a periodic part after a linear increase at the beginning, leading almost directly into the main peak. A drop in the average can be seen in between but the values are clearly periodic in this time frame. Shortly after the peak the value stagnates after a short increase at it's final value. The starting times of each stage and the according surface areas can be seen in 9.

The behaviour of the liquid fraction for $\Delta x = 0.1, 0.3$ mm is shown in fig. 20, showing no interesting features for both of the calculations. Therefore only the final values are listed in tab. 10.

The behaviour of the volume fraction for $\Delta x = 0.1, 0.3$ mm is shown in fig. 21. The 0.1 mm line shows basically 1 plateau, followed by a last step merge into a stagnation curve, while the 0.3 mm line consists of 3 plateaus, one of them climbing slightly. The values are listed in tab. 10.

The visualisation in fig. 22 a) shows the incoming stream, which stays basically the same from the beginning until 31 s. The incoming jet has a length of 10.1 mm and it's widest

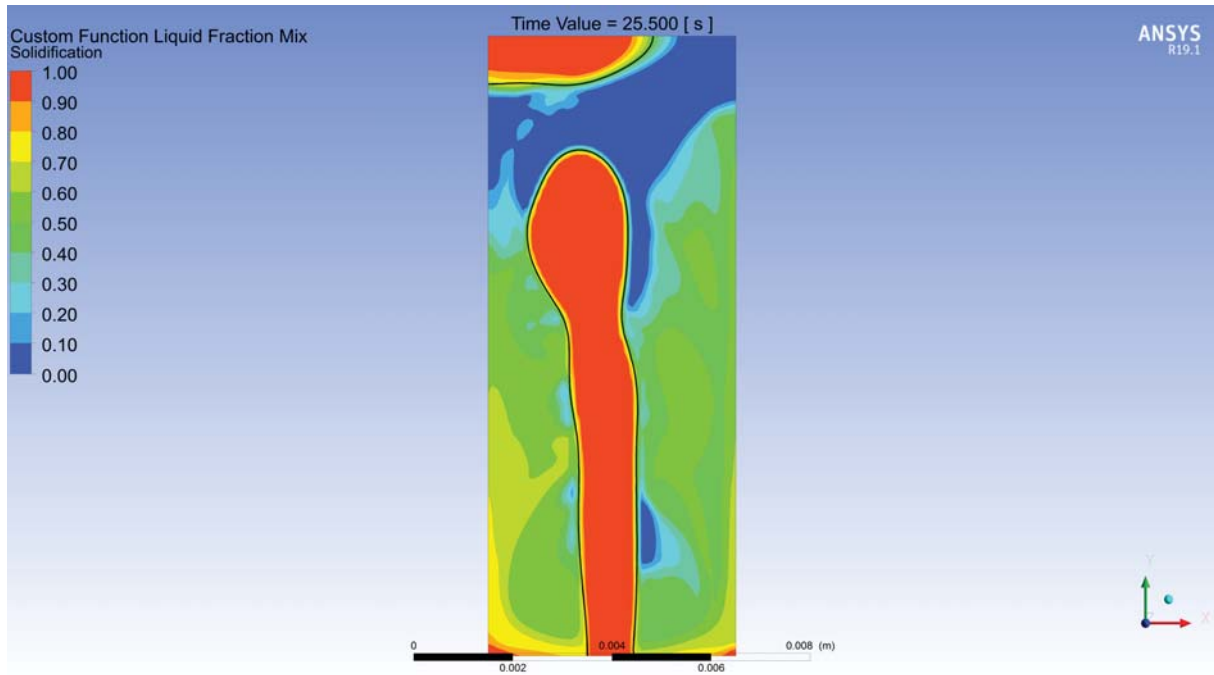


Figure 23: Local liquid-fraction on the centred plane for PCM2 at 25 s
 $D12$, PCM2, $(x, y, z) = (5, 12.5, 5)$ mm, $r_{in} = 0.4$ mm $= r_{out}$, Mesh: multi-zone, hexagonal, 0.1 mm

part at the top of 1.6 mm collides with the already formed top layer of oil with a height in the range of [1.9; 2.7] mm. While the layer fills the whole x-axis, it only uses [2.4; 3.4] mm of the z-axis.

At 31 s (fig. 22 b)) the stream bends to the xy-plane, leaving an asymmetric round imprint with the dimensions of $(x, y) = (3.3, 3.8)$ mm, while it remains connected to the outlet. The top layer has the dimensions in the range of $(y, z) = [0.7; 2.0], [0.6; 1.8]$ mm. The incoming stream connected to this formation has the dimensions of $(x, y) = (1.5, 6.0)$ mm. At around 32.5 s (fig. 22 c)) the oil fills the xy-plane and the yz-plane to a great extent. The stream below has the dimensions of $(y, z) = (5.5, 1.6)$ mm.

At 34 s (fig. 22 d)) the oil flow shifted slightly from the back wall to the front wall.

Fig. 23 shows a time point between fig. 22 a) and fig. 22 b) and will be used in the discussion in the explanation of the HTF behaviour between these two points. The image was taken explicitly at 25.5 s as it matches a tip in the line of the surface area seen in fig. 19. It shows the centre plane of the average values of the liquid fraction calculated over the volume. It can be seen that the top part of this plane between the HTF on top and the stream is completely solidified. The main area of the image shows values near 50%. Higher values are only visible near the bottom and especially on the left wall.

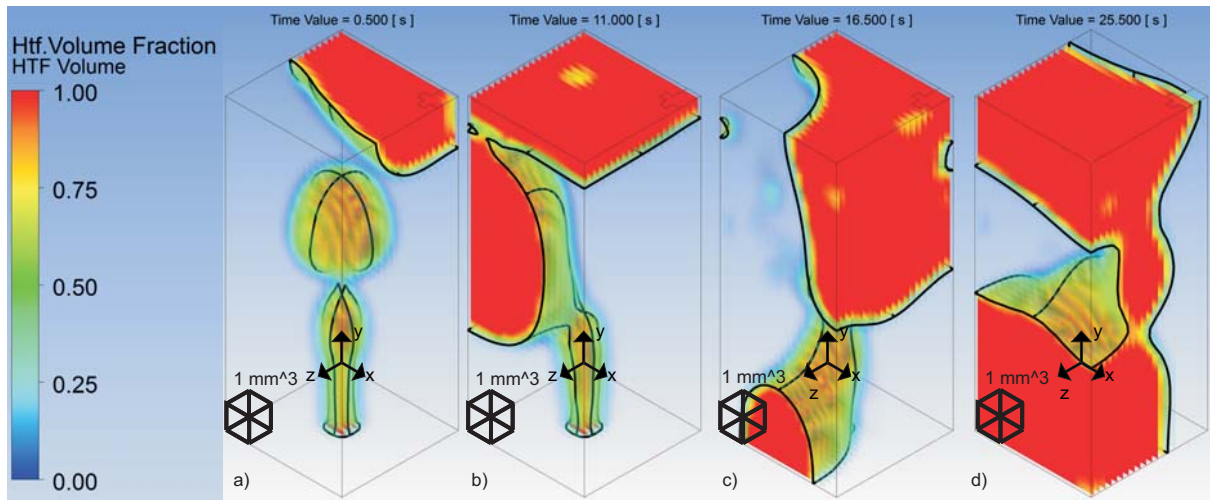


Figure 24: Image series showing a 3D visualisation of the important steps of the model with D12 and PCM2 for 0.3 mm

a) image showing the droplet formation at 0.5 s

b) image showing the incoming stream bending to the front wall and connecting to the top at 11.0 s

c) image showing the HTF creating a channel from the bottom front wall through the centre of the tank coating the front, right and top wall partly at 16.5 s

d) image showing almost two thirds of the tank filled from top and bottom with HTF leaving PCM in between and connected through the right wall

D12, PCM2, $(x, y, z) = (5, 12.5, 5)$ mm, $r_{in} = 0.4$ mm = r_{out} , Mesh: multi-zone, hexagonal, 0.3 mm

The visualisation in fig. 24 a) shows the droplet formation which stays basically the same until 11 s. The incoming jet has a length of 5.4 mm and its widest part at the top is of 1.2 mm. In the upper part of the tank a drop with the dimensions $(x, y) = (3.0, 3.3)$ mm is visible, just under the top layer with a height in the range of [1.5; 2.1] mm D12 and a z-length of 3.6 mm.

At 11 s (fig. 24 b)) the incoming stream leaves a curved imprint on the wall with the dimensions of $(x, y) = (3.3, 7.5)$ mm, that is connected to the top layer. The jet itself has a width of 1.5 mm and bends at a height of 4.2 mm. The top layer now fills the area completely with a height of [0.9; 1.2] mm.

At 16.5 s (fig. 24 c)) the oil leaves imprints on all four surrounding walls in the upper part of the tank and one curved shaped imprint at the bottom.

At 25.5 s (fig. 24 d)) the results show two different layers, connected to each other. The top layer with a height of [2.7; 3.3] mm, the bottom layer [4.8; 5.4] mm. In the z-direction both layers do not fill the model completely. The connection is centred at the yz-plane with a maximum width of 2.4 mm.

6.3 Discussion of the comparison of the main mesh sizes

When comparing the surface area, as shown in fig. 13 one realises that the values for 0.1 mm and 0.3 mm have an overall shape similar to each other. Both graphs start with a linear ascend, turning into a wave shortly, increasing in amplitude after some time. Also both graphs end with a couple of peaks and one last big peak before the drop and stagnation at similar time. The main difference is the part in between. While the 0.1 mm line stays constant for a while, the 0.3 mm line is still in wave form but with smaller amplitude.

When looking at the detailed values, by including the liquid-fraction (fig. 14) and the volume-fraction (fig. 15) and comparing these results to the series of images in fig. 16 of the 0.1 mm simulation and in fig. 18 for 0.3 mm, one realises that the results are quite different.

The first droplet formation process in fig. 16 a) and fig. 18 a) is in principle the same, although the values are different. The average surface area of 0.1 mm is higher by $1.2 \cdot 10^{-5} \text{ m}^2$ or 24 % than the one for 0.3 mm. The incoming jet is similar in shape and size (same width but 7 % longer). The resulting drop is 23 % smaller.

In the next phase the surface area continuously increases and decreases for both calculations in a similar manner. Obviously an increase happens, when a drop is forming, a decrease, when a drop is leaving. Until 8.6 s and 11.2 s the amplitude stays constant. An interesting effect is that the top layer is already fully developed for 0.1 mm at 0.5 s, while it takes 1.5 s for the 0.3 mm model. The increase in the surface amplitude signalizes a deformation of the drops to a higher surface area. This is probably due to solidification in surrounding areas. As explained earlier, Fluent defines solidified fluid material as fluid material with an infinite viscosity. This means that the HTF is able to push solidified zones in front of it and it can be hindered in it's forthcoming. This becomes more and more clear when analysing further steps of the calculations.

Fig. 16 b) for 0.1 mm was taken at 12.0 s showing a single jet. When looking at an image of the cross section showing the liquid fraction at exactly this time step (fig. 17(a)) one realises that the cool-down, as well as the freezing, starts at the top and works it's way to the bottom. This was quite unexpected as the oil increases it's temperature the longer it stays in the tank. The temperature gradient is therefore the strongest on the bottom. Nevertheless the surface area on the droplet is greater than at the bottom of the stream. As the heat transfer is proportional to the surface area this could explain this effect. The image shows that the PCM parts with the lowest liquid fraction are at both sides of the stream at the top facing downwards. As the jet tries to go the way with the least energy consumption, it just shoots upwards and does not create any droplets until 22.0 s. At this point it is interesting to switch to the lower resolution model. For some unknown reason this does not result in a steady stream as in the high resolution model.

The droplets continue to increase their surface and their volume until a wider area directly above solidified over 50 % blocking the passage in fig. 18 b), so that the oil tries to evade and gets blocked again but by the surrounding walls, where it flows upwards in order to

reach the outlet. The following behaviour is similar in both situations.

A big drop is created in fig. 16 c) and fig. 18 c), probably due to the nearly completely frozen area ($\leq 3\%$) directly on the front sides of the incoming drop for 0.1 mm. (fig. 17(b)) This narrows the passage and the drop grows. This happens, however, at different times: 23.0 s for the 0.1 mm calculation and 26.5 s for 0.3 mm. In both cases when this final drop leaves, it seems to take a lot of oil with it. In fact, the HTF only rearranges. The actual volume does actually increase to 33 % for 0.1 mm and 47 % for 0.3 mm at around 27 s. The surface area for the higher resolution is reaching its global maximum value, while the lower resolution is already dropping to its final value. Also noticeable is the drop in the liquid fraction in the 0.3 mm calculation at this time. From this point on it solidifies faster than the 0.1 mm calculation.

In fig. 18 d) it can be seen that the PCM has solidified to a great extent, pushing the HTF to the right corner, where it reaches the outlet through a channel. At 27.5 s in the 0.1 mm model the oil has to evade by using the wall and leaves a small part at the top behind.

The surface area has its peak in fig. 16 d), due to an increase of the stream at the bottom part of the tank.

In the following 2 s (fig. 16 e)) the HTF is only moving fully alongside the wall for the rest of the calculation.

The resulting surface area is by 52 % higher in the 0.1 mm model, than in the 0.3 mm, the liquid fraction is higher by 9 % and the volume fraction is lower by 30 %. While the global liquid fraction is due to its continuity an insufficient indicator of the fluid behaviour it is interesting that it is the only value that is not strongly dependant on the model resolution. The surface area has a similar development but varies quite a lot between 9 s and 23 s and its values are far away. The volume fraction starts very similar but diverges after enough time for a great amount. Moreover the graph shows obvious jumps in the curve, whereas the 0.1 mm line is almost perfectly steady for the most part. All these results show that the 0.3 mm mesh can be a good indicator when a fast evaluation of the quality of the model is needed. For more detailed and quantitative evaluations it is highly recommended to use a mesh size of 0.1 mm, as was done for the parameter study in the next chapter. Smaller might give better results but can only be done when the results have to be extremely accurate and computer power and calculation time do not matter. Nevertheless, as CPU power and efficiency are going to increase with time this is going to change eventually.

When comparing the surface area for both calculations with PCM2, as shown in fig. 19, with each other and with H₂O (fig. 13) there is one major difference. While the 0.3 mm line looks very similar for both PCMs, the line for the 0.1 mm PCM2 has a much smaller fluctuation (10 %) and there is no stagnation at the end of the calculation. The 0.1 mm line is stuck for most of the calculation at $6 \cdot 10^{-5} \text{ m}^2$, followed by a 22 % smaller peak than the calculation with H₂O, reaching its final value 3 % above. In the first 10 s the 0.3 mm PCM2 line is also in the same range as the 0.3 mm H₂O line from 11 s to 17 s. The calculation for PCM2 is, however, followed by a slightly higher peak (11 %) stagnating at a

85 % higher value at the end. The similarity between the surface area of both materials for the 0.3 mm mesh arises from the small changes in the material parameters, as explained in tab. 3.

When analysing the visualisation in fig. 24 the actual flow is only similar in the first few seconds of the calculation.

At 0.5 s fig. (24 a)) for both PCMs a droplet formation is possible, with the beginning of the forming of the top layer. The cross area of the droplet is, however, 83 % bigger for PCM2. The jet has a tip on the top, is 17 % more narrow and 39 % shorter for PCM2. Due to the lower melting heat of TBAB and PCM2 the solidification process starts earlier resulting in a different flow of the HTF.

At 11 s fig. (24 b)) local areas around the jet have been solidified ≤ 30 % bending the stream to the wall. As in other calculations the oil gets cut off from the top layer and finds a new way on the other side, in this case at 15.5 s.

Again a big droplet is trying to unfold at the inlet leading to the global peak and fig. 24 c). From there the bottom fills with oil leading to fig. 24 d), which basically does not change for the rest of the calculation. It is interesting to note that the top layer is still present for PCM2 at the end, additionally to the bottom layer and the path is not exactly in the corner, as in the H₂O calculation. One explanation could be the higher density for PCM2. Although the difference between the density of the PCMs is much smaller than the density difference between PCM and HTF, it may just be sufficient high enough to sink faster, so that the HTF can ascend slightly easier. This means that even during the solidification enough HTF can reach the top layer to keep it filled. Whereas in the case of H₂O the HTF ascends a tick slower and is unable to keep the level. Therefore HTF will leave the tank eventually and the solidification can be completed at the top. This is why the HTF can only use a small channel in a corner far away from the centre and directly leading to the outlet.

The 0.1 mm PCM2 calculation will not be compared in detail, as the results are immensely different. This will be clear, when analysing the series of images in fig. 22.

Image fig. 22 a) was taken explicitly as the first image. The HTF flow stays for the first 30 s nearly identical and this was the first data file where an image from this point of view could be taken, where the stream could be seen good enough. The small fluctuations in the surface area result from fluctuations of the top layer and pulsing of the jet during the tries in forming a droplet. No droplet formation at all is possible as the stream passes so easy through the PCM that it reaches the top too fast. At 25.5 s the frequency of the surface area decreases.

At this point it can be clearly seen that the forming droplet at the top of the HTF jet bends in direction of the front xy-plane eventually reaching fig. 22 b) at 31 s of the series. Fig. 23 shows that the PCM in the top part of the tank has already frozen completely, as expected. The oil can therefore only evade through the side reaching it's global maximal surface area in fig. 22 c).

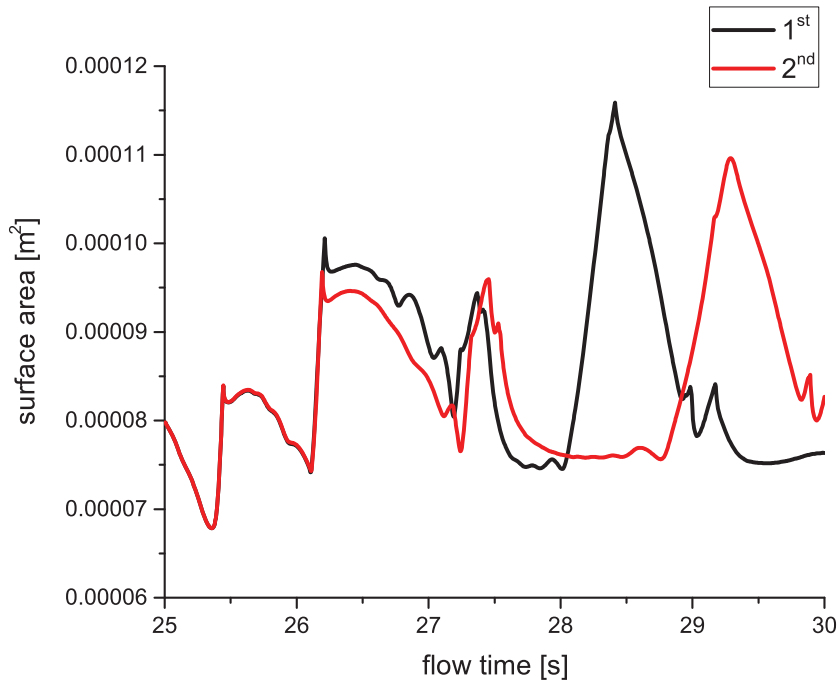
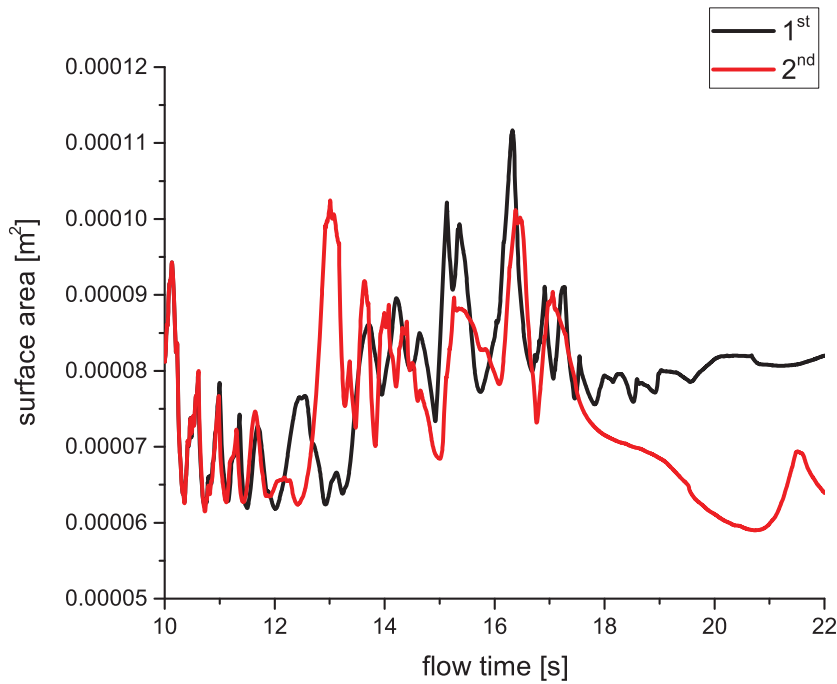
In fig. 22 d) at 34 s it can be seen that there is hardly any HTF left on the back xy-plane.

Consulting tab. 11 shows that the value stays constant for the last 15 s of the calculation. This means that this is only a rearrangement due to the solidification. Actually the incoming stream is slightly thicker in the last image. This implies that the oil at the back layer left the tank but could not be replaced, as the incoming oil got stuck shortly after the inlet. Also the volume-fraction of the 0.3 mm line has similar instabilities for both materials. Another interesting result is that the liquid-fraction in fig. 20 differs by a factor of 2.8. The final liquid-fraction for PCM2 is by 12 % higher than the value for H₂O. This is presumably due to the model specifications. As the geometry is too small for the droplet to form the surface area stays nearly constant for two thirds of the calculation. The heat transfer is proportional to the contact area, as explained earlier. Therefore the PCM needs more time to cool and to solidify when in contact with a single jet, than with droplets. As the parameter study should have been with water-TBAB, which became PCM2 accidentally, this means that some final adaptations had to be made. Before this part of the project is explained, however, it is necessary to check the results on reproducibility.

6.4 Reproducibility

When running the same calculation twice from the beginning the results show divergences for surface area, volume- and liquid-fraction in the range of 10^{-3} and smaller for all 4 calculations, as listed in tab. 12. The calculations for H₂O show negligible deviations after the second calculation, as expected. The calculations for PCM2, however, showed quite different results, mesh independent. When analysing the data more closely it was found that the data file for 34 s was damaged and could not be accessed by ANSYS. The simulation was run two additional times, started from the data point for 33.5 s, and showed exactly the same results as the original calculation. As there was no explanation found and the results stayed the same in three of four calculations it was decided to give it a go and continue with the evaluation process. This was, when the probable cause for the great divergence in the calculation could be found by accident.

As the complete calculation was saved only every 0.5 s it was intended to re-calculate small intervals in between with every 0.1 s saved in order to better understand the results. When analysing these simulations it became clear quickly that some visualisations did not match the results of the full calculation. A more detailed evaluation revealed that short calculations no longer than one second agree perfectly with the same time interval of the full calculation but longer ones differ to a more or less extent. Two diagrams that present the different stages of these divergences are shown in fig. 25. It can be clearly seen that in the first second the results are identical. For the next few seconds the calculations that were started from a later time step behaves in a similar way but mostly delayed and returns lower values. In a few cases the peaks turned up slightly earlier and in one specific case even higher than the original results.

(a) Surface area for the 0.1 mm mesh and H₂O

(b) Surface area for the 0.3 mm mesh and PCM2.

Figure 25: Surface area from the original calculation started at $t = 0$ s, named "1st" in comparison to an additional calculation for each material started at the first time steps shown, named "2nd". The images were taken due to their representative nature.

$D12$, $(x, y, z) = (5, 12.5, 5)$ mm, $r_{in} = 0.4$ mm = r_{out} , Mesh: multi-zone, hexagonal

H₂O 0.1 mm			
parameter	min divergence	ave divergence	max divergence
surface area	$-4 \cdot 10^{-6}$	$-6 \cdot 10^{-8}$	$9 \cdot 10^{-7}$
liquid-fraction	$-1 \cdot 10^{-7}$	$4 \cdot 10^{-8}$	$7 \cdot 10^{-7}$
volume-fraction	$4 \cdot 10^{-9}$	$1 \cdot 10^{-9}$	$1 \cdot 10^{-8}$
H₂O 0.3 mm			
surface area	$2 \cdot 10^{-4}$	$-3 \cdot 10^{-7}$	$2 \cdot 10^{-4}$
liquid-fraction	$7 \cdot 10^{-6}$	$7 \cdot 10^{-7}$	$1 \cdot 10^{-5}$
volume-fraction	$6 \cdot 10^{-6}$	$6 \cdot 10^{-8}$	$9 \cdot 10^{-6}$
PCM2 0.1 mm 2nd			
surface area	-0.09	0.004	0.16
liquid-fraction	-0.03	-0.002	0.004
volume-fraction	-0.001	$-5 \cdot 10^{-4}$	0.005
PCM2 0.1 mm 3rd, 4th	no changes in the precision range		
PCM2 0.3 mm			
surface area	-0.001	$-9 \cdot 10^{-6}$	0.001
liquid-fraction	-0.001	$-5 \cdot 10^{-5}$	0.001
volume-fraction	$-7 \cdot 10^{-6}$	$2 \cdot 10^{-7}$	$4 \cdot 10^{-5}$

Table 12: Relative changes of additional calculations compared to the first for H₂O and PCM2 with 0.1 mm and 0.3 mm mesh

The first diagram shown for H₂O, 0.1 mm, is from a short enough time interval ([25,30] s,) that the difference stays in an acceptable range for the most part of the calculation. (fig. 25(a)) The calculation started at 25s stays identical with the original calculation for nearly 1.2s. The value at 26.2s is 12 % lower as it should be. For the next 1.1s the shape is very similar but the values remain lower. The peak at 27.3 is shifted by 0.1 s to the right and by 3 % higher. The last peak at 28.4s is shifted by 0.9 s and 5 % lower.

For the presented calculation of PCM2 with 0.3 mm the calculation started at 10 s stays identical to very similar for the first 1.9 s. (Fig. 25(b)) The peak at 12.4 s is shifted by 0.6 s to the right and by 34 % higher. The next series consisting of three followed closely peaks differs in (absolute time difference (s), relative surface area difference (%)): (0, 6), (-0.1, -0.1), (-0.2, 3). The double peak is reduced to one plateau at the same time but 13 % lower. The global maximum peak is shifted by 0.1 s to the right and 10 % lower. The next double peak is reduced to one single peak in between. Then the calculation drifts apart quite extensively until reaching a final value that is 22 % smaller. This means not only, that detailed flow analysis with high time resolution saves has to be done for time ranges below 5 s for a qualitative evaluation and below 1 s for a quantitative evaluation, but more importantly that calculations that are intended to be compared with each other have to be resumed from the exact same time step, when kicked out from the server, in order to reassure the reproducibility of the results. This behaviour of ANSYS Fluent was

to this date unknown in the research team and could not be explained. There might be some kind of rounding error that becomes more present when starting the simulation from different time steps but this was just a shot in the dark. The ideal solution would therefore be to run all simulations without abortion, which is not possible on VSC3 without special authorisation. Restarting all jobs from the same data point was therefore the only option available. Although after this evaluation it becomes clear that these results will have an inaccuracy, dependant on the left-over time after the kick-out from VSC3, compared to simulations done in one step. As the task of this thesis was only to be able to estimate the results from the parameter set-up the exact values are only of secondary importance. For more detailed calculations it is recommended to either create a model that is able to run the desired time in under 72 h or to ask for special authorisation for running the simulations as long as necessary.

6.5 Final Model Changes

As explained in the last subsection the model is sufficient when working with H₂O but too small when working with PCM2. Due to time shortening it was not possible to adapt the geometry a second time. A workaround through the settings was required that would made calculations with drop formation possible while keeping geometry and mesh. After a bit of research on simulations and experiments about droplet formation and jet breakup there was a master thesis by Wang that had the ideal solution. While this master thesis actually describes the simulation of an ink-jet printer with a small painting nozzle and droplet of $d = [30; 50]$ microns, velocities in the range of $[9.26; 18.51] \frac{m}{s}$ and Reynolds-numbers between 3 and 10, the important factors were the changes in the flow breakup in dependence of the contact angle. For all simulations the jet becomes shorter and the droplets form faster when using small contact angles. Also the velocity of the first droplet decreases for smaller angles. [27] It was therefore decided to try different contact angles on the model with the intention of shortening the stream enough that a droplet can unfold within the same geometry.

ϕ	coated wall x [mm]	jet length y [mm]	droplet size (x, y) [mm]
0°	5.0	4.1	3.6, 3.3
30°	3.8	7.6	3.8, 3.3
45°	2.4	8.3	4.5, 2.9
60°	1.4	10.8	0.9, 1.5
90°	1.0	≥ 12.5	none

Table 13: Geometric results for different contact angles, as seen in fig. 27

A comparison of calculations with different contact angles in fig. 27 and tab. 13 for 0.5 s shows the droplet formation as good as possible with a time saving interval of 0.1 s. The

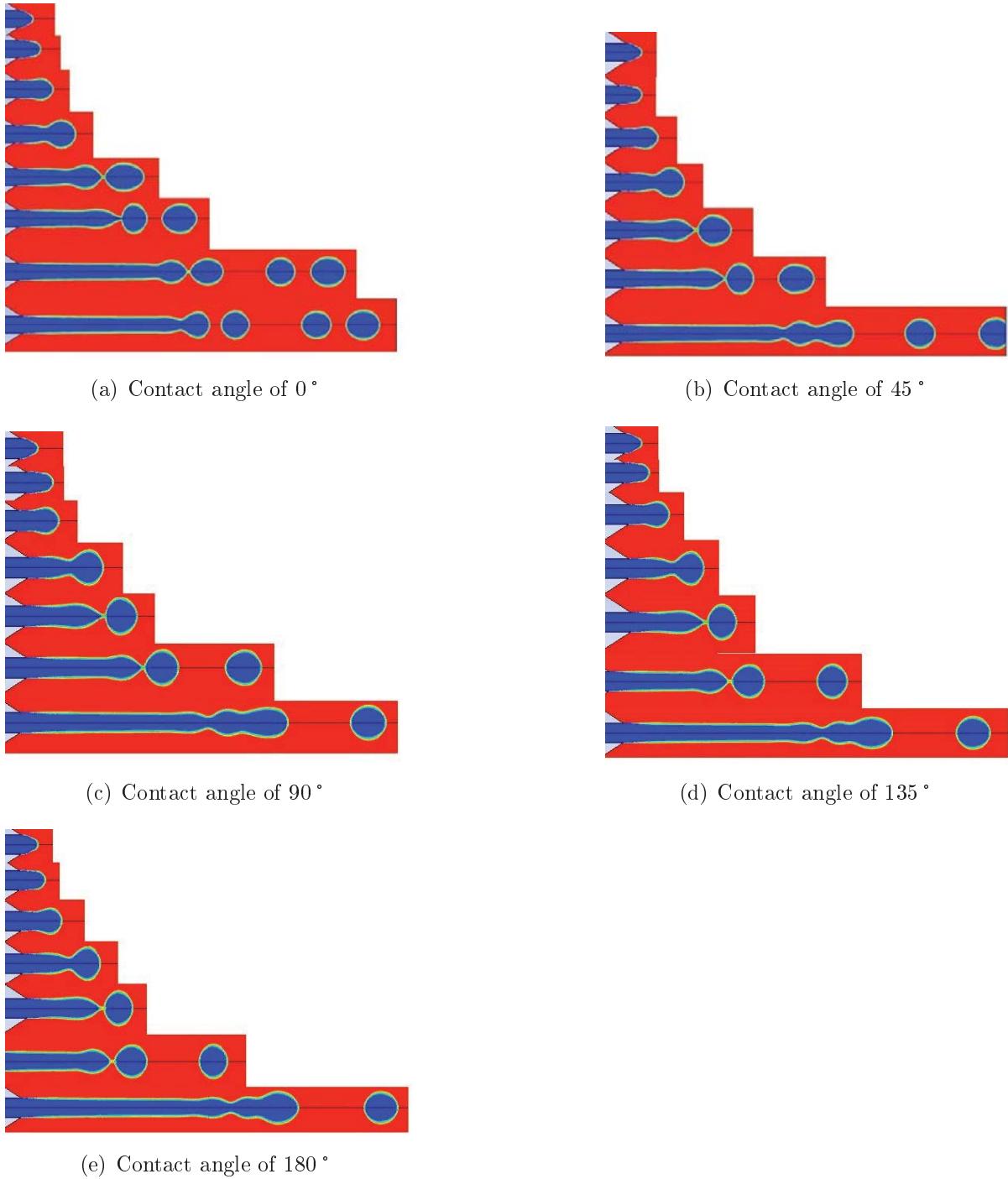


Figure 26: The visualisation of the jet breakup and droplet formation from CFD-simulations for droplet on demand ink-jet printers by Wang [27] shows that the incoming jet length, as well as the time until breakup, increases for higher contact angles. At the last time step for 0° there are already three droplets, while the calculation for 180° shows only a single droplet. Time indexes for each sub-figure from top to bottom: $8.4\mu\text{s}$, $17.7\mu\text{s}$, $37.3\mu\text{s}$, $75.6\mu\text{s}$, $138.0\mu\text{s}$, $181.0\mu\text{s}$, $280\mu\text{s}$, $300\mu\text{s}$.

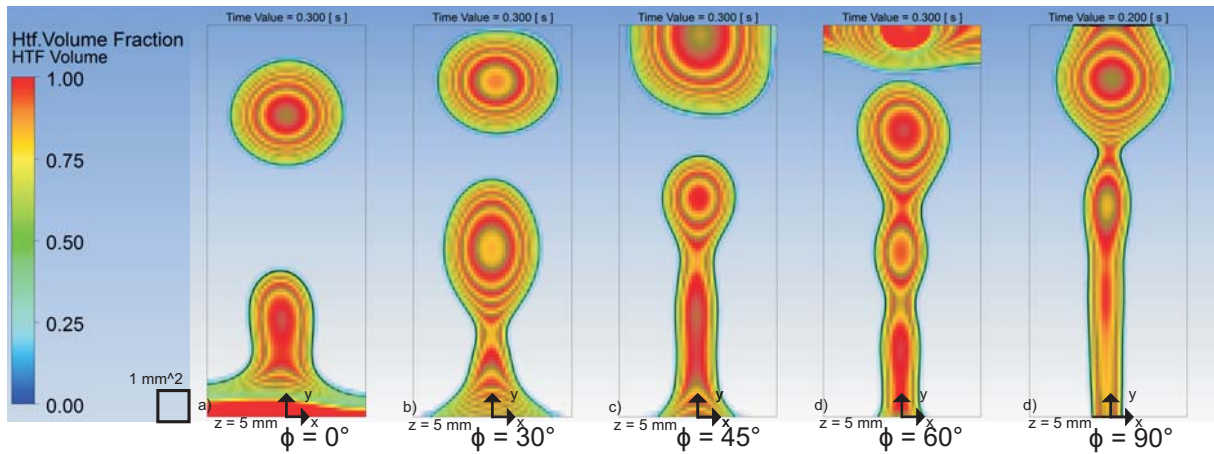


Figure 27: Image series showing a 2D visualisation of different contact angles on $z = 5 \text{ mm}$ at the time step 0.3 s and on 0.2 s for 90° .

- a) $\phi = 0^\circ$, almost circular droplet and an inlet stream coating the bottom wall completely
- b) $\phi = 30^\circ$, elliptic shaped droplet, droplet during formation and almost coated bottom wall
- c) $\phi = 45^\circ$, droplet during leaving and stream coating about half of the bottom
- d) $\phi = 60^\circ$, top layer of HTF with circular shape in the centre, closely followed by a stream of 2 parts with forming droplets
- e) $\phi = 90^\circ$, stream with droplet on top, trying to form, in contact with the outlet

$D12$, $PCM2$, $(x, y, z) = (5, 12.5, 5) \text{ mm}$, $r_{in} = 0.4 \text{ mm} = r_{out}$, Mesh: multi-zone, hexagonal, 0.1 mm

basic setting in Fluent, which was used for the earlier simulations, is 90° . To achieve a broad variation the calculations were initially done with 0° , 30° and 60° . A simulation with 45° was added later for additional support in the decision process.

While the 0° angle shows the shortest stream (fig. 27 a)) and therefore the maximum available space for the droplet, which also is of approximate circular shape, the oil completely coats the bottom, which resulted in a problem at the end of the simulation. Due to the oil layer at the bottom further droplet formation is prevented and the oil continues to ascend as one steady flow.

The calculation with 30° shows an oval shaped droplet that still fits nicely into the geometry (fig. 27 b)) but also a broadened beginning of the incoming jet.

The 45° simulation shows a lesser broadened stream (fig. 27 c)) and while the droplet has enough space to unfold, it quickly touches the top wall.

The calculation with 60° still has enough space for droplet forming (fig. 27 d)) but the stream (including the forming droplets) uses 86 % of the model height. The droplet at the captured time frame is not even visible as droplet any-more, as it coats the top wall completely.

The model used before with 90° was added for comparison (fig. 27 e)) and shows a stream with two forming droplets in front. The last one is already colliding with the top wall.

While the stream for the 45° simulation is in the optimal range it was concluded that the droplet might have insufficient space and the following calculations were done with a

contact angle of 30° .

The calculations with PCM2 in the last subsection also showed that during some stages more HTF enters the model than is able to leave. The idea was then to open the top completely. An outlet at this size introduces, however, two other effects. Firstly the type of back-flow setting is important. When using HTF this means that no HTF is able to leave the outlet and the tank gets filled completely after some time. The option necessary is therefore a full PCM back-flow. As the incoming oil, however, needs space, the equal volume of PCM2 has to leave the model. When the HTF leaves an equivalent of amount of PCM re-enters the tank at the outlet to compensate again for the missing volume. For a small outlet the amount is, of course, smaller, than for a big outlet and does not have to be taken into account. The ideal compensation for this would be, as done in experiments, e.g. [19], is a buffer of air at on top of the PCM, so that the amount of PCM just moves back and fourth and the air takes the part of compensating for the oil. This was not implemented in this model due to the amount of time needed for finding an air buffer big enough for all calculations in the parameter study.

The second change for the analysis of the results compared to the earlier model is that the heat transfer with the model and the outside can be neglected for small outlets. With a completely open top, however, this heat transfer is immense and can falsify the results. As the outlet temperature can only be set to a constant value in Fluent this does indicate that the PCM always has to be cooled or heated from the outside, depending on the setting. The outlet temperature was set to 0.1 K above the solidification temperature in order to minimize heating for the PCM to be still able to freeze and to prevent the PCM from cooling down faster. This however did not work as intended. Due to time reasons, however, this model had to be finally used in the parameter study.

7 Parameter Study

The following itemization specifies all settings used in the parameter study:

- $(x, y, z) = (5, 12.5, 5)$ mm
- $r_{in} = 0.4$ mm defined in geometry
- $A_{out} = 25$ mm², complete top face
- $\Delta x = 0.1$ mm, multi-zone-hexagonal
- $A_{in} = 4.6 \cdot 10^7$ m², irregular shape composed out of cubic cells after meshing
- Global settings: pressure-based solver, absolute velocity, transient
- $\vec{g} = \begin{pmatrix} x \\ y \\ z \end{pmatrix} = \begin{pmatrix} 0 \\ -9.81 \\ 0 \end{pmatrix} \frac{\text{m}}{\text{s}^2}$
- Model settings:
 - Multiphase (VOF):
 - 2 eulerian phases, explicit, sharp interface, volume fraction cut-off 10^{-6}
 - courant number 0.25, implicit body force
 - $\sigma = 0.0173 \frac{\text{N}}{\text{m}}$, continuum surface force, wall adhesion on
 - Energy
 - viscous (laminar)
 - solidification & melting
- Material properties of PCM2 and D12, see tab. 3
- Wall boundary: no slip condition, $\phi = 30^\circ$ on bottom wall, $\phi = 90^\circ$ on all other walls
- Inlet boundary according to tab. 14
- Outlet boundary: $T_{out} = 285.25$ K, $v_{HTF}^{back-flow} = 0$
- Solver settings:
 - Pressure-velocity-coupling – SIMPLE
 - Pressure gradient – Least Squares Cell Based
 - Volume fraction – Geo-Reconstruct
 - Energy – Second order Upwind
 - Transient formulation – First Order Implicit

- Residuals: continuity, $v_{x,y,z}$, energy – absolute convergence of 10^{-6}
- Initialisation: $T_0 = 286.15 \text{ K}$, $v_{HTF} = 0$
- $\Delta t = 1 \text{ ms}$, 20 iterations
- $\Delta t_{save} = 0.5 \text{ s}$
- All calculations were re-started from 30.500 s for reproducibility.

A_{mush}	$-\Delta T [\text{K}]$	$v_{in} [\frac{\text{m}}{\text{s}}]$
10^1	1	0.2
10^4	5	0.3
10^5	10	0.4
10^6	15	
10^9	20	

Table 14: Parameters varied for the parameter study. The **bold values** are the ones of the base model

The varied parameters can be found in tab. 14. Only one parameter was varied at a time. The other two always stayed at the base value for comparison.

7.1 The base model

Results

In order to show the general behaviour, up to four diagrams will be shown at once side-by-side. All diagrams can be found in full scale in the appendix C in the same order and including the captions. The steps of the analysis was kept exactly the same for all other calculations. Therefore this process was only explained on the base model, except where changes were necessary, and all following results were only summarized. Of course, a detailed discussion was included, when needed. Furthermore, each parameter variation has it's own subsection, divided into results and discussion.

The surface area in fig. 28 increases linearly to it's global maximal value of $9.8 \cdot 10^{-5} \text{ m}^2$ at 294 ms. For the rest of the calculation the value jumps in the range of $(Min, Ave, Max) = (5.1, 7.0, 8.6) \cdot 10^{-5} \text{ m}^2$.

The lowest value for the liquid fraction PCM in fig. 29 of 88 % is achieved near 37 s. After that the liquid-fraction increases again to 90 %.

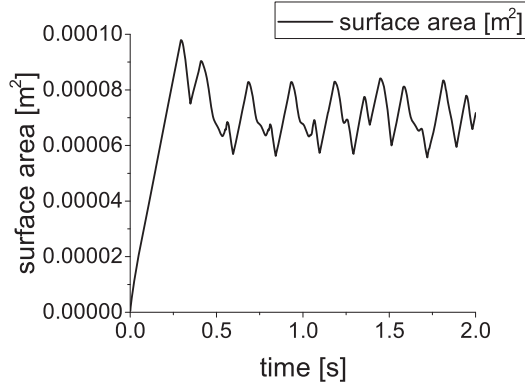


Figure 28: First 2 s of the surface area for the base model

$D12$, $PCM2$, $(x, y, z) = (5, 12.5, 5)$ mm

$$A_{in} = 4.6 \cdot 10^{-7} \text{ m}^2, \quad A_{out} = 25 \text{ m}^2$$

Mesh: multi-zone, hexagonal, 0.1 mm

$$A_{mush} = 10^5, \quad \Delta T = -10 \text{ K}, \quad v_{in} = 0.4 \frac{\text{m}}{\text{s}}$$

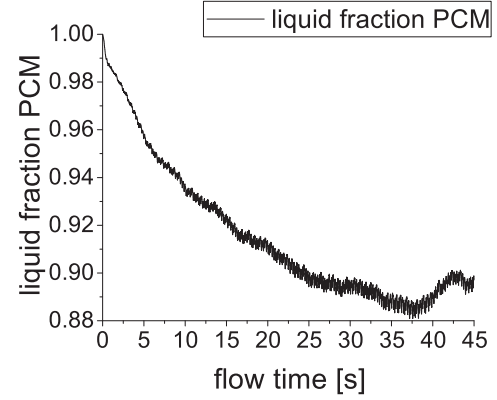


Figure 29: Liquid-fraction for the base model

$D12$, $PCM2$, $(x, y, z) = (5, 12.5, 5)$ mm

$$A_{in} = 4.6 \cdot 10^{-7} \text{ m}^2, \quad A_{out} = 25 \text{ m}^2$$

Mesh: multi-zone, hexagonal, 0.1 mm

$$A_{mush} = 10^5, \quad \Delta T = -10 \text{ K}, \quad v_{in} = 0.4 \frac{\text{m}}{\text{s}}$$

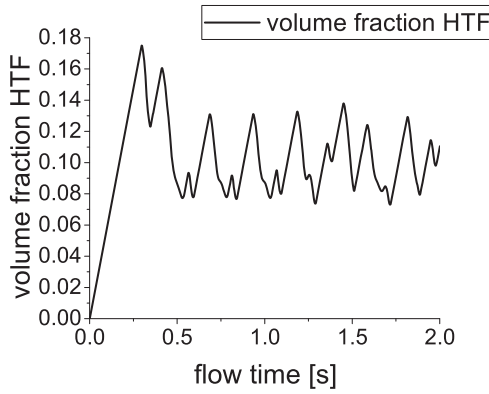


Figure 30: First 2 s of the volume-fraction for the base model

$D12$, $PCM2$, $(x, y, z) = (5, 12.5, 5)$ mm

$$A_{in} = 4.6 \cdot 10^{-7} \text{ m}^2, \quad A_{out} = 25 \text{ m}^2$$

Mesh: multi-zone, hexagonal, 0.1 mm

$$A_{mush} = 10^5, \quad \Delta T = -10 \text{ K}, \quad v_{in} = 0.4 \frac{\text{m}}{\text{s}}$$

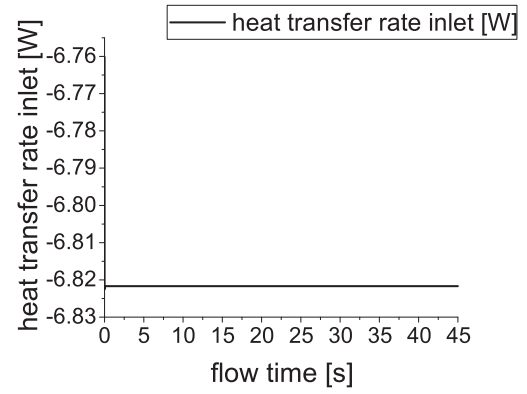


Figure 31: Heat transfer at the inlet for the base model

$D12$, $PCM2$, $(x, y, z) = (5, 12.5, 5)$ mm

$$A_{in} = 4.6 \cdot 10^{-7} \text{ m}^2, \quad A_{out} = 25 \text{ m}^2$$

Mesh: multi-zone, hexagonal, 0.1 mm

$$A_{mush} = 10^5, \quad \Delta T = -10 \text{ K}, \quad v_{in} = 0.4 \frac{\text{m}}{\text{s}}$$

The volume fraction in fig. 30 increases linearly to its global Max value of 18 % at 298 ms. For the rest of the calculation the value jumps in the range of $(Min, Ave, Max) = (7, 10, 14)$ %.

The inlet heat transfer in fig. 31 stays constant with a precision of 0.1 W at -6.8 W.

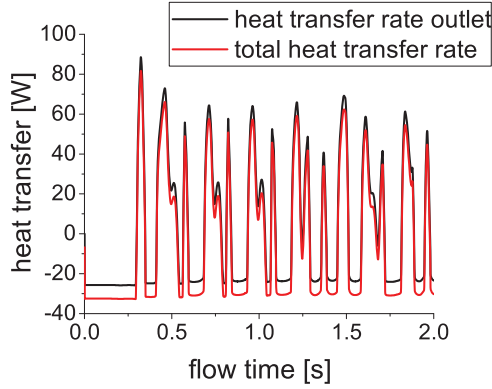


Figure 32: First 2 s of the heat transfer at the outlet, as well as the sum of inlet and outlet, for the base model

$D12$, $PCM2$, $(x, y, z) = (5, 12.5, 5)$ mm

$$A_{in} = 4.6 \cdot 10^{-7} \text{ m}^2, \quad A_{out} = 25 \text{ m}^2$$

Mesh: multi-zone, hexagonal, 0.1 mm

$$A_{mush} = 10^5, \quad \Delta T = -10 \text{ K}, \quad v_{in} = 0.4 \frac{\text{m}}{\text{s}}$$

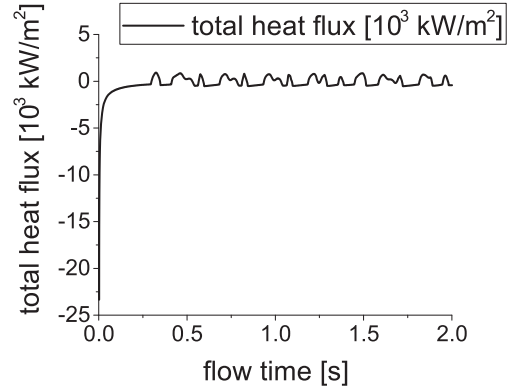


Figure 33: First 2 s of the heat flux calculated by dividing each value of the total heat transfer rate of fig. 32 by the corresponding value of the surface area in fig. 28 for the base model

$D12$, $PCM2$, $(x, y, z) = (5, 12.5, 5)$ mm

$$A_{in} = 4.6 \cdot 10^{-7} \text{ m}^2, \quad A_{out} = 25 \text{ m}^2$$

Mesh: multi-zone, hexagonal, 0.1 mm

$$A_{mush} = 10^5, \quad \Delta T = -10 \text{ K}, \quad v_{in} = 0.4 \frac{\text{m}}{\text{s}}$$

The total heat transfer in fig. 32 reaches its maximum value of 81.7 W at 323 ms. For the rest of the calculation it jumps in the range of $(Min, Ave, Max) = (-31.8, -0.1, 72.9) \text{ W}$.

The heat flux in fig. 33 starts the periodic habit at 295 ms and jumps in the range of $(Min, Ave, Max) = (-557.5, -9.6, 1030.5) \frac{\text{kW}}{\text{m}^2}$, with its maximum value at 28.161 s.

Screen-shots of the heat flux at the outlet were taken at 25.0 s (fig. 34) and 25.5 s (fig. 35), which are going to be used in the discussion section for explaining the values of the heat flux. The first image shows that the flux is positive both inside the 50 % volume-fraction circle and outside on nearly the whole area. The negative contour is around the 50 % volume-fraction. The average value of the heat-flux was calculated by CFD-Post to $2.5 \cdot 10^6 \frac{\text{W}}{\text{m}^2}$.

The second image shows that the flux is positive both inside the 50 % volume-fraction circle and outside on nearly the whole area. The negative contour is around the 50 % volume-fraction and in the corners of the model. The average value of the heat-flux was calculated by CFD-Post to $1.7 \cdot 10^5 \frac{\text{W}}{\text{m}^2}$.

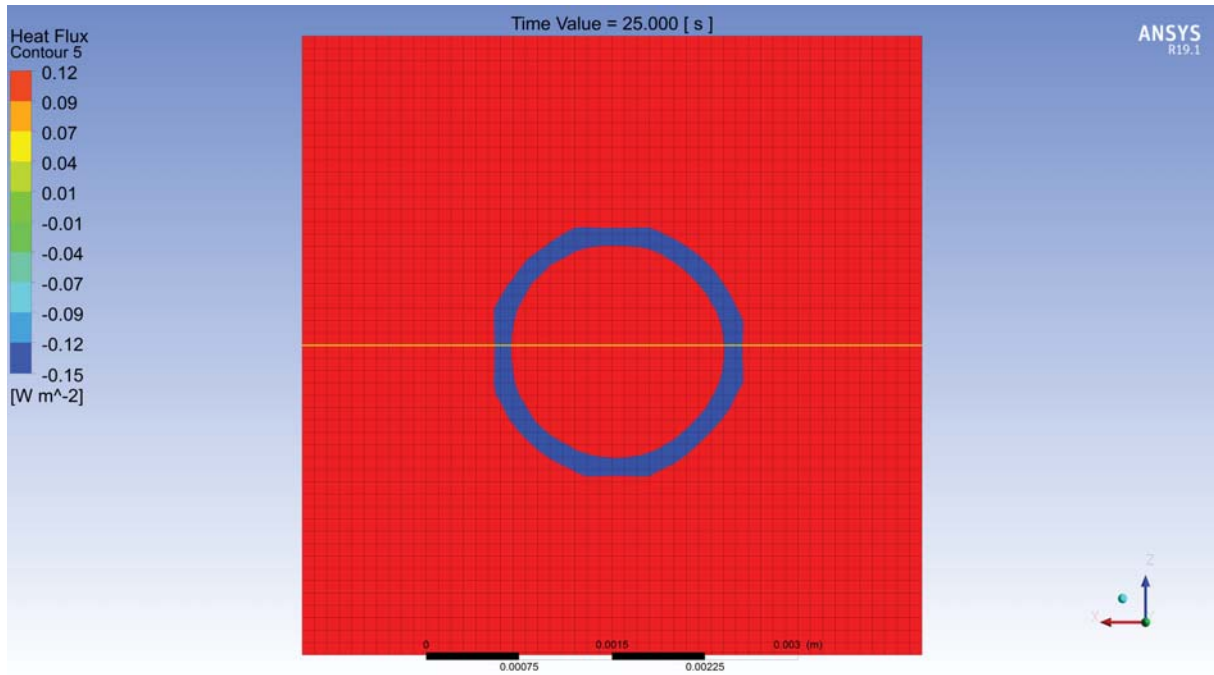


Figure 34: Screen-shot of the heat-flux contour on the outlet of the base model at 25 s. The line in the centre marks the area for the data of fig. 36 and 37

$D12$, $PCM2$, $(x, y, z) = (5, 12.5, 5) \text{ mm}$, $A_{in} = 4.6 \cdot 10^{-7} \text{ m}^2$, $A_{out} = 25 \text{ m}^2$

Mesh: multi-zone, hexagonal, 0.1 mm , $A_{mush} = 10^5$, $\Delta T = -10 \text{ K}$, $v_{in} = 0.4 \frac{\text{m}}{\text{s}}$, $t = 25.0 \text{ s}$

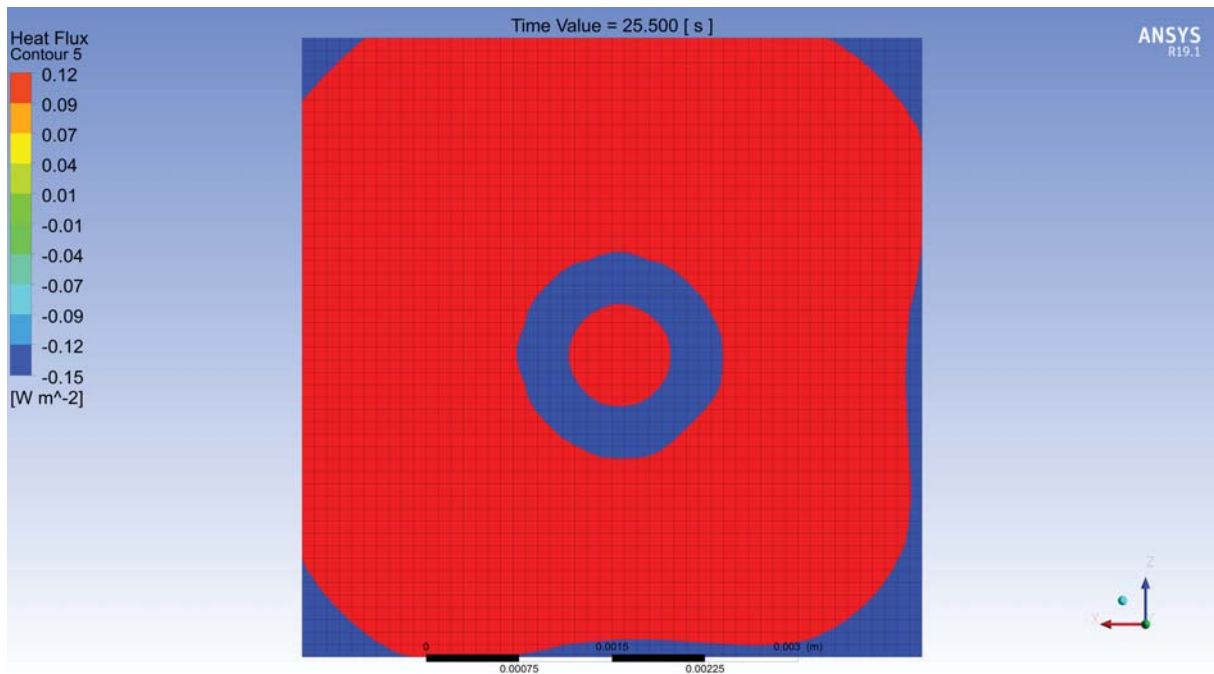


Figure 35: Screen-shot of the heat-flux contour on the outlet of the base model at 25.5 s

$D12$, $PCM2$, $(x, y, z) = (5, 12.5, 5) \text{ mm}$, $A_{in} = 4.6 \cdot 10^{-7} \text{ m}^2$, $A_{out} = 25 \text{ m}^2$

Mesh: multi-zone, hexagonal, 0.1 mm , $A_{mush} = 10^5$, $\Delta T = -10 \text{ K}$, $v_{in} = 0.4 \frac{\text{m}}{\text{s}}$, $t = 25.5 \text{ s}$

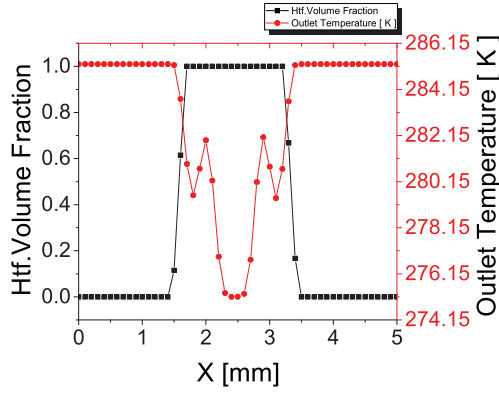


Figure 36: Outlet temperature side by side with the corresponding volume fraction of the base model

D12, PCM2, $(x, y, z) = (5, 12.5, 5)$ mm

$A_{in} = 4.6 \cdot 10^{-7} \text{ m}^2$, $A_{out} = 25 \text{ m}^2$

Mesh: multi-zone, hexagonal, 0.1 mm

$A_{mush} = 10^5$, $\Delta T = -10 \text{ K}$, $v_{in} = 0.4 \frac{\text{m}}{\text{s}}$

$t = 25.0 \text{ s}$

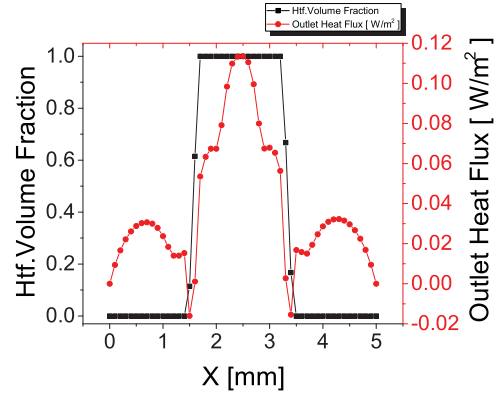


Figure 37: Heat flux side by side with the corresponding volume fraction of the base model

D12, PCM2, $(x, y, z) = (5, 12.5, 5)$ mm

$A_{in} = 4.6 \cdot 10^{-7} \text{ m}^2$, $A_{out} = 25 \text{ m}^2$

Mesh: multi-zone, hexagonal, 0.1 mm

$A_{mush} = 10^5$, $\Delta T = -10 \text{ K}$, $v_{in} = 0.4 \frac{\text{m}}{\text{s}}$

$t = 25.0 \text{ s}$

In order to be able to correlate the outlet heat flux with the HTF measurements of the outlet temperature (fig. 36) and outlet heat flux (fig. 37) were done, shown in a side-by-side comparison with the HTF volume fraction. For this measurements a line was placed crossing the outlet in the centre during a time step at which a D12 droplet is leaving the tank. The lines used were either ranging from $(x, y, z) [\text{mm}] = (0, 12.5, 2.5)$ to $(x, y, z) [\text{mm}] = (5, 12.5, 2.5)$, as shown in fig. 34, or diagonal across the outlet, so that the droplet could be analysed. While the core temperature of the droplet has still it's original value of 275.15 K, the boundary shows a temperature range of [279.15;282.15] K. The average value for $\geq 50 \%$ HTF volume fraction is 279.36 K.

While the core heat flux of the droplet shows the greatest amount in the range of $[0.05; 0.11] \frac{\text{W}}{\text{m}^2}$ and the boundary shows a heat flux in the range of $[-0.02; 0] \frac{\text{W}}{\text{m}^2}$, the areas filled with PCM show a heat flux of up to $0.03 \frac{\text{W}}{\text{m}^2}$. The average value for $\geq 50 \%$ HTF volume fraction is $0.07 \frac{\text{W}}{\text{m}^2}$.

The heat flux was not only evaluated by it's values, but also by it's periodic behaviour. For this a Fast Fourier Transformation (FFT) was done with Origin Pro. According to the official documentation the FFT is calculated by the following equation:

$$F_n = \sum_{i=0}^{N-1} x_i e^{-\frac{2\pi j}{N} ni}, \quad (48)$$

with the input sequence x_i of a length N . [1] The resulting maximal values in fig. 38 of

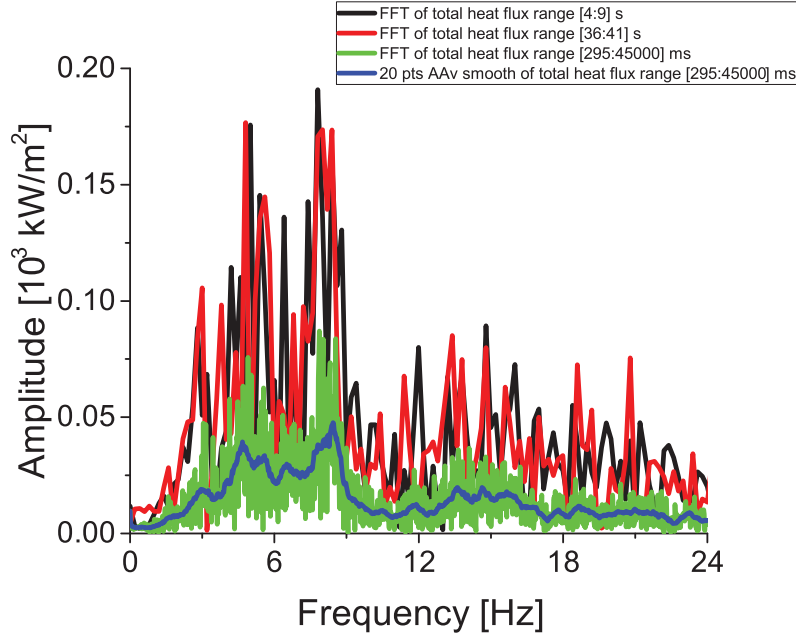


Figure 38: FFTs of three parts of the base model and an additional a smoothed variant, over 20 points

D12, PCM2, $(x, y, z) = (5, 12.5, 5) \text{ mm}$ $A_{in} = 4.6 \cdot 10^{-7} \text{ m}^2$, $A_{out} = 25 \text{ m}^2$

Mesh: multi-zone, hexagonal, 0.1 mm $A_{mush} = 10^5$, $\Delta T = -10 \text{ K}$, $v_{in} = 0.4 \frac{\text{m}}{\text{s}}$

$t [\text{ms}] = [4000; 9000], [36000; 41000], [295; 45000] \text{ s}$

the peak frequency in Hz and the heat flux amplitude in $\frac{\text{kW}}{\text{m}^2}$ over the complete period, at the beginning and at the end are: (7.9, 87.1), (7.8, 190.8), (4.8, 176.7).

When analysing heat flux it is also important to evaluate the changes dependent on the temperature difference between the PCM and the HTF, as the heat transfer takes place at the boundary of these two materials. Therefore the average temperatures of the PCM and HTF were plotted separately in fig. 39 and 40. The first graphs shows that the PCM cools down initially fast. The outlet temperature of 285.25 K is reached after 3 s. It takes 2 s more to reach the final value with a precision of 10^{-2} K of 285.17 K.

The second graphs shows that the D12 hardly cools down, with a greater extent of fluctuation between 285.17 K and 286.15 K. A linear fit shows that the temperature change is of $(-0.0061 \pm 0.00257) \frac{\text{K}}{\text{s}}$.

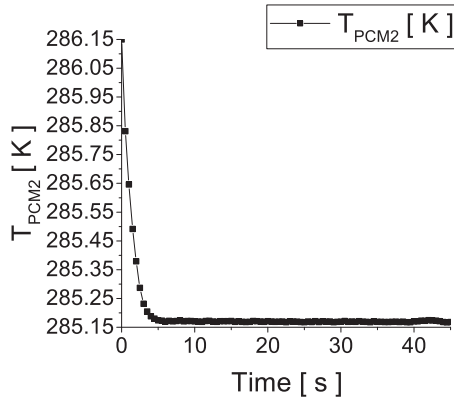


Figure 39: Average temperature of PCM of the base model. As this had to be calculated via post-processing the value could only be resolved at each saved time step and therefore every 0.5 s

$D12, PCM2, (x, y, z) = (5, 12.5, 5) \text{ mm}$

$A_{in} = 4.6 \cdot 10^{-7} \text{ m}^2, A_{out} = 25 \text{ m}^2$

Mesh: multi-zone, hexagonal, 0.1 mm

$A_{mush} = 10^5, \Delta T = -10 \text{ K}, v_{in} = 0.4 \frac{\text{m}}{\text{s}}$

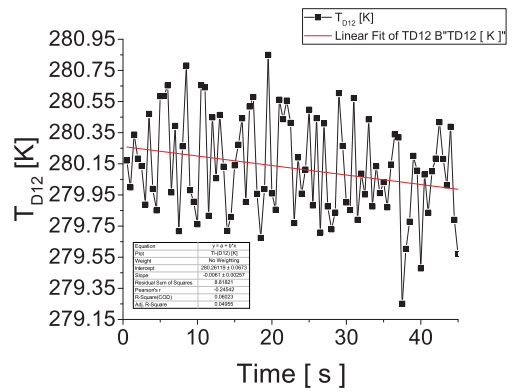


Figure 40: Average temperature of D12 of the base model. As this had to be calculated via post-processing the value could only be resolved at each saved time step and therefore every 0.5 s

$D12, PCM2, (x, y, z) = (5, 12.5, 5) \text{ mm}$

$A_{in} = 4.6 \cdot 10^{-7} \text{ m}^2, A_{out} = 25 \text{ m}^2$

Mesh: multi-zone, hexagonal, 0.1 mm

$A_{mush} = 10^5, \Delta T = -10 \text{ K}, v_{in} = 0.4 \frac{\text{m}}{\text{s}}$

Discussion

As in the last chapter, the analysis will start by examining the basic fluid-dynamic values, such as surface area, liquid fraction and volume fraction. (fig. 28, 29, 30) The surface area increases linearly to a higher point as seen before, but stays in a similar range as in the beginning of fig. 13. Due to the small changes in the period and amplitude of the graph and in order to visualise the periodic behaviour only a small portion of the data will be shown for each calculation, adjusted to the values shown. In this case (fig. 19) it was decided that 2.0 s will suffice. As already explained in the last chapter a periodic surface area is the case for droplet formation and droplet leaving. In the calculations done before, however, the surface area showed an increase in amplitude towards the end that ended in general with a stagnation. This is not the case for the base calculation. This implies that there is hardly any solidification at all. The droplets just continue to grow and leave the tank one after another for the whole simulation time.

The stream itself shows the expected behaviour from fig. 10, although it should be almost 40 mm long and therefore 3.5 times the total height of the geometry. This is probably a result of the different material properties used.

The results from the surface area go well with the values of the volume fraction in fig. 30. In the earlier calculations (fig. 15) the graph experienced a continuous rise with plateaus in between. Due to the completely open top face in the base calculation here the droplets leave the tank immediately instead of creating an oil layer on top. This explains the periodicity in a simple way. The thermodynamic influences of the model changes are,

however, more complicated.

Fig. 29 confirms the initial premise of slow to none solidification. Interestingly the liquid-fraction increases in the last few seconds. This could be due to the change in the outlet and the specified boundary conditions.

From these results it can be assumed that the (negative) heat transfer will be less than the -2.5 W of fig. 11. Furthermore it can be said that the periodicity of the surface area and volume fraction will take over to the heat transfer and heat flux.

As always, the incoming heat transfer can be seen constant with sufficient precision. (fig. 31) A plot of the heat transfer at the outlet shows peaks and a "background noise" of nearly constant -23 W. (fig. 32) As explained in sec. 5.4 the outlet heat transfer is coupled to the outlet volume fraction. One could therefore argue that calculating the heat transfer is an easy task, as just the values above this line have to be used. When analysing the graph more detailed one realises that the sign of the total heat transfer changes from plateau to peak. When combining the first two laws of thermodynamics it becomes clear that the sign of the heat flux should be negative according to the incoming cold and stay negative, when no (positive) heat sources are in contact. In an ideal case the HTF takes the maximum amount of heat possible with it, as it is only able to cool the PCM for exactly this amount. For this case this means that the maximal possible heat flux at the outlet is 6.8 W, as opposed to the inlet. The positive sign of the total heat transfer would therefore imply that the HTF takes more heat with it than the PCM is able to give.

This is a model specific problem and results in a heat flux of $q \leq 1 \frac{\text{MW}}{\text{m}^2}$ (fig. 33) due to the small surface area in fig. 28.

Two hand made approaches with approximated values were executed to find the correct range for the resulting heat transfer and flux in this model. The calculations are based on (1) on page 3. The following input is required:

- $c \approx 2 \frac{\text{kJ}}{\text{kgK}}$ from the data sheet in appendix A, near 285.15 K
- $\Delta T = (279.36 - 275.15) \text{ K} \approx 4 \text{ K}$ from fig. 36 and the defined inlet temperature
- $\dot{m} = \rho \dot{V}$
- $\rho \approx 800 \frac{\text{kg}}{\text{m}^3}$ from the data sheet in appendix A near 285.15 K
 - $\dot{V} = \frac{\bar{v}_{HTF} V}{\nu}$, $\bar{v}_{HTF} = 0.1$, $V = 5 \cdot 12.5 \cdot 5 \text{ mm}^3 \approx 300 \text{ mm}^3$, $\nu = 8 \text{ Hz}$
 - $\dot{V} = v_{in} A_{in}$, $v_{in} = 0.4 \frac{\text{m}}{\text{s}}$, $A_{in} \approx 5 \cdot 10^{-7} \text{ m}^2$

The resulting values are: $Q \approx -0.2 \text{ J}$, $\dot{Q} \approx -1.6 \text{ W}$ and $q \approx -20 \frac{\text{kW}}{\text{m}^2}$ by using the FFT of (48) and $\dot{Q} \approx -1.3 \text{ W}$ (and therefore similar heat flux) by using the incoming volume stream for calculation.

A more detailed analysis shows that, although the heat transfer rate and flux change its sign to positive value, the PCM is able to cool down, since the average heat flux over the whole period is negative. As it's value is only half of the hand calculated value this explains the minimal cool-down and solidification.

The visualisation of the outlet from two following data files shows that almost the complete outlet is covered in a positive heat flux. (fig. 34 and 35). The local heat flux is only negative around the leaving droplet and it returns from the corners, when the area of the passing droplet gets smaller. In case no droplet touches the outlet the heat transfer returns back to it's original value. When multiplying the outlet area the resulting heat transfer rate for this two time-steps is 63.1 W and 4.2 W. For a correct evaluation of the thermal changes resulting only in the HTF flow one would need not only taking the positive values of heat flux but also find a way to subtract the amount of PCM heat flux or calculate solely the HTF heat flux. It seems to be only possible to define a plane or an ISO-surface over the complete model in CFD-Post. No possible solution for setting a user defined area, in which the heat flux could be calculated, was found.

A possible solution could be, however, extracting the heat flux over a line, as the drop is axisymmetric. (Fig. 37) The intention was to calculate the error from the positive heat flux of the PCM and subtract it from the total (positive) value. As no documentation could be found that explains how ANSYS Fluent calculates the heat per unit area over a line the results could not be used for further evaluation.

The reason for this high deviation between hand calculations and Fluent calculations is probably the model itself. As the complete top face was set as outlet, the boundary conditions, such as back-flow and temperature, have a strong imprint on the calculation. Due to the open area and the temperature difference, the incoming PCM from the back-flow has a higher temperature than the PCM in the tank and is able to heat. This prevents the PCM not only from solidifying but also from sufficient cooling. While the PCM cools-down to solidification temperature in a few seconds it gets stuck at this level for the whole simulation. (Fig. 39)

When analysing the average temperature of the HTF one realises that it does cool-down for 0.16 ± 0.12 K, in the whole 45 s. (Fig. 40) The high error originates in the error by one third of the slope per second in the linear fit by Origin Pro. It is, however necessary to state that the actual value of 280.17 K for 0.5 s is not in the range of the fit of 280.26 ± 0.07 K. Nevertheless the fit was only applied with the intention of qualitatively showing the trend of the HTF temperature. The fit shows sufficiently that the HTF temperature does not change significantly over the whole calculation. As the heat transfer depends on the temperature difference between the two materials, this means that the more the PCM cools down the less heat can be absorbed by the HTF. Therefore the HTF does get heated less and it's average temperature sinks over time. This behaviour can be evaluated mathematically by dividing the heat flux through the temperature difference, resulting in the heat transfer coefficient.

As this is a computer simulation all necessary data could be extracted from the materials. In real life experiments the HTF temperature cannot be measured and the PCM temperature only at specific points. The heat transfer coefficient has therefore to be calculated with eq. (15) and (16) leading to a value about half as high as the theoretical value. In this case it would be possible to calculate directly with the averaged temperatures of each fluid.

As the general heat transfer process in fluids is convection and not conduction it can be assumed from (1) and (16):

$$k = \frac{\dot{Q}}{A(T_{D12} - T_{PCM2})} = \frac{q}{T_{PCM2} - T_{D12}} \approx \alpha \quad (49)$$

Equation (49) shows that the heat transfer coefficient should always result in a positive value, as a negative sign from the heat flux is compensated by the sign of the temperature difference. With the model used in this project, the heat flux changes its sign independently of the temperature difference due to the back-flow conditions. As it was not possible to filter out the right values, no correct heat transfer coefficient could be achieved. Therefore no comparisons are possible and this value will not be mention further.

7.2 Mushy-Parameter variations

For the variation of the mushy parameter the temperature difference between inlet and solidification was kept at -10 K and the velocity at $0.4 \frac{\text{m}}{\text{s}}$, according to tab. 14.

Results

A_{mush}	$l_{PCM}[\%]$					
	$t = 2.5 [\text{s}]$	$t = 6 [\text{s}]$	$t = 12.64 [\text{s}]$	$t = 14.05 [\text{s}]$	$t = 17.8 [\text{s}]$	$t = 45 [\text{s}]$
10^1	98	96	93		92	90
10^4	98	96	93		92	90
10^5	98	95	93	92		90
10^6	97	93	84	81	74	62
10^9	33	10	0			

Table 15: Important values of the liquid fraction for the calculations with $A_{mush} = 10^6, 10^9$ in fig. 41. For comparison the values of all other calculations from this parameter variation at the same time steps are included. The **base model is bold**. The calculation with 10^6 shows a drop from 14.05 s to 17.8 s. The calculation with 10^9 decreases linearly in the first 2.5 s, reaches the 10 % mark at 6.0 s and reaches total solidification with sufficient precision at 12.64 s.

Fig. 41 shows the results for the liquid fraction. It can be clearly seen that the values for $A_{mush} = 10^1, 10^4, 10^5$ are in a similar range. The line for $A_{mush} = 10^6$ shows an

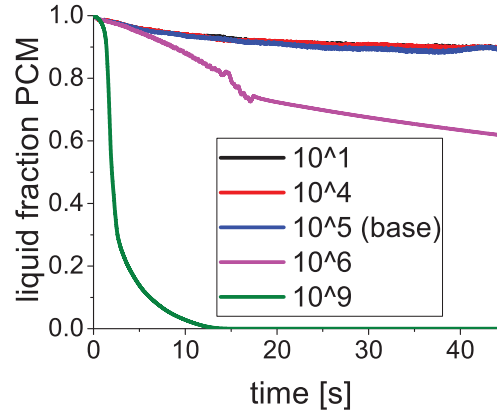


Figure 41: Liquid-fraction for different mushy parameters. The important values are listed in tab. 15

$D12$, $PCM2$, $(x, y, z) = (5, 12.5, 5) \text{ mm}$, $A_{in} = 4.6 \cdot 10^{-7} \text{ m}^2$, $A_{out} = 25 \text{ m}^2$,
 Mesh: multi-zone, hexagonal, 0.1 mm , $A_{mush} = (10^1, 10^4, 10^5(\text{base}), 10^6, 10^9)$, $\Delta T = -10 \text{ K}$,
 $v_{in} = 0.4 \frac{\text{m}}{\text{s}}$

increased drop between 14.05 s and 17.8 s. The graph for $A_{mush} = 10^9$ shows a fast drop and reaches 0 after 12.64 s. The important values can be seen in tab. 15.

A visualisation of the total liquid fraction on the surface area is shown in fig. 42 for $A_{mush} = 10^6$ and in fig. 43 for $A_{mush} = 10^9$.

Fig. 42 a) shows that the boundary on top is the most solidified area with values down to 56 % in circular areas facing the corners of the model. In the main droplet formation part values near 80 % occur. The stream itself is at 90 % for the most part, except some small areas in the upper part and the base, that are at 80 %. The average PCM liquid fraction on the surface area is at 57 %.

In fig. 42 b) the intersection with the wall is the only area left with $\approx 100 \%$. The droplet formation part stays near 80 % in the centre, while top and bottom areas have parts $\leq 60 \%$. The stream has values between 70 % and 80 %, with the base slightly lower. The average PCM liquid fraction on the surface is at 55 %.

In fig. 42 c) the values are similar to the earlier image but shifted in some areas. The centre of the droplet formation part is now more solidified than the bottom and the top surface. The area between base and stream has values near 55 %. The average PCM liquid fraction on the surface is at 51 %.

In fig. 42 d) the area on top of the oil layer has values down to 50 % in a wide area. These values increase in direction to the outlet up to 70 % in the lower part of the path, 80 % in the middle part and a small area on the top part with 90 %. The average PCM liquid fraction on the surface is at 31 %.

Fig. 43 a) shows values are near 100 % in most parts of the surface. The values are lower,

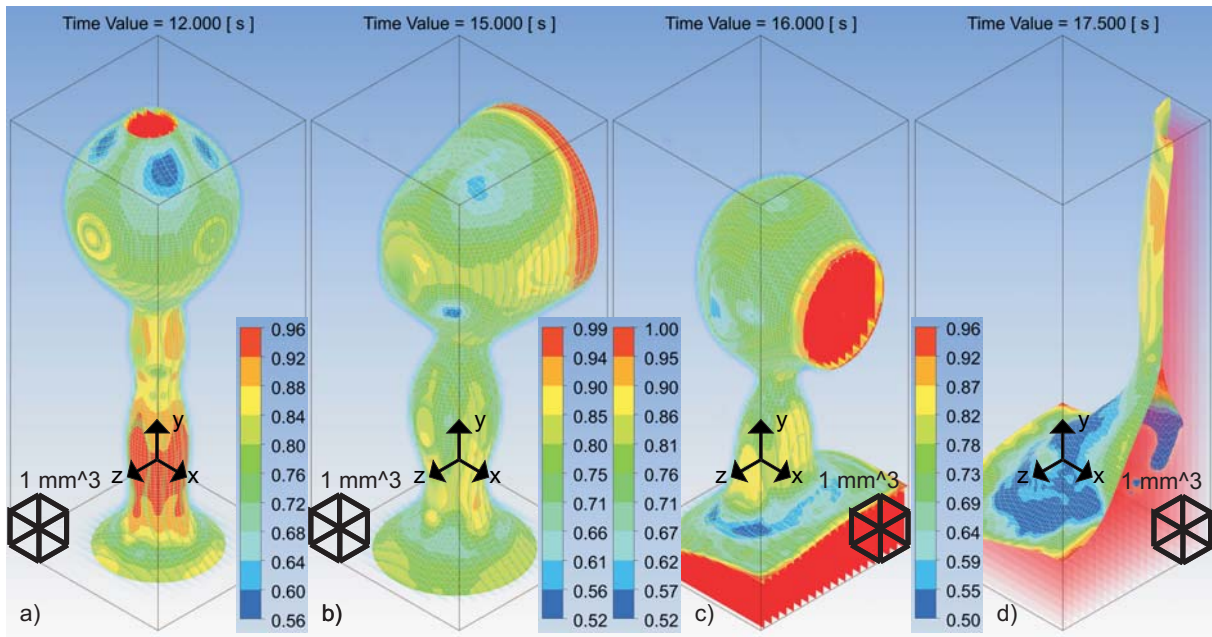


Figure 42: Screen-shot sequence of the total-liquid-fraction contour on an ISO-surface with 50 % volume fraction for the solidification steps with $A_{mush} = 10^6$

a) image showing the last droplet forming and solidification at the top at 12.0 s

b) image showing the HTF connected to the back wall with progressed solidification at the stream at 15.0 s

c) image showing the HTF connected to the right wall and an additional bottom layer of HTF with completely solidified PCM in the areas surrounding the bottom part of the stream at 16.0 s

d) image showing the bottom layer of HTF with completely solidified PCM on top and a path to the outlet on the right corner at 17.5 s, with the transparency of the HTF area set to 90 % for better visualisation

$D12$, $PCM2$, $(x, y, z) = (5, 12.5, 5) \text{ mm}$, $A_{in} = 4.6 \cdot 10^{-7} \text{ m}^2$, $A_{out} = 25 \text{ m}^2$,
 Mesh: multi-zone, hexagonal, 0.1 mm , $A_{mush} = (10^1, 10^4, 10^5(\text{base}), 10^6, 10^9)$, $\Delta T = -10 \text{ K}$,
 $v_{in} = 0.4 \frac{\text{m}}{\text{s}}$

especially in the depressions, at 90 %. Some small parts with PCM can be visible inside the HTF with 80 %. The average PCM liquid fraction on the surface is at 86 %.

In fig. 43 b) the values stay basically in the same range as in the image before, except for at least one small left-out PCM part reaching 55 %, as marked. The average PCM liquid fraction on the surface is at 80 %.

In fig. 43 c) the values stay again, in the same range, although some of the PCM parts dropped to 50 %. The average PCM liquid fraction on the surface is at 54 %.

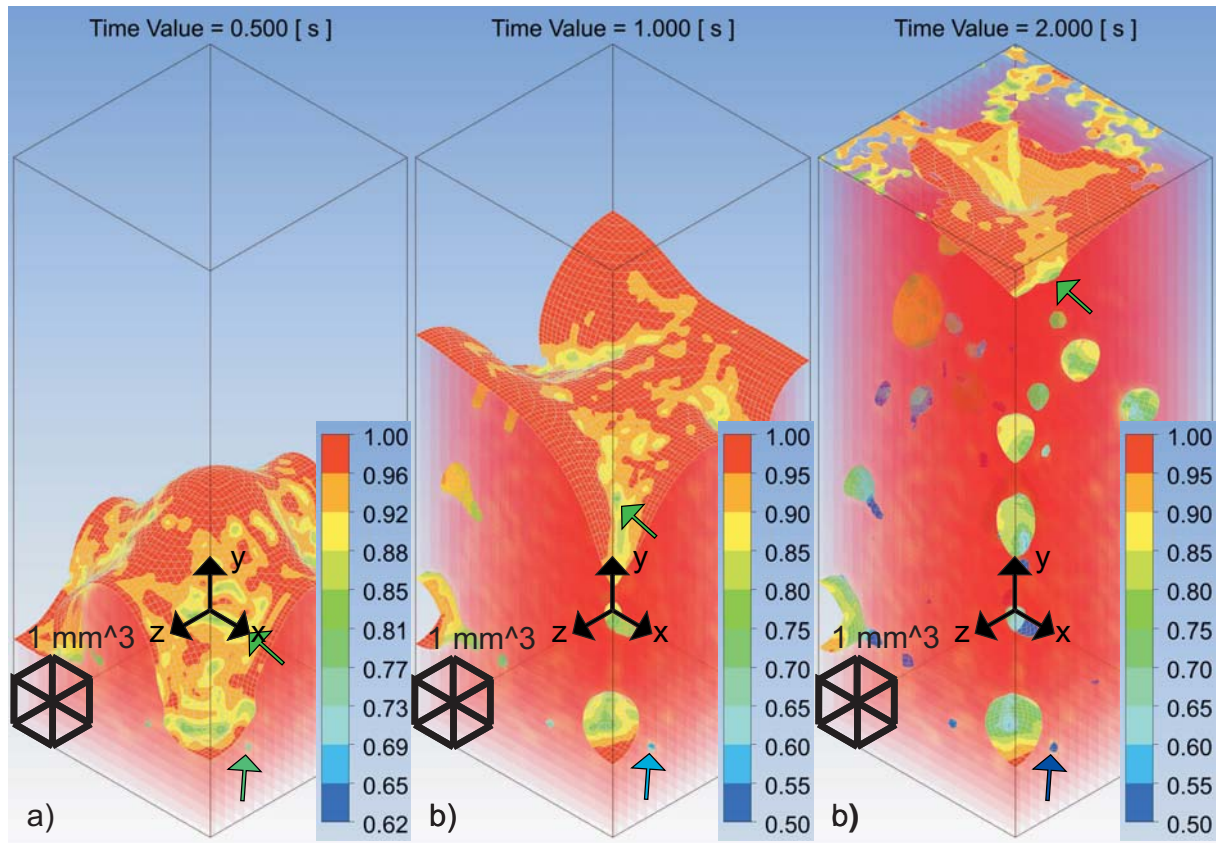


Figure 43: Screen-shot sequence of the total-liquid-fraction contour on an ISO-surface with 50 % volume fraction for the solidification steps with $A_{mush} = 10^9$. The HTF volume fraction was set to 90 % transparent for visualisation inside the HTF. Each image features two arrows. The upper one marking a small area with constant 80 % on the top surface, as being the lowest value in this area. The lower arrow marks a small area filled with PCM, as being the lowest value seen from this perspective, that decreases over this sequence

a) image showing the HTF completely coating the bottom wall and filling the tank from the bottom at 0.5 s

b) image showing almost 75 % of the tank filled with HTF and a few small areas of PCM inside

c) image showing an almost completely filled tank with HTF and multiple PCM areas in between at different sizes

$D12$, $PCM2$, $(x, y, z) = (5, 12.5, 5) \text{ mm}$, $A_{in} = 4.6 \cdot 10^{-7} \text{ m}^2$, $A_{out} = 25 \text{ m}^2$,
 Mesh: multi-zone, hexagonal, 0.1 mm, $A_{mush} = (10^1, 10^4, 10^5(\text{base}), 10^6, 10^9)$, $\Delta T = -10 \text{ K}$,
 $v_{in} = 0.4 \frac{\text{m}}{\text{s}}$

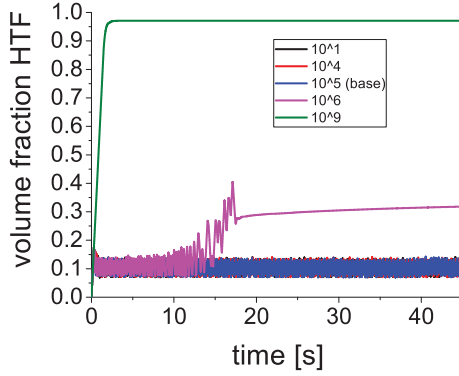


Figure 44: Volume-fraction for different mushy parameters

$D12$, $PCM2$, $(x, y, z) = (5, 12.5, 5) \text{ mm}$,
 $A_{in} = 4.6 \cdot 10^{-7} \text{ m}^2$, $A_{out} = 25 \text{ m}^2$,
 Mesh: multi-zone, hexagonal, 0.1 mm ,
 $A_{mush} = (10^1, 10^4, 10^5(\text{base}), 10^6, 10^9)$,
 $\Delta T = -10 \text{ K}$, $v_{in} = 0.4 \frac{\text{m}}{\text{s}}$

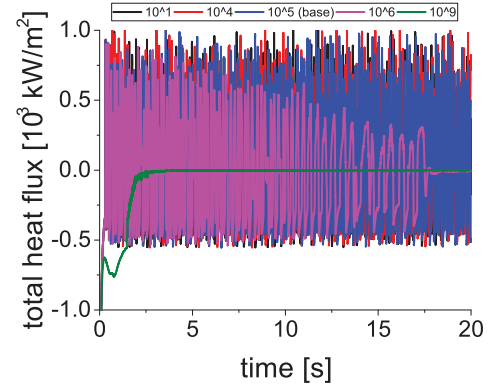


Figure 45: First 20 s of the heat flux for different mushy parameters

$D12$, $PCM2$, $(x, y, z) = (5, 12.5, 5) \text{ mm}$,
 $A_{in} = 4.6 \cdot 10^{-7} \text{ m}^2$, $A_{out} = 25 \text{ m}^2$,
 Mesh: multi-zone, hexagonal, 0.1 mm ,
 $A_{mush} = (10^1, 10^4, 10^5(\text{base}), 10^6, 10^9)$,
 $\Delta T = -10 \text{ K}$, $v_{in} = 0.4 \frac{\text{m}}{\text{s}}$

A_{mush}	$\bar{v}_{HTF} [\%]$		
	$t = 4.458 \text{ [s]}$	$t = 17.8 \text{ [s]}$	$t = 45, \text{ [s]}$
10^1	10		
10^4	10		
10^5	10		
10^6	10	27	32
10^9	97		

Table 16: Important values of the average volume fraction for the calculations with $A_{mush} = 10^6, 10^9$. For comparison the values of all other calculations in fig. 44 were included. The **base calculation** is **bold**. The calculation with 10^6 shows a rise from 4.458 s to 17.1 s, followed by a drop to 17.8 s. The calculation with 10^9 increases linearly in the first 2.5 s and reaches a constant value.

Fig. 44 shows the results for the volume fraction. It can be clearly seen that the values for $A_{mush} = 10^1, 10^4, 10^5$ are in a similar range. The line for $A_{mush} = 10^6$ shows an increase at about 10 s, followed by a stagnation at 17.8 s. The graph for $A_{mush} = 10^9$ shows a fast increase and reaches 97 % after 4.458 s. The important values can be seen in tab. 16.

A_{mush}	time range [ms]	$-\bar{q} [\frac{\text{kW}}{\text{m}^2}]$		$T_{out} [\text{K}]$	$T_{in} [\text{K}]$	$\bar{A} [\text{m}^2]$
10^1	[295;45000]	-9.8	-20	≈ 279.15	275.15	$7 \cdot 10^{-5}$
10^4	[295;45000]	-9.5	-20	≈ 279.15	275.15	$7 \cdot 10^{-5}$
10^5	[295;45000]	-9.6	-20	≈ 279.15	275.15	$7 \cdot 10^{-5}$
10^6	[301;17741]	-17.2				
10^6	1000	427.4	-20	≈ 282.15	275.15	$7 \cdot 10^{-5}$
10^6	[17742;45000]	-5.0				
10^6	18000	-10.2	-10	≈ 278.15	275.15	$7 \cdot 10^{-5}$
10^9	[1920;45000]	-2.6				
10^9	3000	-10.2	-40	≈ 280.15	275.15	$4 \cdot 10^{-5}$

Table 17: Average heat fluxes for different parts of all calculations in fig. 45, as well as the corresponding values for hand calculations. The **base calculation** is **bold**

Fig. 45 shows the results for the heat flux. It can be clearly seen that the values for $A_{mush} = 10^1, 10^4, 10^5$ are in a similar range. The line for $A_{mush} = 10^6$ shows a decrease in the maximum value starting by about 5s. Furthermore the length of one period increases. The graph for $A_{mush} = 10^9$ shows a small peak shortly after the beginning and a continuous increase after 1.92s to a more or less constant value. The important values, as well as corresponding hand calculations can be seen in tab. 17.

The local heat flux for $A_{mush} = 10^6$ at 19.0 s is mostly positive for the HTF flow. (Fig. 46) Some areas of the PCM result in a flux up to $1.6 \frac{\text{MW}}{\text{m}^2}$, while the majority stays below 0 and down to $-0.8 \frac{\text{MW}}{\text{m}^2}$.

The local heat flux for $A_{mush} = 10^9$ at 20.0 s is positive in wide areas, mostly filled by HTF but also by PCM. (Fig. 47) Areas in the left corners exist with negative heat flux, also independent of the material. Some areas of the PCM result in a flux up to $1.6 \frac{\text{MW}}{\text{m}^2}$, while the majority stays below 0 and down to $-0.8 \frac{\text{MW}}{\text{m}^2}$.

An analysis of the FFT in fig. 48 shows the following maximum peaks in chronological order: $(\nu [\text{Hz}], q_A [\frac{\text{kW}}{\text{m}^2}]) = (5.0, 211.2), (2.0, 169.9), (0, 3.9)$

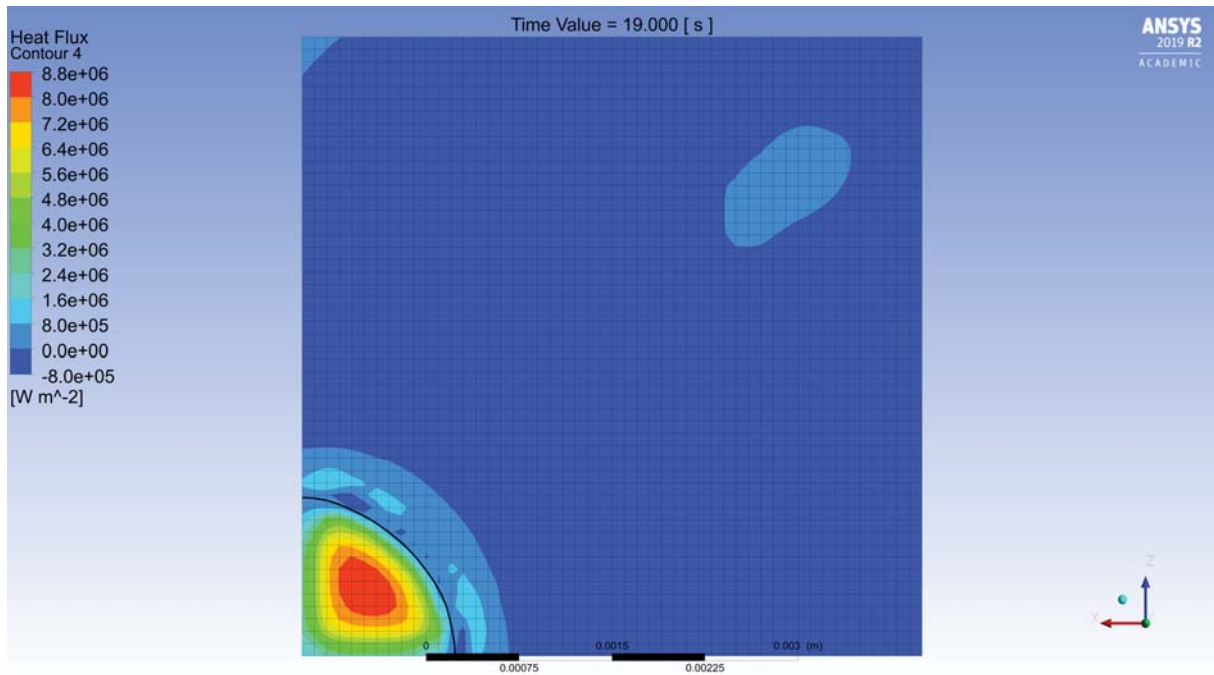


Figure 46: Screen-shot showing the heat transfer at the outlet at 19 s for $A_{mush} = 10^6$
 $D12$, $PCM2$, $(x, y, z) = (5, 12.5, 5) \text{ mm}$, $A_{in} = 4.6 \cdot 10^{-7} \text{ m}^2$, $A_{out} = 25 \text{ m}^2$,
 Mesh: multi-zone, hexagonal, 0.1 mm, $A_{mush} = (10^1, 10^4, 10^5(\text{base}), 10^6, 10^9)$, $\Delta T = -10 \text{ K}$,
 $v_{in} = 0.4 \frac{\text{m}}{\text{s}}$, $t = 19 \text{ s}$

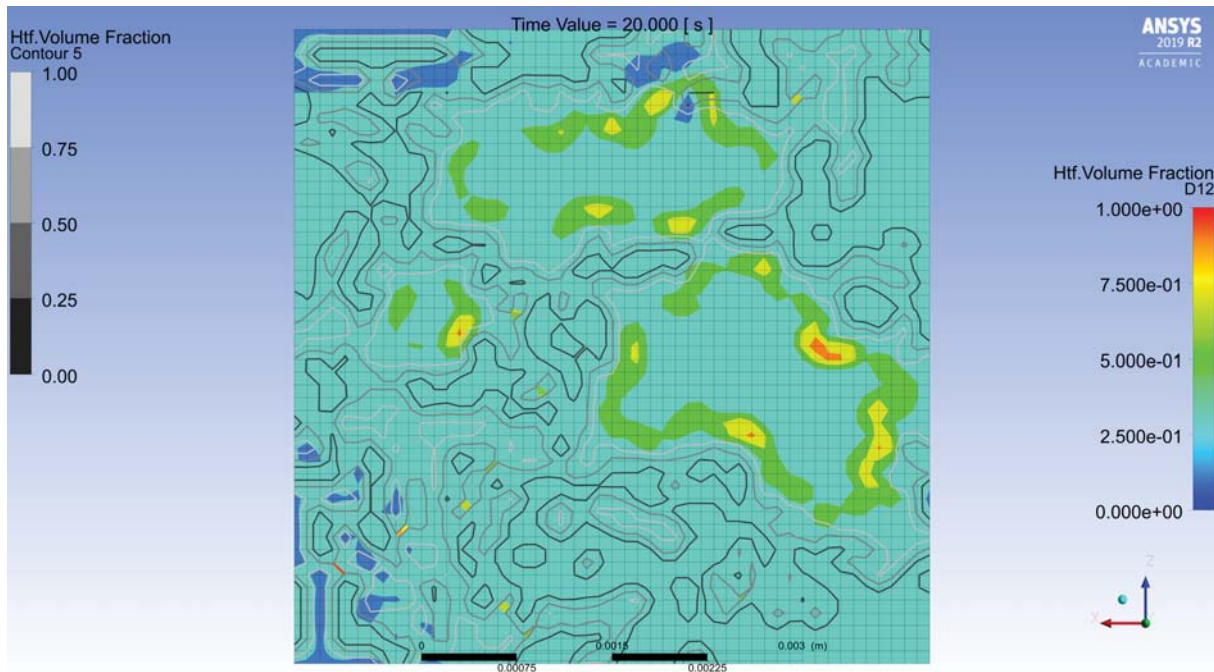


Figure 47: Screen-shot showing the heat transfer at the outlet at 20 s for $A_{mush} = 10^9$.
 $D12$, $PCM2$, $(x, y, z) = (5, 12.5, 5) \text{ mm}$, $A_{in} = 4.6 \cdot 10^{-7} \text{ m}^2$, $A_{out} = 25 \text{ m}^2$,
 Mesh: multi-zone, hexagonal, 0.1 mm, $A_{mush} = (10^1, 10^4, 10^5(\text{base}), 10^6, 10^9)$, $\Delta T = -10 \text{ K}$,
 $v_{in} = 0.4 \frac{\text{m}}{\text{s}}$, $t = 20 \text{ s}$

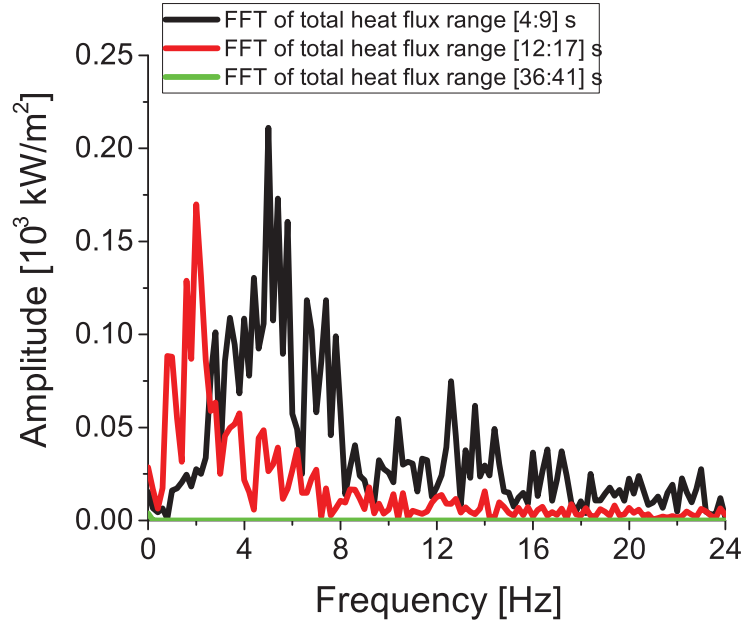


Figure 48: Amplitude and frequency of the Fourier transformations of $A_{mush} = 10^6$ in three parts

$D12$, $PCM2$, $(x, y, z) = (5, 12.5, 5) \text{ mm}$, $A_{in} = 4.6 \cdot 10^{-7} \text{ m}^2$, $A_{out} = 25 \text{ m}^2$,
 Mesh: multi-zone, hexagonal, 0.1 mm , $A_{mush} = (10^1, 10^4, 10^5(\text{base}), 10^6, 10^9)$, $\Delta T = -10 \text{ K}$,
 $v_{in} = 0.4 \frac{\text{m}}{\text{s}}$, $t[s] = [4; 9], [12; 17], [36; 41] \text{ s}$

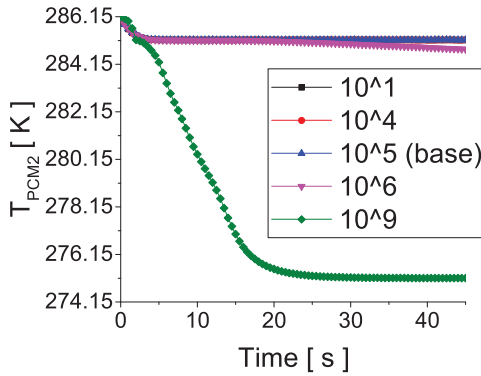


Figure 49: Average temperature of $PCM2$ for different mushy parameters

$D12$, $PCM2$, $(x, y, z) = (5, 12.5, 5) \text{ mm}$, $A_{in} = 4.6 \cdot 10^{-7} \text{ m}^2$, $A_{out} = 25 \text{ m}^2$,
 Mesh: multi-zone, hexagonal, 0.1 mm ,
 $A_{mush} = (10^1, 10^4, 10^5(\text{base}), 10^6, 10^9)$,
 $\Delta T = -10 \text{ K}$, $v_{in} = 0.4 \frac{\text{m}}{\text{s}}$

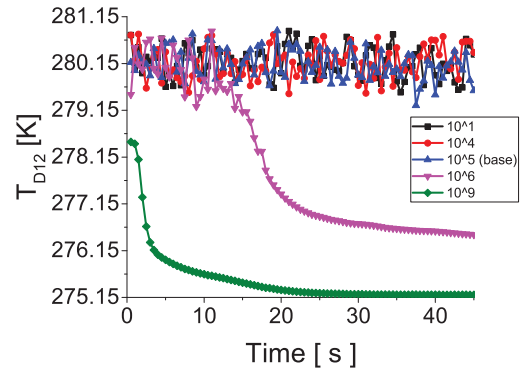


Figure 50: Average temperature of $D12$ for different mushy parameters

$D12$, $PCM2$, $(x, y, z) = (5, 12.5, 5) \text{ mm}$, $A_{in} = 4.6 \cdot 10^{-7} \text{ m}^2$, $A_{out} = 25 \text{ m}^2$,
 Mesh: multi-zone, hexagonal, 0.1 mm ,
 $A_{mush} = (10^1, 10^4, 10^5(\text{base}), 10^6, 10^9)$,
 $\Delta T = -10 \text{ K}$, $v_{in} = 0.4 \frac{\text{m}}{\text{s}}$

The PCM temperature plot in fig. 49 shows that 10^1 , 10^4 and 10^5 have one nearly linear decrease, followed by a stagnation part. $A_{mush} = 10^6$ shows a third decrease starting at

19.5 s. $A_{mush} = 10^9$ shows a plateau of 0.5 s between these two drops and reaches the inlet temperature at 39.0 s. The important values are listed in tab. 18.

A_{mush}	t [s]			T_{PCM2} [K] t=45 s
	reaching 285.17 K	reaching 285.13 K	reaching 275.15 K	
10^1	5.5	> 45		285.17
10^4	5.5	> 45		285.17
10^5	5	> 45		285.17
10^6	5	19.5	> 45	284.78
10^9	2.0	2.5	39.0	275.15

Table 18: Time range of the PCM temperature that it stays near the solidification temperature, the time step it reaches the inlet temperature and the final temperature for all calculations in fig. 49. The **base calculation** is **bold**

The HTF temperature plot in fig. 50 shows that $A_{mush} = 10^1, 10^4, 10^5$ have a nearly identical behaviour and jump around 280.15 K for the whole 45 s. $A_{mush} = 10^6$ has the same behaviour for the first 12.0 s. There it stays near 279 K for 1.5 s, when it cools down until 276.5 K at 41.5 s. $A_{mush} = 10^9$ starts already at 278.5 K, where it stays for the first second and cools down to nearly the exact inlet temperature. It reaches 275.25 K at 24 s and cools down until 275.20 K in a similar curve.

Discussion

The base calculation showed a final liquid fraction after 45 s of 90 %, without any stronger drop in the graph. (fig. 41) The temperature plot in fig. 49 shows a first sensible part followed by a latent part. No additional sensible part is seen. Therefore the solidification has not been completed on a global scale. When the mushy parameter is proportional to the solidification rate this implies that lower mushy parameters will show values for the liquid fraction, the volume fraction and the heat flux in the same range, as no slower solidification than none is possible. When comparing fig., 44 and 45 and the values of the corresponding tables (tab. 15, 16 and 17) this assumption proves to have been accurate. Therefore the values will be discussed only shortly, always in the order $A_{mush} = (10^1, 10^4, 10^5)$, and the focus will then be led on $A_{mush} = (10^6, 10^9)$. The PCM liquid-fraction and the HTF volume fraction are the same for all three calculations, the average heat flux differs only by a few $[\frac{kW}{m^2}]$. Interestingly the value for 10^1 is higher as for the base model by 2 %, which is higher as 10^5 by 1 %, but basically the values are all in the same range. The slight deviation can probably be traced back to a numerical issue. The task of the mushy parameter is only to define the velocity of the solidification front, not the heat transfer itself. As no sufficient solidification occurs, the heat transfer is behaving in the same way. The FFT shows a minimal shift to the right and leads to the following maximum values: $(\nu[H\dot{z}], q_A[\frac{kW}{m^2}]) = (8.3, 115.9), (8.2, 121.1), (7.9, 87.07)$.

The PCM and D12 temperatures are the same for all three calculations with sufficient precision. (Fig. 49, 50 and tab. 18)

The PCM temperature changes of $A_{mush} = 10^6$ in fig. 49 represent a perfect example for the solidification, as explained in section 3.2 and 3.3. It contains the sensible heat transfer before and after the latent heat transfer, during which the solidification process occurs. Based on this results, the calculation can be put to use in explaining the processes in a direct contact latent heat storage.

The liquid fraction surpasses the base model near 4.5s. (Fig. 41) Interestingly in [13] the authors stated that in higher mushy parameter calculations the convection was lower and led to a decreased heat transfer. High mushy parameter simulations should therefore lag behind experimental calculations, at least when calculating the melting process. This results are controversial to the results of this project. Here higher mushy parameter lead to fast solidification and therefore increased (negative) heat transfer. This could however just imply that Fluent does not decrease the absolute value of the heat transfer vector but decreases the number including the sign. Therefore the melting process would tend to values against 0 and return lower heat transfer. For negative heat transfer, this would mean an increase in value, as the heat transfer results in higher negative values. The important stage of the solidification process is between 14.05s and 17.8s.

The first value is consistent with the first increase of the volume fraction to 26 %, the latter with the stagnation part, as seen in fig. 44 and tab. 16.

The value at 19.5s for the PCM temperature in tab. 18 does not match with any other detected feature for the other parameters. This can be explained as the temperature changes do not occur of a sudden, meaning that in the following 1.7s after the main part of the solidification the PCM is not able to access the full extend of the incoming (negative) heat. A closer look on the graph shows indeed that there is a slowing curve between the sensible and latent parts. It can also be possible that the temperature range for the constant part was defined greater than necessary. The 285.17 ± 0.02 K were simply taken as the earlier calculations do not surpass this value. The actual range in which solidification occurs can therefore be smaller.

The HTF temperature (fig. 50) starts to cool-down already at 13.5s, although there is a slight increase to the next data point, which could be a numerical error. The cooling slows down starting by 18.0s. Both values are more or less in the range as the expected solidification.

The heat flux itself stays constant for the first few seconds and decreases until stagnating at 17.742s, also corresponding to the values of the solidification changes. (Fig. 45 and tab. 17)

The FFT shows the expected shift to smaller frequencies and lower amplitudes over time. (Fig. 48) The time index from 36s to 41s was included to show that there appear to be no fluctuations.

The heat flux was checked on it's plausibility by hand calculations, as listed in tab. 17. As explained on the base calculation, the positive local heat flux is mostly caused by HTF

flow. Earlier time-steps of $A_{mush} = 10^6$ resemble therefore fig. 35 from the base model. After the solidification has been completed for wide parts of the model at 18 s the heat flux error from the PCM becomes low enough for the total value to stay not only below 0 but also in the correct range. (Fig. 46) As the volume fraction is continuously and slightly increasing from this point on Fluent does not have to correct by adding heated PCM to the model. This explains why the back-flow is strongest in the earlier stages of the solidification, but almost of no influence afterwards. Due to the good resemblance between the values calculated by Fluent and the hand calculations, as well as the correct negative sign for all values in the stagnation part, the heat transfer coefficients and Nusselt numbers will be stated only for this calculation: $\alpha = 0.6 \frac{\text{kW}}{\text{m}^2\text{K}}$ for the stagnation part, leading to a Nusselt numbers of 4.4 by using the set inlet diameter of 0.8 mm and a heat conduction of $\lambda = 0.114 \frac{\text{W}}{\text{mK}}$.

The droplet flow is visualised in fig. 42 with the liquid fraction contour placed directly on the ISO-surface of a volume fraction of 50 %. It should be repeated that this value is the total liquid fraction, meaning the sum over all phases. As the surface shown is at 50 % volume fraction this means a total liquid fraction of 50 % is equivalent to a PCM liquid fraction of 0, according to (45). The fluid-dynamic behaviour is quite similar to earlier discussed models, especially the final stage resembles fig. 18.

Fig. 42 a) shows the last droplet that is trying to form. While the surrounding area to the incoming stream is almost completely fluid in some areas the surface on top of the forming droplet has almost completely solidified with values down to 16 %.

The oil has to evade this area by connecting with wall faces, similar to earlier discussed models, as shown in the fig. 42 b) and c). The interesting change is the fact that the incoming oil coats the bottom face during this steps. This did only happen in models using 0.3 mm mesh before. A reason could be the change in the contact angle. As it was reduced from 90° to 30° with the intention of shortening the incoming stream the HTF become more likely to attach to the bottom face. As surrounding parts of the stream are already frozen to some extent it is easier for some of the D12 to stay in range of the inlet. Furthermore the outlet was changed from the dimensions of the inlet and surrounded by the wall to a completely open face. This means that no HTF can stay at the top, as the boundary setting only keeps PCM from leaving but lets HTF pass through unhindered. The oil therefore has only the option left to "grow" from the bottom and find a not solidified path to the outlet. These images also show that the PCM lying in concave areas tend to freeze faster than at convex areas. As it gets surrounded more by HTF than by PCM the heat transfer between HTF and PCM gets increased locally, whereas the heat transfer in the PCM itself gets reduced.

In fig. 42 d) the PCM layer on top of the HTF layer at the bottom is almost completely frozen, preventing the D12 from ascending to the top. Interestingly the HTF takes the exact same path as in the models with the outlet placed in this corner. It would be interesting to evaluate if the HTF prefers one path and why or why not, as well as if the path changes, when the outlet is moved or if it just finds a way to move alongside the top wall. This shows that the main solidification occurs between the last two images and

therefore the forming of the channel to the outlet. After that point, there appear minor flow changes, such as an increase in the oil layer but for the most part this model stays the same.

The calculation with $A_{mush} = 10^9$ shows a faster solidification than the other calculations, as expected. The liquid fraction curve shows some kind of hyperbolic shape. (Fig. 41 and tab. 15)

The results of the volume fraction shows, however, that the fluid-dynamic results are basically finished at a much earlier time step. (Fig. 44 and tab. 16)

The heat flux has one oscillation that could not be resolved due to the saving interval of 0.5s and seemingly stagnates at about 5.s at $-2.9 \frac{\text{kW}}{\text{m}^2}$. (Fig. 45) A closer look at the diagram shows, however, that the heat flux still decreases until 20 s, where it stays in the range of $[-2.5, 1] \frac{\text{W}}{\text{m}^2}$. The fluctuations were not detected by a FFT, which was therefore not attached. Also interesting is the fact, that there is still a positive total heat flux, in contrast to the calculation with $A_{mush} = 10^6$, which stays below 0 all the time after the solidification.

In fig. 47 the local heat flux at 20.0s is shown as an example. While there are small areas, especially in the left corners, with local negative flux, the majority is positive. Also the sign seems to be independent from the material. Although negative flux for D12 was detected, this occurred mostly at the boundary to PCM2. This small changes in the heat flux and the positive heat flux for PCM might be explained, when looking more closely at the volume fraction. This value does not stay exactly constant but jumps in the range of $[97.08; 97.10] \%$. It is therefore possible that small error is sufficient enough to change the sign of the heat flux momentarily, as the flux is close to 0.

The image series in fig. 43 shows some interesting results. No droplet formation at all is visible. (Fig. 43 a)) As the droplet tries to form one could get the impression that it gets hindered by a solidified layer on top. The incoming oil just covers the complete bottom and flows upwards in a steady stream pushing the PCM out of the tank, presumably again due to the contact angle of 30° . The PCM liquid fraction, however, stays mostly above 80 % and only in some parts above 60 %, for example the area marked by the upper arrow. Some small PCM parts get left out and show a value of 50 %, lower arrow. The areas more solidified are once again in the depths of the ISO-surface, except the left-out parts, of course. This implies that the HTF can be blocked quite effectively by areas that are not near complete solidification. This could also be a result of the greater mushy parameter.

When continuing the image sequence to fig. 43 b) the PCM on top gets solidified next by a small amount, due to the resulting spherical shape on top of the oil layer. This is sufficient for the HTF to create a singularity in the centre, shown in the last image, with liquid fraction between 70 % and 80 %. In this step there can be clearly seen a few areas that are completely solidified, as they were surrounded by colder HTF. Nevertheless the majority of the surface is still fluid.

The greater part of the freezing occurs between 43 b) and c). Still it takes quite some

time for the whole PCM to solidify. The flow stays basically the same for the rest of the calculation. The oil tries to fill the complete tank, except the areas left behind and some small areas at the top. The hand calculations show not only a major discrepancy between the hand calculations and the values by ANSY Fluent but also theoretically high value due to the higher outlet temperature, compared to the other calculations. This implies that the error is greater than for the base model, which should not occur, if it is produced by back-flow, as the volume changes are minimal during this stage. Furthermore the outlet temperature differs by 0.5 K between the calculated 3.0 s and 5.0 s, from where it stays constant. This results could not be resolved, there should be no reason for this high outlet temperature.

When analysing the average temperature of the used materials it can be seen quite clearly that both of them cool down to 275 K. (Fig. 49 and 50) and tab. 18). The PCM temperature shows the expected short plateau. The PCM and the HTF temperature cool down until reaching the same temperature of 275.24 K at 25.5 s. At this point the solidification temperature is not exactly reached, yet the liquid fraction already reached 0. This is probably due to the high mushy parameter. It can be assumed that this value can be linked to a temperature range in which the phase change occurs. Until the next time step the PCM temperature decreased to 275.23 K but the HTF only to 275.34 K. The PCM temperature is lower by 0.11 K. For the rest of the calculation the PCM stays colder as the HTF. This contradicts the second law of thermodynamics. As these two materials reach a state of balance the system should not undergo any further temperature changes. Additionally, this balance should be achieved at the inlet temperature of 275.15 K as the oil continuously enters the system at this temperature. This is therefore probably a numerical error and means that no values with a temperature dependence after this point can be used.

7.3 Inlet Temperature variations

For the variation of the inlet temperature the mushy parameter was kept at 10^5 and the velocity at $0.4 \frac{\text{m}}{\text{s}}$, according to tab. 14

For the calculation with $\Delta T = -15 \text{ K}$ the output data in range of [29.080;30.500] s was not written in the output file, although the data files did exist. This may have been either a computational error or a user error, as the server experienced crashes in that time. A possible explanation could be that accidentally the output file of the crashed calculation was chosen. As the missing values only appear in a relatively small part of the calculations ($\leq 1.5 \text{ s}$ or 3 %) and the saved data files for each 0.5 s were fully intact, it was decided to simply interpolate the results linearly as done with the temperature values, for calculating the heat transfer coefficient.

Results

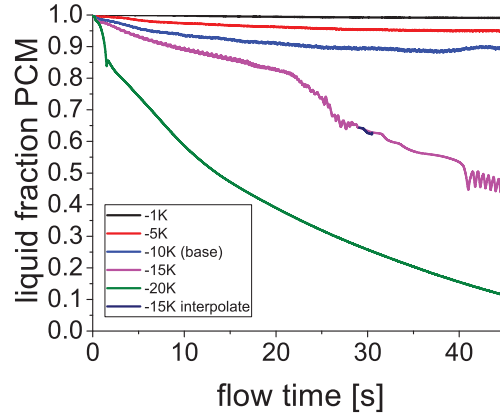


Figure 51: Liquid-fraction for different ΔT . For -15 K the values in the range $[29.080;30499]\text{ ms}$ had to be interpolated, as explained in the running text
 $D12$, $PCM2$, $(x,y,z) = (5,12.5,5)\text{ mm}$, $A_{in} = 4.6 \cdot 10^{-7}\text{ m}^2$, $A_{out} = 25\text{ m}^2$,
 Mesh: multi-zone, hexagonal, 0.1 mm , $\Delta T = (-1, -5, -10(\text{base}), -15, -20)\text{ K}$, $A_{mush} = 10^5$,
 $v_{in} = 0.4 \frac{\text{m}}{\text{s}}$

ΔT [K]	$l_{PCM}[\%]$				
	$t = 1.5$ [s]	$t = 22.0$ [s]	$t = 27.5$ [s]	$t = 40.0$ [s]	$t = 45.0$ [s]
-1	100	99			
-5	99	96	95		
-10	98	91	90	89	90
-15	97	81	65	53	46
-20	85	36	29	16	11

Table 19: Important values of the liquid fraction for the calculations with $\Delta T = -15, -20\text{ K}$ in fig. 51. For comparison the values of all other calculations from this parameter variation at the same time steps are included. The **base calculation** is **bold**. The calculation with -15 K shows a drop from 22 s to 27.5 s and a periodic behaviour from 40.0 s to 45.0 s . The calculation with -20 K shows a small downward facing peak at 1.5 s

Fig. 51 shows the results for the liquid fraction. It can be seen that the value for $\Delta T = -1\text{ K}$ reaches 99 %, $\Delta T = -5\text{ K}$ reaches 95 % and $\Delta T = -10\text{ K}$ reaches 90 %. The calculation with $\Delta T = -15\text{ K}$ has an increased drop at 27.5 s and starts a clearly periodic behaviour at 40 s . The calculation with $\Delta T = -20\text{ K}$ has a strong drop in the first 1.5 s a continuous to fall slower until a final value of 11 %. The important values can be seen in 19.

The visualisation for the $\Delta = -15\text{ K}$ calculation in fig. 52 starts in fig. 52 a), showing a droplet with a surrounding surface area of a total liquid fraction between 64 % and 69 %.

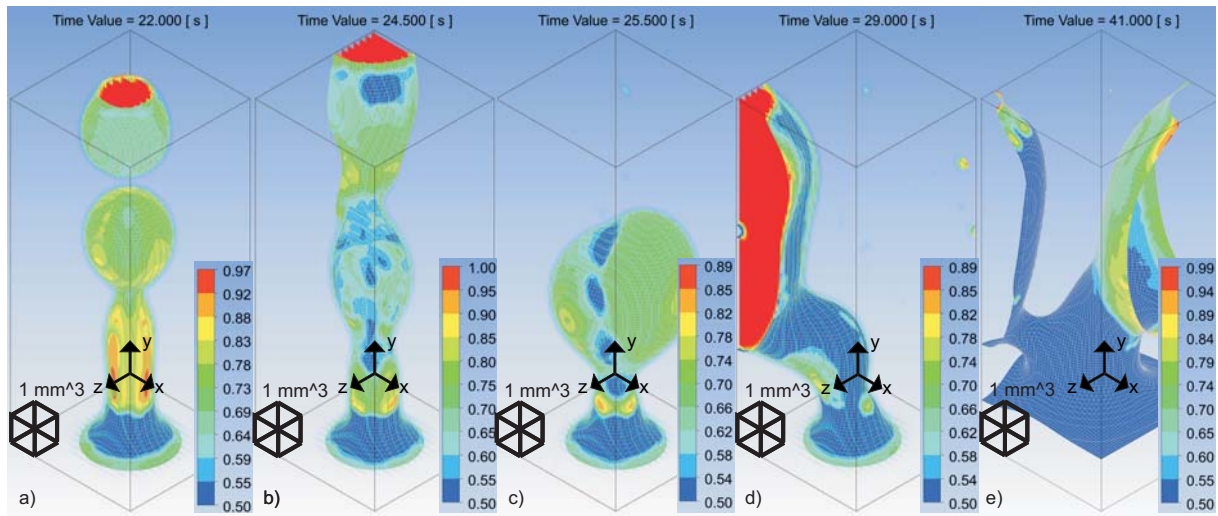


Figure 52: Screen-shot sequence of the total-liquid-fraction contour on an ISO-surface with 50 % volume fraction for the solidification steps with $\Delta T = -15 \text{ K}$

- a) image showing the droplet formation with solidification at the bottom at 22.0 s
 b) image showing an oil stream bending at the centre of the tank to the back with completely solidified areas at the bottom, in the centre and at the top at 24.5 s
 c) image showing an irregular shaped droplet with completely solidified area surrounding the centre and at the bottom at 25.5 s
 d) image showing a bent HTF stream to the left wall with almost completely solidified surface area

e) image showing a completely solidified area above the bottom wall split into two paths to the left and the right side of the tank forming curved areas. The left one is completely solidified, except for small parts at the top. The HTF was set to 100 % transparent for better visualisation

$D12$, $PCM2$, $(x, y, z) = (5, 12.5, 5) \text{ mm}$, $A_{in} = 4.6 \cdot 10^{-7} \text{ m}^2$, $A_{out} = 25 \text{ m}^2$,
 Mesh: multi-zone, hexagonal, 0.1 mm , $\Delta T = -15 \text{ K}$, $A_{mush} = 10^5$, $v_{in} = 0.4 \frac{\text{m}}{\text{s}}$

The jet has values of $\geq 70\%$ on the top, values up to 1 are present at the side of the shaft. The area in the cone at the bottom is the only area with values down to 50 %. The average PCM liquid fraction on the surface is 50%.

In fig. 52 b) additional 50 % areas have appeared in the middle part and on the top. Values at the lower shaft are $\geq 75\%$ and hardly any area close to 1 can be seen. The average PCM liquid fraction on the surface area is 34%.

In fig. 52 c) there is once again a single droplet present values in the range of 50 %, in the centred line on the xy-plane. The majority of the droplet is near 70 %. The average PCM liquid fraction on the surface is 26%.

In fig. 52 d) a stream with a surrounding area of values near 50 % in most parts is visible. Cells with higher values are especially on the edge on the touched faces, as well as in the downside pointing part of the angle. In the right part of the tank two small oil droplets can be seen that are completely surrounded by PCM. The average PCM liquid fraction on the surface is 8%.

Fig. 52 e) shows an ISO-surface filled in most part with values of 50 %. The right path

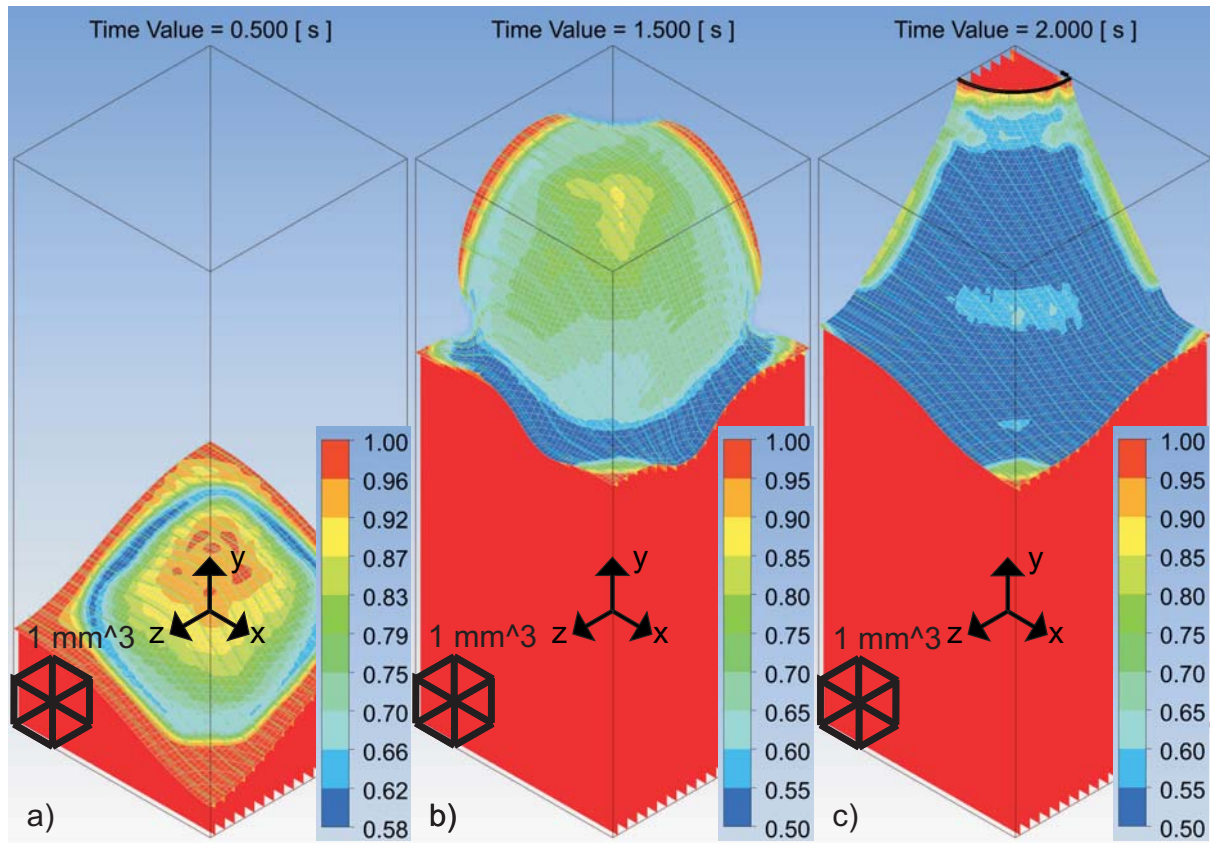


Figure 53: Screen-shot sequence of the total-liquid-fraction contour on an ISO-surface with 50 % volume fraction for the solidification steps with $\Delta T = -20 \text{ K}$

a) image showing the HTF rising continuously filling the whole tank with an almost completely solidified area surrounding the centre in the middle between centre and wall

b) image showing the tank almost filled by 75 % HTF with a big round area on top surrounded by completely solidified PCM, except at the corners

c) image showing a more or less even layer of HTF with a completely solidified surface area, except at the corners, and a path to the outlet in the back of the tank

$D12$, $PCM2$, $(x, y, z) = (5, 12.5, 5) \text{ mm}$, $A_{in} = 4.6 \cdot 10^{-7} \text{ m}^2$, $A_{out} = 25 \text{ m}^2$,
Mesh: multi-zone, hexagonal, 0.1 mm , $\Delta T = -20 \text{ K}$, $A_{mush} = 10^5$, $v_{in} = 0.4 \frac{\text{m}}{\text{s}}$

shows parts of $\geq 70 \%$ in the surrounding cells coating the wall. Furthermore cells on top of the left path have values increased to 70 % or even 85 %. The average PCM liquid fraction on the surface is 12%.

The visualisation in fig. 53 starts with an image showing a total liquid fraction near one at the centre and at the walls. (Fig. 53 a)) The top is covered mostly with a value of $94 \pm 2\%$. The liquid fraction descends from both sides in small layers until reaching 58 % somewhere in the middle. The average value of the PCM liquid fraction on the surface area is 68%.

Fig. 53 b) shows a surface area mostly covered by values of 50 %. Near the corners these values ascend steady to 1. The values on top are up to 90%, the values on the boundary to the walls are near 1. The values are spread less even than in the last image

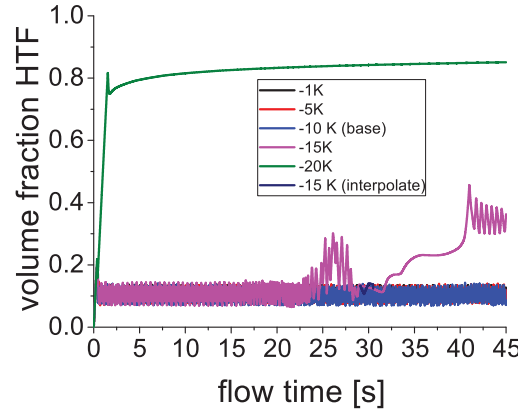


Figure 54: Volume-fraction for distinct temperature differences between inlet and solidification temperature, with only the inlet temperature changed. For $\Delta T = -15\text{ K}$ the values in the range $[29.080; 304.99]\text{ ms}$ had to be interpolated, as explained in the running text

$D12$, $PCM2$, $(x, y, z) = (5, 12.5, 5)\text{ mm}$, $A_{in} = 4.6 \cdot 10^{-7}\text{ m}^2$, $A_{out} = 25\text{ m}^2$,
 Mesh: multi-zone, hexagonal, 0.1 mm , $\Delta T = (-1, -5, -10(\text{base}), -15, -20)\text{ K}$, $A_{mush} = 10^5$,
 $v_{in} = 0.4\frac{\text{m}}{\text{s}}$

but distributed in the same way. In direction of the oil layer below the values descend almost continuously. The average value of the PCM liquid fraction on the surface area is 29%.

In the fig. 53 c) the total liquid fraction is at 50 %, except for a small area in between with values near 55 %, the corners (up to 1) and the boundary on the wall near the outgoing HTF (on the top up to one, on the side up to 80 %). The average value of the PCM liquid fraction on the surface area is 8%.

Fig. 54 shows the results for the volume fraction. It can be clearly seen that the values for $\Delta T = -1, -5, -10\text{ K}$ are in a similar range. The line for -15 K shows an increase and fall from around 22.5s to 31.7s, followed by two increasing discrete steps. For the last 6 s the periodic behaviour returns. The graph for $\Delta T = -20\text{ K}$ shows a fast increase in the first 1.5s, followed by a short fall and a continuous increases to it's final value of 85%. The important values can be seen in tab. 20.

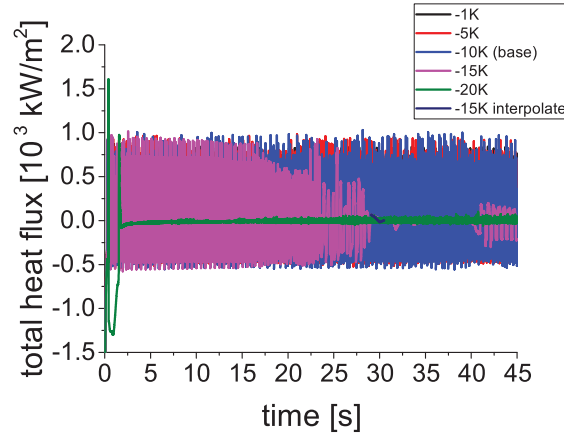


Figure 55: Heat flux for distinct temperature differences between inlet and solidification temperature, with only the inlet temperature changed. For -15 K the values in the range $[29.080;30499]\text{ ms}$ had to be interpolated, as explained in the running text

$D12$, $PCM2$, $(x, y, z) = (5, 12.5, 5)\text{ mm}$, $A_{in} = 4.6 \cdot 10^{-7}\text{ m}^2$, $A_{out} = 25\text{ m}^2$,
 Mesh: multi-zone, hexagonal, 0.1 mm , $\Delta T = (-1, -5, -10(\text{base}), -15, -20)\text{ K}$, $A_{mush} = 10^5$,
 $v_{in} = 0.4\frac{\text{m}}{\text{s}}$

$\Delta T\text{ [K]}$	$\bar{v}_{HTF}\text{ [\%]}$				
	$t = 1.5\text{ [s]}$	$t = 26\text{ [s]}$	$t = 31.7\text{ [s]}$	$t = 39.1\text{ [s]}$	$t = 45, [\text{s}]$
-1	10				
-5	10				
-10	10				
-15	10	26	16	36	34
-20	81	84		85	

Table 20: Important values of the volume fraction for the calculations with $\Delta T = -15 - 20\text{ K}$ in fig. 54 and all other calculations for comparison. The **base calculation** is **bold**. The calculation with -15 K shows a rise rise with a maximum at 26 s , followed by a drop and a stop of the oscillation to 31.7 , another rise until 39.1 s , where it starts oscillating again. The calculation with -20 K increases linearly in the first 1.5 s , followed by a short drop and a continuing rise, reaching a constant value.

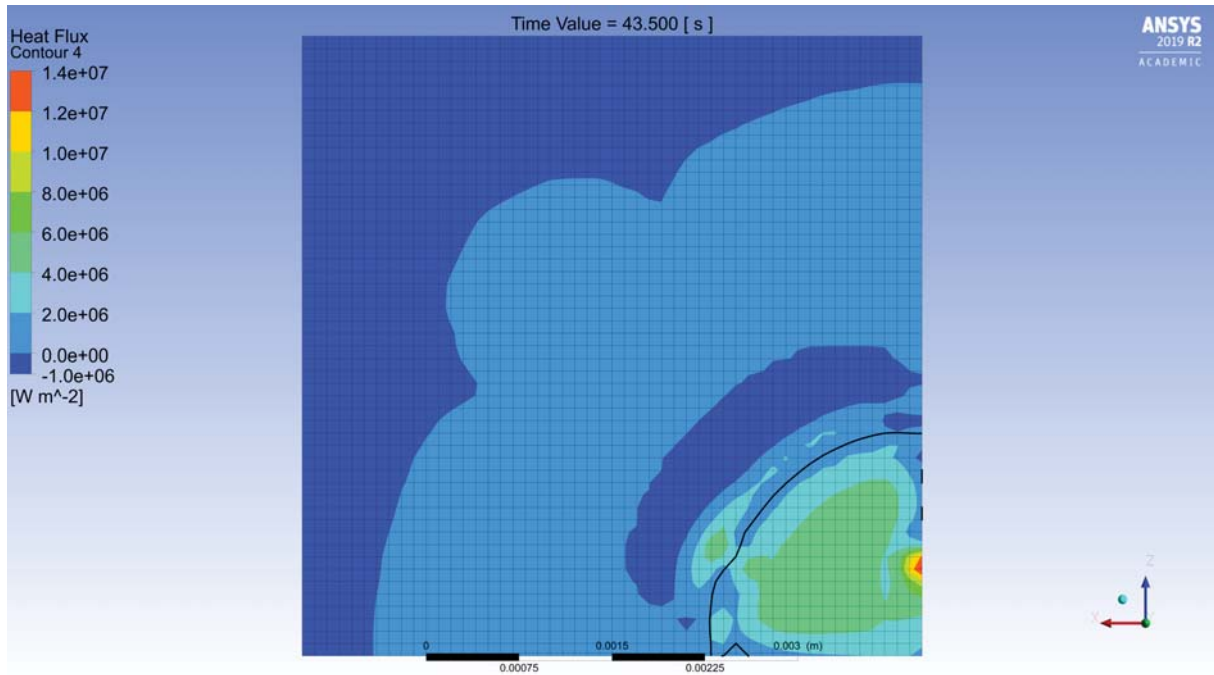


Figure 56: Screen-shot of a visualisation of the heat flux at the outlet at 43.5 s for $\Delta T = -20$ K D12, PCM2, $(x, y, z) = (5, 12.5, 5)$ mm, $A_{in} = 4.6 \cdot 10^{-7} \text{ m}^2$, $A_{out} = 25 \text{ m}^2$, Mesh: multi-zone, hexagonal, 0.1 mm, $\Delta T = -20$ K, $A_{mush} = 10^5$, $v_{in} = 0.4 \frac{\text{m}}{\text{s}}$

ΔT [K]	time range [ms]	$-\bar{q} [\frac{\text{kW}}{\text{m}^2}]$		T_{out} [K]	T_{in} [K]	$\bar{A} [\text{m}^2]$
		Fluent	with (1)			
-1	[264;45000]	5.4	3	284.87	284.15	$7 \cdot 10^{-5}$
-5	[275;45000]	7.8	6	281.44	280.15	$7 \cdot 10^{-5}$
-10	[295;45000]	9.6	20	≈ 279.15	275.15	$7 \cdot 10^{-5}$
-15	[324;29079]	16.6	27.4	276.02	270.15	$7 \cdot 10^{-5}$
-15	[29080;40980]	18.0	4.6	271.17	270.15	$6 \cdot 10^{-5}$
-15	[40981;45000]	2.6	24.9	277.12	270.15	$9 \dots 10^{-5}$
-20	[367;1812]	745.8	could not be resolved		265.15	
-20	[1813;45000]	10.2	[30;5]	[269.22; 265.90]	265.15	$4 \dots 10^{-5}$

Table 21: Average heat fluxes for different parts of all calculations, the **base calculation** in **bold**, in fig. 55, as well as the corresponding values for hand calculations

Fig. 55 shows the results for the volume fraction. It can be clearly seen that the values for $\Delta T = -1, -5 - 10$ K are in a similar range. The line for $\Delta T = -15$ K shows a decrease in the maximum value starting by about 17.5 s. From 29 s on the value stays nearly constant but turns periodic again in the last 5 s. The graph for $\Delta T = -20$ K shows two relatively high peaks at 0.367 s and 1.8 s and seems to stagnate directly after. From around 15 s the deviation to the average value increases but the fluctuations are not in clearly visible range. The important values, as well as corresponding hand calculations can be seen in tab. 21.

The local heat flux at the outlet at 43.5s for the calculation with -20 K in fig. 56 shows mostly positive values, except at the boundary. The PCM has a wide area with slightly positive flux radial symmetric to the corner at which the HTF is leaving the tank. An additional middle strong positive area is close to the HTF and overlapping surpassing the boundary.

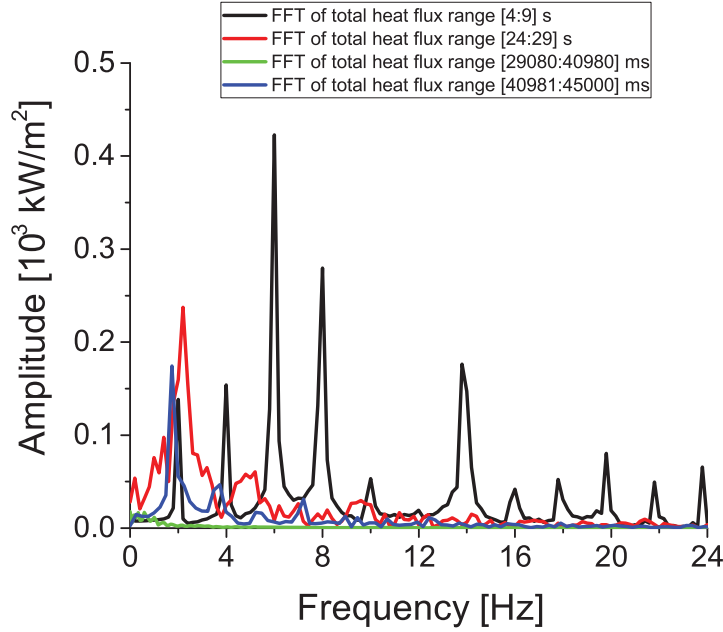


Figure 57: Amplitude and frequency of the Fourier transformations of $\Delta T = -15$ K in four parts

$D12$, $PCM2$, $(x, y, z) = (5, 12.5, 5)$ mm, $A_{in} = 4.6 \cdot 10^{-7} \text{ m}^2$, $A_{out} = 25 \text{ m}^2$,
 Mesh: multi-zone, hexagonal, 0.1 mm, $\Delta T = -15$ K, $A_{mush} = 10^5$, $v_{in} = 0.4 \frac{\text{m}}{\text{s}}$, $t [\text{ms}] =$
 [4000; 9000], [24000; 29000], [29080 : 40980], [40981 : 45000]

The FFT of the $\Delta -15$ K calculation in fig. 57 shows the maximum values chronologically ordered: $(\nu [\text{Hz}], q_A [\frac{\text{kW}}{\text{m}^2}]) = (6.0, 422.8), (2.2, 237.3), (0, 17.4), (1.7, 174.4)$.

The PCM temperature plot in fig. 58 shows that the $\Delta T = -1, -5, -10$ K calculations have one nearly linear decrease, followed by a stagnation part. -15 K shows a third decrease starting at 22.5s. $\Delta T = -20$ K shows no plateau at all, the temperature is dropping more or less linearly to a final value of 278.27 K The important values are listed in tab. 22.

The average D12 temperature in fig. 59 for $\Delta T = -1$ K jumps in the range of [284.65;284.80] K, for $\Delta T = -5$ K in the range of [282.50;283.28] K, and for $\Delta T = -10$ K in the range of [279.25;280.85] K. The line for $\Delta T = -15$ K has a drop in the first 3 s from 278.48 K to 277.02 K. From there it slowly decreases until 276.48 K at 13 s. Then a short increase for 1 s appears, reaching 277.50 K followed by a drop to 272.84 K at 30.0, followed by a short increase for 2.5 s to 273.92 K The value then drops to slowly 272.73 K

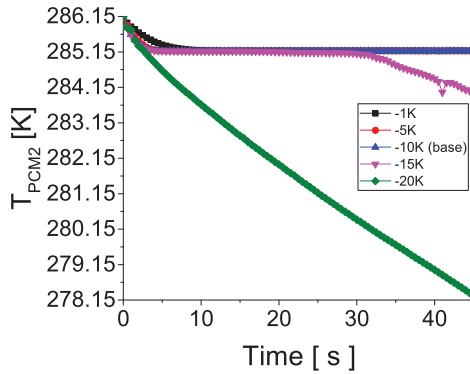


Figure 58: Average temperature of PCM2 for different inlet temperatures

$D12$, $PCM2$, $(x, y, z) = (5, 12.5, 5) \text{ mm}$,
 $A_{in} = 4.6 \cdot 10^{-7} \text{ m}^2$, $A_{out} = 25 \text{ m}^2$,
 Mesh: multi-zone, hexagonal, 0.1 mm ,
 $\Delta T = (-1, -5, -10(\text{base}), -15, -20) \text{ K}$,
 $A_{mush} = 10^5$, $v_{in} = 0.4 \frac{\text{m}}{\text{s}}$

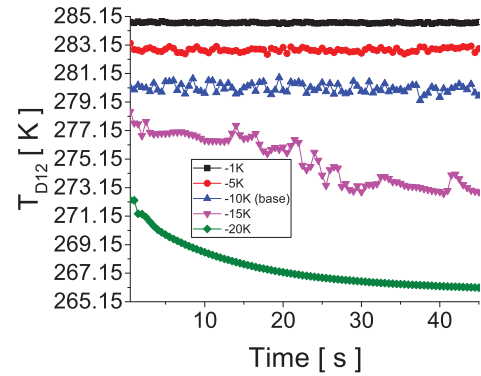


Figure 59: Average temperature of the D12 for different inlet temperatures

$D12$, $PCM2$, $(x, y, z) = (5, 12.5, 5) \text{ mm}$,
 $A_{in} = 4.6 \cdot 10^{-7} \text{ m}^2$, $A_{out} = 25 \text{ m}^2$,
 Mesh: multi-zone, hexagonal, 0.1 mm ,
 $\Delta T = (-1, -5, -10(\text{base}), -15, -20) \text{ K}$,
 $A_{mush} = 10^5$, $v_{in} = 0.4 \frac{\text{m}}{\text{s}}$

at 40.5 s. With the exception of a small increase to 274.09 K at 42 s the value stays in that range. This behaviour can be approximated by a short decrease followed by a plateau and a longer decrease, followed by another plateau. The $\Delta T = -20 \text{ K}$ line experiences a drop from 280.15 to 271.29 K in the first 2 s followed by a slowing drop to its final value of 278.27 K.

$\Delta T \text{ K}$	$t \text{ [s]}$		$T_{PCM2} \text{ K}$ t=45 s
	reaching 285.17 K	reaching 285.13 K	
-1	> 45		285.18
-5	22.0	> 45	285.18
-10	5.0	> 45	285.17
-15	5.0	22.5	284.05
-20	3.0	3.0	278.27

Table 22: Time range of the PCM temperature that it stays near the solidification temperature and the final temperature for all calculations in fig. 58. The **base calculation** is **bold**

Discussion

Due to the lower inlet temperatures the results of the simulations with $\Delta T = (-1, -5)$ were expected to achieve less heat transfer and therefore less solidification than the base model. When comparing fig. 51, 54, 55 and 58 this assumption proves to have been accurate. Therefore the values will be discussed only shortly, always in the order $\Delta T = (-1, -5, 10) K$, and the focus will then be led on $\Delta T = (-15, -20) K$. It was expected for calculations with a smaller temperature difference to result in smaller heat exchange and therefore higher liquid fraction values. When analysing the important values in tab. 19, 20, 21 and 22 it can be clearly seen that this is the case for the corresponding PCM liquid fractions, heat fluxes and PCM temperature. For liquid fraction and heat flux the -5 K values lay in between the other two values. For the PCM temperature this is not the case but this is probably as the final values were taken and not the average values and has a numerical origin. The FFT is similar for all values but no trend can be detected. The following maximum values can be found: $(\nu[H\dot{z}], q_A[\frac{kW}{m^2}]) = (7.8, 219.3), (8.4, 87.3), (7.9, 87.1)$.

When comparing $\Delta T = -15 K$ to the curve of the mushy parameter variations with $A_{mush} = 10^6$ and $\Delta T = -10 K$ (here $A_{mush} = 10^5$) there is especially at the beginning a good resemblance. The important values can be found in tab. 23. As the mushy parameter describes the solidification and the heat transfer is strongly dependent on temperature difference it was expected for stronger ΔT to cool down faster, whereas for higher A_{mush} to solidify faster. When comparing only the results for each "calculation stack" with each other this is definitely the case. When comparing however, the results across some interesting behaviour can be seen. Although the 10^6 line reaches the main solidification part earlier and finish faster, the $\Delta T = -15 K$ line reaches a higher solidification during the main part and afterwards. This shows that the main parameter to control solidification is still the temperature on a global scale. The mushy parameter seems only to control the starting time and the time necessary for the main solidification part. Furthermore the solidification from the $\Delta T = -15 K$ calculation seems to become unstable in the last seconds.

Parameter	$l_{PCM} [\%]$			$t [s]$		
$A_{mush} = 10^6$	81	74	62	14.05	17.8	45
$\Delta T = -15 K$	81	65	46	22	27.5	45

Table 23: Important values of the liquid fraction (decrease start and end, as well as the final value) for the calculations with $\Delta T = -15 K$ and $A_{mush} = 10^6$ that share similar behaviour on a global scale

When comparing the average PCM temperatures it is visible that the results of the liquid fraction do not contradict the initial premiss completely. The important data can be

found in tab. 24. While both calculations reach the latent stage nearly at the same time, which does not match the impression from tab. 23, the calculation with 10^6 stays shorter. In the following sensible stage the mainly solidified PCM cools faster in the calculation with -15 K .

Parameter	t [s]		T_{PCM2} [K]
	reaching 285.17 K	reaching 285.13 K	t=45 s
$A_{mush} = 10^6$	5.0	19.5	284.78
$\Delta T = -15\text{ K}$	5.0	22.5	284.05

Table 24: Time-steps of the changes in the behaviour of the PCM temperature for the calculations with $\Delta T = -15\text{ K}$ and $A_{mush} = 10^6$, that share similar behaviour on a global scale

The behaviour of the liquid fraction is consistent with the volume fraction. (Fig. 54 and tab. 20) This is mathematically explained, as the liquid fraction for the PCM was extracted by the total value with the help of the volume fraction. This behaviour can, however, also be explained on a basis of fluid-dynamics and thermodynamics. As the solidification process is not consistent and has higher gradients, this could imply that the oil can find a way through the frozen area and start flowing again. Due to incoming and outgoing oil at different time steps, the volume fraction does not stay constant any more. This leads to increased back-flow and therefore solidified PCM can be liquefied back, resulting in a positive heat flux, which stayed negative in the smoothed part of the solidification and volume fraction line, as seen in fig. 55 and tab. 21. The behaviour is therefore similar to $A_{mush} = 10^6$ in fig. 45, except for the last few seconds with periodic behaviour.

The FFT comparison consists the expected shift to the left at increased time steps of the $\Delta T = -15\text{ K}$ line. (Fig. 57) A comparison to the calculation with mbox $A_{mush} = 10^6$ (fig. 48) shows, however, at the first look a completely different FFT. For $\Delta T = -15\text{ K}$ the spectrum from 4s to 9s shows 10 discrete peaks, while the plot for $A_{mush} = 10^6$ shows much more noise. A closer look reveals that all peaks are at similar areas for the periodic part. The main peak of 6.0 Hz does exist in $A_{mush} = 10^6$ but is surpassed by a peak at 5.0 Hz. The comparison shortly before the stagnation part shows a much more similar image, although the peaks are better visible for $A_{mush} = 10^6$. Even the main peak is almost exactly at the same frequency (2.2 Hz and 2.0 Hz). The stagnation part shows no detectable period for $A_{mush} = 10^6$. The $\Delta T = -15\text{ K}$ FFT shows some values below 2 Hz but in a negligible range. The amplitudes for the $\Delta T = -15\text{ K}$ calculation show values twice as high as for $A_{mush} = 10^6$ for all ranges. This is not unexpected, as the frequencies are less widespread, meaning the flux is less steady, but the values of the flux jump around in nearly the same range.

In the first part the flux is once again shifted to a positive range due to the back-flow, as seen in tab. 21. Although it's value is in the correct range between the first and the second hand calculation. Interestingly the second average value is more negative than

the first one. The explanations are the small downward peaks detected in the diagram, implying that the outflow of the HTF is reduced during these steps.

The final stage is interesting. As the PCM is getting solidified and liquefied periodically in some areas this leads to a fast increase of the outlet temperature. The hand calculated heat flux is then in the end nearly as high as in the beginning. It is, however, highly plausible that the HTF outlet temperature decreases again for the rest of the calculation or the error is big enough due to the fluctuations, as the value, calculated by ANSYS Fluent, is lower at the end than in the other two stages. The fast increase in the outlet temperature should not be possible without additional heating and origins probably in the model itself.

Although the data is on overall very similar until the final periodic stage to the calculation with $A_{mush} = 10^6$ the fluid-dynamic and thermodynamic behaviour of the system is actually very different. (Fig. 52 and 42) Fig. 52 a) shows a droplet formation, in spite of the corrected PCM liquid fraction by eq. (45), which is down to 0 in some areas. While the $A_{mush} = 10^6$ model started to solidify on the top, with $\Delta T = -15\text{ K}$ the solidification start, as originally expected, only at the bottom near the inlet, to be precise at the neck between bottom layer and incoming jet. The lower mushy parameter is probably the reason for the PCM to solidify more unsteady. As opposed to second image of $A_{mush} = 10^6$, where the surrounding area is in a similar state, except for minor areas at the top, here all images contain values throughout the complete scale. Also for $A_{mush} = 10^6$ the model started to freeze at the top, blocking the incoming oil and leading to an additional solidification from the bottom. In this case it is the other way around. As the bottom is almost completely frozen but the top is still fluid the HTF can still find an easy way through and behaves as if nothing had happened. The rest of the stream is in a similar state as for $A_{mush} = 10^6$, although with lesser area near to 1.

Starting with fig. 52 b) the flow is totally different from the calculation with $A_{mush} = 10^6$. During it's main solidification drop the oil flows in one stream with a bend to the back in direction of the outlet, explaining the short increase in the volume fraction. The surface covering the HTF is now completely frozen, not only in the neck, but also in wide areas of the angle and on the top. This means, that the HTF is stuck in some parts at the middle of the tank and is therefore unable to shift completely to the wall, as in the calculation with $A_{mush} = 10^6$.

One second later (fig. 52 c)) the volume fraction returns near it's starting level, as the stream almost completely left the tank and the remains create a big droplet at the centre. This state leads to the stagnation part of the heat flux.

As the HTF can only evade the blocking from the solidified PCM by the side, it bends again, now to the left, as seen in fig. 52 d). For a few seconds this state can be held, as the surroundings are completely frozen, except for a few minor spots, e.g. at the inner side of the "knee".

Until fig. 52 e) the volume fraction increases in two stages. The incoming D12 covers the bottom wall, as already seen in the calculation with 10^6 . A final increase in the volume fraction takes place at 41s. As the incoming oil has to go somewhere but most of the

bottom part is now completely frozen, the HTF uses the only output points on the top side of the neck available and creates a second stream on exactly the opposite side of the tank. The interesting factor is now the liquid fraction on the surface. It can be seen quite clearly that the new dish on the right side surrounding the oil consists of areas with a PCM liquid fraction of 30 % and upwards. This shows that wide areas of the PCM are still more or less fluid. Only the stream connected to the dish is completely solidified. Some HTF is therefore able to separate from the stream and leaves the tank in form of the droplet. This, however, creates a drop in the volume fraction, which has to be filled as usual by the defined back-flow, with relatively hot PCM. This means for the rest of the calculation that Fluent has to try once again to find a balanced result by increasing and decreasing parameters, leading to a periodic fluctuation of the results. This can be best visualised on the left part of the model. The surface area that had been almost completely solidified, except for the surroundings shows values up to 70 % up to 1 mm away from the top, in the y-direction. A comparison on the averaged PCM liquid fraction of the surface area shows that the main parts of the solidification occurs between the first two images and between the third and the fourth. Also the PCM gets liquefied between the last two images.

For $\Delta T = -20\text{ K}$ it was expected to achieve a fast cool-down and a higher solidification. The decrease in the liquid fraction is consistent with a decrease in the volume fraction. (Fig. 54, fig. 51 and 54, as well as tab. 19 and 20) According to the PCM temperature there is no visible latent part. (Fig. 58 and tab. 22) Due to the high temperature difference the PCM solidifies so fast that it could not be detected with a saving interval of 0.5 s.

The heat flux shows three abnormalities before the stagnation occurs, the first and the latter one could not be resolved for the same reason. (Fig. 45 and tab. 17) Although it can be assumed from previous results that a substantial amount of oil is leaving the tank, consistent with a strong back-flow, leading to such immense values. The second value is negative and shows the heat flux when no oil is leaving the tank. After the third value the line goes relatively close to 0, where it kind of stagnates. An average of the heat flux in this first part is negative with a relatively high value, compared to the other calculations. This explains the fast cool-down and solidification. It can be clearly seen that the line in the "stagnation part" is quite thick, so it can be assumed that there is some kind of periodic behaviour, which could not be resolved with a FFT. This and the data for volume and liquid fraction rule the volume fraction (and therefore back-flow) out as a potential explanation. A visualisation of the heat flux contour at 43.5 s (total $q = 2.48 \frac{\text{kW}}{\text{m}^2}$) shows the correct positive sign for the HTF, as well as the correct negative sign in wide parts of the PCM and around most of the boundary between. There is, however, one small area of the PCM near the HTF showing a flux of $4 \frac{\text{MW}}{\text{m}^2}$. This indicates that the PCM in this area is heated from the outside. Additionally a heat flux on the PCM with slightly positive value can be seen in a wide area. It's origin is not clear. If it had been related to the set outlet temperature an even distribution would be expected. It is interesting to

note, however, that the PCM flux is radial symmetric to the corner in which the HTF is visible.

A visualisation of the total liquid fraction on the ISO-surface for 50 % volume fraction shows the important stages during the solidification process. (Fig. 53) Due to the saving interval of 0.5s it is not easy to interpret the first image of the series. Fig. 53 a) shows a bottom layer of oil with something on top that could be a droplet in formation, although the shape is more quadratic with curved edges than spherical. The only completely solidified area is a small ring of no more than three cells side-by-side at the middle distance around the bulb in the centre. As the outer ring and the inner bulb are nearly completely fluid, there seems to be no reason to prevent a droplet formation. It is also unclear why the HTF creates a layer on the bottom so early in the calculation. The global value of the PCM liquid fraction (fig. 54) shows that the PCM is still fluid in most parts. The HTF should therefore be able to easily break through any solidified area, ascending to the top, as in the last calculation.

In fig. 53 b) the HTF continues to push the PCM layer forward. The surface area is solidified completely, except for the corners and a bigger bulb in the centre. It seems plausible that the edges solidified faster than the centre, which stayed on top. Therefore this was the only direction for the HTF to flow, building this structure on the way to the outlet, as it comes in contact with the back walls.

In the next 0.5s (fig. 53 c)) this D12 bulb leaves the tank, resulting in a layer ascending to the outlet in the back corner, as in the last image. This stage stays basically constant, except for additional incoming oil, which increases the layer slowly but continuously for the rest of the calculation.

7.4 Inlet Velocity variations

For the variation of the inlet velocity the mushy parameter was kept at 10^5 and the inlet temperature at 275.15 K, according to tab. 14.

Results

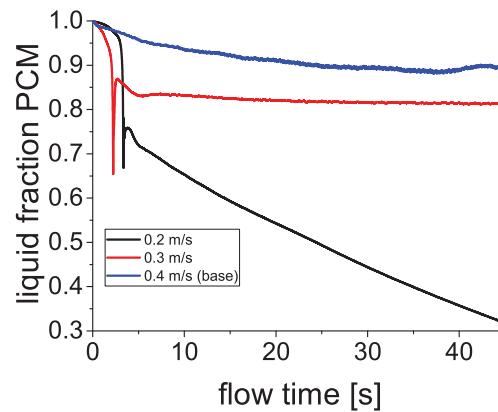


Figure 60: Liquid-fraction for different inlet velocities

$D12$, $PCM2$, $(x, y, z) = (5, 12.5, 5) \text{ mm}$, $A_{in} = 4.6 \cdot 10^{-7} \text{ m}^2$, $A_{out} = 25 \text{ m}^2$,
 Mesh: multi-zone, hexagonal, 0.1 mm , $v_{in} = (0.2, 0.3, 0.4(\text{base})) \frac{\text{m}}{\text{s}}$, $A_{mush} = 10^5$,
 $\Delta T = -10 \text{ K}$

$v_{in} [\frac{\text{m}}{\text{s}}]$	$l_{PCM} [\%]$				
	$t = 2.234 [\text{s}]$	$t = 2.7 [\text{s}]$	$t = 3.37 [\text{s}]$	$t = 3.386 [\text{s}]$	$t = 45.0 [\text{s}]$
0.2	98	97	67	77	32
0.3	65	87	86		81
0.4	98		97		90

Table 25: Important values of the liquid fraction for the calculations with $v_{in} = 0.2, 0.3 \frac{\text{m}}{\text{s}}$. For comparison **the base calculation** was included **bold**. The calculation with $0.2 \frac{\text{m}}{\text{s}}$ shows a peak at 2.234s and reaches it's original value followed by a final drop. The calculation with $0.3 \frac{\text{m}}{\text{s}}$ shows a peak at 3.37s and reaches it's original value followed by a short drop and a stagnation

Fig. 60 shows the results for the liquid fraction. It can be seen that the graphs for $v_{in} = 0.2, 0.3 \frac{\text{m}}{\text{s}}$ have two downward facing peaks at 2.234s and 3.37s. Furthermore the first one stagnates from 10s, while the latter calculation keeps dropping until reaching 32%. The base calculation does not have any detectable features. The important values can be seen in 25.

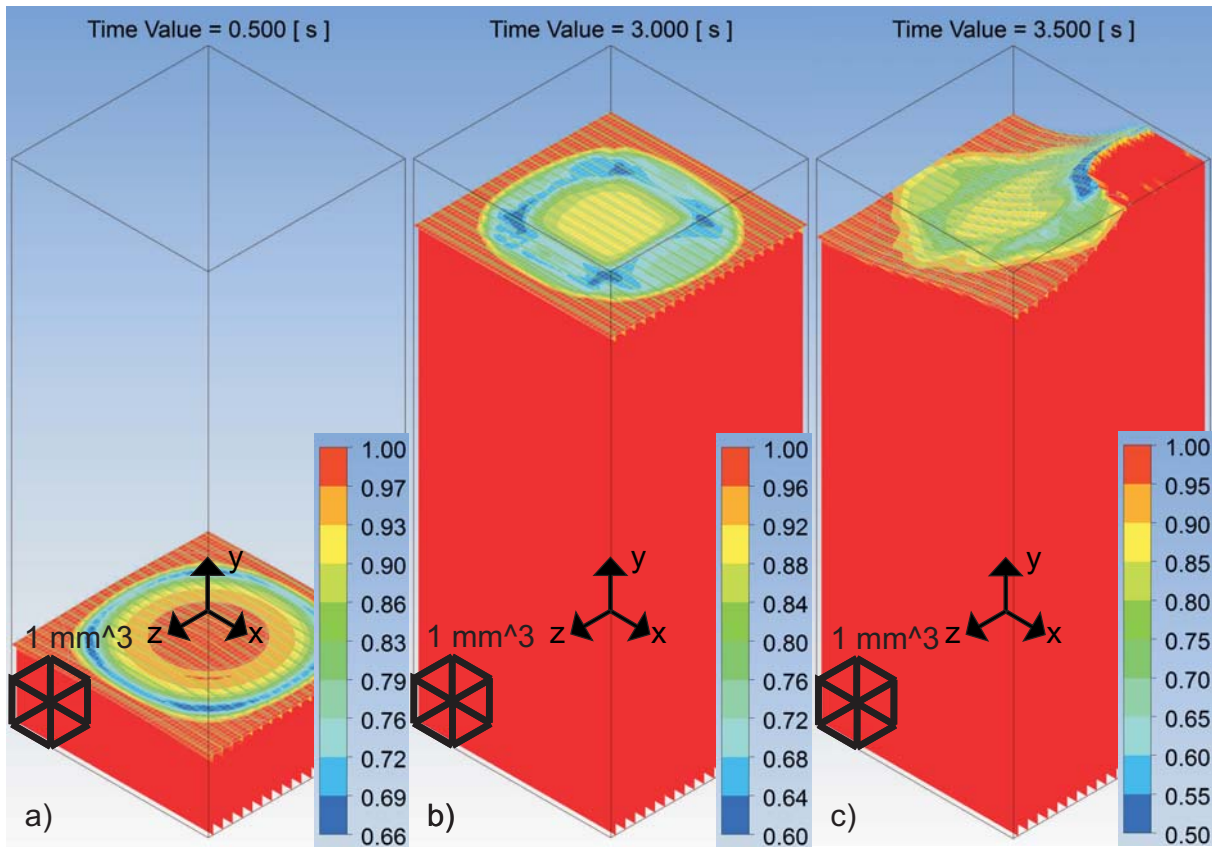


Figure 61: Screen-shot sequence of the total-liquid-fraction contour on an ISO-surface with 50 % volume fraction for the solidification steps with $v_{in} = 0.2 \frac{m}{s} K$

a) image showing an evenly filled tank with HTF with a stronger solidified curved area between centre and walls

b) image showing an almost completely filled tank with HTF and a wider and stronger solidified area between centre and walls

c) image showing an almost completely filled tank with HTF and a path to the outlet on the right corner with a completely solidified area on the top

$D12$, $PCM2$, $(x, y, z) = (5, 12.5, 5) mm$, $A_{in} = 4.6 \cdot 10^{-7} m^2$, $A_{out} = 25 m^2$,
Mesh: multi-zone, hexagonal, $0.1 mm$, $v_{in} = 0.2 \frac{m}{s}$, $A_{mush} = 10^5$, $\Delta T = -10 K$

A visualisation for $0.2 \frac{m}{s}$ in fig. 61 shows a total liquid fraction descending to the middle of the centre and the edges, reaching a square shaped area with curved edges of $0.2 mm$ with values down to 66% in fig. 61 a). The average PCM liquid fraction on this surface is at 74% .

In fig. 61 b) the area in the centre shows values of $90 \pm 2\%$, the coldest area increased to $0.7 mm$ with values down to 60% . The average PCM liquid fraction on this surface is at 66% .

Fig. 61 c) shows the coldest area with 50% at the top of the slope, with a width of $0.5 mm$, leaving out only $0.7 mm$ to the right edge on the front. The values in the centre decreased by 2% the values of it's surroundings increased to $70 \pm 5\%$. The average PCM liquid fraction on this surface is at 70% .

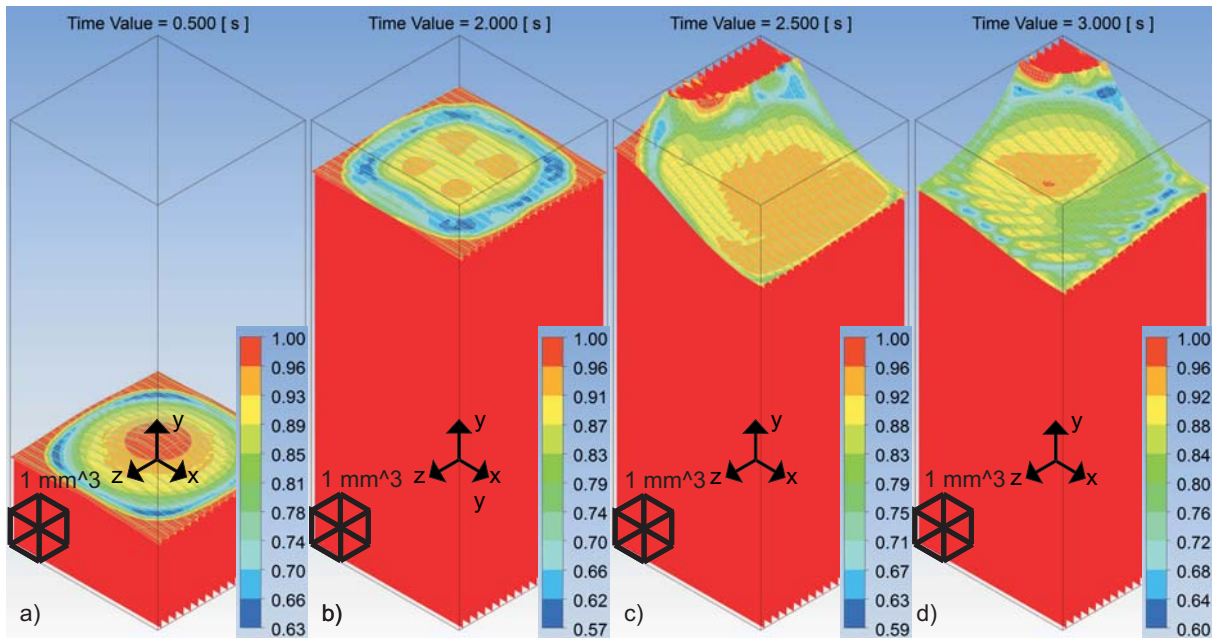


Figure 62: Screen-shot sequence of the total-liquid-fraction contour on an ISO-surface with 50 % volume fraction for the solidification steps with $v_{in} = 0.3 \frac{m}{s}$

a) image showing an evenly filled tank with HTF with a stronger solidified curved area between centre and walls

b) image showing an almost completely filled tank with HTF and a wider and stronger solidified area between centre and walls

c) image showing a path to the outlet at the left wall and the most solidified area on top

d) image showing a path to the outlet on the back corner with the most solidified area on the top D12, PCM2, $(x, y, z) = (5, 12.5, 5) \text{ mm}$, $A_{in} = 4.6 \cdot 10^{-7} \text{ m}^2$, $A_{out} = 25 \text{ m}^2$, Mesh: multi-zone, hexagonal, 0.1 mm , $v_{in} = 0.3 \frac{m}{s}$, $A_{mush} = 10^5$, $\Delta T = -10 \text{ K}$

The visualisation for $0.3 \frac{m}{s}$ in fig. 62 shows a total liquid fraction near 1 in a circular shape in the centre with a diameter of 1.6 mm and on the edges with 0.1 mm in the most narrow part in fig. 62 a). The value descends to the middle of the centre and the edges, reaching a square shaped area with curved edges of 0.3 mm with values down to 63%. The average PCM liquid fraction on this surface at 70%.

In fig. 62 b) the area in the centre shows values of $89 \pm 2\%$, for the most part, with four curved areas pointing to the centre, on the cross linking the edges to the centre, with values up to 96%. The coldest area increased to 0.7 mm with values down to 57%. The average PCM liquid fraction on this surface is at 56%.

Fig. 62 c) shows small areas near the slope down to 59%, and the main area in the range range of $94 \pm 2\%$. The average PCM liquid fraction on this surface is at 53%.

Fig. 62 d) shows the coldest area with 60% at the top of the slope and near the edges, composed out of small pieces with only a few cells. The value in the centre is still up to 96%, except to cells closer to 1, and it's surroundings have wider areas in the range of 80 ± 4 . The average PCM liquid fraction on this surface area is at 60%.

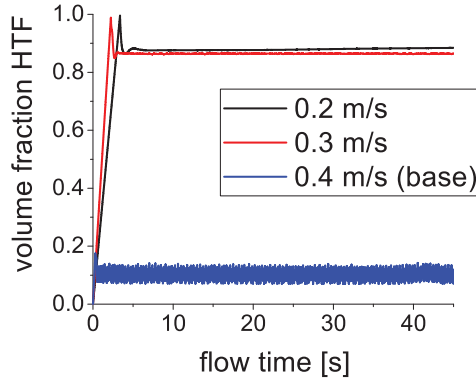


Figure 63: Volume-fraction for different inlet velocities

$D12$, $PCM2$, $(x, y, z) = (5, 12.5, 5) \text{ mm}$,
 $A_{in} = 4.6 \cdot 10^{-7} \text{ m}^2$, $A_{out} = 25 \text{ m}^2$,
 Mesh: multi-zone, hexagonal, 0.1 mm ,
 $v_{in} = (0.2, 0.3, 0.4(\text{base})) \frac{\text{m}}{\text{s}}$, $A_{mush} = 10^5$,
 $\Delta T = -10 \text{ K}$

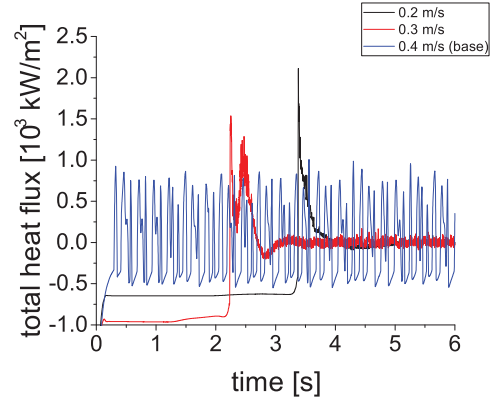


Figure 64: First 6 s of the heat flux for different inlet velocities

$D12$, $PCM2$, $(x, y, z) = (5, 12.5, 5) \text{ mm}$,
 $A_{in} = 4.6 \cdot 10^{-7} \text{ m}^2$, $A_{out} = 25 \text{ m}^2$,
 Mesh: multi-zone, hexagonal, 0.1 mm ,
 $v_{in} = (0.2, 0.3, 0.4(\text{base})) \frac{\text{m}}{\text{s}}$, $A_{mush} = 10^5$,
 $\Delta T = -10 \text{ K}$

$v_{in} [\frac{\text{m}}{\text{s}}]$	$l_{PCM} [\%]$				
	$t = 2.2 [\text{s}]$	$t = 2.7 [\text{s}]$	$t = 3.376 [\text{s}]$	$t = 4 [\text{s}]$	$t = 45.0 [\text{s}]$
0.2	66	85	100	86	88
0.3	99	79	87		86
0.4	10				

Table 26: Important values of the volume fraction for the calculations with $v_{in} = 0.2, 0.3 [\frac{\text{m}}{\text{s}}]$ in fig. 63. For comparison the value of the **base model** is **bold**. The calculation with $0.2 \frac{\text{m}}{\text{s}}$ shows a peak at 3.376 s , followed by a drop at 4 s and a slow rise until it's final value. The calculation with $0.3 \frac{\text{m}}{\text{s}}$ shows a peak at 2.2 s , followed by a drop at 2.7 s and a slow rise until it's final value

Fig. 63 shows the results for the volume fraction. It can be clearly seen that the values for $v_{in} = 0.2, 0.3 \frac{\text{m}}{\text{s}}$ show one peak at 3.376 s and 2.2 s to 100% and 99% , followed by a stagnation. The line for $v_{in} = 0.4 \frac{\text{m}}{\text{s}}$ shows a periodic behaviour for the whole 45 s , without any visible deviation. The important values can be seen in tab. 26.

$v_{in} [\frac{\text{m}}{\text{s}}]$	time range [ms]	$\bar{q} [\frac{\text{kW}}{\text{m}^2}]$		$T_{out} [\text{K}]$	$T_{in} [\text{K}]$	$\bar{A} [\text{m}^2]$
		Fluent	with (1)			
0.2	[4274;45000]	-4.8	-[16;3.2]	[277.62;275.68]	275.15	$2.5 \cdot 10^{-5}$
0.3	[2804;45000]	-1.5	-2.9	[278.17;278.16]	275.15	$2.5 \cdot 10^{-5}$
0.4	[295;45000]	-9.6	-20	≈ 279.15	275.15	$7 \cdot 10^{-5}$

Table 27: Average heat fluxes for different parts of all calculations in fig. 64, as well as the corresponding values for hand calculations, with the **base model** in **bold**.

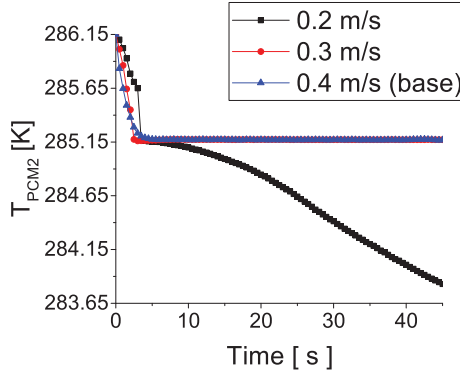


Figure 65: Average temperature of PCM2 for different inlet velocities

$D12$, $PCM2$, $(x, y, z) = (5, 12.5, 5) \text{ mm}$,
 $A_{in} = 4.6 \cdot 10^{-7} \text{ m}^2$, $A_{out} = 25 \text{ m}^2$,
 Mesh: multi-zone, hexagonal, 0.1 mm ,
 $v_{in} = (0.2, 0.3, 0.4(\text{base})) \frac{\text{m}}{\text{s}}$, $A_{mush} = 10^5$,
 $\Delta T = -10 \text{ K}$

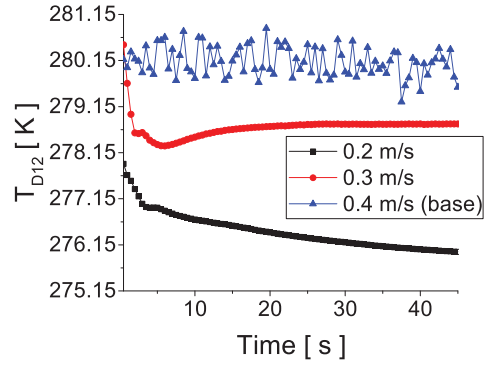


Figure 66: Average temperature of D12 for different inlet velocities

$D12$, $PCM2$, $(x, y, z) = (5, 12.5, 5) \text{ mm}$,
 $A_{in} = 4.6 \cdot 10^{-7} \text{ m}^2$, $A_{out} = 25 \text{ m}^2$,
 Mesh: multi-zone, hexagonal, 0.1 mm ,
 $v_{in} = (0.2, 0.3, 0.4(\text{base})) \frac{\text{m}}{\text{s}}$, $A_{mush} = 10^5$,
 $\Delta T = -10 \text{ K}$

Fig. 64 shows the results for heat flux. It can be clearly seen that the values for $v_{in} = 0.2, 0.3 \frac{\text{m}}{\text{s}}$ shows peaks. The calculation with $v_{in} = 0.2 \frac{\text{m}}{\text{s}}$ shows one at 3.3 s with $q = 2.1 \frac{\text{MW}}{\text{m}^2}$, the $v_{in} = 0.3 \frac{\text{m}}{\text{s}}$ shows the main peak at 2.3 s with $q = 1.5 \frac{\text{MW}}{\text{m}^2}$ and a second peak at 2.4 s with $q = 1.2 \frac{\text{MW}}{\text{m}^2}$. The values of the following stagnation part, as well as corresponding hand calculations can be seen in tab. 27.

$v_{in} [\frac{\text{m}}{\text{s}}]$	t [s]		$T_{PCM2} \text{ K}$ t=45 s
	reaching 285.17 K	reaching 285.13 K	
0.2	3.5	7.5	283.83
0.3	2.5	> 45	285.17
0.4	5.0	> 45	285.17

Table 28: Time range of the PCM temperature that it stays near the solidification temperature, the time step it reaches the inlet temperature and the final temperature for all calculations in fig. 65, with the **base model** in **bold**.

The PCM temperature plot in fig. 49 shows that $v_{in} = 0.2, \frac{\text{m}}{\text{s}}$ shows a linear decrease, followed by a plateau between 3.5 s and 7.5 s before decreasing further, reaching a linearity after about 20 s . The calculations with $v_{in} = 0.3, 0.4 \frac{\text{m}}{\text{s}}$ have one nearly linear decrease, followed by a stagnation part. The important values are listed in tab. 18.

The average HTF temperature in fig. 66 shows that the $0.2 \frac{\text{m}}{\text{s}}$ line cools linearly to 276.97 K after 3.5 s , where it stays constant for 1.5 s . The temperature continuous to

decrease slowly until reaching it's final value of 275.99 K. The $0.3 \frac{\text{m}}{\text{s}}$ line cools linearly to 278.58 K after 2.0 s, where it stays constant for 1.0 s. A slow drop to 278.29 K is reached at 6 s followed by a slow increase until reaching it's final value of 278.70 K.

Discussion

Both calculations show no droplet formation at all and only one of them shows solidification to a sufficient extent. Furthermore the results of both calculations are similar to each other, leaving out the necessity of describing each calculation isolated from each other. The liquid fraction shows the same behaviour, although with slightly different peaks. (Fig. 60 and tab. 60) Due to the saving interval of 0.5 s the peak could only be resolved for the higher velocity. As results are similar it can be assumed with high chance that the origin of this peak is the same for both calculations.

The peak matches the volume fraction peak with a precision of 0.01 s. (Fig. 63 and tab. 63) This shows also, that the HTF pushes out most of the PCM in the tank.

An image series of the total liquid fraction on the ISO-surface for 50% volume fraction can be seen in fig. 61 and 62. In both calculations the HTF fills the tank continuously, however for the higher velocity a better try of a droplet formation can be seen. This contradicts the results of fig. 10, where a stream with 3 mm length should appear for $0.2 \frac{\text{m}}{\text{s}}$ and 8 mm length for $0.3 \frac{\text{m}}{\text{s}}$. The discrepancies in the value can probably be related to the different materials properties used. Nevertheless not even the qualitative impression is the same. This can be explained as a combination of the relatively low velocity and the contact angle of 30° . The calculation with slower velocity needs more time to reach the outlet, leading to peaks more on the right than for the higher velocity.

This goes also for the heat flux shown in fig. 64. The simulation with the faster velocity has two peaks close to each other, which could not be resolved due to the saved time interval. It is interesting to note that HTF flow is different, when reaching the outlet. The final images are similar, but on different positions of the tank. This behaviour cannot be explained, as small changes in the flow could not be resolved. However, there appears to be great similarity in the visualisation of the beginning steps. The value for 5.5 s for the slower velocity, where stagnation is reached, is at 32% and for comparison at 62% for the higher velocity, at the same time. These values go well with the liquid fraction over the complete model and show that the $0.3 \frac{\text{m}}{\text{s}}$ calculation solidifies faster at the beginning, but keeps it's state after 3 s, whereas the $0.2 \frac{\text{m}}{\text{s}}$ calculation is able to reach a state of solidification eventually.

This can also be seen in the PCM temperature plot in fig. 65 and tab. fig. 28. The higher velocity follows a similar path as the base calculation, although the flow is completely different. The slower velocity, on the other hand, shows a short latent state before it continues to cool further, matching the values discussed earlier. These observations seem to contradict each other and could not be resolved.

An interesting feature is visible for the HTF temperature in fig. 66. While the slower velocity calculation cools down as expected, the graph for the higher velocity shows a short

cool down, followed by heating and a stagnation. This trend should not be possible. The temperature should cool down over time. Furthermore the PCM temperature is staying constant during this time. The back flow can also be ruled out as the volume fraction stays constant. It could be possible that the HTF is taking some energy from the outlet boundary settings but then the change would be continuous through the whole calculation. In other words this short heating can not be explained without further investigation.

7.5 Results Summary

A summary of the resulting liquid fraction, volume fraction, heat fluxes and heat transfer coefficients is placed in tab. 29, 30 and 31 for efficient comparison.

A_{mush} [%]	l_{PCM} [%]	v_{HTF} [%]	\bar{q} [$\frac{kW}{m^2}$]
10^1	90	10	-9.8
10^4	90	10	-9.5
10^5	90	10	-9.6
10^6	74, 62	27, 32	-17.2, -5.0
10^9	0	97	-3.2

Table 29: Results (final liquid fraction and volume fraction, as well as average heat flux) for the variations of the mushy parameter. For all calculations that change in their behaviour, e.g. a periodic part and a stagnation part, the results will be given in chronological order for each part.

ΔT K	l_{PCM} [%]	v_{HTF} [%]	\bar{q} [$\frac{kW}{m^2}$]
-1	99	15	-5.4
-5	95	12	-7.8
-10	90	10	-9.6
-15	64, 53, 45.5 ± 2.0	13, 41, 34 ± 4	-16.6, -17.5, -2.6
-20	85, 11	75, 85	-745.8, -10.2

Table 30: Results (final liquid fraction and volume fraction, as well as average heat flux) for the variations of the temperature. For all calculations that change in their behaviour, e.g. a periodic part and a stagnation part, the results will be given in chronological order for each part.

v_{in} $\frac{m}{s}$	l_{PCM} [%]	v_{HTF} [%]	\bar{q} [$\frac{kW}{m^2}$]
0.2	32	88	-4.8
0.3	12	86	-1.5
0.4	90	10	-9.6

Table 31: Results (final liquid fraction and volume fraction, as well as average heat flux) for the variation of the velocity. For all calculations that change in their behaviour, e.g. a periodic part and a stagnation part, the results will be given in chronological order for each part.

8 Conclusion and Outlook

Early calculations shows qualitatively high results for the droplet formation of D12 in tank of $5 * 12.5 * 5 \text{ mm}^3$, with $d_{in} = 0.08 \text{ mm} = d_{out}$, filled with H_2O , when working with a time step size of $\Delta t \approx \frac{40 \text{ s}}{3 \text{ m}} \Delta x$. A detailed analysis of the data for $\Delta x = 0.3, 0.1 \text{ mm}$ (12,138 and 312,500 cells) reveals that, while the results of the wider mesh experience similar behaviour, the surface area for 0.1 mm is 24% higher during the droplet formation and 52% higher after the solidification. The volume fraction has more and unsteady steps for 0.3 mm and reaches a value of 30% lower than the the higher mesh size of 0.1 mm. Nevertheless the resulting liquid fraction is higher by only 9%. This means that the 0.3 mm mesh can be used for qualitative evaluations if the simulation has to be done in short time. When data for quantitative use is necessary, a higher mesh size, such as 0.1 mm, has to be set. A much higher mesh size is not recommended as it drastically increases the calculation time.

The heat flux shows the expected results when working with an outlet of $r_{out} = 0.4 \text{ mm}$. The model size with $(x, y, z) = (5, 12.5, 5) \text{ mm}$ was big enough for one D12 droplet in H_2O and small enough for minimizing necessary computer resources. Due to the higher density and viscosity of water-TBAB it was necessary to adapt the model, as no droplet formation could be visible and PCM partly blocked the outlet at times. The final value used therefore had a decreased contact angle at the bottom, to shorten the incoming stream, and a complete open top to prevent solidification of PCM at the outlet.

Due to the increase in the outlet area to the complete extent of the wall the outlet heat flux not only stays positive for outgoing HTF but surpasses the inlet heat flux in its value, reaching to a positive total heat flux. The energy equilibrium is therefore not full-filled any- more, as the HTF gains additional energy when leaving through the outlet. Therefore, the results are, while physically correct when considering additional heating from the outside, impracticable for comparison with other simulations or experimental results, for the most part, as no possible solution was found for splitting the values for each material. As the error only applies when HTF is leaving the tank the average heat flux is still negative and allows the PCM to cool-down, although much slower than it would in a real life experiment. This resulted calculations with $A_{mush} = 10^6, \Delta T = -15 \text{ K}$ achieving a sufficient solidification. Both show temperature plots composed of two sensible parts, one before and one after the latent heat part. While the $A_{mush} = 10^6$ calculation reaches a sufficient solidification faster and even shows the correct negative heat flux after the main solidification process, on a global scale the $-\Delta T = -15$ calculation solidifies faster. Nevertheless the later showed an unstable solidification in the last few seconds, due to the heating from the outside.

A comparison with the experimental results of Anmann in [9] and presented in sec. 3 it becomes clear that simulations follows a different behaviour. No solidification blocking the inlet was visible. Also the PCM2 did not get porous and no HTF parts got surrounded

by ice floating to the top. The only effect that came close to the experimental results was the small PCM parts with $A_{mush} = 10^9$ that were surrounded by HTF, although this is far from the emulsion of small water droplets with ADX 10. This discrepancy could be related to the small geometry modelled but also origin in the model specific problems discussed in the last paragraph.

For future research this means that, when using water-TBAB, the model still has to be further adapted in two ways: Firstly, not all material parameters were used in this simulation, secondly, the complete outlet at the top face resulted in a false and high positive heat flux, due to the back-flow condition.

There are three possibilities of overcoming the second problem. One could simply use a higher geometry with an outlet, big enough to prevent blocking by PCM but small enough to minimize the effect of the boundary conditions. This was not done in this project, as the initial testing consumed the time available for creating the model and the parameter study had yet to be done. Another possibility would be to place an additional layer on top of the PCM, so that the air can take over the back-flow part. This should minimize the heat flux effect on the PCM. Another solution would be to set the model size in a way that the volume stays constant the whole time. Theoretically, when the volume flow stays constant or is increasing, no back-flow and therefore no additional heat flux should occur. This was shown in the final steps after achieving solidification in the simulation with $A_{mush} = 10^6$.

As only each 0.5 s has been saved in order to minimize storage space but the calculations with $A_{mush} = 10^9$ and $v_{in} = (0.2, 0.3) \frac{m}{s}$ solidified in the first few seconds to a great extend, the complete fluid-dynamic and thermodynamic behaviour could not be explained, due to missing resolution. This is why, they should be redone with a higher saving interval.

Appendices

A Data Sheet for Therminol D12

Produktinformation

FRAGOL

THERMINOL®* D12

Wärmeträgerflüssigkeit
-85°C bis 230°C

Anwendung

THERMINOL® D12 ist eine Wärmeträgerflüssigkeit, die speziell für das Heizen und Kühlen verfahrenstechnischer Anlagen entwickelt wurde. Es eignet sich besonders für Anwendungen in der pharmazeutischen Industrie und in Klimakammern.

THERMINOL® D12 ist für Betriebstemperaturen von -85°C bis 190°C in drucklosen Systemen und bei Überlagerung mit einem geeigneten Systemdruck bis 230°C ausgelegt.

THERMINOL® D12 kann als Einzelflüssigkeit in kombinierten geschlossenen Systemen für den gesamten Aufheiz- und Kühlbedarf benutzt werden. Dies ist ein bedeutender Vorteil verglichen mit dem „Zweiflüssigkeits“-Konzept, z.B. Dampf/Sole oder Dampf/Wasser-Glykol, bei dem ein Spülen zwischen den Zyklen unerlässlich ist.

THERMINOL® D12 bleibt bei Temperaturen bis -85°C gut pumpfähig. Die häufig bei Chargensystemen auftretenden Anfahrprobleme entfallen; eine Dampf- oder Elektro-Begleitheizung ist nicht erforderlich.

Qualität

THERMINOL® D12 ist eine synthetische Wärmeträgerflüssigkeit auf der Basis von aliphatischen Kohlenwasserstoffen.

Die chemische Zusammensetzung der Wärmeträgerflüssigkeit THERMINOL® D12 wurde sorgfältig ausgewählt, um die Bildung von Niedersiedern zu minimieren und die Bildung von unlöslichen Hochsiedern sowie Fouling zu vermeiden. Voraussetzung für eine lange Lebensdauer der Wärmeträgerflüssigkeit ist eine sorgfältige Auslegung der Anlage und die Einhaltung der empfohlenen maximalen Vorlauf- und Filmtemperaturen.

THERMINOL® D12 wirkt nicht korrosiv auf Kohlenstoffstähle und andere in Wärmeträgeranlagen verwendete Metalllegierungen. Es enthält keine Halogene und gilt als eine ungefährliche und für die Umwelt praktisch unschädliche Flüssigkeit.

Die Grundflüssigkeit von THERMINOL® D12 entspricht folgenden FDA Anforderungen:

FDA – 21 CFR 172.882

FDA – 21 CFR 172.884

FDA – 21 CFR 178.3530

FDA – 21 CFR 178.3650

Verpackung

THERMINOL® D12 ist standardmäßig in Stahlfässern zu 155 kg und in Kanistern zu 15,4 kg verfügbar.

Hinweise

Beim Umgang mit dem Produkt ist das Sicherheitsdatenblatt zu beachten.

Bitte sprechen Sie uns an, wenn Sie weitergehende Informationen oder eine allgemeine technische Beratung wünschen.

Eigenschaften

THERMINOL® D12			Methode
Dichte @ 20°C	[kg/m³]	762	
Viskosität @ 40°C	[mm²/s]	1,24	
Viskosität @ 100°C	[mm²/s]	0,64	
Pourpoint	[°C]	<-85	ISO 3016
Flammpunkt	[°C]	62	EN 22719
Siedepunkt @ 1013 mbar	[°C]	192	
Filmtemperatur max.	[°C]	245	
Vorlauftemperatur max.	[°C]	230	
Wassergefährdungsklasse	[-]	1	
Gefahrgut	[-]	nein	

30008dQb

Alle Informationen erfolgen nach bestem Wissen. Jegliche Rechtsverbindlichkeit für den Inhalt dieser Information und die Eignung des Produkts für bestimmte Anwendungen wird abgelehnt. Technische Daten sind ca.-Werte und unterliegen den üblichen Produktionsschwankungen.

FRAGOL GmbH+Co. KG, Solinger Straße 16, D - 45481 Mülheim, Tel.: +49 (0)208 30002-50, waermetraeger@fragol.de

www.FRAGOL.de

Produktinformation

FRAGOL

THERMINOL®* D12

Temp. °C	Dampfdr. kPa(abs)	Dichte kg/m³	Spez. WK kJ/kgK	Wärmeleitf. W/mK	Visk. (kin) mm²/s	Visk. (dyn) mPas	Prandtl- Zahl
-85		835	1,635	0,124	354,35	295,88	3901,30
-70		824	1,714	0,122	71,50	58,92	827,72
-60		818	1,759	0,121	29,25	23,92	347,76
-50		811	1,805	0,119	14,89	12,07	183,15
-40		804	1,850	0,118	8,78	7,06	110,67
-30		797	1,895	0,117	5,77	4,59	74,42
-20		790	1,941	0,116	4,09	3,23	54,12
-10		783	1,989	0,114	3,08	2,41	42,04
0		776	2,025	0,113	2,49	1,93	34,57
10		769	2,065	0,111	2,03	1,56	29,04
20		762	2,108	0,110	1,70	1,29	24,78
30		756	2,154	0,108	1,44	1,09	21,67
40	0,3	748	2,197	0,107	1,24	0,93	19,03
50	0,5	740	2,235	0,105	1,09	0,80	17,12
60	0,9	733	2,280	0,104	0,96	0,70	15,43
70	1,4	726	2,326	0,102	0,86	0,62	14,20
80	2,3	717	2,361	0,100	0,78	0,56	13,12
90	3,9	710	2,406	0,098	0,70	0,50	12,24
100	6,0	702	2,445	0,096	0,64	0,45	11,48
110	8,7	695	2,485	0,095	0,59	0,41	10,73
120	12,4	687	2,528	0,093	0,55	0,37	10,18
130	17,6	679	2,571	0,091	0,51	0,35	9,76
140	24,4	670	2,607	0,089	0,47	0,32	9,28
150	33,2	662	2,645	0,087	0,44	0,29	8,80
160	44,3	653	2,690	0,085	0,41	0,27	8,47
170	58,2	644	2,725	0,083	0,38	0,25	8,08
180	75,4	635	2,773	0,081	0,36	0,23	7,91
190	95,7	625	2,806	0,079	0,35	0,22	7,66
200	122,3	615	2,857	0,076	0,33	0,20	7,56
210	146,6	607	2,883	0,074	0,31	0,19	7,35
220	186,7	596	2,928	0,072	0,29	0,17	7,10
230	228,7	585	2,971	0,070	0,28	0,16	6,88
240	276,8	574	3,009	0,067	0,27	0,15	6,91
250	320,2	562	3,045	0,065	0,26	0,15	6,82
260	396,2	550	3,100	0,063	0,25	0,14	6,77

* Therminol® is a registered trademark of Eastman Chemical Company or its subsidiaries.

Alle Informationen erfolgen nach bestem Wissen. Jegliche Rechtsverbindlichkeit für den Inhalt dieser Information und die Eignung des Produkts für bestimmte Anwendungen wird abgelehnt. Technische Daten sind ca.-Werte und unterliegen den üblichen Produktionsschwankungen.

FRAGOL GmbH+Co. KG, Solinger Straße 16, D - 45481 Mülheim, Tel.: +49 (0)208 30002-50, waermetraeger@fragol.de

www.FRAGOL.de

B Model choosing process

B.1 Geometry and mesh

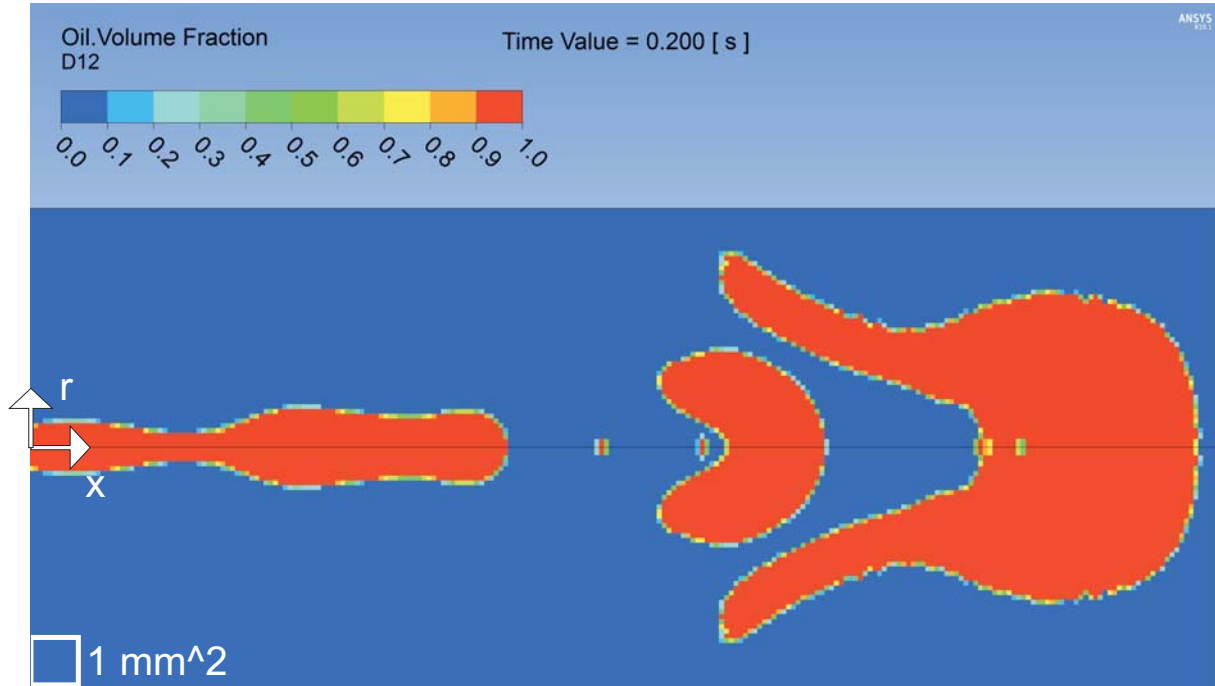


Figure 67: Droplet formation of D12 in water in a 2D axisymmetric model

$r = 5\text{mm}$, $x = 25\text{mm}$, $r_{in} = 0.4\text{mm} = r_{out}$, edge mesh sizing of 0.1mm

$$\text{time-step-size } 0.001\text{ s}, \quad \vec{g} = \begin{pmatrix} x \\ y \\ z \end{pmatrix} = \begin{pmatrix} 0 \\ -9.81 \\ 0 \end{pmatrix} \frac{\text{m}}{\text{s}^2}$$

The original model was based upon a 1:80 model of an experimental setup as used in the preliminary real life experiments by Krimmel [19] and resulted in the following geometry: $((x, y) = (2.5, 7.46)\text{mm}$ and $d_{in} = 0.08\text{mm} = d_{out}$), excluding the nozzle part and the outlet tube. In the intention of achieving short calculation times it was tried to work in 2D space. The first tries had to be done on a notebook. The calculations had therefore to run in a few hours time frame on an Intel Core i7-4720HQ, an Nvidia GeForce GTX 960M and 16 GB of RAM. This worked well for the 2D axisymmetric simulations, but bigger 3D models could not be calculated due to the limited amount of resources. Therefore a considerably amount of time had to be invested in finding the right model. The calculations were done with different materials and boundary settings but all of them resulted in some kind of even jet. After a couple of tries without any droplet formation the geometry was changed to 2D-axisymmetric $((r, y) = (1.25, 10)\text{mm}$, resulting in a droplet shaped tip at the end of the stream. The height was adapted to the complete tank, including the nozzle and the outlet tube, for simplification. As the model was too small, the droplet could not detach. The length of all edges, as well as inlet and outlet diameter, was therefore

increased by a factor 10, resulting in the formation of multiple droplets. The droplet shape did, however, not correlate with existing theory, as discussed in [14]. It is not even close to circular, elliptic or cone shaped, but some kind of rotation-symmetric jellyfish-like shape. Also noticeable was that the droplet changed its form during the flow, due to interaction with faster droplets, that were formed later, amongst other things. In order to limit the necessary resources for calculations, especially when adding the 3rd dimension to correct the droplet shape, the model size was reduced accordingly in 2D-axisymmetric. The result of one of this models reduced in size is presented in fig. 67.

The first 3D model with D12 in water-TBAB with an inlet velocity of $0.4 \frac{m}{s}$ that could be achieved with relevant data had the dimensions of $(x, y, z) = (10, 25, 10)$ mm. An approximation of the jet size was done and the model could be resized to $(x, y, z) = (5, 10, 5)$ mm. The latter represents basically the geometry that was used for further calculations. The result of two such calculations with the same mesh, boundary conditions and time-step-size at the same time of 0.150 s is compared in fig. 68. A comparison shows differences in the droplet formation originating in size and resolution from the cross-section view of 3D simulations.

Fig. 68 a) is from a $(x, y, z) = (10, 25, 10)$ mm model, while fig. 68 b) and c) belong to a smaller $(x, y, z) = (5, 10, 5)$ mm geometry. One interesting effect is noticeable. While the left model seems to already exceed the height of the smaller model, although this accounts only cells below 50 % HTF volume fraction, the droplet of the smaller model fits perfectly into the geometry. This could be the result of the boundary conditions, which can be reached faster by the droplet in the smaller model, and therefore come to effect earlier and on a greater scale. Geometric measurements are listed in tab. 32. For $\Delta x = 0.3$ mm the jets are identical, while the droplets are very similar.

A calculation of an additional 0.050 s led to a disappearance of the similarity between these two results. While the jet of the bigger geometry still had enough space to unfold, the stream in the smaller geometry collided with the top wall and hence it could be overtaken by the following droplet, that had still been in the process of release from the stream.

Fig. 68 c) shows the same simulation as fig. 68 b), although with higher resolution, $\Delta x = 0.1$ mm compared to $\Delta x = 0.3$ mm. The stream shows a thick part at the end, presumably a droplet shortly before its formation. The final geometry had to be adapted to $(x, y, z) = (5.0, 12.5, 5.0)$ mm in order to compensate for this unwanted effect.

It was tried to reduce the cross section further resulting in a hindered droplet formation due to the closeness to the wall at ≈ 0.14 s making this geometry unusable.

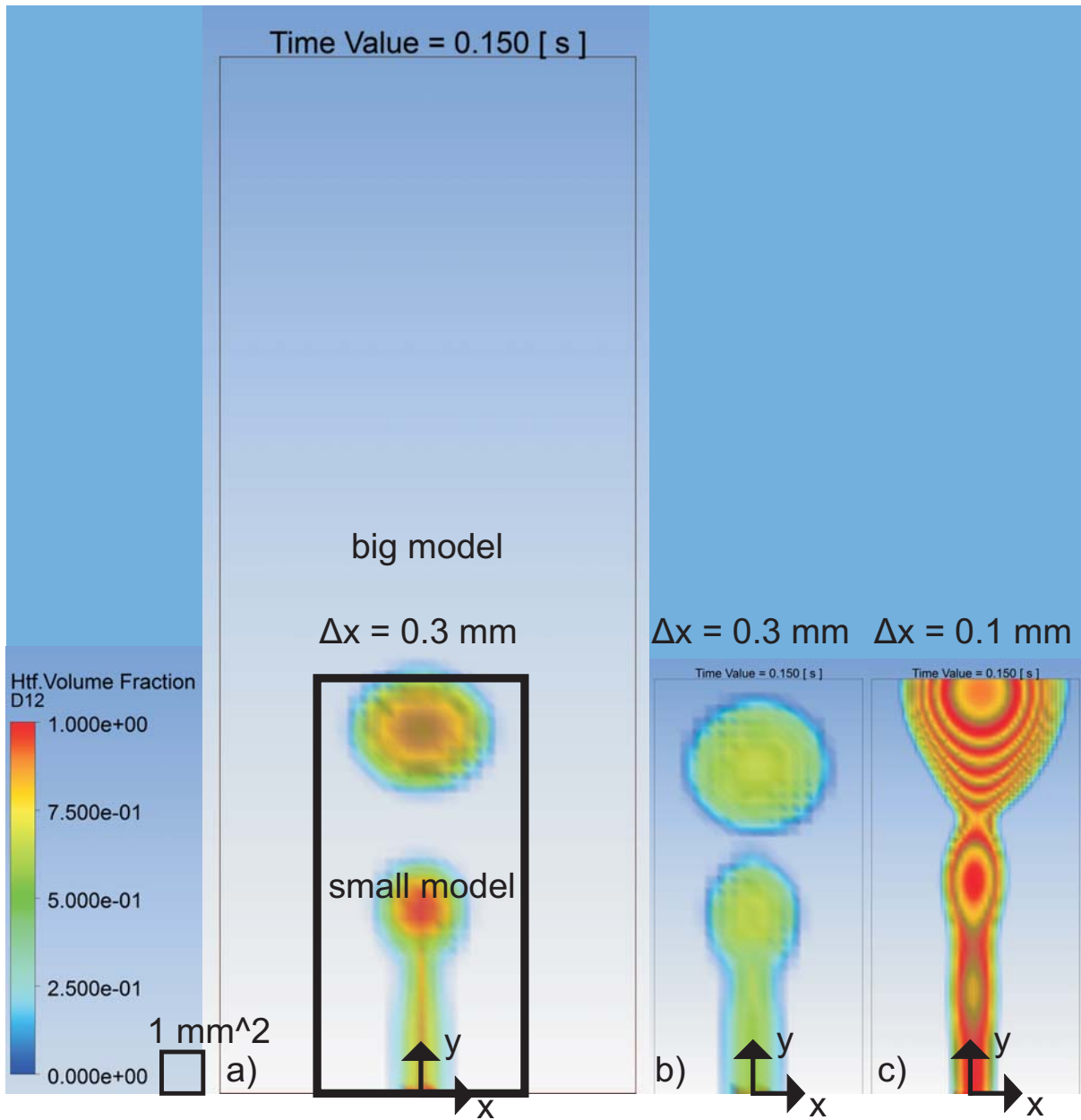


Figure 68: IDroplet formation for different geometry and Δx

a) big model ($(x, y, z) = (10, 25, 10) \text{ mm}$) with $\Delta x = 0.3 \text{ mm}$

b) small model ($(x, y, z) = (5, 10, 5) \text{ mm}$) with $\Delta x = 0.3 \text{ mm}$

c) small model ($(x, y, z) = (5, 10, 5) \text{ mm}$) with $\Delta x = 0.1 \text{ mm}$

D12, PCM2, $r_{in} = 0.4 \text{ mm} = r_{out}$, time-step-size 1 ms , time-step shown 0.15 s

model size (x, y, z) [mm]	Δx , [mm]	droplet size (x, y) [mm]	jet length y mm
10, 25, 10	0.3	3.0, 2.4	5.4
5, 10, 5	0.3	2.7, 2.4	5.4
5, 10, 5	0.1	none	≥ 10

Table 32: Geometric measurements of fig. 68

B.2 time-step-size

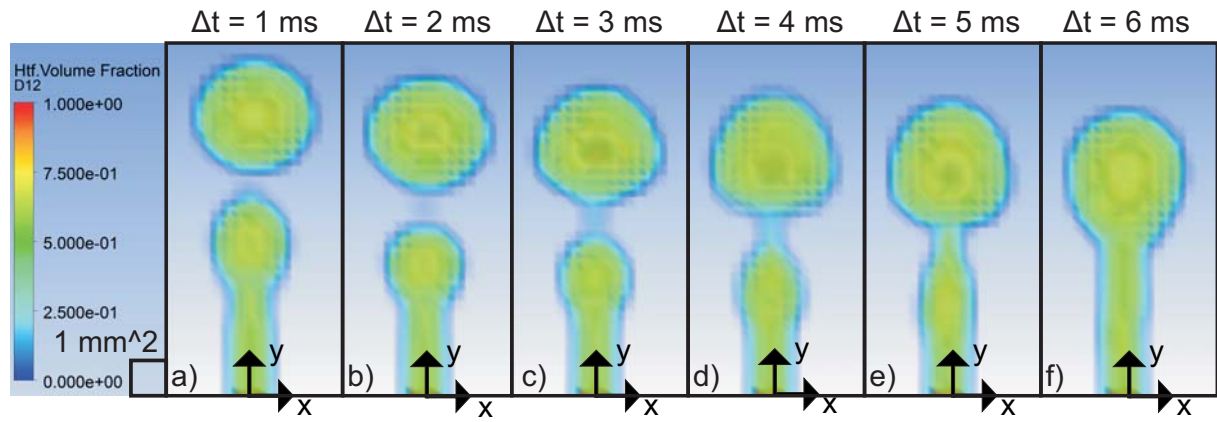


Figure 69: Front view ($z = 5 \text{ mm}$) of the same calculation at the same time for different Δt
a) $\Delta t = 1 \text{ ms}$, b) $\Delta t = 2 \text{ ms}$, c) $\Delta t = 3 \text{ ms}$, d) $\Delta t = 4 \text{ ms}$, e) $\Delta t = 5 \text{ ms}$, f) $\Delta t = 6 \text{ ms}$
D12, PCM2, $(x, y, z) = (5, 12.5, 5) \text{ mm}$, $r_{in} = 0.4 \text{ mm} = r_{out}$, Mesh: multi-zone, hexagonal, 0.1 mm
time-step shown 0.15 s

$\Delta t [\text{ms}]$	droplet size $(x, y) [\text{mm}]$	jet length $y \text{ mm}$
1	2.7, 2.4	3.3
2	2.7, 2.4	2.7
3	2.7, 2.4	2.4
4	2.7, 2.7	2.1
5	none	8.1
6	none	7.8

Table 33: Geometric measurements of fig. 69

Multiple simulations with the same geometry and mesh were done with different time-step sizes. An analysis of fig. 69 shows differences in the droplet formation originating in time-step size from the cross-section view of 3D simulations, listed in tab. 33. While the droplet sizes are identical for $\Delta t = [1; 3] \text{ ms}$ and similar for 4 ms), as well as the distances between drops and jets for $\Delta t = [1; 4] \text{ ms}$ there are greater differences in the size of the streams. It can be seen that the stream is shorter and more narrow for higher time-step sizes. For $\Delta t = 5 \text{ ms}$ the droplet doesn't detach any more. An additional calculation with $\Delta t = 6 \text{ ms}$ resulted in a more even stream. Due to the small differences up to $\Delta t = 4 \text{ ms}$ all further calculations were done with a time-step size of $\Delta t \leq \frac{40 \text{ s}}{3 \text{ m}} \Delta x$. The value actually used was favoured in a way that a data point could be achieved at exactly each second.

C Full Scale Diagrams of the parameter study

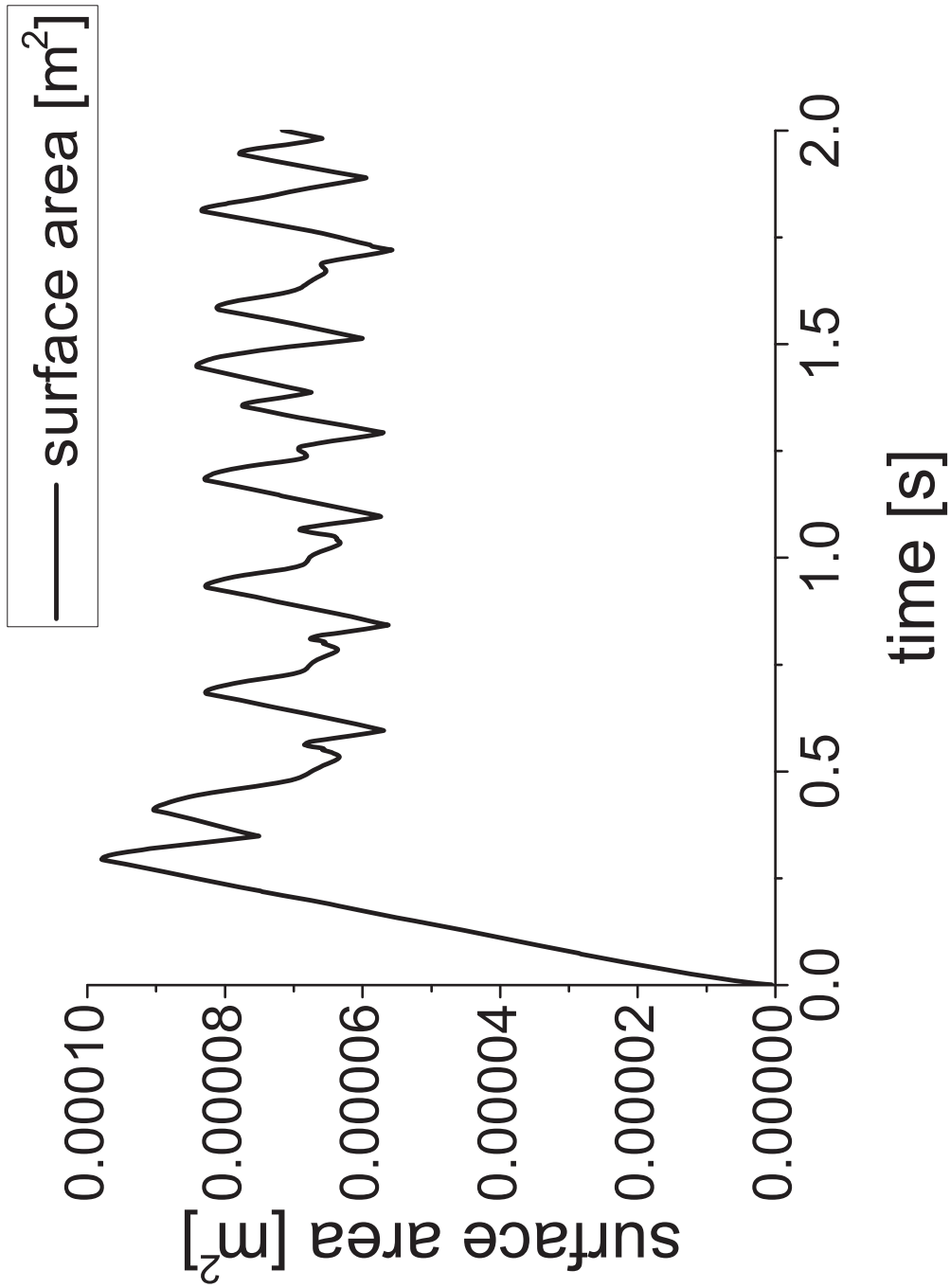


Figure 70: First 2 s of the surface area for the base model

$(x, y, z) = (5, 12.5, 5) \text{ mm}$, $A_{in} = 4.6 \cdot 10^{-7} \text{ m}^2$, $A_{out} = 25 \text{ m}^2$, Mesh: multi-zone, hexagonal, 0.1 mm , PCM2, $A_{mush} = 10^5$, $\Delta T = -10 \text{ K}$, $v_{in} = 0.4 \frac{\text{m}}{\text{s}}$

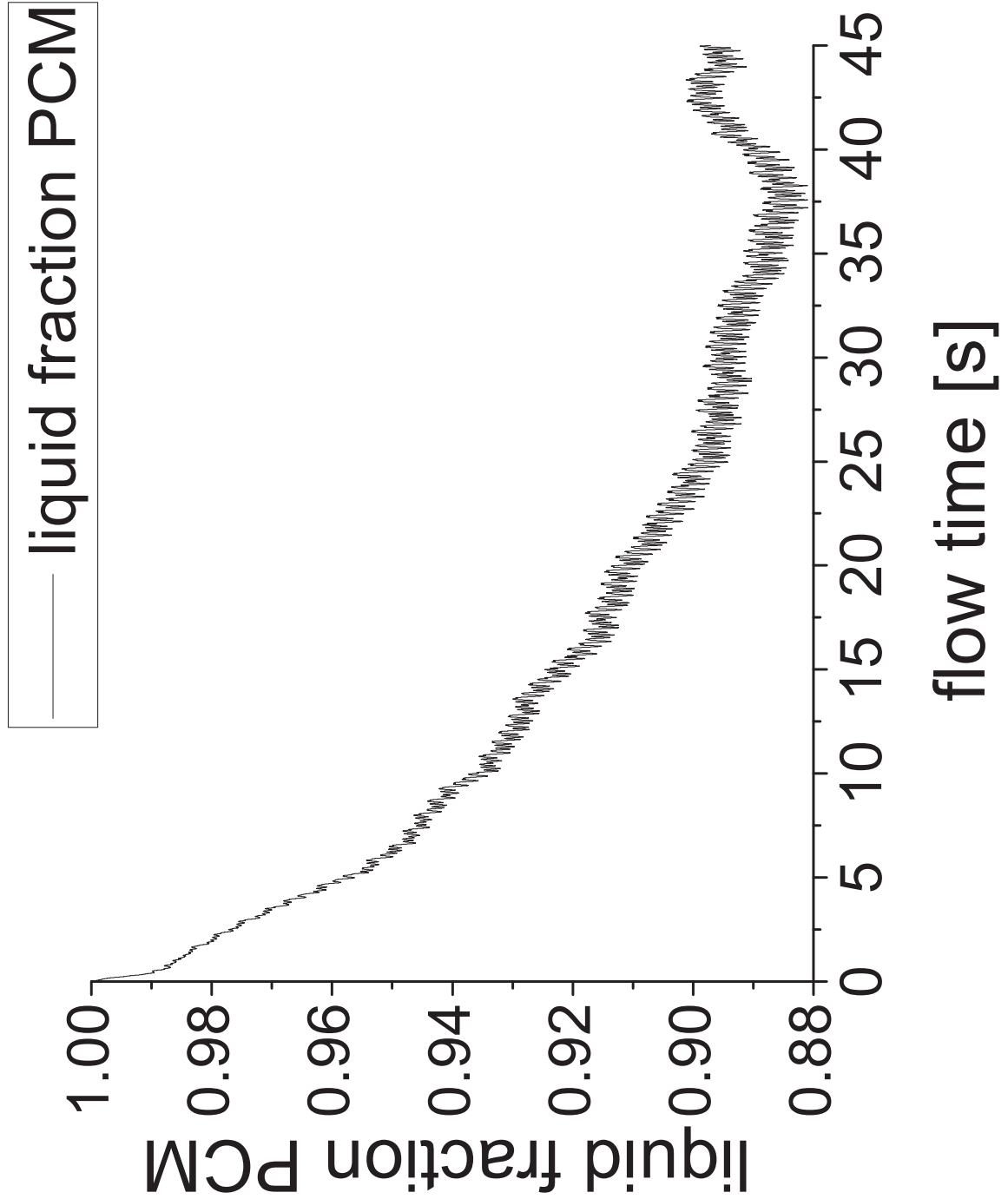


Figure 71: Liquid-fraction for the base model

$(x, y, z) = (5, 12.5, 5) \text{ mm}$, $A_{in} = 4.6 \cdot 10^{-7} \text{ m}^2$, $A_{out} = 25 \text{ m}^2$, Mesh: multi-zone, hexagonal, 0.1 mm , PCM2, $A_{mush} = 10^5$, $\Delta T = -10 \text{ K}$, $v_{in} = 0.4 \frac{\text{m}}{\text{s}}$

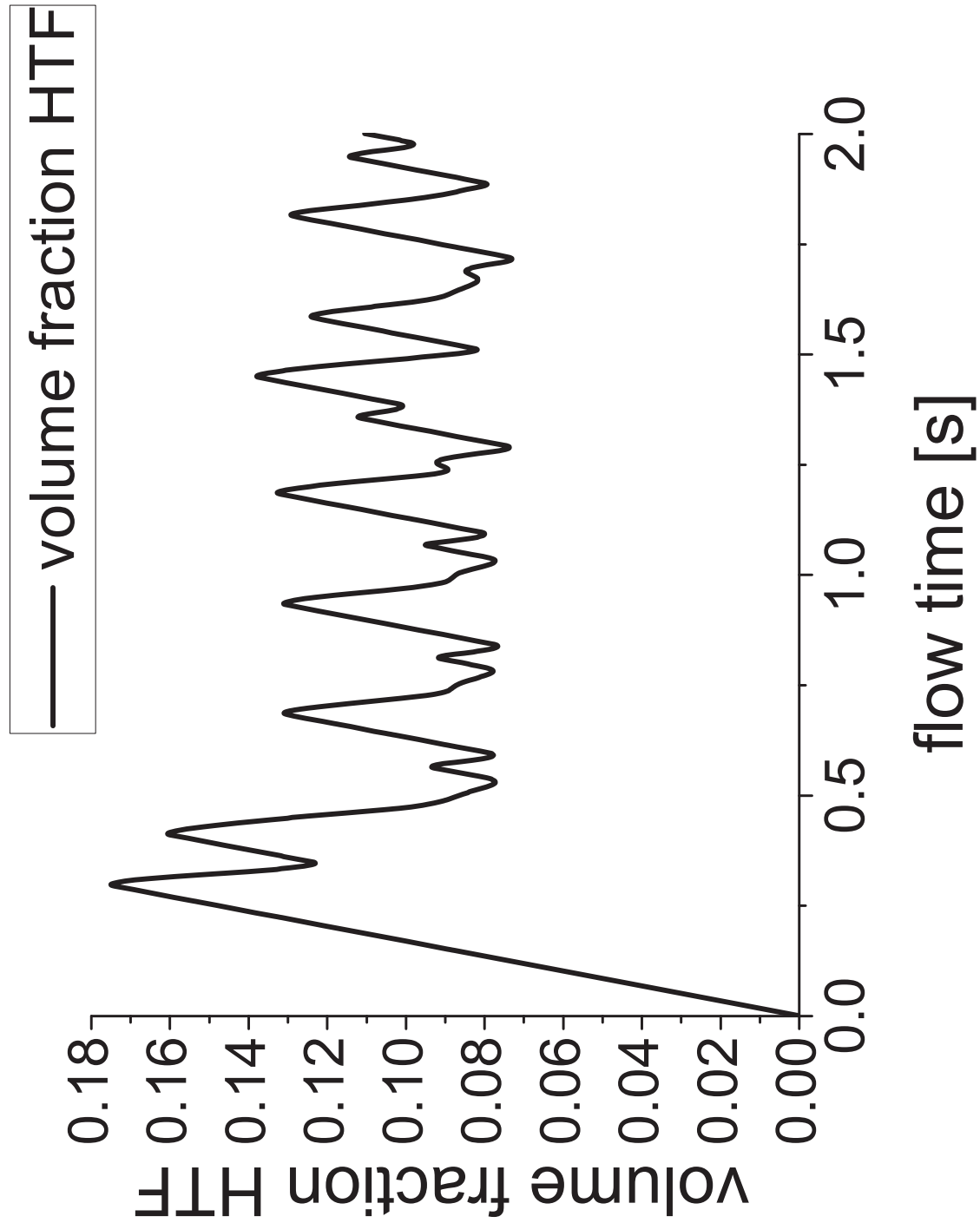


Figure 72: First 2s of the volume-fraction for the base model

$(x, y, z) = (5, 12.5, 5) \text{ mm}^3$, $A_{in} = 4.6 \cdot 10^{-7} \text{ m}^2$, $A_{out} = 25 \text{ m}^2$, Mesh: multi-zone, hexagonal, 0.1 mm , PCM2, $A_{mush} = 10^5$, $\Delta T = -10 \text{ K}$, $v_{in} = 0.4 \frac{\text{m}}{\text{s}}$

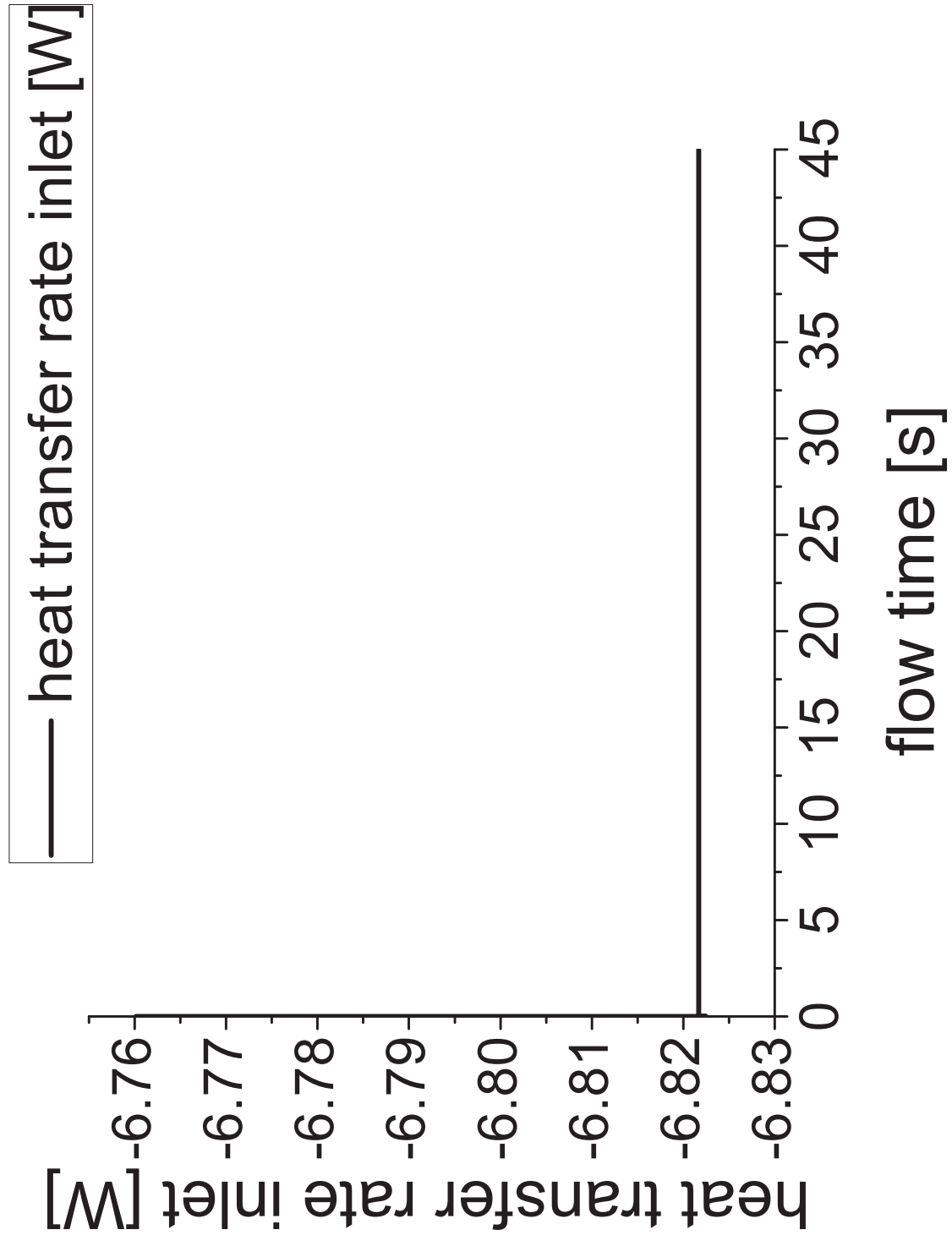


Figure 73: First 0.1 s of heat transfer at the inlet for the base model

$(x, y, z) = (5, 12.5, 5) \text{ mm}^3$, $A_{in} = 4.6 \cdot 10^{-7} \text{ m}^2$, $A_{out} = 25 \text{ m}^2$, Mesh: multi-zone, hexagonal, 0.1 mm, PCM2, $A_{mush} = 10^5$, $\Delta T = -10 \text{ K}$, $v_{in} = 0.4 \frac{\text{m}}{\text{s}}$

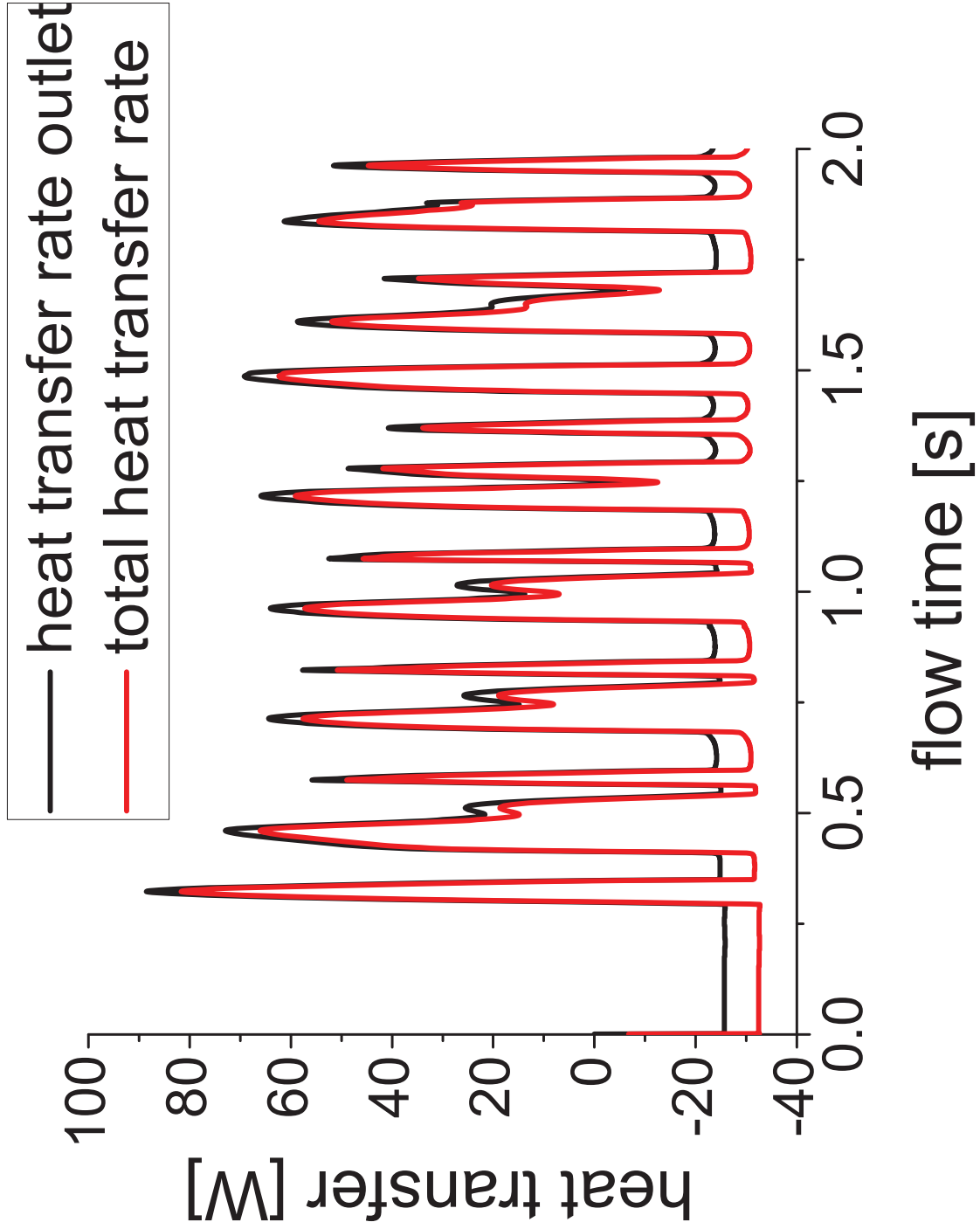


Figure 74: First 2 s of the heat transfer at the outlet, as well as the sum of inlet and outlet, for the base model

$(x, y, z) = (5, 12.5, 5) \text{ mm}$, $A_{in} = 4.6 \cdot 10^{-7} \text{ m}^2$, $A_{out} = 25 \text{ m}^2$, Mesh: multi-zone, hexagonal, 0.1 mm , PCM2, $A_{mush} = 10^5$, $\Delta T = -10 \text{ K}$, $v_{in} = 0.4 \frac{\text{m}}{\text{s}}$

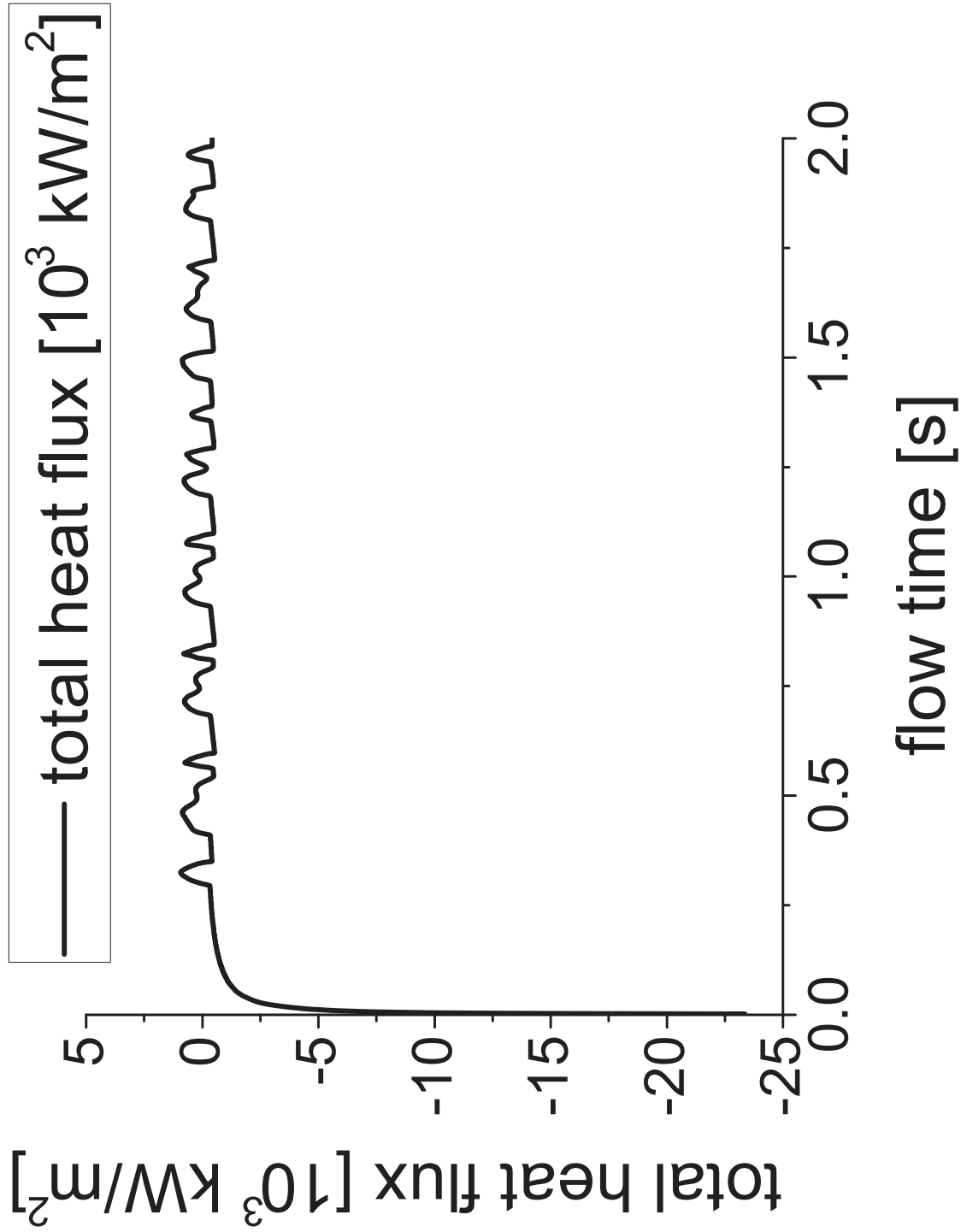


Figure 75: First 2s of the heat flux for the base model

$(x, y, z) = (5, 12.5, 5) \text{ mm}$, $A_{in} = 4.6 \cdot 10^{-7} \text{ m}^2$, $A_{out} = 25 \text{ m}^2$, Mesh: multi-zone, hexagonal, 0.1 mm , PCM2, $A_{mush} = 10^5$, $\Delta T = -10 \text{ K}$, $v_{in} = 0.4 \frac{\text{m}}{\text{s}}$

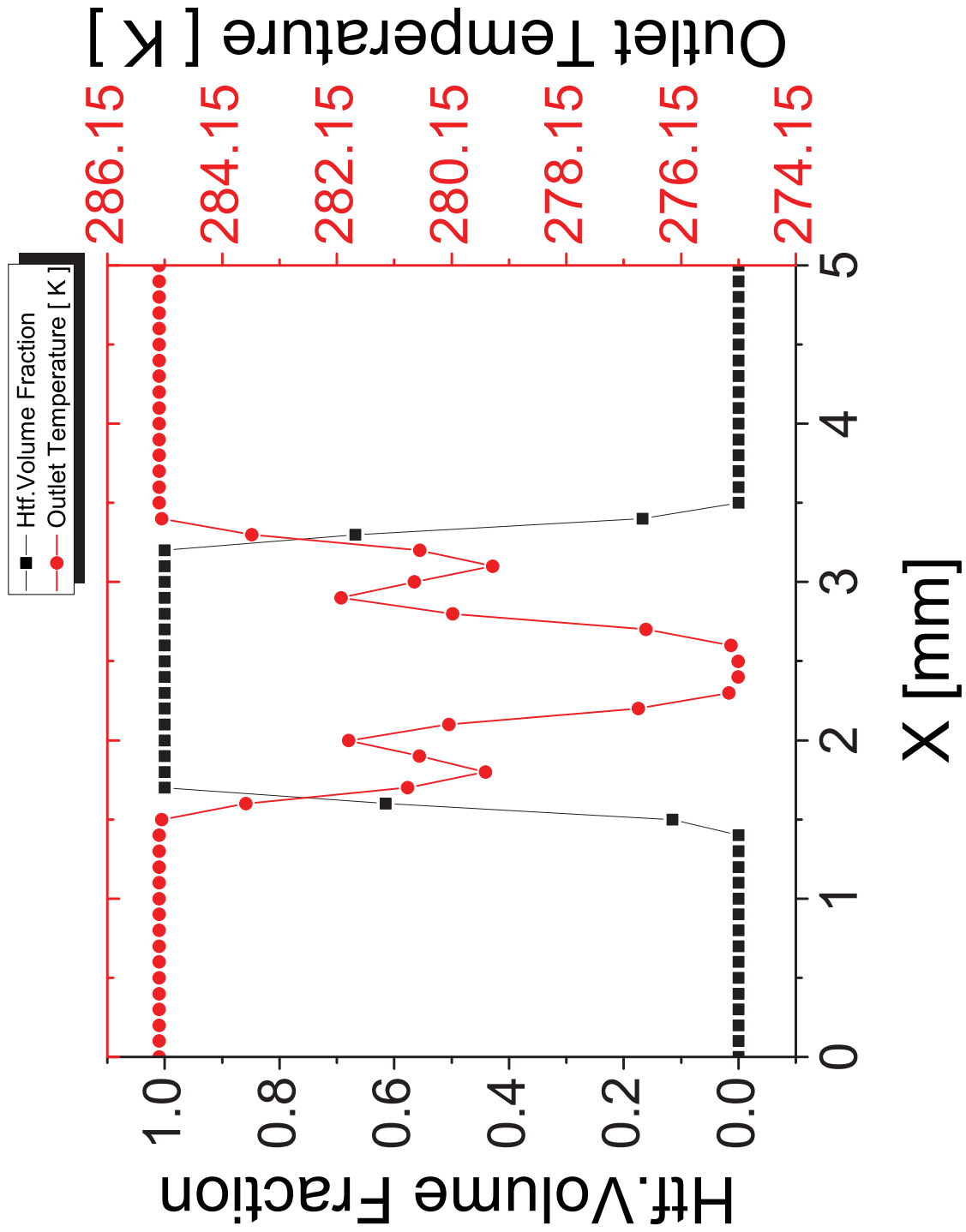


Figure 76: Outlet temperature side by side with the corresponding volume fraction
 $(x, y, z) = (5, 12.5, 5) \text{ mm}$, $A_{in} = 4.6 \cdot 10^{-7} \text{ m}^2$, $A_{out} = 25 \text{ m}^2$, Mesh: multi-zone, hexagonal, 0.1 mm, PCM2, $A_{mush} = 10^5$, $\Delta T = -10 \text{ K}$, $v_{in} = 0.4 \frac{\text{m}}{\text{s}}$, $(x, y, z) = ([0; 5], 12.5, 2.5) \text{ mm}$, time step 25.0 s

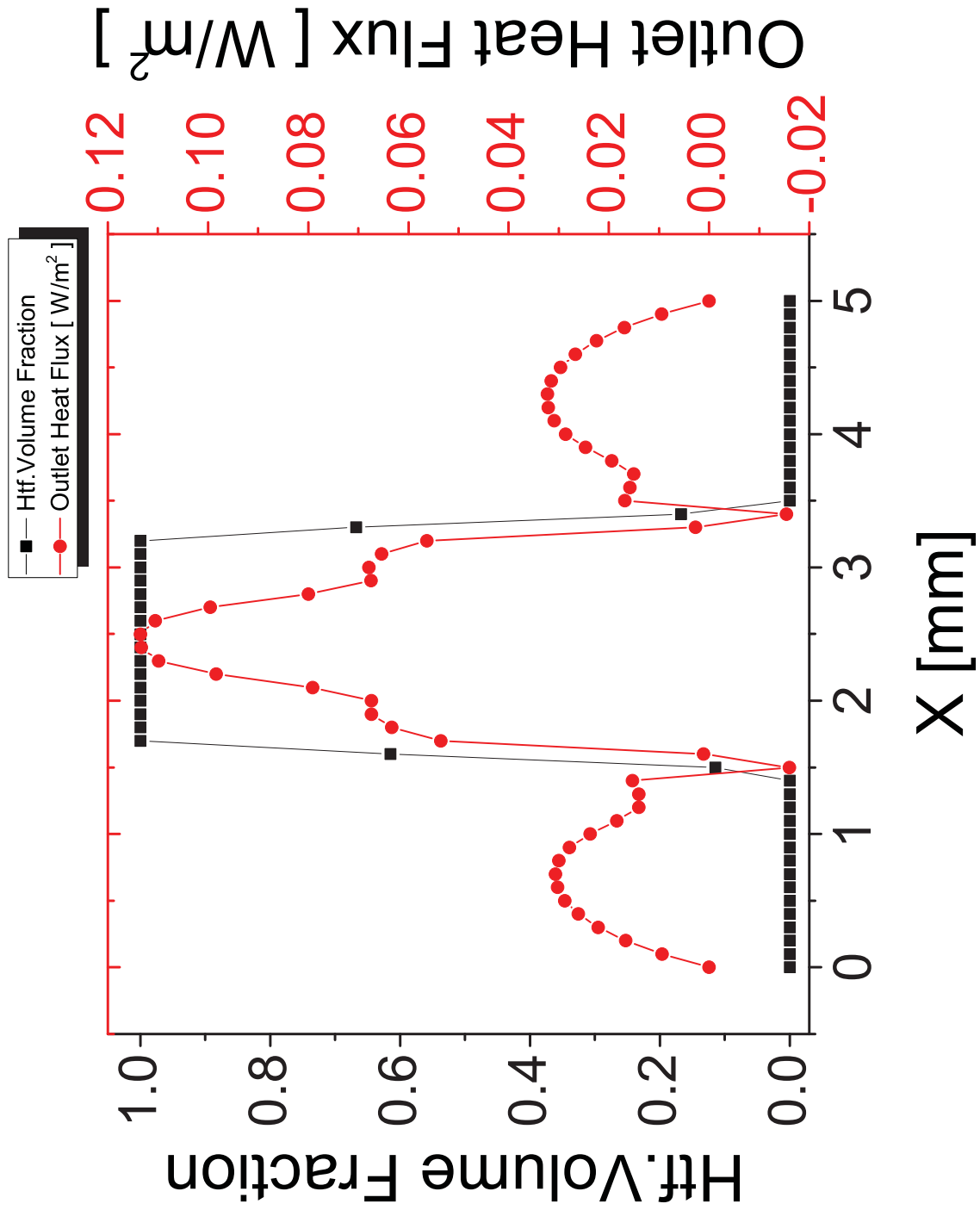


Figure 77: Heat flux side by side with the corresponding volume fraction

$(x, y, z) = (5, 12.5, 5) \text{ mm}$, $A_{in} = 4.6 \cdot 10^{-7} \text{ m}^2$, $A_{out} = 25 \text{ m}^2$, Mesh: multi-zone, hexagonal, 0.1 mm, PCM2, $A_{mush} = 10^5$, $\Delta T = -10 \text{ K}$, $v_{in} = 0.4 \frac{\text{m}}{\text{s}}$, $(x, y, z) = ([0; 5], 12.5, 2.5) \text{ mm}$, time step 25.0 s

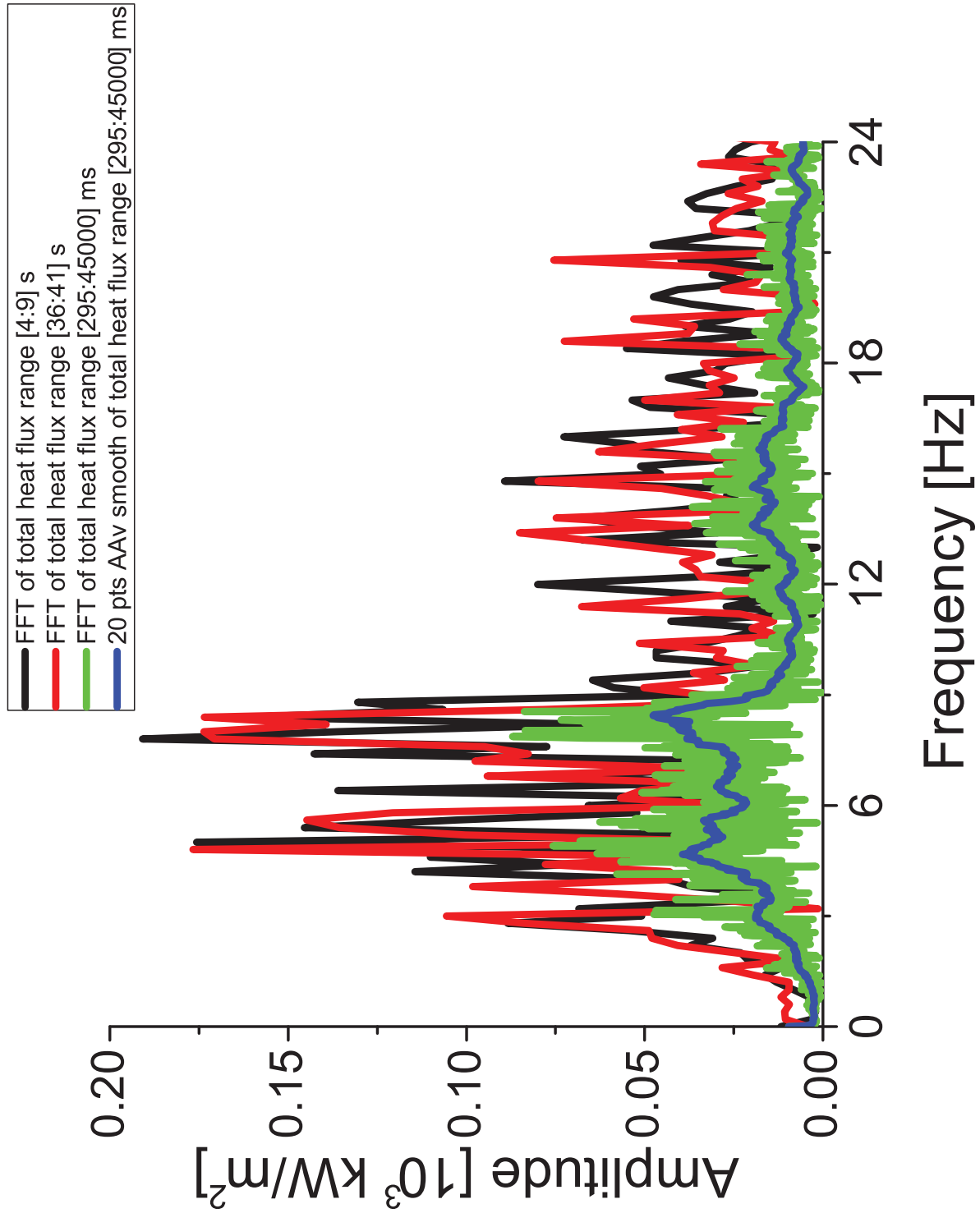


Figure 78: Amplitude and frequency of the Fourier transformations of three parts (each 5 s close to the beginning and close to the end, as well as one over the complete period) from the base model calculation and an additional a smoothed variant, average of 20 points, over the whole period for better visualisation of the global behaviour

$(x, y, z) = (5, 12.5, 5) \text{ mm}$, $A_{in} = 4.6 \cdot 10^{-7} \text{ m}^2$, $A_{out} = 25 \text{ m}^2$, Mesh: multi-zone, hexagonal, 0.1 mm, PCM2, $A_{mush} = 10^5$, $\Delta T = -10 \text{ K}$, $v_{in} = 0.4 \frac{\text{m}}{\text{s}}$

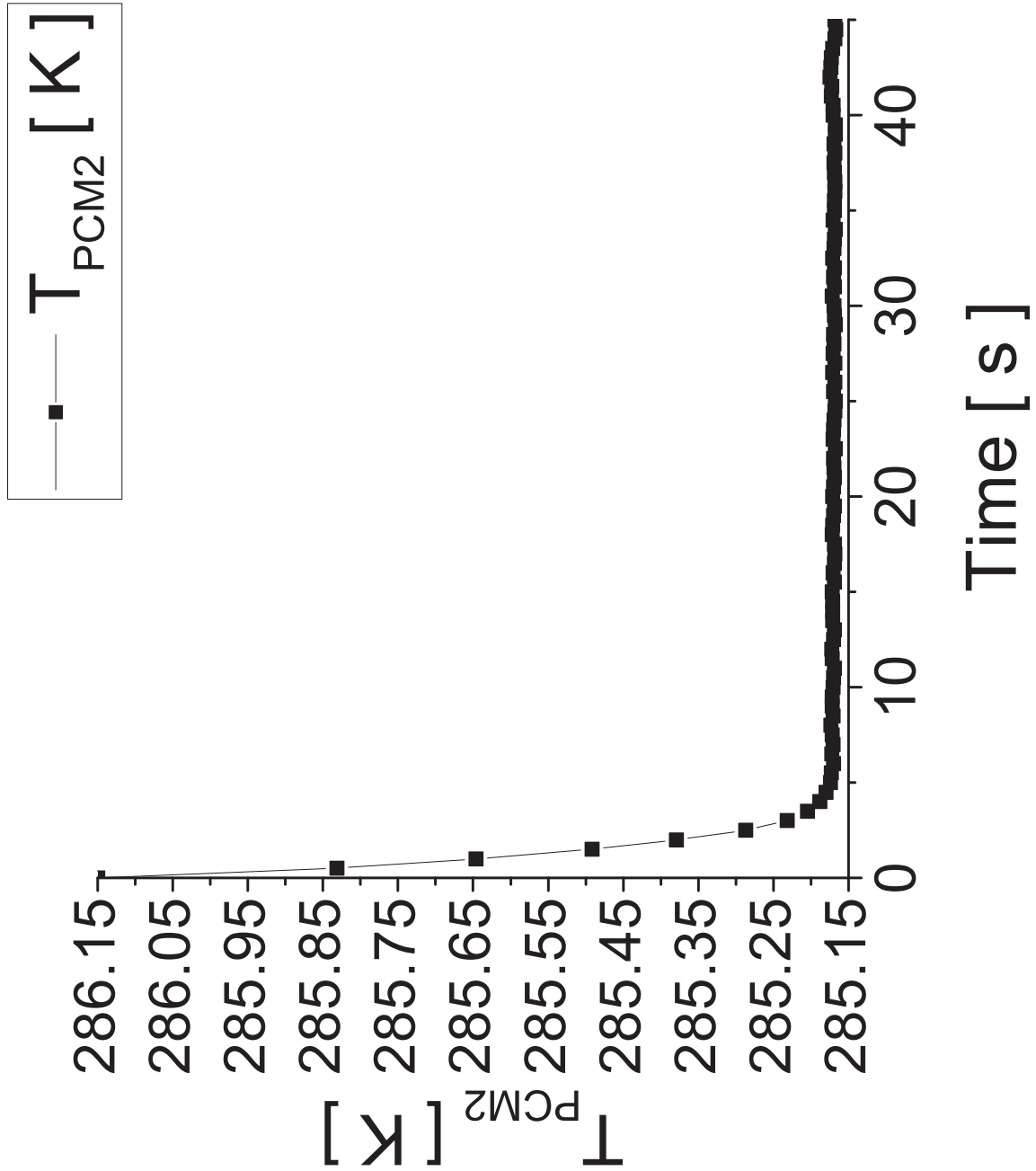


Figure 79: Average temperature of PCM2 As this had to be calculated via post-processing the value could only be resolved at each saved time step and therefore every 0.5 s

$(x, y, z) = (5, 12.5, 5) \text{ mm}$, $A_{in} = 4.6 \cdot 10^{-7} \text{ m}^2$, $A_{out} = 25 \text{ m}^2$, Mesh: multi-zone, hexagonal, 0.1 mm, PCM2, $A_{mush} = 10^5$, $\Delta T = -10 \text{ K}$, $v_{in} = 0.4 \frac{\text{m}}{\text{s}}$

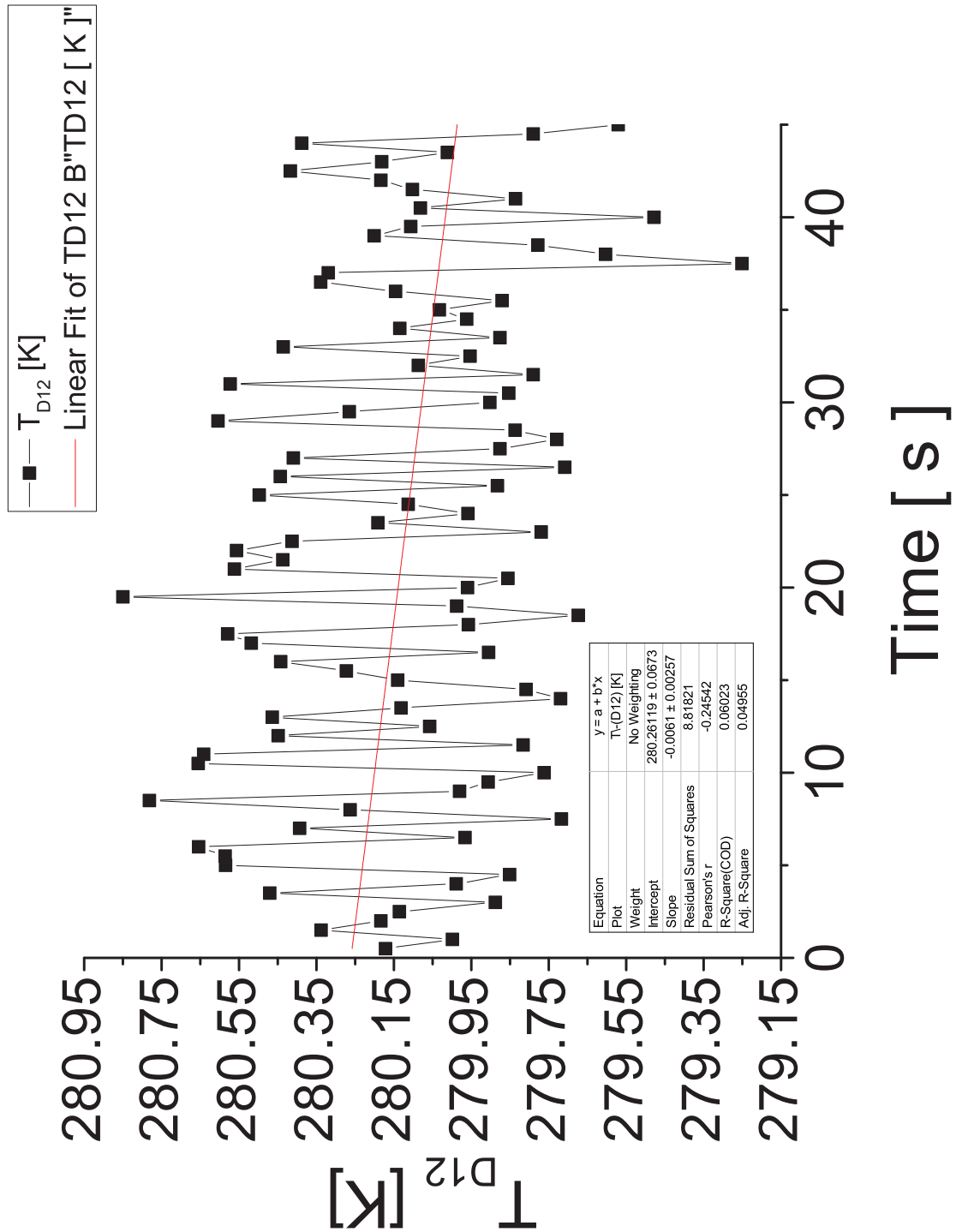


Figure 80: Average temperature of D12As this had to be calculated via post-processing the value could only be resolved at each saved time step and therefore every 0.5 s
 $(x, y, z) = (5, 12.5, 5) \text{ mm}$, $A_{in} = 4.6 \cdot 10^{-7} \text{ m}^2$, $A_{out} = 25 \text{ m}^2$, Mesh: multi-zone, hexagonal, 0.1 mm, PCM2, $A_{mush} = 10^5$, $\Delta T = -10 \text{ K}$, $v_{in} = 0.4 \frac{\text{m}}{\text{s}}$

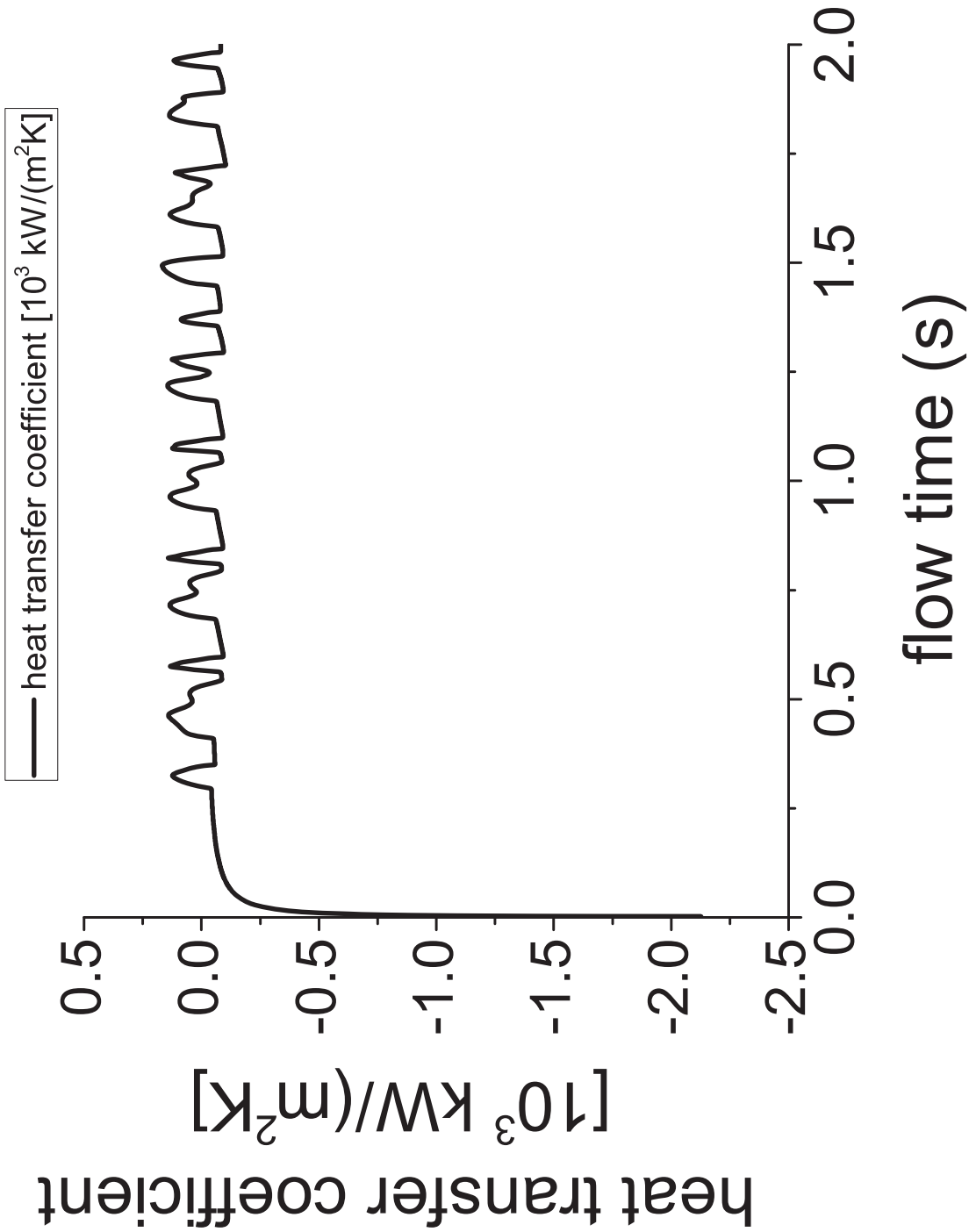


Figure 81: First 2 s of the heat transfer coefficient calculated by dividing each value of the total heat flux of fig. 33 by the difference between the corresponding values of the temperatures of PCM2 (fig. 39) and D12 (fig. 40) for the base model. Due to the lack of time resolution the temperature values had to be interpolated linearly in order to keep the time resolution as best as possible

$(x, y, z) = (5, 12.5, 5) \text{ mm}$, $A_{in} = 4.6 \cdot 10^{-7} \text{ m}^2$, $A_{out} = 25 \text{ m}^2$, Mesh: multi-zone, hexagonal, 0.1 mm, PCM2, $A_{mush} = 10^5$, $\Delta T = -10 \text{ K}$, $v_{in} = 0.4 \frac{\text{m}}{\text{s}}$

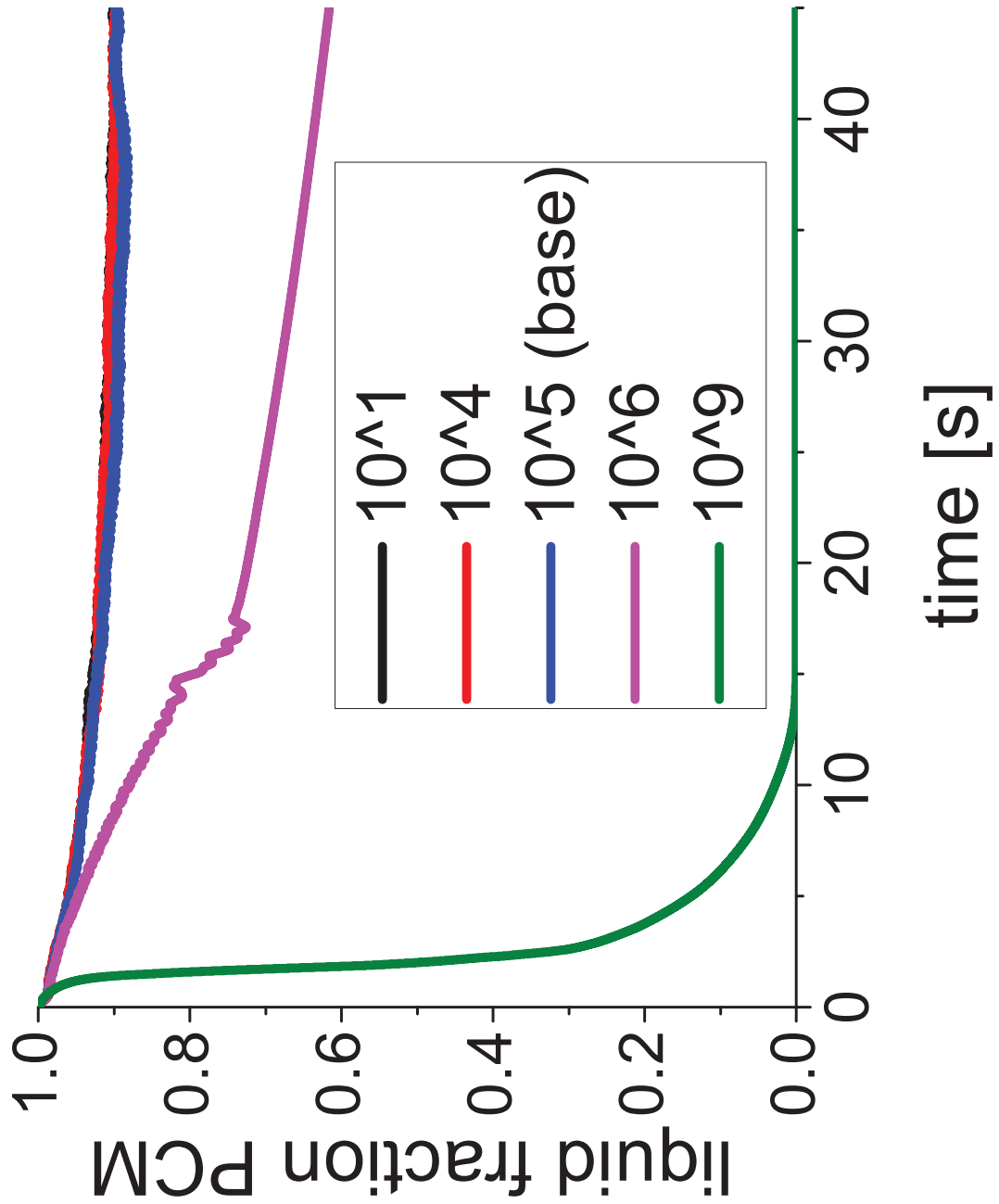


Figure 82: A comparison of the liquid-fraction for different mushy parameters
 $(x, y, z) = (5, 12.5, 5) \text{ mm}$, $A_{in} = 4.6 \cdot 10^{-7} \text{ m}^2$, $A_{out} = 25 \text{ m}^2$,
 Mesh: multi-zone, hexagonal, 0.1 mm, PCM2, $A_{mush} = (10^1, 10^4, 10^5(\text{base}), 10^6, 10^9)$,
 $\Delta T = -10 \text{ K}$, $v_{in} = 0.4 \frac{\text{m}}{\text{s}}$

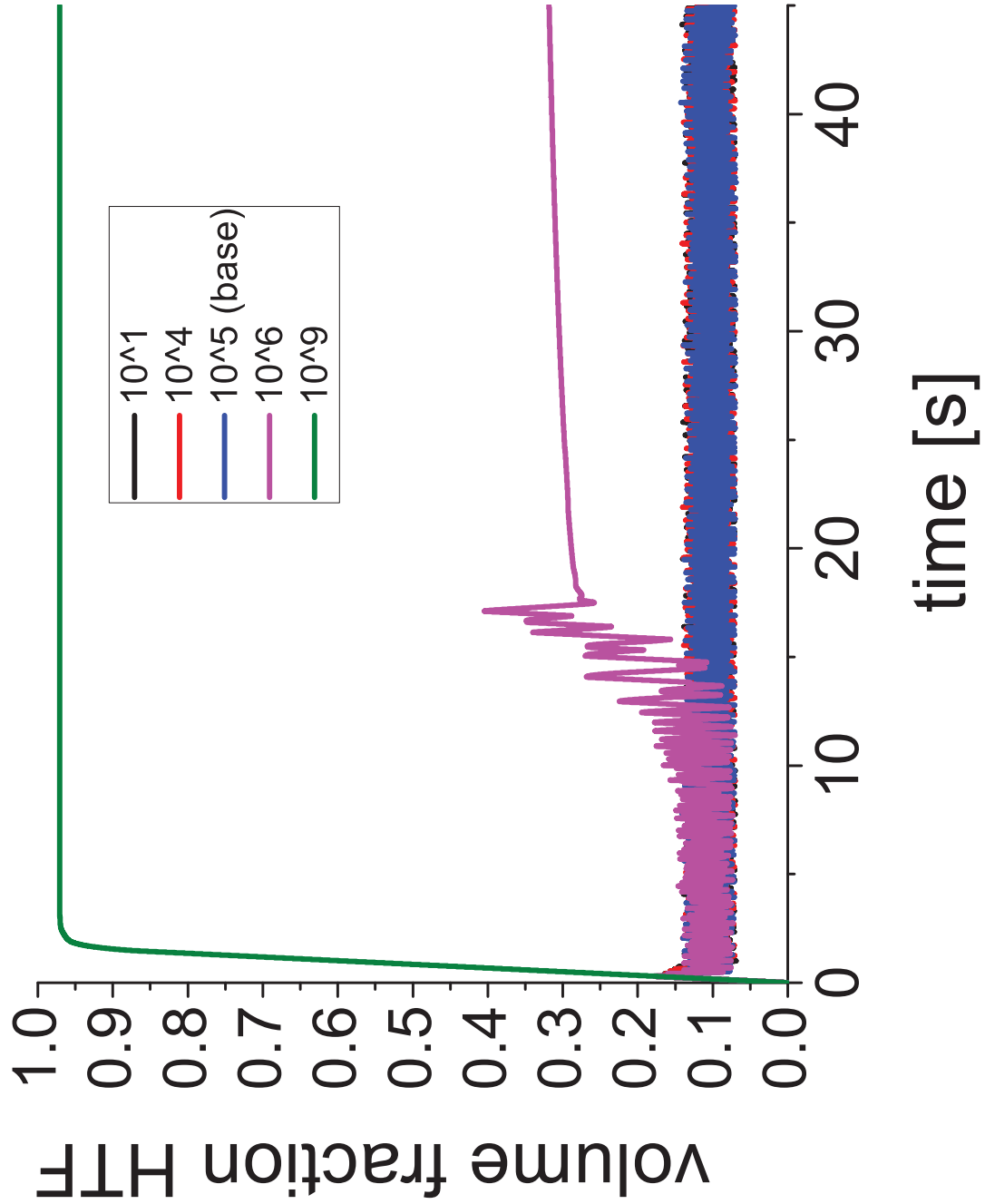


Figure 83: A comparison of volume-fraction for different mushy parameters

$(x, y, z) = (5, 12.5, 5) \text{ mm}$, $A_{in} = 4.6 \cdot 10^{-7} \text{ m}^2$, $A_{out} = 25 \text{ m}^2$,
 Mesh: multi-zone, hexagonal, 0.1 mm, PCM2, $A_{mush} = (10^1, 10^4, 10^5(\text{base}), 10^6, 10^9)$,
 $\Delta T = -10 \text{ K}$, $v_{in} = 0.4 \frac{\text{m}}{\text{s}}$

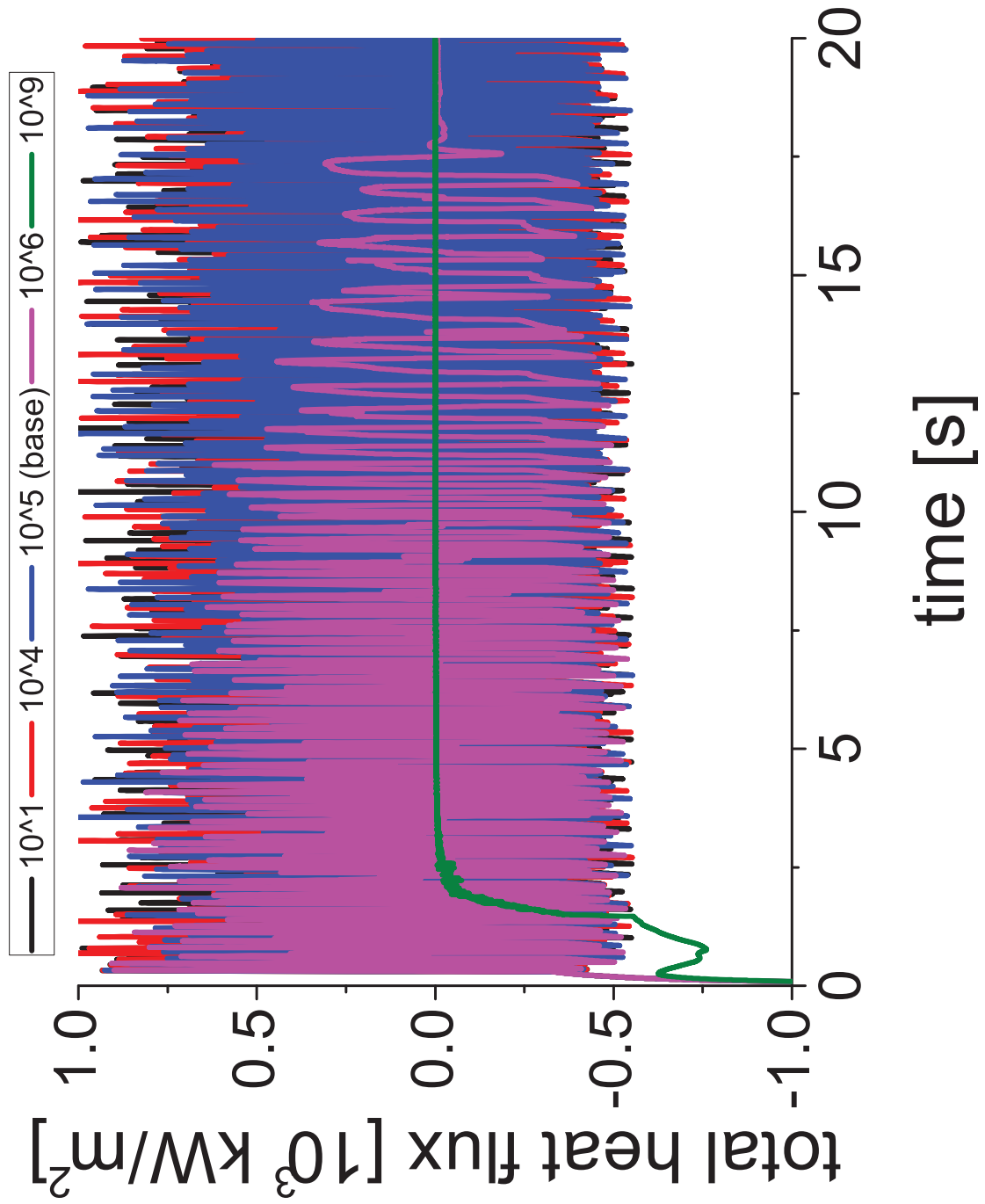


Figure 84: First 20 s of the heat flux for different mushy parameters

$(x, y, z) = (5, 12.5, 5) \text{ mm}$, $A_{in} = 4.6 \cdot 10^{-7} \text{ m}^2$, $A_{out} = 25 \text{ m}^2$,
 Mesh: multi-zone, hexagonal, 0.1 mm, PCM2, $A_{mush} = (10^1, 10^4, 10^5(\text{base}), 10^6, 10^9)$,
 $\Delta T = -10 \text{ K}$, $v_{in} = 0.4 \frac{\text{m}}{\text{s}}$

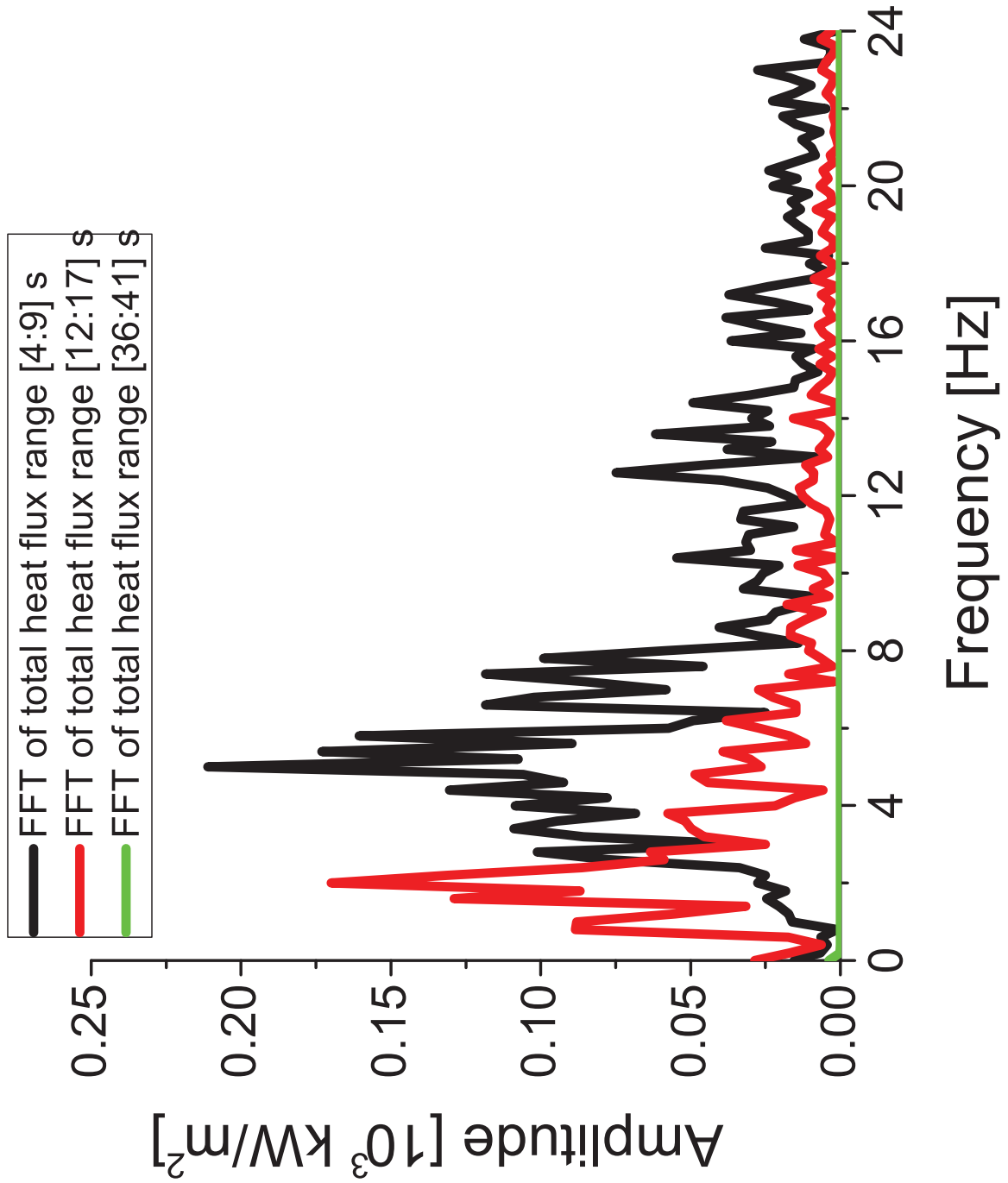


Figure 85: Amplitude and frequency of the Fourier transformations of 10^6 in three parts (each 5 s close to the beginning, before the stagnation and close to the end)

$(x, y, z) = (5, 12.5, 5) \text{ mm}$, $A_{in} = 4.6 \cdot 10^{-7} \text{ m}^2$, $A_{out} = 25 \text{ m}^2$,
Mesh: multi-zone, hexagonal, 0.1 mm, PCM2, $A_{mush} = 10^6$, $\Delta T = -10 \text{ K}$, $v_{in} = 0.4 \frac{\text{m}}{\text{s}}$

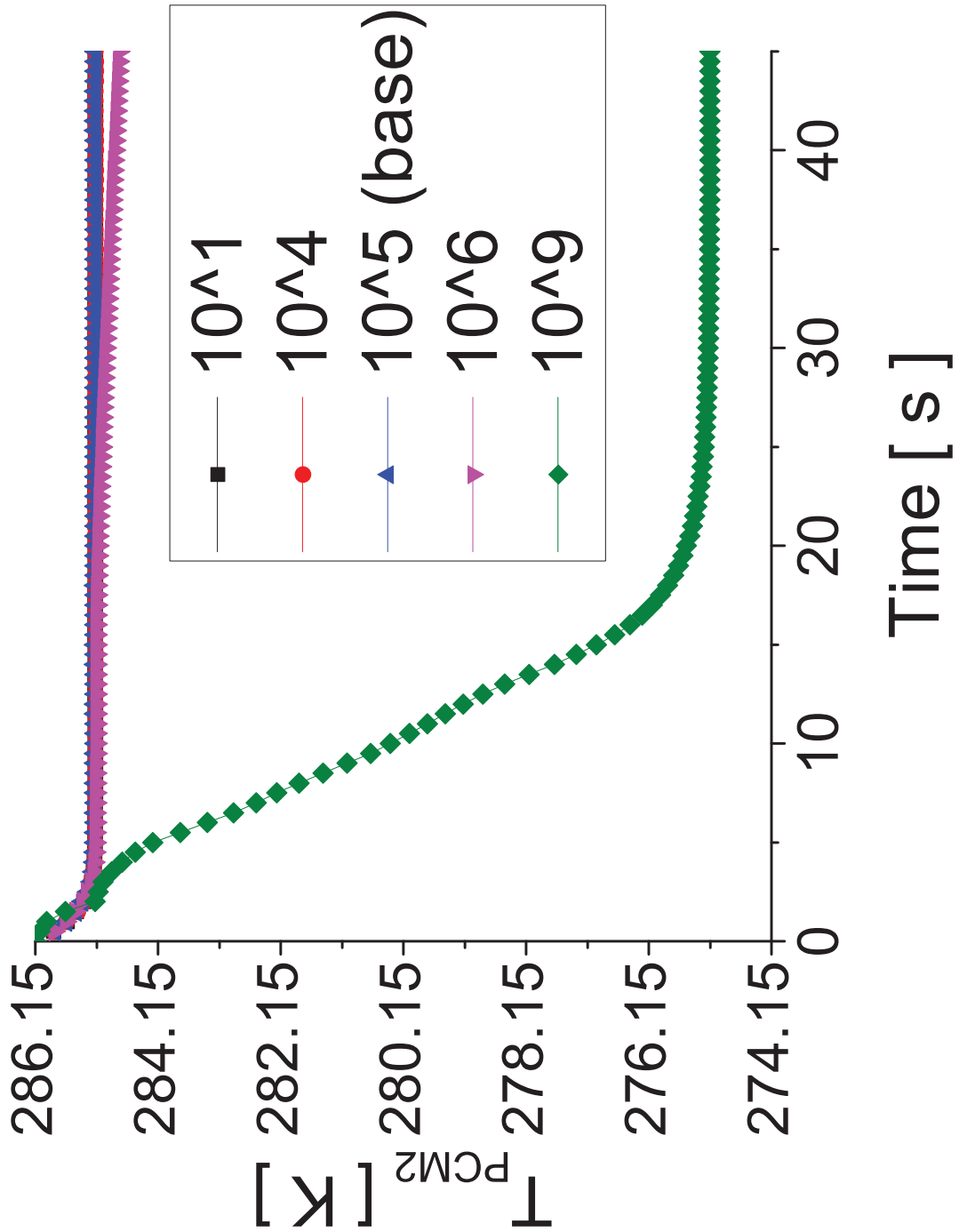


Figure 86: Average temperature of PCM2 for different mushy parameters

$(x, y, z) = (5, 12.5, 5) \text{ mm}$, $A_{in} = 4.6 \cdot 10^{-7} \text{ m}^2$, $A_{mush} = (10^1, 10^4, 10^5(\text{base}), 10^6, 10^9)$,
 Mesh: multi-zone, hexagonal, 0.1 mm , PCM2, $A_{mush} = 10^5$, $\Delta T = -10 \text{ K}$, $v_{in} = 0.4 \frac{\text{m}}{\text{s}}$

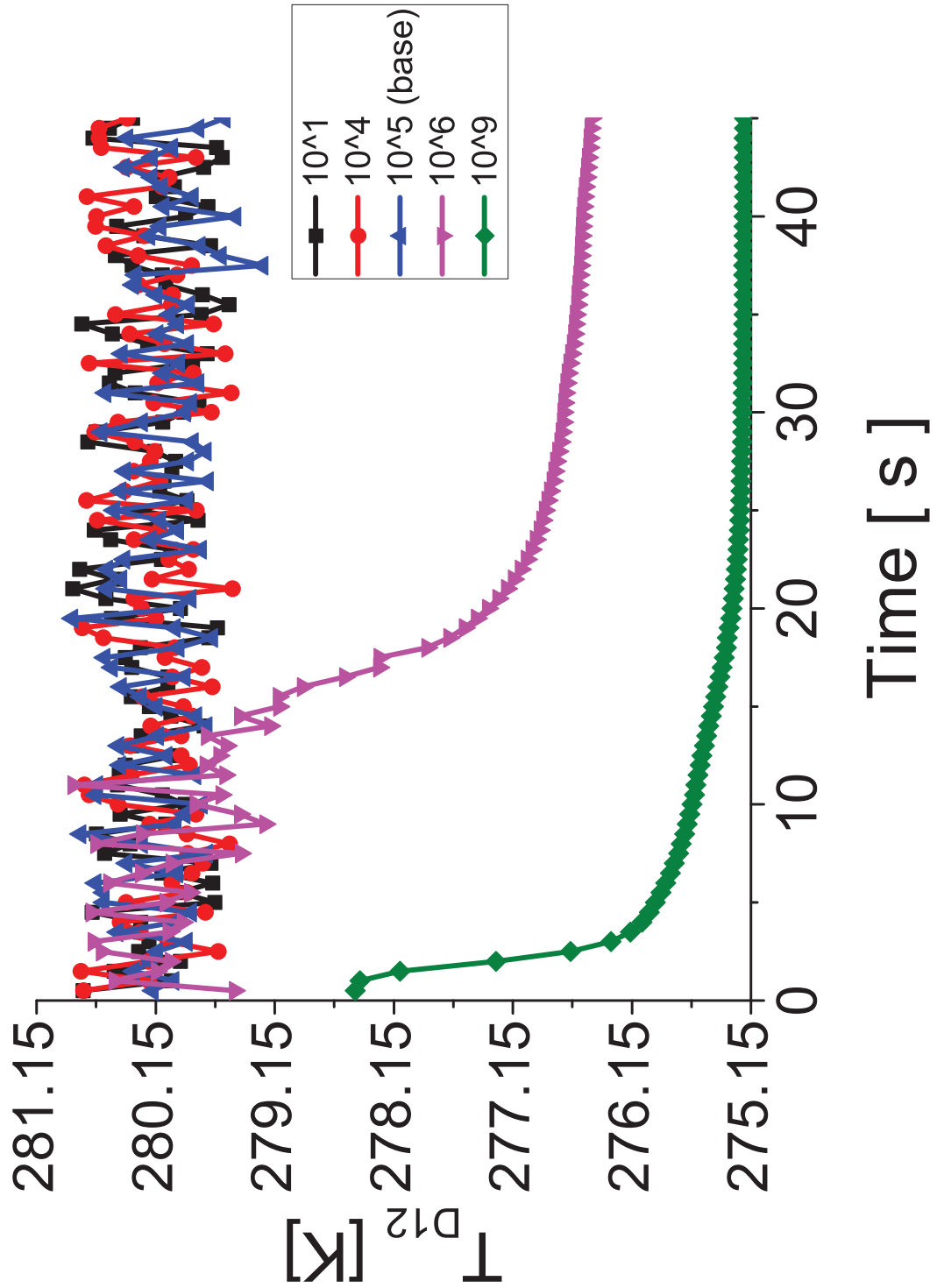


Figure 87: Average temperature of D12 for different mushy parameters

$(x, y, z) = (5, 12.5, 5) \text{ mm}$, $A_{in} = 4.6 \cdot 10^{-7} \text{ m}^2$, $A_{out} = 25 \text{ m}^2$,
 Mesh: multi-zone, hexagonal, 0.1 mm, PCM2, $A_{mush} = (10^1, 10^4, 10^5(\text{base}), 10^6, 10^9)$,
 $\Delta T = -10 \text{ K}$, $v_{in} = 0.4 \frac{\text{m}}{\text{s}}$

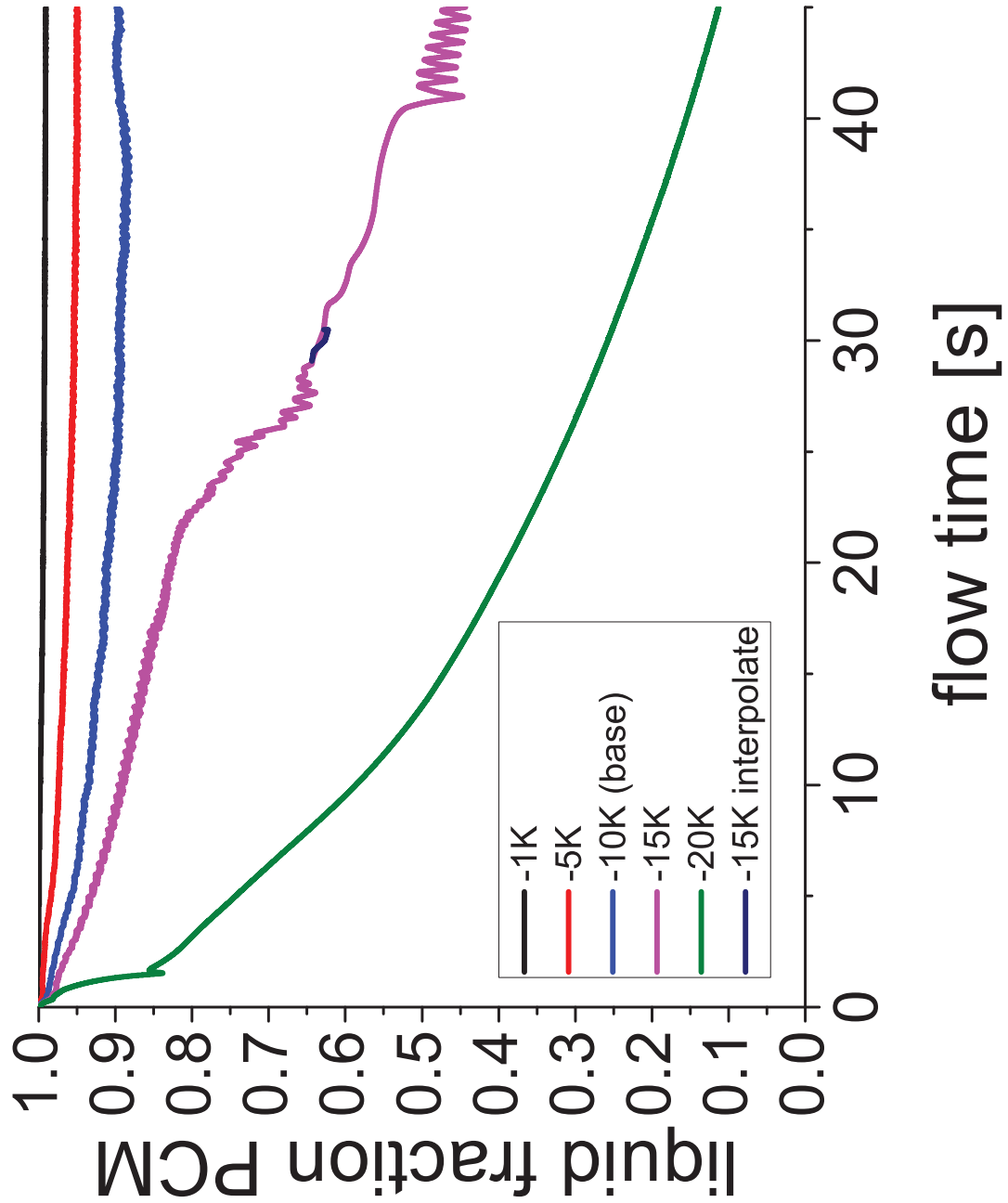


Figure 88: A comparison of the liquid-fraction for distinct temperature differences between inlet and solidification temperature, with only the inlet temperature changed. As explained in the running text the data in the range of [29.080;30499] was not present, except for full 0.5 s. The missing values had to be linearly interpolated and highlighted in this diagram

$(x, y, z) = (5, 12.5, 5) \text{ mm}, \quad A_{in} = 4.6 \cdot 10^{-7} \text{ m}^2, \quad A_{out} = 25 \text{ m}^2,$
 Mesh: multi-zone, hexagonal, 0.1 mm, PCM2, $A_{mush} = 10^5,$
 $\Delta T = (-1, -5, -10(\text{base}), -15, -20) \text{ K}, \quad v_{in} = 0.4 \frac{\text{m}}{\text{s}}$

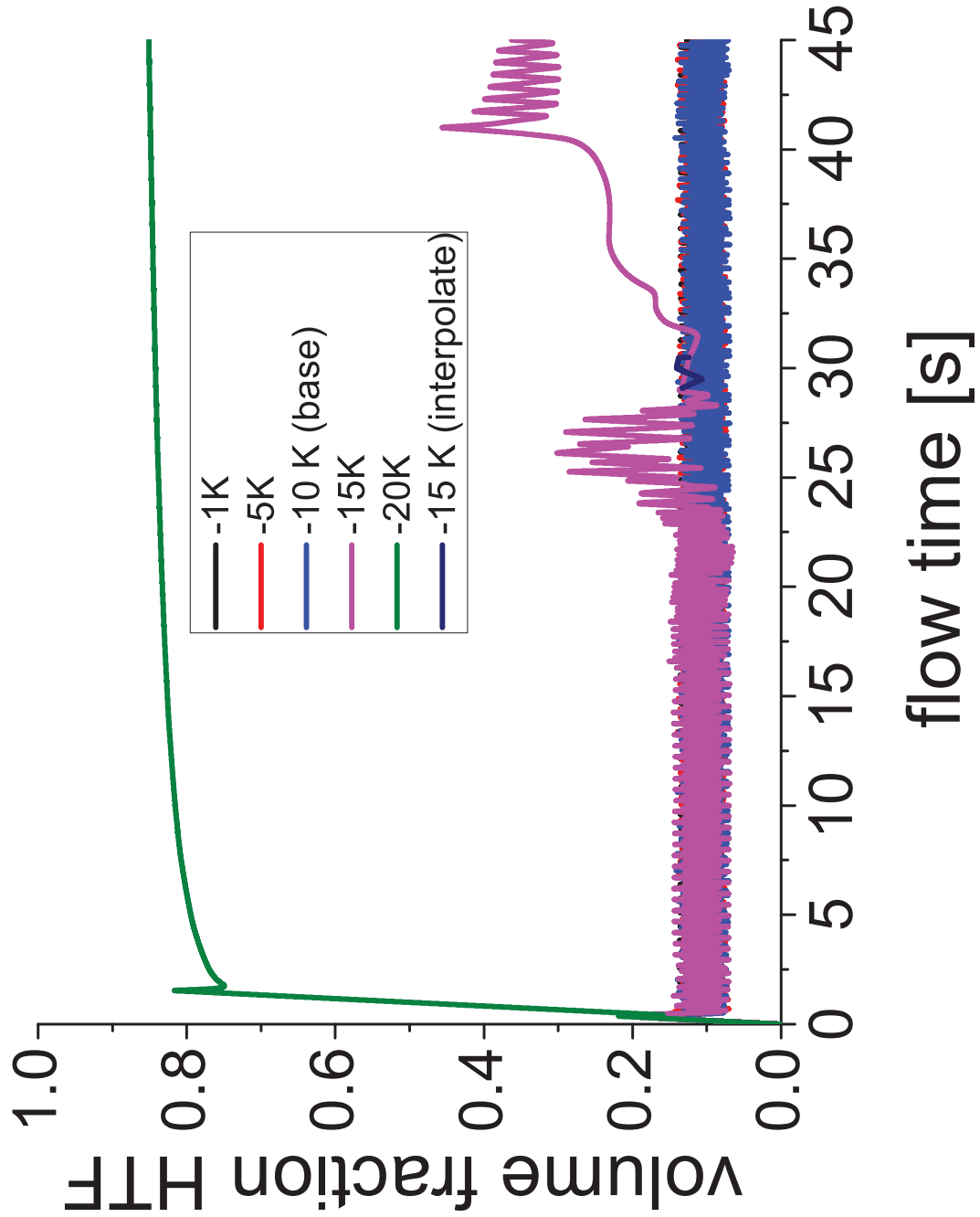


Figure 89: A comparison of the volume-fraction for distinct temperature differences between inlet and solidification temperature, with only the inlet temperature changed. As explained in the running text the data in the range of [29.080;30499] was not present, except for full 0.5 s. The missing values had to be linearly interpolated and highlighted in this diagram

$(x, y, z) = (5, 12.5, 5) \text{ mm}, \quad A_{in} = 4.6 \cdot 10^{-7} \text{ m}^2, \quad A_{out} = 25 \text{ m}^2,$
 Mesh: multi-zone, hexagonal, 0.1 mm, PCM2, $A_{mush} = 10^5,$
 $\Delta T = (-1, -5, -10(\text{base}), -15, -20) \text{ K}, \quad v_{in} = 0.4 \frac{\text{m}}{\text{s}}$

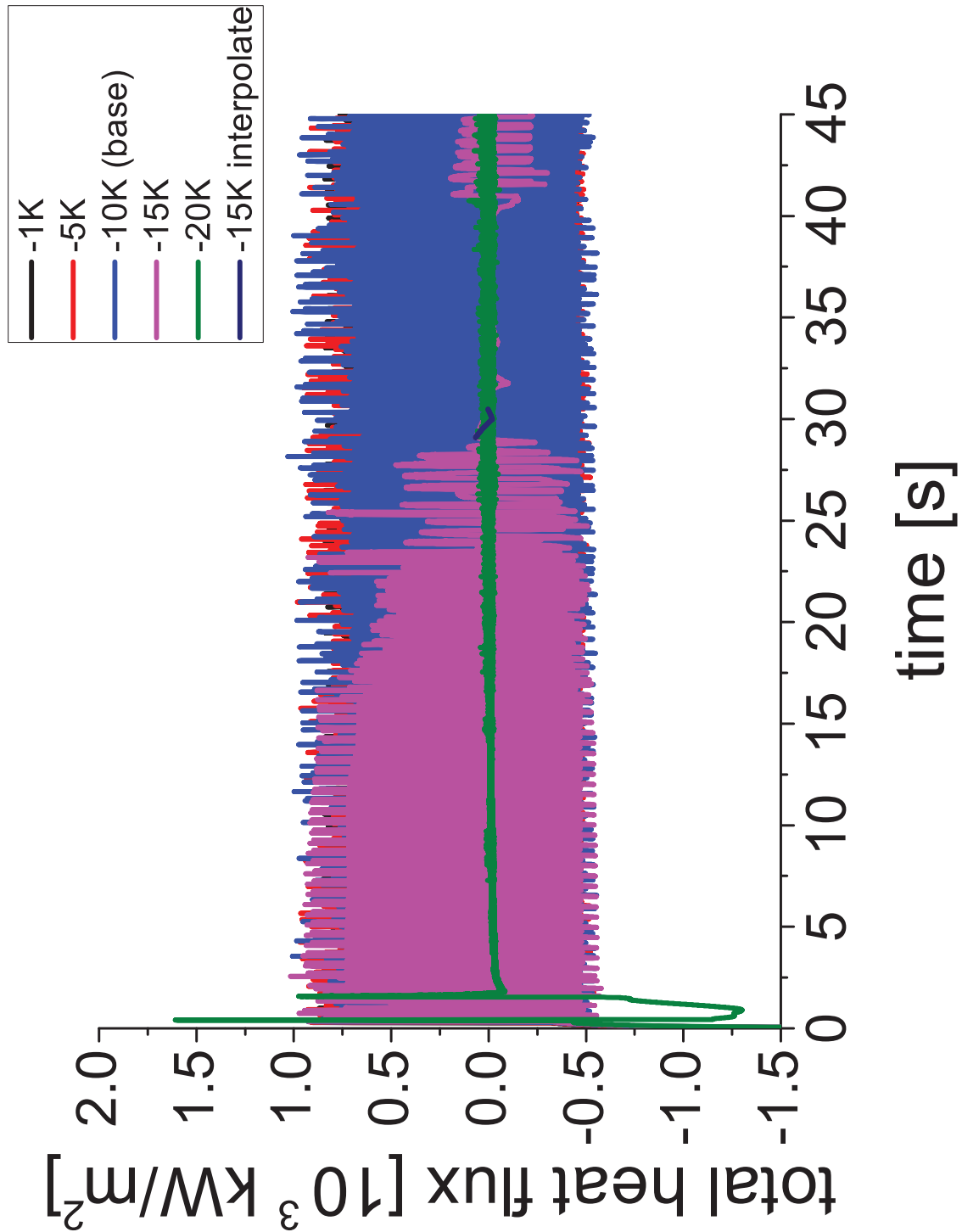


Figure 90: Heat flux for distinct temperature differences between inlet and solidification temperature, with only the inlet temperature changed. As explained in the running text the data in the range of $[29.080;30499]$ was not present, except for full 0.5 s. The missing values had to be linearly interpolated and highlighted in this diagram

$$\begin{aligned}
 (x, y, z) &= (5, 12.5, 5) \text{ mm}, & A_{in} &= 4.6 \cdot 10^{-7} \text{ m}^2, & A_{out} &= 25 \text{ m}^2, \\
 \text{Mesh: multi-zone, hexagonal, } 0.1 \text{ mm}, & \text{PCM2}, & A_{mush} &= 10^5, \\
 \Delta T &= (-1, -5, -10(\text{base}), -15, -20) \text{ K}, & v_{in} &= 0.4 \frac{\text{m}}{\text{s}}
 \end{aligned}$$

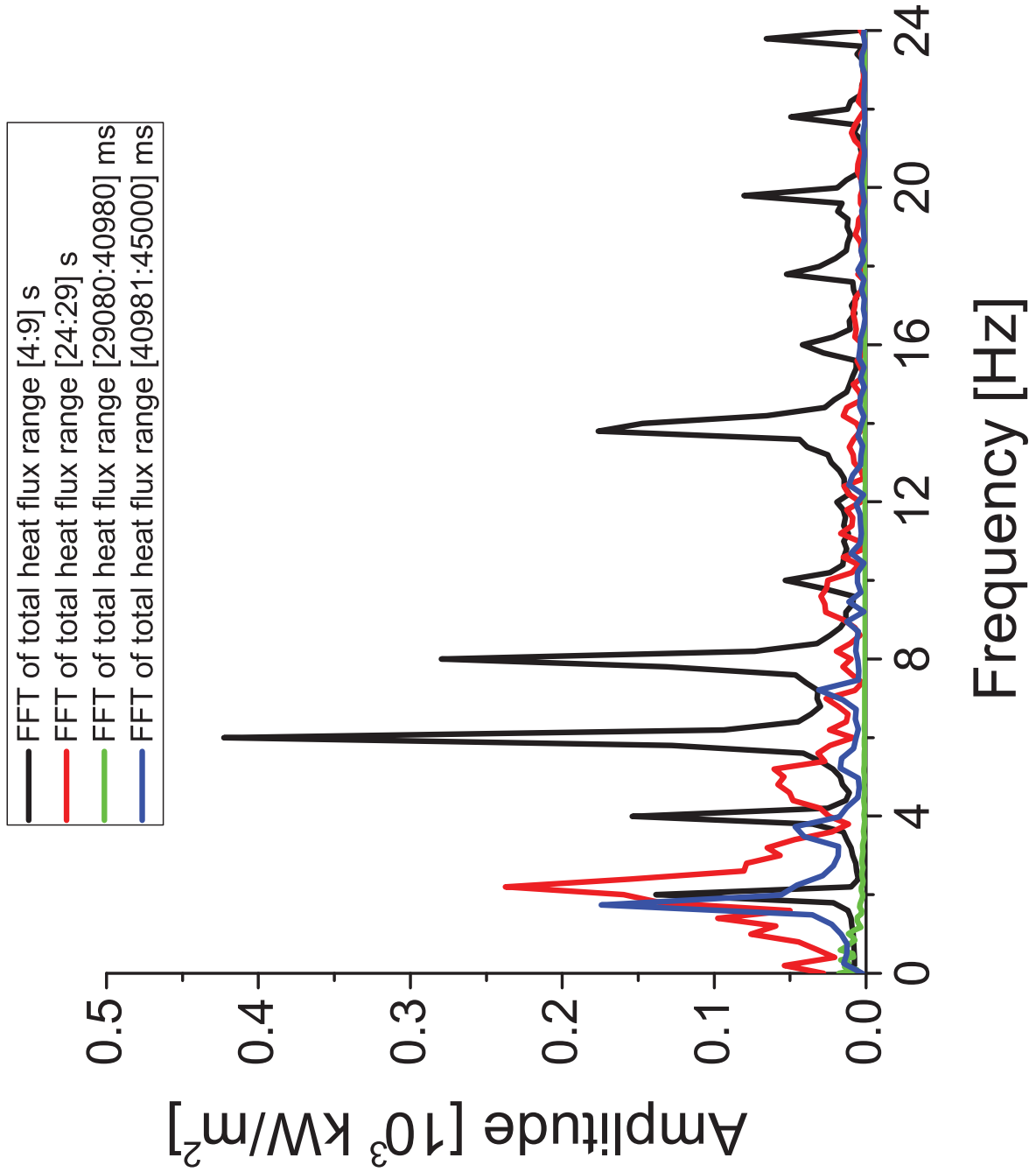


Figure 91: Amplitude and frequency of the Fourier transformations of $\Delta T = -15\text{ K}$ in four parts (5 s at the beginning, 5 s before the stagnation, the whole stagnation area and the complete final part)

$(x, y, z) = (5, 12.5, 5)\text{ mm}$, $A_{in} = 4.6 \cdot 10^{-7}\text{ m}^2$, $A_{out} = 25\text{ m}^2$,
Mesh: multi-zone, hexagonal, 0.1 mm , PCM2, $A_{mush} = 10^5$, $\Delta T = -15\text{ K}$, $v_{in} = 0.4\frac{\text{m}}{\text{s}}$

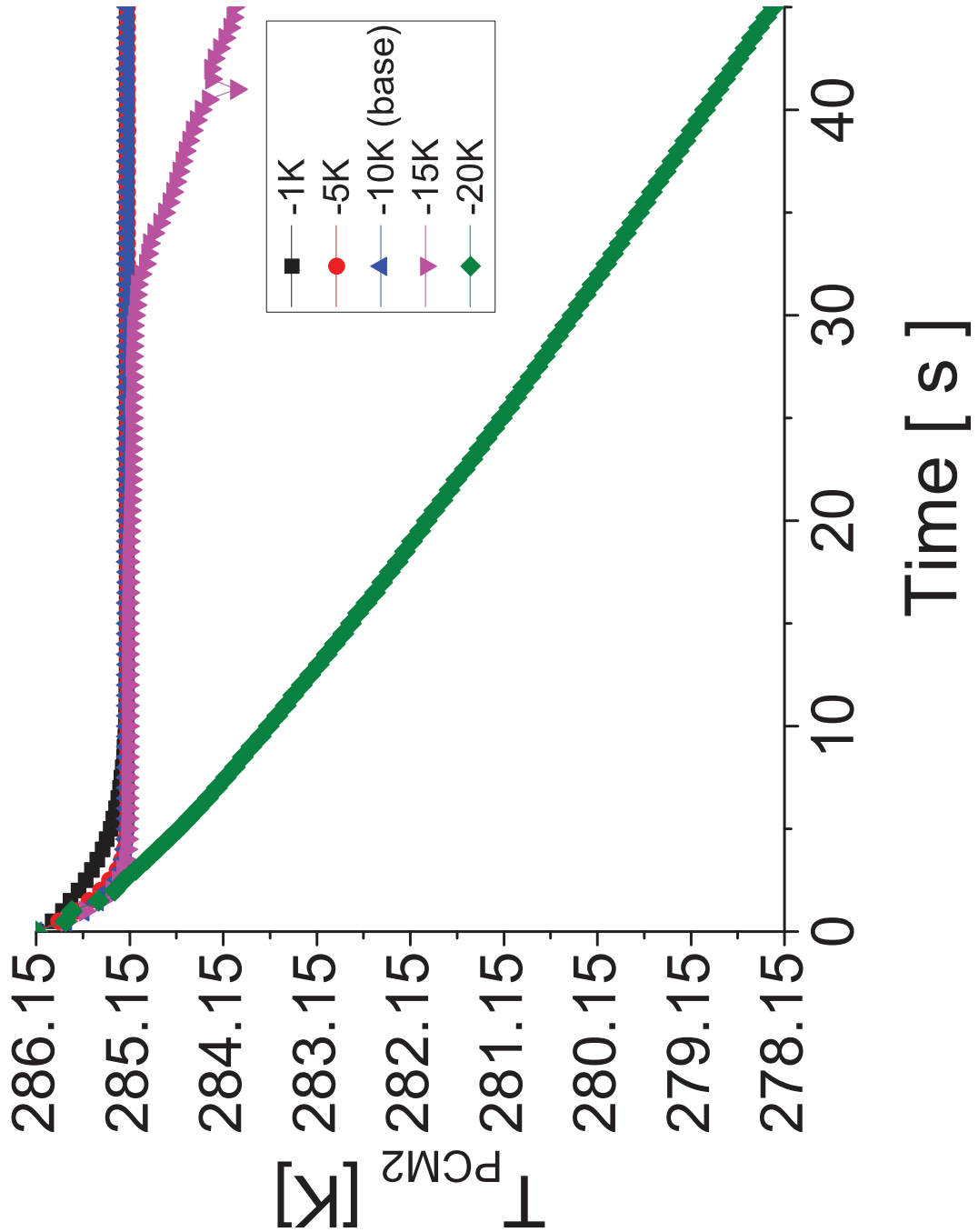


Figure 92: Average temperature of PCM2 for distinct temperature differences between inlet and solidification temperature

$(x, y, z) = (5, 12.5, 5) \text{ mm}, \quad A_{in} = 4.6 \cdot 10^{-7} \text{ m}^2, \quad A_{out} = 25 \text{ m}^2,$
 Mesh: multi-zone, hexagonal, 0.1 mm, PCM2, $A_{mush} = 10^5,$
 $\Delta T = (-1, -5, -10(\text{base}), -15, -20) \text{ K}, \quad v_{in} = 0.4 \frac{\text{m}}{\text{s}}$

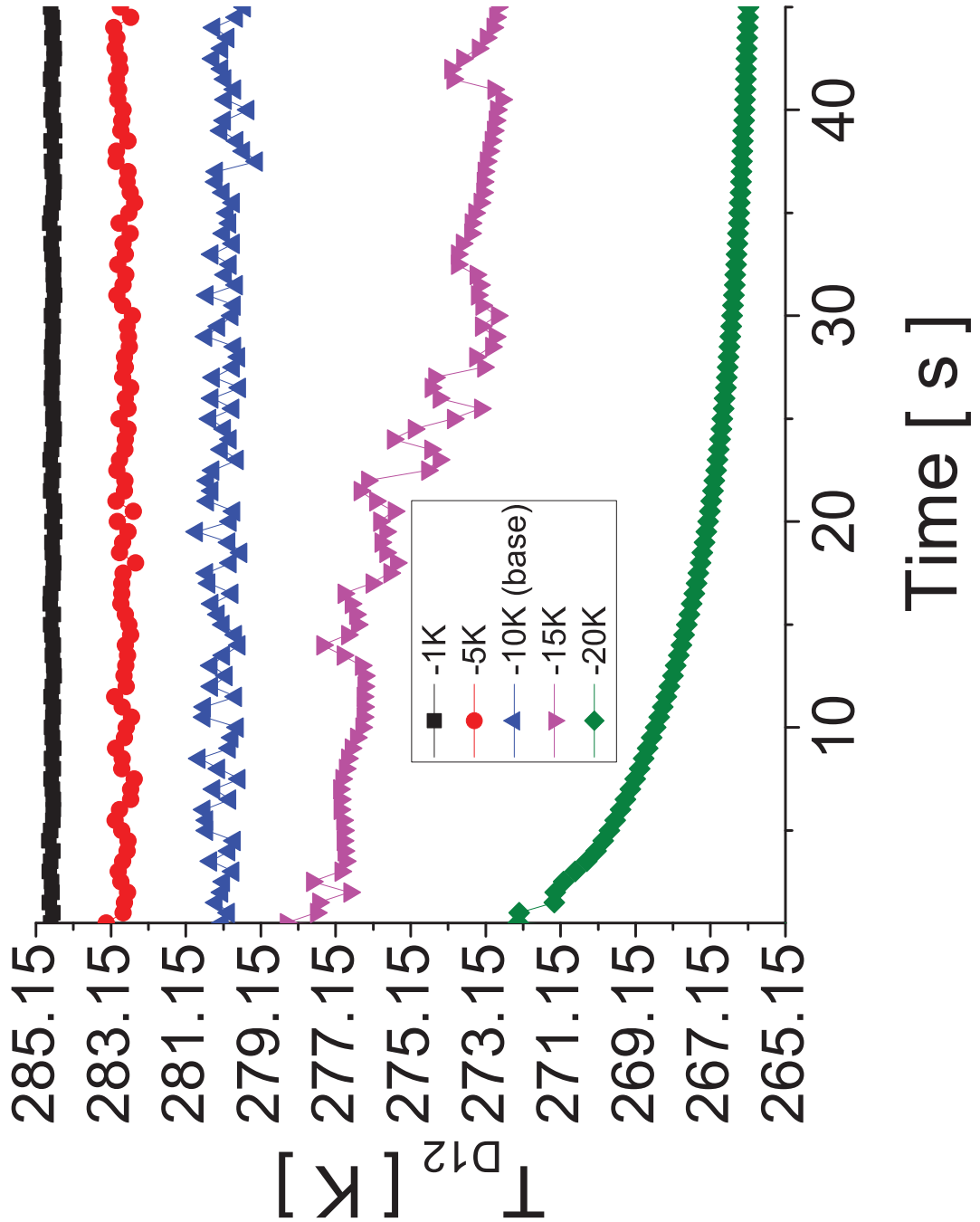


Figure 93: Average temperature of D12 for distinct temperature differences between inlet and solidification temperature, with only the inlet temperature changed

$(x, y, z) = (5, 12.5, 5) \text{ mm}, \quad A_{in} = 4.6 \cdot 10^{-7} \text{ m}^2, \quad A_{out} = 25 \text{ m}^2,$
 Mesh: multi-zone, hexagonal, 0.1 mm, PCM2, $A_{mush} = 10^5,$
 $\Delta T = (-1, -5, -10(\text{base}), -15, -20) \text{ K}, \quad v_{in} = 0.4 \frac{\text{m}}{\text{s}}$

References

- [1] Originlab/all books/origin help /18 signal processing. <https://www.originlab.com/doc/Origin-Help/FFT>. [Online; accessed 26-September-2019].
- [2] Schmelzwärme. <https://www.chemie.de/lexikon/Schmelzw%C3%A4rme.html>. [Online; accessed 19-October-2019].
- [3] *ANSYS FLUENT 12.0 User's Guide*, 2009. [Online; accessed 3-August-2019].
- [4] *Erneuerbare Energien, 9th edition*. Martin Kaltschmitt, Wolfgang Streicher, Andreas Wiese, Springer Vieweg Verlag, 2013.
- [5] Vsc - vienna scientific cluster. <http://typo3.vsc.ac.at/systems/vsc-3/>, 2014. [Online; accessed 21-September-2019].
- [6] *ANSYS FLUENT 18.0 User's Guide*, 2017. [Online; accessed 20-March-2019].
- [7] *ANSYS FLUENT 19.1 User's Guide*, 2018. [Online; accessed 20-March-2019].
- [8] Heat transfer coefficient. https://en.wikipedia.org/wiki/Heat_transfer_coefficient, 2019. [Online; accessed 20-March-2019].
- [9] Andreas Anmann. Aufbau, Inbetriebnahme und Messungen an einem Latentwärmespeicher mit Direktkontakt-Wärmeübertragung. 2017.
- [10] Andreas Anmann. Erfassung des Wärmedurchgangskoeffizienten aufsteigender Öltropfen in einer wässrigen Phase mit CFD unter Verwendung des Volume of Fluid Ansatzes. 2017.
- [11] Richard Bellman and Ralph H. Pennington. Effects of surface tension and viscosity on taylor instability. *Quarterly of Applied Mathematics*, 1 July 1954, Vol.12(2), pp.151-162. The model used is that of two fluids of infinite depth, with the interface initially in the form of a sine wave with amplitude small compared to wave length. The fluids are considered incompressible, and only the linear terms in the equations of hydrodynamics are used. The first four sections discuss the effects of surface tension and viscosity. The fifth gives a few numerical results to illustrate the main points of the preceding sections.
- [12] Stefan Braun. *Strömungslehre für TPh*. Technische Universität Wien, Institut für Strömungsmechanik und Wärmeübertragung E322, 2014.
- [13] Ali Cherom Kheirabadi and Dominic Groulx. The effect of the mushy-zone constant on simulated phase change heat transfer. 05 2015.
- [14] Roland Clift, John R. [VerfasserIn] Grace, and Martin E. [VerfasserIn] Weber. *Bubbles, drops, and particles*. Academic Press, New York, N.Y., [u.a.].

- [15] Wolfgang Demtröder. *Experimentalphysik*, volume 5. Springer, 2008.
- [16] JR Grace, T Wairegi, and J Brophy. Break-up of drops and bubbles in stagnant media. *The Canadian Journal of Chemical Engineering*, 56(1):3–8, 1978.
- [17] J. J. Milón Guzman and S. L. Braga. Supercooling water in cylindrical capsules. *International Journal of Thermophysics*, 26(6):1781, Nov 2005.
- [18] C.W Hirt and B.D Nichols. Volume of fluid (vof) method for the dynamics of free boundaries. *Journal of Computational Physics*, 39(1):201 – 225, 1981.
- [19] Stefan Krimmel, Anastasia Stamatiou, Jörg Worlitschek, and Heimo Walter. Experimental characterization of the heat transfer in a latent direct contact thermal energy storage with one nozzle in labor scale. *International Journal of Mechanical Engineering*, 3, 2018.
- [20] Günter Jakob Lauth and Jürgen Kowalczyk. *Einführung in die Physik und Chemie der Grenzflächen und Kolloide*. Springer, 2016.
- [21] Bernard J Meister and George F Scheele. Prediction of jet length in immiscible liquid systems. *AIChE Journal*, 15(5):689–699, 1969.
- [22] Hiroshi Nogami, Kosuke Ikeuchi, and Kiko Sato. Fundamental flow characteristics in a small columnar latent heat storage bath. *ISIJ international*, 50(9):1270–1275, 2010.
- [23] Leiv Magne Siqueland and Svein Skjaeveland. Derivations of the young–laplace equation. *Unpublished research*. <https://doi.org/10.13140/RG.2.4485.5768>, 2014.
- [24] John William Strutt and Lord Rayleigh. On the instability of jets. *Proc. London Math. Soc.*, 10(4), 1878.
- [25] Friedrich Lindner und Kurt Scheunemann. Die entwicklung eines dynamischen glaubersalz-latentwärmespeichers bis zur serienreife, 1981.
- [26] Thorsten Urbaneck. *Kältespeicher: Grundlagen, Technik, Anwendung*. Walter de Gruyter, 2012.
- [27] Peiding Wang. Numerical analysis of droplet formation and transport of a highly viscous liquid. 2014.